Plasma assisted hybrid friction stir welding of similar and dissimilar materials

Deepak Kumar Yaduwanshi

Department of Mechanical Engineering

Indian Institute of Technology Guwahati

2017

Plasma assisted hybrid friction stir welding of similar and dissimilar materials

submitted in partial fulfillment of the requirements
for the degree of

Doctor of Philosophy

by

Deepak Kumar Yaduwanshi

(11610316)

Supervisors:

Swarup Bag and Sukhomay Pal

Department of Mechanical Engineering

Indian Institute of Technology Guwahati

2017

Dedicated to

My mother, teachers, two elder sisters, elder brother and my wife

Department of Mechanical Engineering
Indian Institute of Technology Guwahati
Guwahati-781039
INDIA

CERTIFICATE

It is certified that the work contained in the thesis entitled **"Plasma assisted hybrid friction stir welding of similar and dissimilar materials"** submitted by **Mr. Deepak Kumar Yaduwanshi** to the Indian Institute of Technology Guwahati for the award of the degree of doctor of Philosophy has been carried out under my supervision in the Department of Mechanical Engineering, Indian Institute of Technology Guwahati. This work has not been submitted elsewhere for the award of any other degree or diploma.

The thesis, in my opinion, has reached the standard fulfilling the requirements for the award of degree of Doctor of Philosophy in accordance with the regulations of the Institute.

Date: 21th Feb, 2017

Swarup Bag

and

Sukhomay Pal

Department of Mechanical Engineering, Indian Institute of Technology Guwahati, Guwahati, Assam 781039, India

Declaration

I declare that the present written submission is my thoughts in my own words. I have adequately cited and referenced the original sources, where others' work have been involved. I also declare that I have followed to all principles of academic morality and honesty and have neither fabricated nor falsified any idea/data in the present thesis. I realize that any defilement of the above will be cause for disciplinary action by the Institute and can also induce disciplinary action from the sources which have thus not been properly cited.

(Deepak Kumar Yaduwanshi)

Date: 21th Feb, 2017 Roll No: 11610316

Abstract

Friction stir welding (FSW) is considered to be the most significant development of metal joining processes in recent era. FSW gained significant attention as a solid-state joining process of aluminum alloys, but now its application is extended to relatively harder metals and also to some extent to plastics. However, it is quite challenging task to achieve a defect-free joint for dissimilar materials due to the difference in their thermo-physical properties. On the other hand, it is important to understand the synergistic interaction of physical phenomena of FSW involved during welding of similar or dissimilar materials because it have its own practical significance. Models of increasing complexity and sophistication have been used beneficially in exploring and understanding the underlying physics of the FSW process. However, FSW has encountered a number of challenges in the welding of materials with intermediate and higher melting points. Therefore, hybridizing the FSW process using a low cost plasma arc is developed to investigate the feasibility of solid state joining of dissimilar materials like commercially pure copper and aluminum. The controlled energy input into the system by introducing an extra heat source (here plasma) may overcome the loss of heat from copper, reduce the difference in plasticization temperature and enhance the material flow along with the reduction of plunging force.

This thesis work is primarily motivated to develop plasma assisted hybrid FSW (P-FSW) process for joining of similar and dissimilar materials and the validation of the experimental results with the development of physics based numerical model. At first major efforts are put forward to experimentally investigate the heat transfer process in P-FSW process for joining both similar and dissimilar materials. The thermal history influences the mechanical properties and microstructural changes that decide the final weld joint quality. In addition, different tool profiles also influence the mechanical and microstructural characterization of friction stir welded aluminum alloy due to variation in material flow pattern during welding. A comparative study between FSW and P-FSW put forward the fundamental advantages of hybrid welding process. However, tool-offset is one of the most significant parameters during joining of dissimilar materials by FSW process. An investigation was carried out on the effect of tool offset towards thermal history, welding force, weld joint morphology, material flow pattern, and mechanical properties of the weld joint. It was found that offsetting towards aluminium side along with a

plasma-assisted heat source is an effective way to address one of the most important difficulties in aluminium-copper solid-state welding process. The offset influences the amount of intermetallic at the joint interface and in-effect impacts on final strength and material flow behaviour. There exists optimum continuous layer of intermetallic that produces the maximum weld joint strength. The specimen welded with optimum tool offset shows the highest strength using 55 A plasma current in hybrid FSW process.

Quantitative calculation by a sophisticated mathematical model of hybrid friction stir welding for dissimilar materials is a daunting task due to complex issues like mixed property in the weld zone, flow mixing action and solid state phase transformation. A 3D finite element based phenomenological model is developed to study various aspects of P-FSW between aluminum and copper. A dedicated heat generation model at various contact conditions between tool and workpiece, and a Gaussian distributed heat flux from plasma arc is used for the simulation. In weld zone, the impression of time-varying functionally graded material (FGM) is used for material behavior. The numerical model results are validated with experimental measurement of P-FSW in terms of time–temperature history and computed isotherm of nugget zone.

Keywords: Friction stir welding, hybrid friction stir welding, plasma assisted friction stir welding, preheating, finite element method, heat transfer analysis, dissimilar material joining.

CONTENTS

No.	Title	Page No.
	Abstract	**i-ii**
	Contents	**iii-vi**
	List of Figures	**vii-xix**
	List of Tables	**xxi-xxii**
	Nomenclature	**xxiii-xxviii**
1	**Introduction**	**1-12**
	1.0 General background	1
	1.1 FSW process	2
	1.1.1 Limitation of FSW process	5
	1.2 Hybrid FSW process	7
	1.3 Research Objectives	9
	1.4 Layout of thesis	10
2	**Literature Survey**	**13-63**
	2.0 General background	13
	2.1 Heat transfer in friction stir welding	14
	2.1.1 Experimental investigation	17
	2.1.2 Mathematical model	20
	2.1.3 Representation of heat source	24
	2.1.4 Flow stress analysis	28
	2.2 Material flow behavior	29

No.		Title	Page No.
	2.3	Hybrid friction stir welding	34
		2.3.1 Electrically assisted FSW (EAFSW)	35
		2.3.2 Induction assisted FSW (IAFSW)	36
		2.3.3 Laser assisted FSW (LAFSW)	37
		2.3.4 Arc assisted FSW (AAFSW)	39
		2.3.5 Ultrasonic vibration assisted FSW (UAFSW)	40
		2.3.6 Other thermally assisted FSW	42
	2.4	Design and performance of FSW tool	43
	2.5	Dissimilar material joint	49
		2.5.1 Mechanical properties and process parameters	49
		2.5.2 Formation Mechanism of IMCs	51
	2.6	Microstructural study	54
	2.7	Summary	60
	2.8	Scope of present work	62
3	**Theoretical Background**		**65-91**
	3.0	Introduction	65
	3.1	Heat transfer model	67
		3.1.1 Governing equations and boundary conditions	68
		3.1.2 Heat generation model by different tool geometries	70
		3.1.3 Hybrid heat source model	75
		3.1.4 Finite element discretization	78

No.		Title	Page No.
	3.1.5	Analytical model of strain and strain rate in weld zone	80
	3.2	Material property for dissimilar materials	85
	3.3	Computational aspects	88
	3.4	Summary	91
4	**Experimental Investigation**		**93-154**
	4.0	Introduction	93
	4.1	Friction stir welding	93
	4.1.1	Experimental set-up	94
	4.1.2	Non-symmetry in thermal history during FSW	99
	4.1.3	Effect of tool pin profile during FSW	103
	4.2	Hybrid FSW	114
	4.2.1	Experimental set-up	114
	4.2.2	Effect of preheating on thermal and mechanical properties of similar joint	118
	4.2.3	Dissimilar welding	131
	4.3	Experimental data taken from literature	152
	4.4	Summary	153
5	**Results and Discussion**		**154-214**
	5.0	Introduction	154
	5.1	Observation from experimental investigation	156
	5.2	Numerical model and material properties	157

No.	Title	Page No.
	5.2.1 Model geometry	158
	5.2.2 Calibration of numerical model	159
	5.2.3 Material properties	161
	5.2.4 Identification of model parameters	163
	5.3 Heat transfer analysis	165
	5.3.1 Reliability of the process	165
	5.3.2 Heat transfer for joining similar materials	175
	5.3.3 Strain rate and grain size	188
	5.4 Process efficiency of hybrid FSW	194
	5.5 Effect of tool off-set for dissimilar materials	197
	5.6 Cooling rate and microstructure	208
	5.7 Summary	212
6	**Conclusions and future scope**	**215-219**
	6.0 Introduction	215
	6.1 Conclusions of the Present Work	216
	6.2 Scope of future work	218
	References	**221-246**
	Bibliography	**247**
	List of Publications	**249-250**
	Acknowledgments	**251**

List of Figures

Figure No.	Caption	Page no.
1.1	Basic principal of FSW.	3
1.2	Schematic representation of FSW process [10].	4
1.3	Cylindrical threaded pin type probe.	5
1.4	Basic principle of plasma-assisted friction stir welding of dissimilar material joint.	8
2.1	A conceptual model for the process variables related to heat generation in FSW.	15
2.2	(a) Schematic of mutual dependencies between generated heat and dominant influencing parameters (b) Partial algorithm for generated heat estimation.	17
2.3	Schematic view of tool geometry with applied linear heat source on tool shoulder in 2D thermal model.	27
2.4	(a) FSW zones of different mechanical process and (b) The mechanical interacting these processes.	30
2.5	Flow-partitioned deformation zone geometries forming within the extrusion zone.	31
2.6	Schematic illustration of electrically assisted FSW process.	35
2.7	Schematic illustration of principle of laser assisted friction stir welding [151].	38
2.8	Schematic illustration of principle of dissimilar hybrid FSW process using GTAW as preheating source.	40
2.9	Different method to apply ultrasonic vibration during FSW process [162-165].	41
2.10	Hot gas stream assisted FSW setup using a nitrogen stream to preheat the workpieces [20].	43
2.11	Different FSW tools (a) fixed, (b) adjustable and (c) self-reacting [12].	44

Figure No.	Caption	Page no.
2.12	Summarizes the typical shoulder outer surfaces, the bottom end surfaces and the end features [176].	45
2.13	Different re-entrant features, flutes, threads and or flats on pin surface [184-185].	47
2.14	SEM image of Cu-Al interface layer and IMCs [228].	54
2.15	Transverse section of friction stir weld showing different regions of the weld. HAZ, heat-affected zone; TMAZ, thermos-mechanically affected zone and weld nugget [1, 4].	55
3.1	Schematic illustration of primary and secondary heat affected zones and mechanical deformation zone: (a) Isometric view (b) Top view.	66
3.2	Schematic illustration of thermal boundary condition used in heat transfer model.	69
3.3	Schematic illustration of nomenclature of straight pin tool.	73
3.4	Illustration of nomenclature of taper cylindrical pin profile.	74
3.5	Schematic illustration of moving heat source model for P-FSW (a) similar material (b) dissimilar material joining.	75
3.6	Schematic illustration of surface heat flux distribution in moving heat source model for preheating source.	75
3.7	Schematic illustration of heat flux distribution in moving heat source model for FSW.	77
3.8	(a) Schematic illustration of shoulder and pin interface with workpiece and (b) Velocity presentation in r and θ direction (top view).	82
3.9	Formation of functionally graded material during plunging of tool at (a) 2 mm (b) 3 mm and (c) 5 mm plunging depth.	85
3.10	Schematic illustration of applied functionally graded material in welding zone of dissimilar material joining.	86

Figure No.	Caption	Page no.
3.11	Variation of material properties in welding zone (as FGM): (a) volume fraction, (b) density, (c) specific heat, and (d) thermal conductivity.	87
3.12	Schematic illustration of time phase of welding with respect to change in tool contact surfaces during a complete cycle of welding.	88
3.13	Overall procedure followed in heat transfer analysis.	90
3.14	Flow chart for strain and strain rate analysis	90
4.1	Experimental setup for FSW.	94
4.2	Layout of thermocouples for temperature measurement.	95
4.3	Tensile test sample.	96
4.4	Bending test sample.	97
4.5	(a) Three point bending test setup (b) Tensile test setup with extensometer.	97
4.6	(a) Vickers indenter for vickers micro hardness test (b) Schematic illustration of three lines in cross-section of different weld zone for hardness at 30 points in 1 mm of spacing.	98
4.7	(a) An optical microscope (MEJI, Japan; model MIL-7100) for microstructure (b) An optical microscope (Leica S6D) for macrograph.	99
4.8	Thermal history of Exp. 1 in Table 4.3 (a) Advancing side (b) Retreating side for aluminium alloy.	101
4.9	Thermal history of Exp. 3 in Table 4.3 (a) Advancing side (b) Retreating side for aluminium alloy.	101
4.10	Thermal history of Exp. 4 in Table 4.3 (a) Advancing side (b) Retreating side for aluminium alloy.	101
4.11	Comparison of peak temperature of four experimental conditions at four points in advancing side and four points in retreating side for aluminum alloy.	102

Figure No.	Caption	Page no.
4.12	(a) Straight cylindrical pin tool C, (b) Straight cylindrical square thread pin tool CS, (c) Straight cylindrical V-thread pin tool CV, (d) Taper cylindrical pin tool T, (e) Taper cylindrical square thread pin tool TS and (f) Taper cylindrical V-thread pin tool TV.	104
4.13	Schematic illustration of tool profile (C) Straight cylindrical pin tool, (T) Straight cylindrical square thread pin tool, (CS) Straight cylindrical V-thread pin tool, (CV) Taper cylindrical pin tool, (TS) Taper cylindrical square thread pin tool and (TV) Taper cylindrical V-thread pin tool.	104
4.14	Thermal history at 1100 rpm and CS pin profile tool (a) advancing side (b) retreating side.	106
4.15	Comparison of peak temperature of different experimental conditions at TC1 advancing side and TC5 retreating side for experimental condition (a) 400 rpm, (b) 1100 rpm and (c) 1500 rpm.	107
4.16	Variation of axial force at experimental condition of 1100 rpm, 98 mm/min welding speed and CS tool pin profile.	108
4.17	Comparison between average welding forces at various welding conditions.	108
4.18	Tensile strength, yield strength and % of elongation of welded joint at various welding conditions (a) 400 rpm, (b) 1100 rpm and (c) 1500 rpm.	109
4.19	Comparison between ultimate bending loads of various welding conditions (a) 400 rpm, (b) 1100 rpm and (c) 1500 rpm.	107
4.20	Hardness distributions on the transverse cross-section for joints fabricated at a rotational speed of 1100 rpm and 98 mm/min welding speed for different pin profiles (a) C, (b) CS (c) CV (d) T (e) TS and (f) TV.	111
4.21	Macrographs for weld joints in longitudinal cross section at 1100 rpm for different pin profile (a) C, (b) CS (c) CV (d) T (e) TS and (f) TV.	112

Figure No.	Caption	Page no.
4.22	Microstructure of nugget zone for joints fabricated at a rotational speed of 1100 rpm and 98 mm/min welding speed for different pin profiles (a) C, (b) CS (c) CV (d) T (e) TS and (f) TV.	113
4.23	Comparison between average grain sizes of nugget zone at various welding conditions.	114
4.24	(a) Experimental setup for P-FSW; (b) Front view of P-FSW setup; (c) Side view of P-FSW setup.	116
4.25	Layout of thermocouple points during welding for dissimilar material joint.	117
4.26	Comparison between temperature profiles of case 2 at 13 mm from weld centre line: (a) Advancing side and (b) Retreating side.	120
4.27	Comparison between peak temperatures of different welding conditions at 13 mm from weld centre line in both sides.	121
4.28	The estimated cooling rate for case 2 of Table 4.11: (a) Advancing side and, (b) Retreating side.	121
4.29	The axial (plunging) force signals of case 2: (a) FSW and (b) P-FSW.	122
4.30	Comparison between average plunging force of different welding conditions during tool travel phase.	122
4.31	Comparison between tensile strength of various welding conditions.	123
4.32	Comparison between percent of elongation of various welding conditions.	124
4.33	Comparison between joint efficiency of various welding conditions.	125
4.34	Comparison between the stress-strain curves of the case 2 in Table 4.11 under two different welding conditions.	126
4.35	Hardness distributions on the transverse cross-section for case 2: (a) FSW and (b) P-FSW.	127
4.36	Macroscopic cross section with the four characteristic regions of the weld indicated of case 2: (a) FSW and (b) P-FSW.	128
4.37	Comparison of optical microstructures of the nugget zone for case 2: (a) FSW and (b) P-FSW.	129

Figure No.	Caption	Page no.
4.39	Comparison of fractured surface of the tensile test specimens of case 2: (a) FSW and (b) P-FSW.	130
4.40	Fracture surface EDX analysis results of tensile test specimens of case 2: (b) FSW and (a) P-FSW.	131
4.41	Thermal history at experimental condition of 815 rpm, 98 mm/min welding speed and 2 mm tool off-set - (a) without preheating and (b) with preheating current of 55 A.	133
4.42	Variation of axial force at experimental condition of 815 rpm, 98 mm/min welding speed and 2 mm tool off-set - (a) without preheating and (b) with preheating of 55 A plasma current.	134
4.43	Difference in peak temperature and corresponding flow stress difference with average welding force for: (a) preheating current (b) tool offset (c) welding speed and (d) tool rotational speed.	135
4.44	The stress-strain profile at welding condition of 2 mm tool offset, rotational speed of 815 rpm and 98 mm/min welding speed along with base materials.	136
4.45	Comparison of tensile strength and percentage of elongation for: (a) preheating current (b) tool offset (c) welding speed and (d) tool rotational speed.	138
4.46	Comparison of bending strength and displacement at failure for: (a) preheating current (b) tool offset (c) welding speed and (d) tool rotational speed in Table 4.12.	139
4.47	Hardness distributions on the transverse cross-section for: (a) without preheating and (b) with preheating of 55 A current at 2 mm of tool offset, 815 rpm and 98 mm/min welding speed.	140

Figure No.	Caption	Page no.
4.48	Average hardness distribution extend upto 4 mm on both side of tool pin centre line on the transverse cross section of welded specimen: (a) preheating current (b) tool offset (c) welding speed and (d) tool rotational speed.	141
4.49	Fracture surface morphologies of joints at different welding condition: (a) without preheating and (b) with preheating of 55 A at 2 mm of tool offset, 815 rpm and 98 mm/min welding speed.	142
4.50	Crown appearance and macrograph of weld joint corresponding to welding conditions of Table 4.14 from Exp. 1 to Exp. 7.	143
4.51	Crown appearance and macrograph of weld joint corresponding to welding conditions of Table 4.14 from Exp. 8 to Exp. 14.	144
4.52	Material flow pattern and types of bond formation during welding at 2 mm of tool offset, 815 rpm and 98 mm/min welding speed and without any preheating.	145
4.53	The material flow pattern in the weld zone at welding condition of 55 A preheating current, 2 mm of tool offset, 815 rpm and 98 mm/min welding speed.	146
4.54	Microstructure of base material (a) copper and (b) aluminium.	146
4.55	Microstructures of different zone at welding condition of 2 mm of tool offset, 815 rpm, 98 mm/min welding speed and without any preheating: (a) macrograph of weld zone, (b) HAZ in the aluminium side, (C) TMAZ in the aluminium side, (d) SZ in the aluminium side, (e) SZ in the copper side, (f) TMAZ in copper side and (g) HAZ in the copper side.	147

Figure No.	Caption	Page no.
4.56	Microstructures of different zone at welding condition of 2 mm of tool offset, 815 rpm, 98 mm/min welding speed and with preheating current of 55 A: (a) macrograph of weld zone, (b) HAZ in the aluminium side, (C) TMAZ in the aluminium side, (d) SZ in the aluminium side, (e) SZ in the copper side, (f) TMAZ in copper side and (g) HAZ in the copper side.	148
4.57	Microscope images of intermetallic layer for different preheating conditions: (a) without preheating and (b) with preheating current of 55 A at 2 mm of tool offset, 815 rpm and 98 mm/min welding speed.	150
4.58	XRD patterns of dissimilar aluminium 1100 and pure copper welds at transverse sections: (a) without preheating and (b) with preheating of 55 A at welding conditions of 2 mm of tool offset, 815 rpm and 98 mm/min speed.	150
4.59	XRD pattern of dissimilar joint at three different longitudinal sections of 4 mm from the weld centre-line to both copper and aluminium side and the weld centre-line: (a) without preheating and (b) with preheating of 55 A at 2 mm of tool offset, 815 rpm and 98 mm/min welding speed.	151
4.60	Experimental thermal history of weld joint at rotational speeds of 637 rpm and welding speed is 95 mm/min [53].	152
4.61	FSW microstructural morphology consists of the weld nugget, the thermal-mechanical-affected zone (TMAZ), the heat-affected zone (HAZ) and the base material [53].	153
5.1	Finite element mesh for model geometry.	158
5.2	Peak temperature obtained at a thermocouple point using different meshes.	160

Figure No.	Caption	Page no.
5.3	Temperature dependent thermal properties used in the present numerical work: (a) AA 6061; and (b) AA 7075.	162
5.4	Temperature dependent thermal properties of (a) AA 1100; and (b) Pure copper.	162
5.5	Temperature dependent yield stress of (a) AA 1100 and (b) Pure copper.	163
5.6	Coefficient of friction as a function of temperature.	164
5.7	Profile of plunging (axial) force vs time during welding phase.	165
5.8	Temperature history of three experimental conditions in Table 5.2 during simulation (a) Exp. 1, (b) Exp. 2 and (c) Exp. 3 for AA6061-T6.	167
5.9	Comparison between experimental [13] and calculated time temperature profile on the advancing side of Exp. 2 in Table 5.2 for AA6061-T6.	168
5.10	Estimated percentage error of peak temperature in comparison between simulated and experiments corresponding to Table 5.2.	169
5.11	Comparison between experimental and calculated time temperature profile on the advancing side at 98 mm/min transverse speed and 600 rpm of tool (Exp. 2 in Table 4.5).	170
5.12	Experimental and calculated peak temperature percentage of error at TC1 and TC5 thermocouple point with reliability of calculated result.	171
5.13	Comparison between experimental and simulated thermal cycle at TC1 for: (a) Exp. No. 1, and (b) Exp. No. 3.	172
5.14	Effect of process parameters on error in peak temperature and reliability.	172
5.15	Comparison between experimental and calculated thermal cycle at welding condition of 815 rpm, 98 mm/min weld speed (a) without preheating (b) with preheating of 65 A.	173

Figure No.	Caption	Page no.
5.16	Effect of process parameters on error in peak temperature and reliability (a) preheating current, (b) tool offset, (c) welding speed, and (d) tool rotational speed.	174
5.17	Comparison of experimental and simulated weld zone at 95 mm/min welding speed and 637 rpm (a) Experimentally measured macrograph [13] (b) Simulated isothermal temperature profile of AA6061-T6.	175
5.18	Temperature distribution of Exp. 2 in Table 4.5 during simulation (a) Isometric view (b) Cross-section view for AA1100.	176
5.19	Simulated temperature distribution of Exp. 2 in Table 4.5.	177
5.20	Comparison of experimental and simulation weld zone for Exp. 2 in Table 4.5 (a) Experimentally measured macrograph (b) Simulated isothermal temperature profile of AA1100.	177
5.21	(a) Temperature profile and (b) corresponding yield stress at the middle line of the workpiece for different preheating current at welding condition of 815 rpm, 98 mm/min weld speed.	179
5.22	Simulated temperature distribution at welding condition of 815 rpm, 63 mm/min weld speed without preheating.	179
5.23	Simulated temperature distribution at welding condition of 815 rpm, 63 mm/min weld speed with 35 A preheating.	179
5.24	Cross sectional view of simulated results at welding condition of 815 rpm, 63 mm/min weld speed without preheating.	180
5.25	Cross sectional view of simulated result at welding condition of 815 rpm, 63 mm/min weld speed with 35 A preheating.	180
5.26	Comparison of simulated and experimental measured weld zone at welding condition of 815 rpm, 63 mm/min weld speed without preheating.	181
5.27	Comparison of simulated and experimental measured weld zone at welding condition of 815 rpm, 63 mm/min weld speed with 35 A preheating.	181
5.28	Calculated thermal history for (a) Exp. No. 1 and (b) Exp. No. 5.	183

Figure No.	Caption	Page no.
5.29	(a) Temperature profile and (b) corresponding yield stress at the middle line of the workpiece for different preheating current at welding condition of 815 rpm, 98 mm/min weld speed and 2 mm tool off-set.	183
5.30	Temperature isotherm during plunging stage at zero preheating current corresponding to Exp. No. 1: (a) at 5 s, (b) at 18 s and (c) at 33 s.	184
5.31	Temperature isotherm during plunging stage at 65 A corresponding to Exp. No. 5: (a) at 5 s, (b) at 18 s and (c) at 33 s.	184
5.32	Simulated temperature distribution for Exp. No. 1.	185
5.33	Simulated temperature distribution for Exp. No. 5.	185
5.34	Cross sectional view of simulated results for Exp. No. 1.	186
5.35	Cross sectional view of simulated result for Exp. No. 5.	186
5.36	Comparison of simulated and experimentally measured weld zone for Exp. No. 1.	187
5.37	Comparison of simulated and experimental measured weld zone for Exp. No. 5.	187
5.38	Macrographs of Al–Cu joint cross section in aluminum side at joint interface for (a) Exp. No. 1 and (b) Exp. No. 5.	188
5.39	Validation of strain rate with Buffa et al. [22].	189
5.40	Strain rate in weld cross section from 0.001 m of top surface at different welding condition (a) 600 rpm and 63 mm/min welding speed, (b) 600 rpm and 98 mm/min welding speed, (c) 815 rpm and 63 mm/min welding speed and (d) 815 rpm and 98 mm/min welding speed.	190
5.41	Temperature in weld cross section from 0.001 m of top surface at different welding condition (a) 600 rpm and 63 mm/min welding speed, (b) 600 rpm and 98 mm/min welding speed, (c) 815 rpm and 63 mm/min welding speed and (d) 815 rpm and 98 mm/min welding speed.	191

Figure No.	Caption	Page no.
5.42	Calculated and experimental grain size distribution in different zone during at 815 rpm and 63 mm/min welding speed.	192
5.43	Grain size estimation in weld cross section from 0.001 m of top surface at different welding condition (a) 600 rpm and 63 mm/min welding speed, (b) 600 rpm and 98 mm/min welding speed, (c) 815 rpm and 63 mm/min welding speed and (d) 815 rpm and 98 mm/min welding speed.	193
5.44	Experimental and estimated grain size in nugget zone with percentage of error.	194
5.45	Schematic illustration of mixing amount of two dissimilar materials with respect to tool offset under the shoulder.	198
5.46	(a) Schematic illustration of the amount of copper and aluminum stir by tool. (b) Effect of tool off-set on the mixing ratio (Cu/Al) with respect to variation in shear layer thickness.	200
5.47	(a) Thermal history in advancing side (b) Thermal history in retreating side and (c) Welding force at experimental condition of 815 rpm, 98 mm/min welding speed and without tool off-set (0 mm) with preheating current of 55 A.	201
5.48	(a) Peak temperature and difference in peak temperature at different tool offset and (b) Average welding force at different tool offset.	202
5.49	Tensile strength and bending strength at various tool offset.	203
5.50	Fracture surface morphologies of joints in zone at tool offset (a) 0.0 mm, (b) 0.5 mm, (c) 1.25 mm and (d) 2.0 mm.	204
5.51	(a) Hardness distributions on the transverse cross-section at 0.0 mm tool offset and (b) Variation of average hardness at 4 mm on both side of weld centre line.	205
5.52	Macrograph of weld zone and material flow pattern in nugget zone at tool offset (a) 0.0 mm and (b) 2.0 mm.	206

Figure No.	Caption	Page no.
5.53	Variation of average intermetallic compound layer thickness at different tool offset.	207
5.54	Micrograph of intermetallic layer at different tool offset (a) 0.0 mm, (c) 0.5 mm (d)1.0 mm, (e) 1.25 mm, (f) 1.75mm, (g) 2.0 mm, (h) 2.25 mm and (d) 2.75 mm.	207
5.55	XRD patterns of weld zone at (a) without tool offset and (b) 2 mm tool offset at the weld center in nugget zone.	208
5.56	Comparison of calculated and experimental rate of temperature change at 815 rpm, 98 mm/min welding speed and 2 mm tool-offset: (a) Aluminium side and, (b) Copper side.	209
5.57	Comparison of microstructure of nugget zone in Al side at different preheating current from 0 to 65 A at 815 rpm, 98 mm/min welding speed and 2 mm tool-offset: (a) 0 A, (b) 35 A, (c) 45 A, (d) 55 A and (e) 65 A.	210
5.58	Effect of process parameters on variation of grain size in nugget zone of Al side with respect to average and maximum cooling rate at TC5 (a) Preheating current (b) Tool offset (c) Welding speed and (d) Tool rotational speed.	211

List of Tables

Tables	Title	Page no.
4.1	Chemical composition of aluminum alloys.	95
4.2	Mechanical properties of aluminum alloys.	96
4.3	FSW process parameters for aluminum alloy.	99
4.4	Maximum temperatures at different thermocouple points corresponding to experimental conditions of Table 4.3.	100
4.5	The detailed configuration of the designed FSW tool geometry	103
4.6	Design of Experiment of similar FSW joints.	105
4.7	Elemental compositions (in wt %) of aluminum alloy used in the present experiment.	115
4.8	Mechanical properties of the aluminum alloy.	115
4.9	Elemental compositions (in wt %) of aluminum alloy used in the present experiment.	117
4.10	Mechanical properties of the pure copper base material.	118
4.11	Process parameters for FSW and P-FSW.	119
4.12	Design of experiments for welding of aluminum and copper dissimilar joint.	132
5.1	Constant material properties at room temperature of aluminum alloy and pure copper used in the numerical model.	163
5.2	FSW process parameters for AA6061-T6 [17].	167
5.3	Input parameters for heat generation calculation and hybrid FSW process efficiency at different preheating condition for aluminum joint.	196

Tables	Title	Page no.
5.4	Input parameters for heat generation calculation and hybrid FSW process efficiency at different preheating condition for Cu-Al joint.	196

Nomenclature

Symbol	Description	Unit
T	Temperature in solution domain	K
K	Thermal conductivity	W/(m. K)
$\dot{Q}$	Heat generation	W/m^3
ρ	Density	Kg/m^3
C_p	Specific heat	J/(kg·K)
V_T	Welding speed	m/s
T_i	Initial Temperature	K
T_o	Ambient temperature at time t = 0	K
h	Convective heat transfer coefficient	$W/(m^2K)$
δ	Emissivity of surface	-
θ	Stefan Boltzmann constant	-
Q_{total}	Total heat generation	W
Q_{pre}	Heat input by plasma arc	W
Q_{FSW}	Heat input by FSW tool	W
η	Thermal efficiency of plasma arc	W
I	Plasma arc current input	A
V	Plasma arc voltage input	V
Q_f	Heat generation due to friction	W
Q_p	Heat generation due to plastic deformation	W
δ	Contact state variable	-
V_{matrix}	Peripheral velocity of workpiece	m/s
V_{tool}	Peripheral velocity of tool	m/s
$\tau_{contact}$	Contact shear stress	N/m^2

Symbol	Description	Unit
τ_y	Contact shear stress during plastic deformation	N/m^2
σ_y	Yield stress of workpiece material	N/m^2
μ	Coefficient of friction	-
P	Plunging force during welding phase	N
ω	Angular velocity of tool	rad/s
r	Radial distance from tool axis	m
dA	Elemental area of unit element	m
$Q_{FSW,sticking}$	Heat generation during sticking condition	W
$Q_{FSW,sliding}$	Heat generation during sliding condition	W
$d\theta$	Angle span by unit element	rad
dr	Radial length span by unit element	m
dF	Force on unit element	N
dM	Torque on unit element	N-m
Q_1	Heat generated at shoulder surface	W
Q_2	Heat generated at pin side surface	W
Q_3	Heat generated at pin bottom surface	W
$R_{shoulder}$	Tool shoulder radius	m
R_{probe}	Tool pin radius	m
α	Convex angle of shoulder surface	rad
H_{probe}	Height of tool pin	m
R_{top}	Top radius of conical tool pin	m
R_{bottom}	Bottom radius of conical tool pin	m
ψ	Inclined angle of conical tool pin	rad
$q_a(r)$	Surface flux at radius r	W/m^2

Symbol	Description	Unit
τ_y	Contact shear stress during plastic deformation	N/m^2
$\bar{r}$	Effective arc radius over which 95 % energy falls	m
$q_{shoulder}$	Heat flux at tool shoulder	W/m^2
q_{pside}	Heat flux at tool pin side surface	W/m^2
$q_{pbottom}$	Heat flux at tool pin bottom surface	W/m^2
q_s	Heat flux generated by FSW tool	W/m^2
$[N_i]$	Shape functions of i^{th} node	-
$\emptyset$	Weighting function	-
Ω	Volume of the solution domain	Kg/m^3
$\{T_i\}$	Temperature of i^{th} node	K
$[H^e]$	Shape function for any specific element 'e'	-
$\{T\}$	Temperature matrix	-
$[S^e]$	Shape function for any specific element 'e'	-
$\left\{f_{\dot{Q}}^e\right\}$	Shape function of heat generation for any specific element 'e'	-
$\{f_q^e\}$	Shape function of FSW heat source for any specific element 'e'	-
$\{f_h^e\}$	Shape function of convection heat loss for any specific element 'e'	-
h_{eff}	Effective convection heat transfer coefficient	$W/(m^2K)$
α	Load vector	-
γ	Contact state variable between workpiece and tool pin	-
β	Contact state variable between workpiece and tool shoulder	-
z	Distance from top to bottom in the thickness direction	m
A B C D	Constant for contact state condition (between 0 to 1)	-

Symbol	Description	Unit
$U_{(s)\theta}$	Material velocity component caused by shoulder in the θ direction	m/s
θ	Angle from the radial axis at the middle section of the tool	rad
$U_{(s)r}$	Material velocity component caused by shoulder in the r direction	m/s
$U_{(P)\theta}$	Material velocity component caused by pin in the θ direction	m/s
$U_{(P)r}$	Material velocity component caused by pin in the r direction	m/s
$\delta_{(s)\theta}$	Shoulder weight function in the h direction	-
$\delta_{(p)\theta}$	Pin weight function in the h direction	-
$\delta_{(s)r}$	Shoulder weight function in the r direction	-
$\delta_{(p)r}$	Pin weight function in the r direction	-
U_{θ}	Material resultant velocity component in the h direction	m/s
U_r	Material resultant velocity component in the r direction	m/s
U_z	Material resultant velocity component in the z direction	m/s
$\dot{\varepsilon}_{eff}$	Effective strain rate	1/s
$\dot{\varepsilon}_{rr}$, $\dot{\varepsilon}_{\theta\theta}$, $\dot{\varepsilon}_{zz}$, $\dot{\varepsilon}_{r\theta}$, $\dot{\varepsilon}_{\theta z}$ and $\dot{\varepsilon}_{zr}$	Strain rate components in the respective plane of r-θ-z coordinate	1/s
$\dot{\varepsilon}_{ij}$	Strain rate in i direction on the area normal to the j direction	1/s
ε_{eff}	Effective strain	-
N	Tool rotational speed	rpm
D_{CDRX}	Grain size after continuous dynamic recrystallization	ηm
D_i	Initial grain size	ηm

Symbol	Description	Unit
$\dot{\varepsilon}$	Strain rate for particular condition	1/s
ε	Strain for particular condition	-
Q	Activation energy	kJ/mole
R	Gas constant	J/(kg.K)
C_1, k, j, h	Constant	-
v_1	Volume fraction of copper	-
v_2	Volume fraction of aluminum	-
F	Experimental constant	-
κ	Experimental constant	-
E_r	Error percentage of peak temperature	-
T_{exp}	Experimentally measured peak temperature	K
T_{cal}	Calculated peak temperature	K
E_{RR}	Non-dimensional predictable errors of peak temperature on retreating side	%
E_{RA}	Non-dimensional predictable errors of peak temperature on advancing side	%
T_{RE}	Experimental peak temperature on retreating side	K
T_{RC}	Calculated peak temperature on retreating side	K
T_{AE}	Experimental peak temperature on advancing side	K
T_{AC}	Calculated peak temperature on advancing side	K
R_s	Overall reliability of the system	-
η	Process efficiency of FSW	-
$\eta_{overall}$	Overall efficiency of P-FSW	-
BE	Half-length of cord on weld center line under the shoulder	m
X	Tool offset distance	m

Symbol	Description	Unit
ED	Distance moved in 10 sec at velocity v	m
CD	Difference of radius and tool offset	m
A_V	Area cover by shoulder at velocity v in 10 sec	m^2
A_θ	Area cover by θ angle in copper side	m^2
$A_{total}(ABCD)$	Total area cover by shoulder	m^2
A_{Cu}	Total area in Cu side	m^2
A_{Al}	Total area in Al side	m^2
δ_{eff}	Shoulder creates a uniform shear layer	m
δ_{Cu}^{eff}	Shear layer thickness in Cu side	m
δ_{Al}^{eff}	Shear layer thickness in Al side	m
M_{total}	Mass flow rate	Kg/s
v	Welding speed	m/s
ρ_{Cu}	Density of copper	Kg/m^3
ρ_{Al}	Density of aluminum	Kg/m^3
ϵ	Emissivity of surface	-

Chapter 1

Introduction

1.0 General background

With the advancement of technology, the demand for complex products, that are impossible to manufacture as a single piece or their manufacturing cost is too high, has increased tremendously. The weldability of materials used in the engineering applications has enhanced through the development of solid state welding processes. Welding of Al-, Mg-, Cu-alloys, stainless steels, which are difficult-to-weld through conventional welding methods such as arc welding or impossible to weld such as non-weldable Al 7075 alloy, is now possible by friction stir welding (FSW) process [1]. FSW was invented by Wayne Thomas at TWI Ltd in 1991 and overcome many of the problems associated with traditional joining techniques [2]. FSW is a solid state process which produces welds of high quality in difficult to weld materials such as aluminum and becoming the process of choice for manufacturing light weight structures in almost all industrial applications [3]. FSW offers significant benefits over conventional joining processes and has initially become widespread as a butt joint technique to weld aluminum alloy sheets [4]. Researchers have explored different aspects of this process specifically, fundamental understanding and modeling of the process and the microstructures and properties of the welded joints [1-5]. Based on the astounding success, FSW has found widespread commercial applications in diverse industries such as aerospace, aeronautics, maritime, railway, automotive and electronic sectors on a global scale with a greater vision of achieving weight reduction, structure compression, energy consumption and environmental preservation. Numerous advantages of FSW process to make it as a curious candidature in the welding of a wide variety of softer, harder and dissimilar materials. Efficient investigations have been carried out in the welding of materials with low and intermediate melting points,

i.e. Mg alloys and Cu alloys. Friction stir welding tests have also been expanded to high strength structural materials with high melting points, i.e. Fe, Ti and Ni alloys, dissimilar alloys, metal matrix composites, polymers etc. [5]. However, commercial implementation of FSW to materials beyond aluminum alloys is previously limited, and such implementation in the near future would still require higher levels of FSW technology, model based investigations and better design and materials for manufacturing FSW tools. Therefore, innovative welding processes are continuously gaining industrial interest and exhibit great promise by having numerous advantages over the conventional FSW in terms of improved process window, heat generation, material flow, reduced load on the tools and mechanical properties of the joints [6].

1.1 FSW process

FSW process fabricates joint by using a constantly rotating cylindrical-shouldered tool with plane or profiled pin that is having traversal feed at a constant rate into a butt joint between two clamped pieces of material. The pin is slightly shorter than the weld depth required with the tool shoulder riding on the top of the work surface. This non-consumable welding tool softens the work piece locally through heat produced by friction and plastic deformation, thereby allowing the tool to stir the joint surfaces. The shoulder makes firm contact with the top surface of the workpiece. Heat generated by friction at the shoulder and to a lesser extent at the pin surface, softens the material being welded. Severe plastic deformation and flow of this plasticized metal occurs as the tool moves along the length of the plate. Material is transported from the front of the tool to the trailing edge where it is forged into a joint. The dependence on friction and plastic deformation for the heat source precludes significant melting in the workpiece, avoiding many of the difficulties arising from a change in state, such as change in gas solubility and volumetric expansion [7]. In **Fig. 1.1**, the advancing side corresponds to the plate over which the direction of tool rotation is same as the tool translation direction and the other side is called the retreating side. In the advancing side the relative velocity between the tool and the workpiece goes through a maximum while it goes through a minimum in the retreating side. This difference can lead to asymmetry in heat generation, material flow and the properties of the two sides of the weld [8].

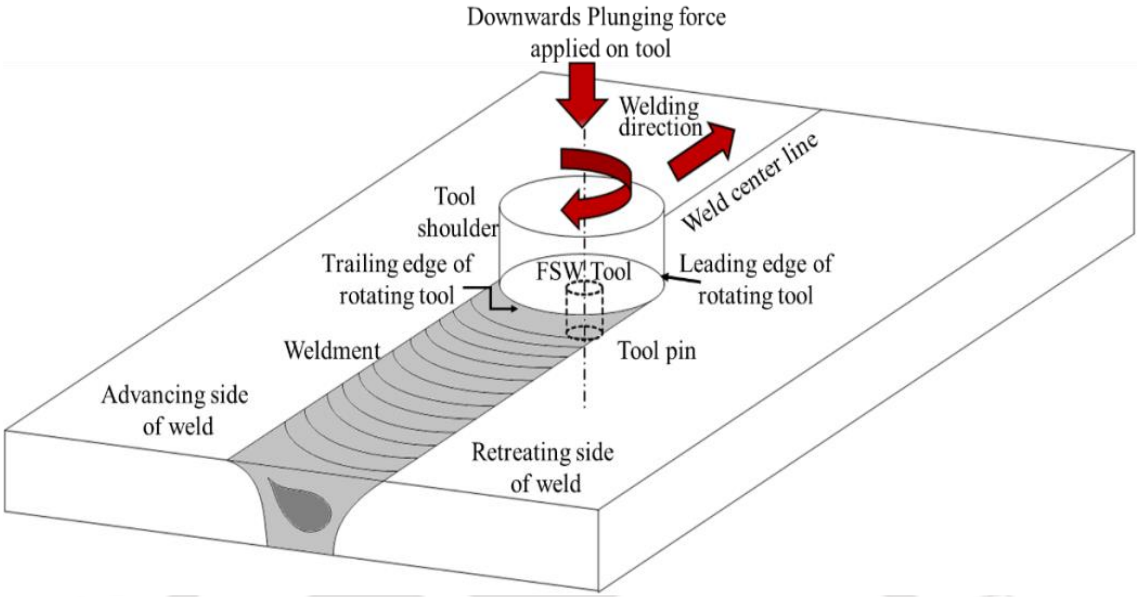

Figure 1.1. Basic principal of FSW.

The operations during FSW consist of several phases of action and each phase can be described as a time period where the welding tool and the work piece are moved relative to each other. In the first operation, the tool is plunged vertically into the joint line between the work pieces while the tool rotates. This action takes place in the plunge period. The plunge period is followed by the dwell period, where the tool is held steady relative to the work piece but still rotates. The mechanical interaction, due to the velocity difference between the rotating tool and the stationary work piece produces heat by frictional work and material deformation. This heat dissipates into the surrounding material that result in temperature rise and softening of materials. The actual welding process can be initiated by moving either the tool or the work piece relative to each other along the joint line [9]. The traverse velocity is in the range of 1–10 mms^{-1} depending on welding parameters i.e. the rotation speed, plunge force or plunge depth and tilt angle, tool design and weld piece materials. When the weld distance is covered, the tool is pulled out of the work piece leaving behind an exit hole as a footprint of the tool [10]. A schematic representation of the sequence of FSW is described in **Fig. 1.2**.

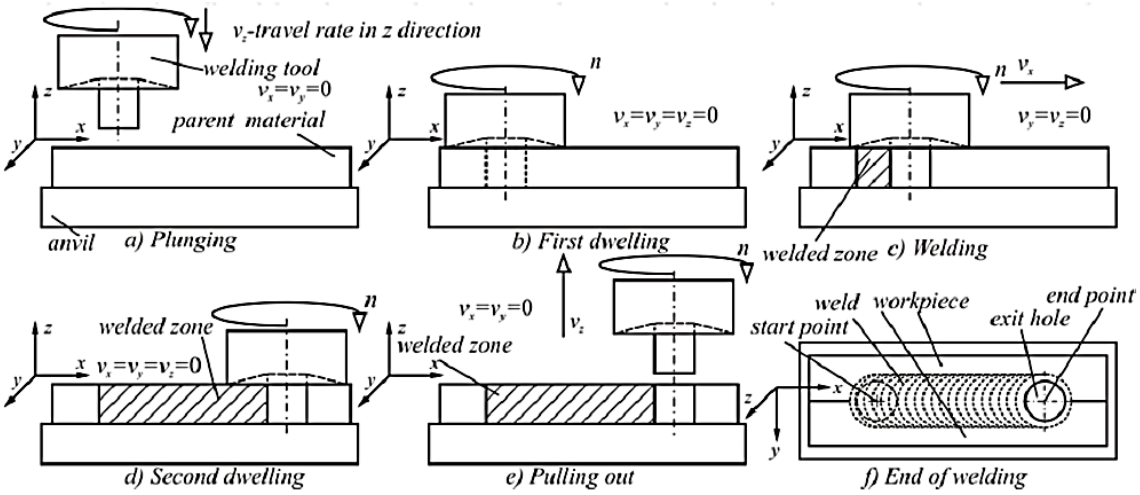

Figure 1.2. Schematic representation of FSW process [10].

In FSW, the tool is obviously a critical component to the success of the process. The tool typically consists of a rotating round shoulder and different profile pins that deforms the work piece, mostly by friction, and moves the softened alloy around it to form the joint as shown in **Fig. 1.3**. The probe height is limited by the work piece thickness; the probe tip must not penetrate the work piece, or damage the backing plate or support frame is unavoidable [11]. The combination of the shoulder and the pin stretches and folds material and creates a solid joint between originally free surfaces that are intersected by the pin. In general, two tool surfaces are needed to perform the heating and joining processes in the friction stir welding. The shoulder surface is the area where the majority of the heat is generated whereas the probe surface is where the work pieces are joined together and only a fraction of the total heat is generated. Secondly, the shoulder confines the underlying material so that the void formation and porosity behind the probe are prevented. The conical tool shoulder helps establish a pressure under the shoulder, but also acts as an escape volume for the material displaced by the probe during the plunge action. Newer tool designs employ special features, e.g. multi-facets, threads and flutes [12, 13] which are thought to produce advantageous conditions to assist the joining process. But, the simple cylindrical probe shape has proven to work satisfactorily. However, the FSW tool is subjected to severe stress and high temperatures particularly for the welding of hard alloys such as steels and titanium alloys and the commercial application of FSW to these alloys is now limited by the high cost and short life

of FSW tools. Although significant efforts have been made in the recent past to develop cost effective and reusable tools, most of the efforts have been empirical in nature and further work is needed for improvement in tool design to advance the practice of FSW to hard alloys [14].

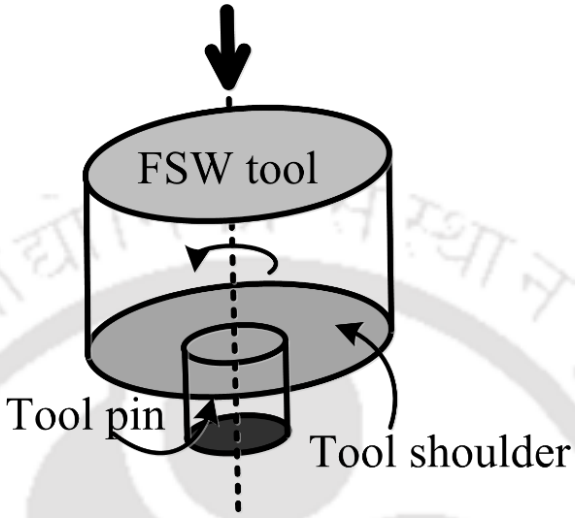

Figure 1.3. Cylindrical threaded pin type probe FSW tool.

1.1.1 Limitation of FSW process

The FSW process offers significant advantages as compared to fusion welding processes of aluminum and aluminum alloy, several of which are particularly important to the automotive industry. Despite of these advantages FSW encountered a number of challenges in the welding of materials with intermediate to high hardness and higher melting points. There are several complex phases in FSW process which are difficult to visualize during the process. These phases of the FSW process and the metallurgy of the resultant weld depend on the material of the workpiece, tool material, tool geometry and process parameters such as tool rotation speed, tool tilt angle, welding speed and plunge depth which affect the heat generation and material flow during the process. In FSW, the amount of heat input is the most important factor. A high tool traverse speed or harder material would cause the lowering of the coefficient of friction between the tool and the workpiece. This confine the frictional heat generation that leads to insufficient material softening and the material flow presenting the risk of weld defects and issues with weld quality. The necessary heat generation during process is also controlled by optimized FSW process parameters such as rotation speed,

traverse speed, etc. The process optimization is time consuming and narrows the process window, thus minimizes the application potential of the FSW process.

It is mostly observed that FSW process has been successful for softer alloys because the load requirements are relatively lower than that for the harder alloys. This indicates that partial or additional softening of the harder alloys is required before or during the FSW. Also additional softening reduces the load requirement on the tool and thus improves the tool performance, tool life, FSW process window, welding efficiency and weld quality. The additional softening of the harder workpiece in FSW can be achieved by applying additional preheating or pre-softening mechanism on the workpiece. With this objective several variants of FSW have been incessantly developed over the past few years.

FSW of harder aluminum alloys, high strength, high hardness, high melting point and high conductivity materials such as ferrous, titanium, nickel and copper alloys, dissimilar materials and other metal matrix composites is feasible only if the localized frictional heat generation is sufficiently high to plasticize the workpiece near the weld region. This necessitates imposing high downward axial force and spindle torque on the tool that leads to poor tool performance and failure. The rapid tool wear causes premature tool failure that results in poor weld quality and high production cost. This issue also applies to the aluminum alloys with intermediate hardness such as the precipitation hardened aluminum alloys of class 2xxx, 6xxx and 7xxx. Furthermore, the variations in mechanical, thermal and chemical properties of the tool material during the FSW process affect the tool performance, durability and weld quality. Even the highly durable tools based on the polycrystalline cubic boron nitride (PCBN), tungsten alloys, Si_3N_4 and molybdenum are susceptible to tool wear that is governed by diffusion, abrasion and chemical affinity of the tool material for oxide and nitride formation. Also a great amount of tool wear takes place during the plunging stage as the work piece material is cold at this time [12]. Another issue of the FSW process is the heavy load requirement that leads to large and sophisticated design of the FSW welding equipment. Although, the travel speeds have been an issue, the travel speeds are now competitive with other fusion joining processes, such as gas metal arc welding (GMAW). Weld speeds in FSW are slower which can lead to time-consuming joining process. Therefore, the use of standard FSW machines runs into high capital cost requirements and relatively poor productivity.

1.2 Hybrid FSW process

Modification of conventional FSW processes is continuously gaining industrial interest. Specific applications of hybrid technology include construction of high strength steel pipelines, fabrication and repair of aero engine components made of Ni-based super-alloys and mechanically alloyed materials, titanium-alloy intensive aircraft, spacecraft, and ship superstructures, and ultra-high-strength steels for light weight, high performance auto vehicle body-structures [11]. With the aim to expand FSW to hard or high melting point materials and to decease the rapid wearing of the rotation tools, different approaches have been proposed in literature. Nearly all materials lose strength as they are heated and this is the reason that FSW tools are able to "stir" the material together once the frictional forces raise the local temperature. However, if an additional source of heating is introduced in a controlled manner so that the peak temperature remains well below melting temperature, the heat input required from the FSW tool is obviously reduced. This scientific principle is followed by several researchers and the development of the process is called "hybrid" or "assisted" FSW. The idea of hybrid FSW is to reduce the stresses of the tool which can be used to improve the productivity or to increase the range of applications. Various possibilities to combine conventional FSW with an adjacent heat source are reported in the literature. As compared with conventional friction stir and fusion welding, H-FSW technology reduces energy consumption during welding by as much as 50 % [15]. H-FSW eliminates the need for expensive and labor intensive pre- and post- weld heat treatments, and reduces material use [1]. Hybrid FSW is developed in combination with laser, ultrasonic vibrations, resistance heating and plasma arc heating [16]. The hybrid technology reduces the process loads in welding of high-temperature materials and thick sectioned structures, and enhances FSW technology to overcome "single" pass process that limits current technology to join thin-section structures only [15]. One common way to implement another heat source is to attach with under-powered fusion welding tool, just in front of the FSW tool [17]. However, the position of the rotating tool and the preheating source is decided by the type of welding i.e. whether similar or dissimilar type of materials is joined.

In case of dissimilar joint, the additional local heat source is generally used to preheat the harder material side that provides adequate metal flow around the tool and simultaneously

prevents the formation of a large amount of brittle intermetallic compounds. The regions to be plasticized are heated in a more effective and more uniform manner, as a result of which faster joining speeds and better joint quality are achieved. Although, the preheating technique in FSW process is quite effective to improve mechanical properties and reduction of plunging forces, it needs to investigate from various aspects [18]. First, the selection of preheating source, which should have the unique combination of high arc stability, concentrated energy density and low equipment cost such as plasma arc. Secondly, the position of the preheating source in front of FSW tool should be optimized to reduce the disparity in flow stress behavior of two different materials. As shown in **Fig. 1.4,** the preheating source is positioned in harder material side to compensate the difference in thermos-physical properties of the two materials. Also, it influences the formation of intermetallic compound and its distribution within the weld zone.

H-FSW system increases the flexibility and feasibility for joining high-melting temperature materials such as widely-used structural steels [19]. The complexity of the equipment for hybrid FSW and the interaction between process parameters increase considerably. Heat sources integrated with the FSW tool are far more complex as compared to the use of external heat sources. External heating is also beneficial for dissimilar material combinations since the heat can be applied individually to one of the parts being joined together. However, controlling of external heat is difficult and needs a lot of trials to find the feasible range of parameters [20].

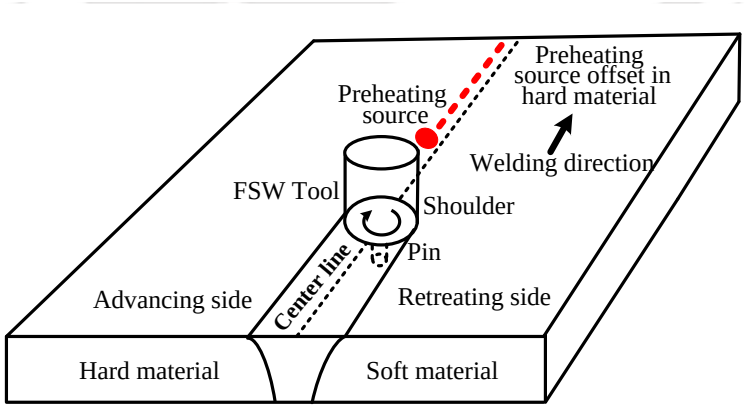

Figure 1.4. Basic principle of plasma-assisted friction stirs welding of dissimilar material joint.

In summary, the development of hybrid FSW technology is the major thrust of the present research work where application is imposed on joining of similar and dissimilar type of materials. The successful application on joining aluminum alloy and between aluminum and copper may be considered as a novel contribution of the present work. The development of a sophisticated heat transfer model for P-FSW process to simulate temperature distribution is also a major contribution of the present work. The implementation of hybrid heat flux model in finite element based commercial software desires considerable effort. All the temperature dependent material properties and the concept of functionally graded materials during joining of dissimilar materials are incorporated to the numerical model. The macro-microstructural characterization of the weld joint for similar and dissimilar materials shows the sustainability and feasibility of the developed P-FSW process. The thickness of intermetallic layer for dissimilar material joint has great influence on the joint efficiency that is influenced by plasma heating in hybrid FSW process. Also, the tool pin offset efficiently controls the intermetallic compounds during joining of dissimilar materials.

1.3 Research Objectives

The overall objective of the present research work is to overcome the limitation of FSW by developing hybrid system that is known as plasma assisted hybrid friction stir welding process (P-FSW). The feasibility study of the P-FSW process during joining of similar and dissimilar materials is sole objective of present investigation. The secondary objective is the quantitative understanding of heat transfer and material flow of PFSW process based on phenomenological modeling approach. Finally, the influence of microstructure of dissimilar weld joint and their link with mechanical properties are worthy of investigation. The following modules are accomplished either simultaneously or sequentially which are developed over the whole duration of research work.

- Development of FSW system and preliminary evaluation of FSW process using different tool geometry. The FSW system has been established using a vertical milling machine. An in-house developed force measurement system is used to capture the tool forces during FSW process. The temperature is measured using thermocouple during the process. The

standard metallography is followed for macro and microstructural analysis of the samples. The mechanical properties i.e. the strength hardness of the weld joint and the fractography analysis for all the test conditions are evaluated.

- Development of the plasma assisted hybrid FSW system. The central idea is to supply additional heat energy at the abutting faces of the workpiece to be joined that enhance the plastization of the material. The position of the plasma arc energy is effectively decided by the combination of similar or dissimilar materials.
- To better demonstrate the feasibility of hybrid friction stir welding of similar and dissimilar materials by characterization of microstructure and mechanical properties of welded joints on similar and dissimilar materials. The focus is here the effect of preheating by plasma arc in mechanical, thermal and microstructural properties of weld joint.
- A physical model of conventional FSW and hybrid FSW processes are developed for quantitative understanding on the differential influence of process parameters. The conduction heat transfer based numerical process model using finite element method compute the temperature field considering temperature dependent material properties. An explicit derivation of heat flux model in conventional FSW process is evaluated. The heat source model is also extended to hybrid source for P-FSW process. The heat generation model is estimated using contact condition between tool and the workpiece.
- Development of time dependent material model based on functionally graded material (FGM) for joining dissimilar materials like aluminum and copper. The composition of FGM changes with respect to the motion of tool and mixing of material in the weld zone as well as tool offset.

1.4 Layout of thesis

The thesis consists of six chapters that describe the aspects aimed at research objectives. Chapter 1 describes the general background of friction stir welding process, address important issues related to FSW process, basic principal of hybrid FSW of similar and dissimilar materials. The review of existing work related to FSW and hybrid FSW is depicted in Chapter 2. At first, this chapter describes coupled thermo-mechanical phenomena involved in heat generation during FSW. Next, the experimental work conducted earlier to understand

the effect of various parameters which influence the heat generation and heat transfer process during FSW are presented. Subsequently, the influence of these parameters for the development of numerical and analytical models is critically reviewed. Thereafter, important issues such as flow stress-strain model and experimental and numerical investigation of material flow criteria are discussed. Recent progress in H-FSW is also reviewed in this chapter including different variant and approaches to overcome the shortcomings of the conventional FSW process. The different aspect of the FSW tool is highlighted in this chapter. Joining of dissimilar materials faces huge challenges and many generic issues such as the different deformation behaviors, formation of intermetallic compounds are reviewed here. Lastly, the microstructural changes in weld zone with respect to different process parameters are discussed.

In Chapter 3, overall discussion is devoted to the modeling of the FSW processes. The governing equations and boundary conditions for FSW and P-FSW are described to develop the thermal model of the processes. A detail description of the heat generation model of FSW process is included in this chapter. The analytical model for strain and strain rate are also illustrated here. Next, the material model for joining of dissimilar materials is demonstrated. Finally, the computed methodology of the process is described.

Chapter 4 presents the experimental results on FSW and hybrid FSW process. The experimental investigation is carried out on joining of both similar and dissimilar materials. The time-temperature history is measured in both advancing and retreating side to investigate any asymmetrical heat generation. The reduction in tool forces and any improvement of mechanical properties are investigated with the effect of plasma heat source in hybrid FSW process. The microstructural changes i.e. the refinement of grain size in nugget zone and heat affected zone are investigated as well. The tool offset in hybrid FSW of dissimilar aluminum and copper affects the intermetallic compound formation. An investigation is carried out on the effect of tool off-set towards weld joint morphology, material flow pattern, and mechanical properties of the weld joint. The XRD patterns of the weld zone are also described in this chapter. Finally, the thermal results are employed to validate the computed results from numerical model.

Chapter 5 addresses mainly the validation of the computed results from experimentally measured data. It includes effect of preheating in thermal, mechanical and microstructural properties of friction stir welded aluminum alloy and copper-aluminum dissimilar joint. The numerical model estimates the weld zone geometry and temperature history. In the final chapter, the accomplished work is concluded and further scope of proposed work is presented.

Chapter 2

Literature Survey

2.0 General background

Friction stir welding is still considered to be the most significant development in joining of materials in last 25 years. Presently, this welding technique is commercially used in several industries [2]. As a result, significant progress has been made in the fundamental understanding and modeling of the FSW process and the microstructures and properties of the welded joints. In the above perspective, the FSW process and the weld properties have been periodically studied and modeled. These studies were followed by better estimation of thermal history, material flow stress and strain rate which provide bare insight detailed of the FSW process.

However, commercial implementation of FSW to materials beyond aluminum alloys is hitherto limited, and such implementation in the near future would still require higher levels of FSW technology, model based investigations and better design and materials for manufacturing of FSW tools. Some FSW variants have recently been developed for improved joint performance. For example, the dual-rotation FSW variant was developed at TWI, whereby the probe and shoulder rotate separately [21]. Another FSW variant recently developed is Twin-stir technique which involves a pair of tools applied on opposite sides [22]. This FSW variant offers certain advantages over conventional FSW, such as a reduction in reactive torque and a more symmetrical weld and heat input through the thickness [3, 19]. Similarly, recently developed, the use of the auxiliary energies source to assist FSW through thermal energy from electric resistance heat, induction heat, laser, plasma, arc, etc. and mechanical energy in the form of ultrasonic vibration. The subject of

FSW and HFSW covers a wide range of topics, it is not viable to review all the topics in this chapter. Hence, key problems and issues pertinent to the subject of this study are selected for review. The aim of this chapter is to look into certain extent the experimental investigations of FSW and HFSW and the issues related to numerical modeling approaches for heat transfer and material flow during FSW process.

2.1 Heat transfer in friction stir welding

Heat generation and heat transfer in FSW became a topic of research during mid-1990s. However, understanding heat generation and heat transfer processes within FSW requires understanding of several other physical processes: material flow around the welding tool, contact pressure inflicted by the welding tool, the friction coefficient, wear, change of thermo-mechanical properties and heat transfer coefficients etc. [7]. The understanding of the heat transfer mechanism in the workpiece can be helpful to predict thermo-mechanical interactive phenomena, thermal history during the welding process and the mechanical properties of the weld joint that finally evaluate the weld joint quality.

FSW is a highly complex process comprising several highly coupled (and non-linear) physical phenomena. These phenomena include large plastic deformation, material flow, mechanical stirring, surface interaction between the tool and the workpiece, dynamic structural evolution and heat generation resulting from friction and plastic deformation as explain in **Fig. 2.1**. Multiple parameters greatly influence the quality of the FSW joints. Tang et al. [23] were first to measure the thermal history of the workpiece during FSW by thermocouple to perceive the heat generation phenomena and reported the maximum temperature generated during the process ranges from 80% to 90% of the melting temperature of the welding material. Consequently, heat generated by friction occurs on the surface in contact with the tool is observed. The process also experiences severe plastic deformation surrounding the tool and flow of the plasticized metal, from around the front of the tool to the trailing edge where it is forged into a joint [24, 25].

The understanding of the heat transfer process can be helpful in predicting the thermal history during welding, which subsequently influences the mechanical properties to evaluate weld joint quality. Modelling of process plays a key role in accelerating

development and reducing experimental cost. First modelling task for FSW process is to describe heat generation and conduction during welding, to capture thermal history in weld zone. A simple model for the temperature distribution in the workpiece was proposed by Gould and Feng [26]. Chao and Qi [27] developed a moving heat source model in a finite element analysis for studying the temperature, residual stress and distortion of the FSW process. Colegrove et al. [28] performed simulation of FSW for both thermal and material flow including the pin. Russel and Shercliff [29] postulated a heat input dependent upon the shear strength of the material. Using an assumed friction coefficient, Frigaard et al. [30] arrived at a formula for heat generation in their modeling. Song et al. [31] consider melting temperature of the workpiece material at the tool-workpiece interface to model moving heat source for estimation of thermal fields in FSW.

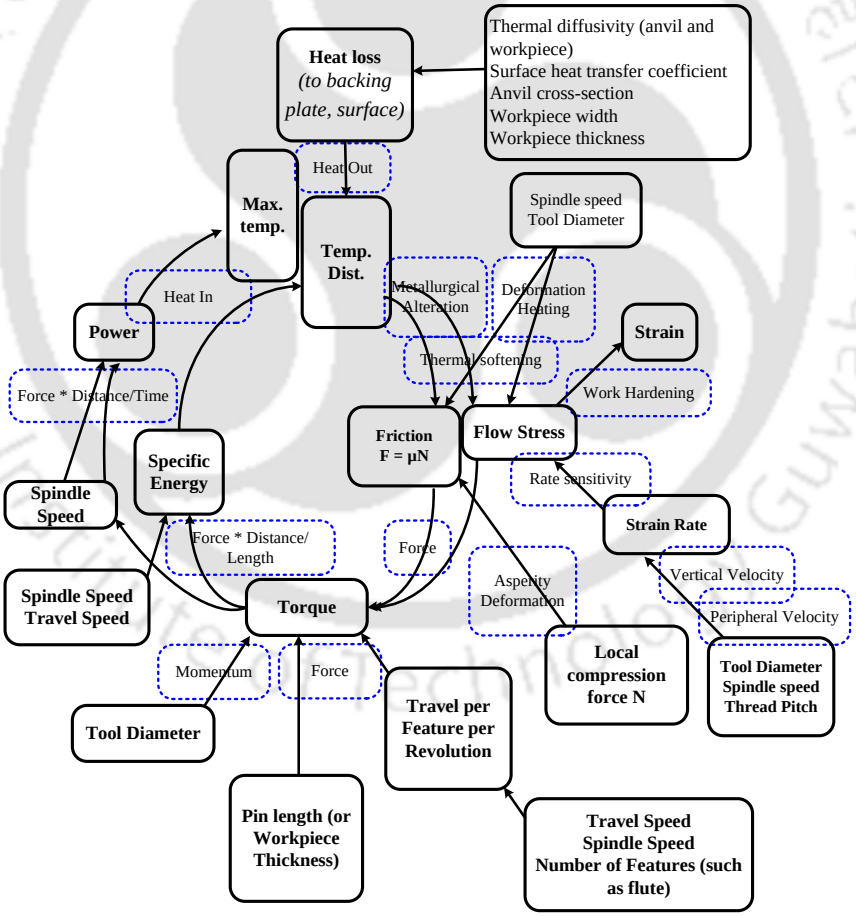

Fig. 2.1. A conceptual model for the process variables related to heat generation in FSW.

Chao et al. [32] formulated the heat transfer of the FSW process into two boundary value problems first as a steady state condition for the tool and second as a transient condition for the workpiece. To quantify the physical values of the process, the temperatures in the workpiece and the tool were measured during FSW. They found that the majority of the heat generated from the friction, i.e., about 95%, is transferred into the workpiece and only 5% flows into the tool and the fraction of the rate of plastic work dissipated as heat is about 80%. They also concluded that the amount of the heat flows to the tool make effect on the life of the tool and the capability of the tool for the joining process. Schmidt et al. [33] developed an analytical model for heat generation for straight cylindrical pin profile having concave shoulder in FSW based on different assumptions in terms of contact condition between the rotating tool surface and the weld piece. The analytical heat generation estimate correlates with the experimental heat generation, by assuming either a sliding or a sticking condition. For the sliding condition, a friction coefficient that lies in the reasonable range of known metal to metal contact values is used in order to estimate the experimental heat generation. Assuming the sticking condition, a yield shear stress, which is descriptive for the weld piece material at elevated temperatures, is used to correlate the values. Furthermore, Gadakh et al. [34] developed an analytical model for heat generation for tapered cylindrical pin profile having flat shoulder in FSW based on different assumptions in terms of contact condition. From the obtained results, it was observed that less temperature is generated using taper cylindrical pin profile than straight cylindrical pin profile under given set of working conditions. Biswas and Mandal [35] reported that tools having a concave shoulder led to lesser temperature rise. At the same time, conical tool pins exhibited somewhat lesser peak temperature compared to that of a straight cylindrical pin profile.

In all modeling activities it is vital to have clear view of problem to be address and hence level of complexity required in modelling technique. So the question arises is that what are the uncertain parameters in FSW and how can they be determined? The uncertain parameters include the friction coefficient, the extent of slip between the tool and the work-piece, the heat transfer coefficient at bottom workpiece surface, the mechanical efficiency and the scaling factor for viscous dissipation as shown in **Fig. 2.2**. The uncertainty occurs

because these parameters cannot be determined either from scientific principles or from straight forward experiments. Several investigators [36-40] have examined the effects of uncertain parameters related to the specification of the boundary conditions at the bottom surface. These investigations included an estimation of the thermal contact resistance at the interface between the workpiece and backing plate and the determination of the convective heat transfer coefficient at the bottom surface. Chao et al [32] have used high heat transfer co-efficient at the bottom face of the work piece to include the effect of contact conductance. Khandkar et al. [36] reported that for FSW of AA6061-T651 plates, an overall convective heat transfer coefficient of 1000W/m^{-2}K^{-1} might be appropriate for the bottom surface of the workpiece if the backing plate is not considered. The main unknown parameters in these expressions are either the friction coefficient under the assumption of sliding and the material yield shear stress under the assumption of sticking [37].

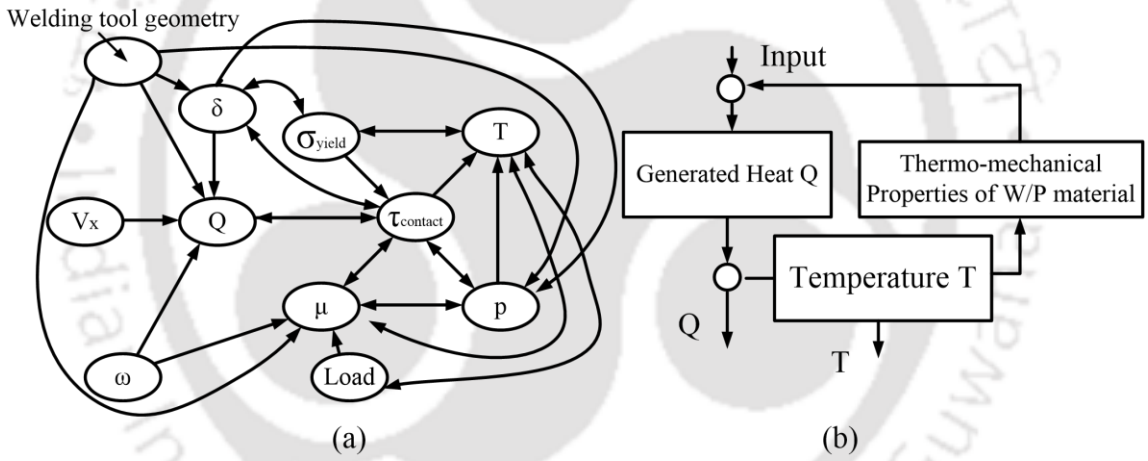

Figure 2.2. (a) Schematic of mutual dependencies between generated heat and dominant influencing parameters (b) Partial algorithm for generated heat estimation.

2.1.1 Experimental investigation

Experimental investigation of FSW is imperative for development of process in all respect to adept in manufacturing industry. Therefore, different types of experimental setup is developed to weld similar and dissimilar material in different joint configuration. Joint configurations for FSW include square butt [42], T-butt [43], lap [43], multiple lap [43], T-lap [43], pipe joint [44] etc. Most commercial FSW applications use simple butt joint configurations and alternative designs such as T-sections and corner welds are very rarely

considered. Martin et al [45] developed the welding mechanism which consisted of a rotating pin located in a non-rotating shoulder shaped to the internal corner of the plates to be welded. The shaped shoulder contains the stirred material and slides over the surface of the material during T joint welding. Lammlein et al. [46] conducted experimental studies on pipe joining through FSW. They found that pipe butt joint can be done successfully with full penetration but there were some issues that emerged relating to the tool geometry, secondary heating, system eccentricity and the method of internal support and tool disengagement. In order to produce good penetration, the tool offsets about 6 mm with respect to weld interface. However, the key issues facing in conducting experiment on FSW machine include design of a proper fixture to hold the workpiece, position it correctly with respect to the FSW tool, and support it during welding operation and measurement of forces acting on the workpiece. Baghel [47] developed a fixture that accommodates both backing plate and metal plate to be welded. Fratini et al. [48] also prepared a fixture to overcome the shortcomings of FSW of titanium alloys with particular attention to the choice of the materials and to the cooling systems, both under the back plate and around the tool.

A premature failure of the welding tool can lead to unacceptable weld joint quality and loss of welding productivity. Real time monitoring of thermal cycles, torque and traverse force experienced by the tool in the proximity of the tool are requisite for appropriate design of friction stir welding (FSW) process. Temperature measurements have been successfully made by embedding thermocouples into the weld zone. However, the temperature profile has been captured until the thermocouples were consumed in the stirred zone. In some cases, the thermocouples continue to collect data even after the weld tool has passed. Tang et al. [23] measured the temperature distribution during FSW of Aluminum as a function of the distance from the centerline of the weld, the rotational speed and traversing speed. Edwards et al. [49] the first to use this method of embedding thermocouples to experimentally measure the temperatures in the weld zone during FSW of Titanium.

Also, monitoring the process through the measurement of forces and torques during welding and which can also be used as input parameter to validate numerical models. Threadgill et al. [50] and Luo et al. [51] demonstrated how these can be measured indirectly by monitoring electrical control signals to the motor provided they have been adequately

calibrated. In early work by Midling et al. [52] the heat input was determined from the size of the HAZ. This work showed that different shoulder materials produced different heat inputs when welding separately 7108 and AA6082-T6 aluminium alloy. A more sophisticated method reported by Johnson et al. [53-54] used a dynamometer to measure the forces. While this method is far more accurate, care needs to be taken not to overheat or overload the equipment. Another problem with this technique is that the equipment is prohibitively expensive. Reynolds et al. [55] measured the traversing force with the hydraulic cylinder pressure and the torque by the pressure drop across a hydraulic motor. The torque measurement is reasonably accurate provided the efficiency of the motor is taken into account. Another approach used by Lienert et al. [56] used strain gauges on the tool to measure the welding forces and torques.

Material selection for tool and tool design deeply affect the performance of tools, weld quality and cost. In FSW, the tool remains under severe heating condition during welding and significant wear may result if the tool material has low yield strength at high temperature. Stresses experienced by the tool are dependent on the strength of the workpiece at high temperatures common under the FSW conditions. FSW has been applied to metals with moderate melting points. Initially, FSW was applied primarily to aluminum alloys, which could be easily welded due to the relatively low softening temperatures of these alloys (such as copper, lead, zinc, and magnesium). Steel tools have also been used for the joining similar and dissimilar in different configuration [57-59]. But tool wear was found at high temperature strain condition, which suggests that process parameters can be adjusted to increase tool life. Prado et al. [60] analysis change in shape of tool due to severe tool wear during FSW of Al 6061 z 20% Al_2O_3 MMC. They suggest that the need for threads in the tools is not required because the tools continued to produce good quality welds even after the threading had worn out and tool had obtained a smooth shape.

In contrast, for a number of years it was difficult to weld ferrous alloys and other high softening-temperature metals due to the lack of suitable tool materials. Until recently, there were no tool materials that would stand up to the high stresses and temperatures necessary for FSW of materials with higher melting points, such as steels, stainless steels, and nickel-base alloys. In 1998, tungsten alloys and polycrystalline cubic boron nitride

(PCBN) were developed to create FSW tools for use in steel, stainless steel, titanium alloys, and nickel-base alloys. Weinberger et al. [61] analyses the weldability, microstructure and mechanical properties of friction stir welded steel 15-5PH using tungsten based tools. They produced good quality welds on martensitic precipitation hardened steels using a W25Re alloy tool. Park et al. [62] studied the fundamentals of pcBN tool wear during FSW of five types of ferritic, duplex, and austenitic stainless steels. Their results suggest that with increase in the flow stress causes the severe tool wear during FSW of austenitic stainless steels, which results in greater nitrogen pickup in austenitic stainless steel FS welds. Whereas, Seighalani et al. [63] examine the effect of tool material, tool geometry, tilt angle, tool rotational speed, welding speed, and axial force on the weld quality of titanium alloys. Due to the excessive erosion, tool material and geometry play the main roles in FSW of titanium alloys. Properties of the resultant welds have been shown to be outstanding. Although some issues remain (primarily limited tool life with tungsten base tools), FSW has been demonstrated as a technically and economically feasible process in high-temperature materials [64-65]. Zhang et al. [66] studied FSW of commercially pure titanium using a pcBN tool and observed severe tool wear. The debris from the tool reacted with titanium alloy to form titanium borides; both titanium borides and pcBN debris contributed to the grain refinement as well as increase in surface hardness. This situation suggests that a pcBN tool can be utilized for FSW of titanium and its alloys high quality welding.

2.1.2 Mathematical model

During FSW process, control of heat generation is significant to prerequisite the generation of high quality welds. Many properties of the final welds are directly a function of the thermal history to which workpiece is exposed. So, it is important to have an adequate mathematical model capable to precisely describe heat generation during FSW. There are many parameters identified which affecting the calculation of the amount of heat generated during FSW. The model identifies geometrical, kinematic, physical and energetic possibilities of heat generation during FSW, recognizes dominant parameters affecting the heat generation process and uses them to estimate how much mechanical power is transformed into heat. Some of them are topology and geometry of the welding tool, technological parameters (tool rotation speed, welding speed, loading (axial force, torque

etc.), physical phases of FSW, duration of the welding procedure, duration of certain phases of the welding procedure, etc. Furthermore, these parameters initiate other parameters that affect heat generation process: friction coefficient, contact pressure, shear stress, contact condition, etc. However, presented models simplify FSW assuming e.g. constant friction coefficient, constant contact pressure, pure frictional heat generation, heat generation only due work of the largest part of the welding tool, no heat generation when temperature in the workpiece reaches melting point etc. Such assumptions are affecting the usability and the precision of results derived by developed models.

Mijajlovic et al. [67] developed a mathematical model to estimate the generated heat in the welding zone. An attempt was also made to validate the analytical model of the heat generation in the FSW process. Their mathematical model describes/defines contact pressure, contact condition, friction coefficient, thermal history of the welding plates and points out the dual nature of heat generation process in FSW-adhesion and deformation component in total heat generation. They also concluded that the vertical load is crucial parameter and determine the peak temperature, x-direction force, torque and the power features of the process [68]. Khandkar et al. [37] introduced a torque based heat input model where experimentally estimated torque is a heat source. There model improve heat transfer within the FSW process with frictional and deformational heat input into the process. The power, obtained from experimental investigation, has been distributed to the different interfaces formed between the tool and the weld piece based on the torques generated at different tool surfaces. Song and Kovačević [69] investigated the influence of the preheating period on the temperature fields in FSW. A sliding condition of the welding tool over the base metal was assumed and an effective friction coefficient and experimental plunge force are input into the heat source expression.

The plunging force effect contact condition under the shoulder can be described by sliding friction, using a friction coefficient and interfacial pressure, or sticking friction, based on the interfacial shear strength at an appropriate temperature and strain rate. Mathematical approximations for the total heat generated by the tool shoulder have been developed using both sliding and sticking friction models. Shercliff and Colegrove [70] developed a material flow model that investigates the influence of threads on the probe on material flow. An advanced viscous material model is introduced and the influence of

different contact conditions prescribed as the boundary condition is analyzed. A thorough presentation of analytical estimates of the heat generation in FSW and influence of material flow on heat generation is given, as well. Chao and Qi [27] have introduced a 3-D heat transfer model in FSW with constant heat input. Constant heat flux at the shoulder of the welding tool, constant contact pressure and pure Coulomb's friction law for estimating shear stress, and heat were the main assumptions of the model. The experimental welding of plates made of aluminum alloy 6061-T6 was performed and the temperature history of welding plates was estimated. Heat input was adjusted ("trial and error" principle) until numerical and experimental temperatures were matched. As such, this model is the first model developed for estimating the amount of heat generated during FSW. Schmidt and Hattel [33] have defined an analytical model for estimating the amount of heat generated during FSW that recognizes the shoulder and the probe of the welding tool as heat sources and concludes that about 89% of heat is generated at the shoulder. Heat has friction and deformation components and the total heat is a sum of both with influence of the contact state variable.

Schmidt et al. [71] provide an excellent discussion on the calculation of interfacial heat generation rates during FSW. A problem in the calculations of heat generation is that the friction coefficient cannot be determined from fundamental principles or it seems, by straight forward representative experiments of relevance to the conditions of FSW. Two contact models, the classical Coulomb contact model and the modified Coulomb contact model, were used in a fully coupled thermo-mechanical numerical model of the FSW and the suitabilities of the two models to simulate the FSW process were analyzed [72]. There is little difference between the numerical results of the two contact models for the FSW at low rotating speeds. In high rotating speed, the classical Coulomb contact model fails because the shear stress at the interface is not limited, but the modified Coulomb contact model may be used. A semi-analytical thermal model for the FSW was proposed [73]. The formulation of heat flow during the FSW process is based on generic solutions of the differential equation for heat conduction in a solid body, formulated for a point heat source with constant linear velocity. The heat generation was considered as a function of the tool-matrix interface temperature, which is calculated by means of a numerical routine written in MATLAB code. A comparison with the experimental measurements taken from the

literature showed that the results from the present semi-analytical model are in good agreement with the test data. In previous simulation studies, the contact conditions occurring in the FSW are generally described as stick and/or slip, according to different methodologies but these descriptions have their limitations. A new combination method was presented for characterizing the contact conditions that occur during FSW processes [74]. The thermal and mechanical outcomes from models with prescribed stick and slip conditions were compared to identify the results and drawbacks of assuming different contact conditions. This new method yields more reasonable estimates of heat generation, as validated by the experimental thermal measurements [75].

Kumar et al. [76] proposed an experimental model for estimating the friction coefficient during FSW. The model is based on the experimental estimation of the momentum of friction and axial force, which are necessary for estimating the friction coefficient [41]. Frigaard and Grong [77] presented a process model for heat flow in FSW, where they assumed that heat is generated only by friction on the tops of shoulders and probes. Heat input and friction coefficients were adjusted during the welding process to keep the calculated temperature below the melting point of base metal material. Heat input was a moving heat source with a linear distribution of heat flux at the contact surface.

Schmidt et al. [78] presented a model which accounted the compressibility of material by including the elastic response of the aluminum matrix in form of effective yield stress. It is possible to use an effective yield stress, back calculated from the experimentally determined average power input to the system or estimated from the local shear stress using a temperature and strain rate dependent yield stress [37]. Russell and Shercliff [79] provides the theoretical estimation of the heat generation based on a constant friction stress equal to the shear yield stress at elevated temperature, which is set to 5% of the yield stress at room temperature. The heat input is a pure point or line source. Ulysse [80] developed a 3-D visco-plastic FEA model using the commercial software FIDAP. The heat generation was determined to be a product of the effective stress and the effective strain-rate. Results show that the model consistently over predicted the measured temperatures probably from an inadequate representation of the constitutive behavior of the material used in FSW. Steuwer et al. [81] used the experimentally observed mechanical power as input in the model to investigate the influence of tool loads on residual stresses. They identified the asymmetry of

the welding process but the peak residual strain is typically 30% higher than measured by synchrotron X-ray diffraction. This may be due to stress measurement principles e.g. the area over which it is measured. Heurtier et al. [40] formulate a three dimensional model based on the fluid-velocity fields where the tool shoulder and the plastic strain of base material near the welding tool were heat sources. This semi-analytical model can be used to obtain the strains, strain rates, and estimations of the temperatures and micro-hardness in the various weld zones. The model also predicts the oxide distribution after welding to indicate the presence of a weakened zone in the weld.

2.1.3 Representation of heat source

The heat transfer analysis requires a heat source model that can accurately predict the temperature field in the weldment. So, correct estimation of heat source shape is important for comprehending welding process. However, same assumptions except about the heat source still applied to the analytical solutions, thus constraining their precision. Therefore, the level of refinement of the heat source model depends on the purpose of the thermal analysis. For modelling of residual stresses/distortions, a rough heat source model has proven sufficient for estimating 'correct' temperatures some distance away from the heat source (tool) [82]. Russel and Shercliff [79] used a combined point/line heat source for solving the temperature fields via a modified analytical Rosenthal solution to predict thermal fields. The predicted thermal fields were used as input for microstructure evolution models, which have previously been modelled by using some simplified heat source. Whereas, Frigaard et al. [30] used a uniform (constant) heat source distributed on several square shaped sheets to estimate temperature field. The heat input is proportional to the cube of the shoulder diameter. However, the contact area between the shoulder and the material surface has a significant effect on the heat input. Therefore, a non-uniform heat generation due to friction is considered during welding. Apart from this approach Fonda and Lambrakos [83] applied an inverse analysis of the heat flow in FSW for estimating analytical solutions composed of infinite series of point source solutions for temperature profiles adjusted to experimental observations of microstructures. Hattel et al. [84] presented six models (cases) for describing the heat source during heat transfer analysis. Each case is configured to verify the effect of refining the model with respect to the description of the probe and the effect of

the contact condition. The refinements of the heat source consist of three stages: (i) shoulder heat source only; (ii) shoulder and probe heat source, the latter as a volume flux in the matrix volume displaced by the probe; and (iii) shoulder heat source and probe heat source distributed at the probe/matrix interface. The volume displaced by the probe is removed, thereby avoiding heat transfer through the probe volume. However, Schmidt et al [85] applied a refined heat source model at tool/matrix contact interface. The heat flux distribution of heat source is radially dependent to obtain detailed transient thermal results, which cannot be simulated using less detailed heat source models. In particular, the estimation of temperatures close to the tool/matrix interface is of interest, because temperatures in the highly deformed zone are difficult to measure experimentally.

The tool-workpiece interface can be further subdivided into shoulder-workpiece and tool pin-workpiece interface. In most of the models [35, -102] the heat generation from the tool pin is neglected. Chao et al. [35] considered heat generation between work-piece and tool shoulder and formulated the standard boundary value problem which is solved by inverse approach by minimizing the error between experimental measured temperature profiles and numerically calculated frictional heat generation at the tool shoulder-workpiece interface. Chao and Qi [86] assumed a constant heat flux input from a tool shoulder-workpiece interface and used a heat transfer model using trial and error procedure in order to adjust the heat input until all calculated temperatures matches with experimental values. They also developed a moving heat source model in a finite element analysis and simulated the transient temperature, residual stress, and distortion of the FSW process considering heat generated from shoulder workpiece interface due to friction and plastic deformation [87]. Gould et al. [88] developed an analytical heat transfer model based on the well-known Rosenthal equation which describes a quasi-stationary temperature field over a semi-infinite plate due to a moving heat source by considering frictional heat on tool shoulder. Several authors have find the estimates of the heat source flux distribution in tool shoulder which depends on radial distance from tool center. In early work some researchers adapted the heat generation equation used by Midling and Grong [89] for friction welding.

$$Q_{friction} = \frac{2}{3}\pi\tau\omega R^3 \qquad (2.1)$$

where τ is the effective material flow stress, ω is the rotation speed in rad/s and R is the tool radius. Frigaard et al. [90] used an alternative approach based on the surface pressure and coefficient of friction between the shoulder and material:

$$Q_{friction} = \frac{2}{3}\pi\mu p R^3 \quad (2.2)$$

where μ is the coefficient of friction and p is the surface pressure. Chao and Qi [35], Colegrove et al. [91] and Song and Kovacevic [92] used a similar approach and adjusted the heat input till there was a good match with the experimental temperature results. They presented a mathematical model to describe the detailed three-dimensional transient heat transfer process in friction stir welding The heat input from the tool shoulder is modelled as a frictional heat and the heat from the tool pin is modelled as a uniform volumetric heat generated by the plastic deformation near the pin. Both of the above analyses assumed that the heat input from the pin could be ignored. Therefore, Colegrove et al. [91] estimated the threaded pin heat input with the following equation:

$$Q_{pin} = 2\pi r_p h\bar{y}\frac{V_m}{\sqrt{3}} + \frac{2\bar{\mu y}\pi r_{phv_{rp}}}{\sqrt{3(1+\mu^2)}} + \frac{4F_p\mu v_m cos\theta}{\pi} \quad (2.3)$$

Whereas, Schmidt and Hattel [93] adopted an engineering approach in which an inverse method is used to determine the heat flux quantities under the shoulder as shown in **Fig 2.3**. The distribution of flux depends on radial distance and intensity of flux is increased as it goes away from tool center which is explained in **Eq. 2.4**. The heat flux in the FSW process is primarily generated by the friction and the deformation process. This heat is conducted to both the tool and the workpiece. The amount of the heat conducted into the workpiece dictates a successful FSW process, the quality of the weld, shape of the weld, micro-structure of the weld, as well as the residual stress and the distortion of the workpiece.

$$q_{shoulser} = \frac{3Q_{total}r}{2\pi R^3_{shoulser}d} \quad (2.4)$$

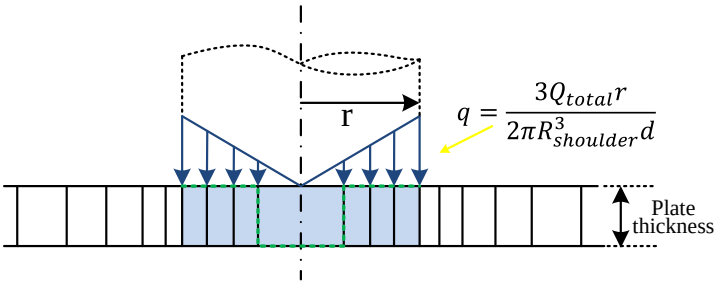

Figure 2.3. Schematic view of tool geometry with applied linear heat source on tool shoulder in 2D thermal model.

It is obvious that most of the models consider the heat input from the tool shoulder only, the heat generated at the tool-pin and workpiece interface is rarely considered. But, as previous studies specify that there are two sources of heat generation in FSW. One is due to friction and the other is due to plastic deformation at the tool-workpiece interface and at the thermo-mechanically-affected zone (TMAZ) as volumetric heat generation [94-95]. Colegrove et al. [96] shows that 20% of the total heat is attributed to the pin through the developed moving heat source model although the addition of heat due to the pin had little effect on the thermal profile. Russell et al. [97] investigated the effect of tool shoulder and pin geometry on heat input during FSW and used the Rosenthal equation for a uniformly moving point heat source to describe the effects of pin geometry on heat generation. Maalekian et al. [98] conducted thermal analysis of friction welding process using various heat generation models based on different friction mechanisms at the tool shoulder-workpiece interface. The inverse heat conduction approach predicted the heat-generation rate accurately, whereas the constant friction coefficient approach produced the most inaccurate temperature profile. Dong et al. [99] carried out a coupled thermo-mechanical analysis of the FSW process using a simplified two-dimensional axisymmetric heat transfer model. Song et al. [100-101] used a moving heat source to model the heat transfer during FSW and the heat generated at the tool shoulder/workpiece interface is considered as sliding contact frictional heat. The heat generation between tool-workpiece interfaces is greatly influenced by frictional heat but the effect of heat generated due to plastic deformation is rarely considered. Moreover, the difference in temperature distribution between advancing and retreating sides due to non-symmetric heat flux distribution is rarely observed in

literatures. There is lack of considerable information about the simplified shape of moving heat source during numerical study of heat transfer process in FSW.

2.1.4 Flow stress analysis

Material flow during FSW is very complex and many studies were conducted to understand plastic flow of material. These studies were followed by better calculations that included plastic flow, but fully three dimensional calculations are more recent and have revealed detailed insight into the FSW process, some of which cannot be understood using experimental techniques alone. Arora et al. [102] developed a three dimensional visco-plastic model of FSW to estimate temperature history and material flow and validated the same with experimental data. They assumed material as a non-newtonian fluid and flow stress as a function of temperature and strain rate. Kovacevic [103] conducted thermo-mechanical simulation of FSW to predict the transient temperature field, material flow stress, and forces in all the three dimensions. The thermal stresses constitute a major portion of the total stress developed during the process. Boundary conditions in the thermal modelling of the process play a vital role in the final temperature profile. Buffa et al. [104] performed a three dimensional analysis of FSW in DEFROM 3D to predict temperature history and strain profile during welding. They used flow stress as function of temperature, strain and strain rate. Regression analysis was used to calculate material constants. Zhang et al. [105] developed a fully coupled thermo-mechanical model to estimate temperature and strain profiles. Material flow was also simulated for different time intervals of the simulation. They used arbitrary lagrangian and eulerian analyses to simulate FSW in ABAQUS/Explicit. Simple coulomb law of friction was considered for the analysis.

Zhao et al. [106] used eulerian formulation that considers coupled visco-plastic flow and heat transfer in the proximity of the tool to predict temperature and strain rate during FSW. With the results of temperature and strain rate from the model, the micro hardness along the weld zone was predicted using the Hall-Petch relation. It was found that the predicted micro-hardness distribution along the friction stir zone agrees well with experimental results and the hardness is found to be essentially related to grain size in the stir zone. Similarly, Kim et al. [107] simulated the strain rate and temperature history to

compute the nucleation, growth, and coarsening of precipitates using microstructural modeling. With the distribution of the precipitates, the yield stress of the joint was calculated. Khandkar et al. [37] also predicted the temperature distribution and thermal history during FSW based on mathematical models. The working temperature and strain rate variables were combined and expressed by the Zener–Holloman parameter, which was shown to have an influence on the resulting grain size in extruded Mg based alloys. Whereas, Hattel et al. [108] studied the post-welding stress state, strain history and material conditions of friction stir welded joints in combination with subsequent structural analysis. Their approach in numerical model is combined with an in-situ weld simulation for a post-welding failure analysis. They found that the effect of residual stresses on subsequent load carrying capacity which was strongly affected by the applied boundary conditions.

2.2 Material flow behavior

During FSW heat generated by a rotating tool softens the material in the vicinity of the tool. The material undergoes intense plastic deformation following quite complex paths around the tool, depending on the tool geometry, process parameters and material to be welded [109-111]. The comprehension of the material flow is essential to prevent voids and other internal defects which may form during welding [112]. The flow of material during FSW is a complex process that is not fully understood despite numerous investigations and models. Several studies have compared material flow during FSW with wrought metal processes and have modeled weld nugget development as an extrusion process as shown in **Fig. 2.4** [1]. Therefore, its obligatory to comprehend and visualize material flow during process. But it is the most difficult aspects of the process to unambiguously characterize experimentally due to the difficulty in material flow measurement and visualization in metals. Metallographic analysis can be performed after welding and based on the resulting weld microstructure conclusions can be drawn about the temperatures and deformation but not temperately about material flow in the weld zone during the process. The following four different methods are reported in the open literatures to investigate material flow in FSW by experiments: particles as tracers [113], marker insert technique [114], metallographic, and electron backscatter diffraction technique [115], and X-ray transmission real-time imaging technique [116]. However, the marker technique provides the data on the initial and final

positions of the marker in the welded material and the flow is then reconstructed from these positions.

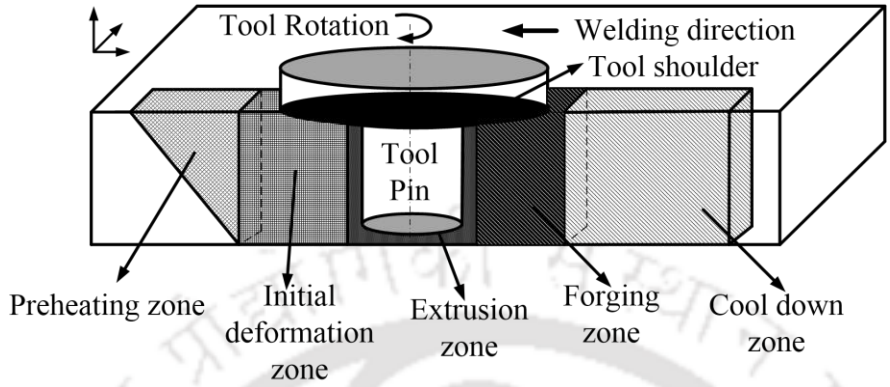

Figure 2.4. (a) FSW zones of different mechanical process and (b) The mechanical interacting these processes.

In an attempt to better understand FSW, many investigators have used experimental techniques to visualize the material flow. To visualize the flow of material during the FSW process a tracer technique can be used. Colligan [117] used steel spheres into grooves of threaded pin. The radiography test of the post-weld indicates that the vertical motion of the steel spheres is minimal and tended to move upward. Guerra et al. [118] used a copper foil at the faying surface of lap joint configuration of dissimilar aluminum alloy of 2xxx and 6xxx series. The material directly in contact with the pin rotates with the velocity of the tool. However, a longitudinal vortex is generated that creates significant vertical mixing in the weld. Other FSW material flow experiments included Schneider and Nunes [119] who used wire marker materials to follow the weld zone material deformation. It was found that material entering the weld zone on the retreating side was extruded around the pin while material on the advancing side was stirred around the tool before being deposited behind. Zhao et al. [120] studied the material flow of three different pins: column pin, taper pin and taper screw thread pin using a marker insert technique, and a 3D flow visualization showed that the vertical material flow is more obvious when taper thread pin is used. Several researchers have investigated the flow patterns in butt welds of similar and dissimilar aluminum alloys [121-124].

To understand the friction stir welding process, it is very important to know the nature of the material flow in and around the tool. The numerical simulations are very much

essential in order to obtain a complete knowledge of the process as well as the physics underlying it. The model simultaneously predicts shear strain fields, shear strain rates and shear stress. The flow fields generated by the streamline plot give an idea of the material flow. Several researchers, such as Arbegast [125], have attempted to develop flow-partitioned deformation zone model of the material flow during FSW as shown in **Fig. 2.5**. It describes the conditions under which volumetric defects is formed, such as voids and lack of penetration, which are directly associated with the material flow behavior. Whereas, Zhang et al. [126] developed a finite element technique based on the nonlinear continuum mechanics. They estimate the material flow around the tool and suggested that the material flow can be accelerated with the increase of the translational velocity and the angular velocity of the pin. There exists a swirl on the advancing side and the material flow in the swirl on the advancing side becomes faster with the increase of the translational velocity. This is similar to the two-dimensional model developed by Hamilton et al. [127]. Zhang and Zhang [105] expanded their model to three dimensions, similarly including particle tracking for flow analysis. They estimated that the material flows in different thicknesses are different. The shoulder can have a significant effect on material behaviors on the top surface, but this effect is greatly weakened when the material gets closer to the bottom surface of the welding plate.

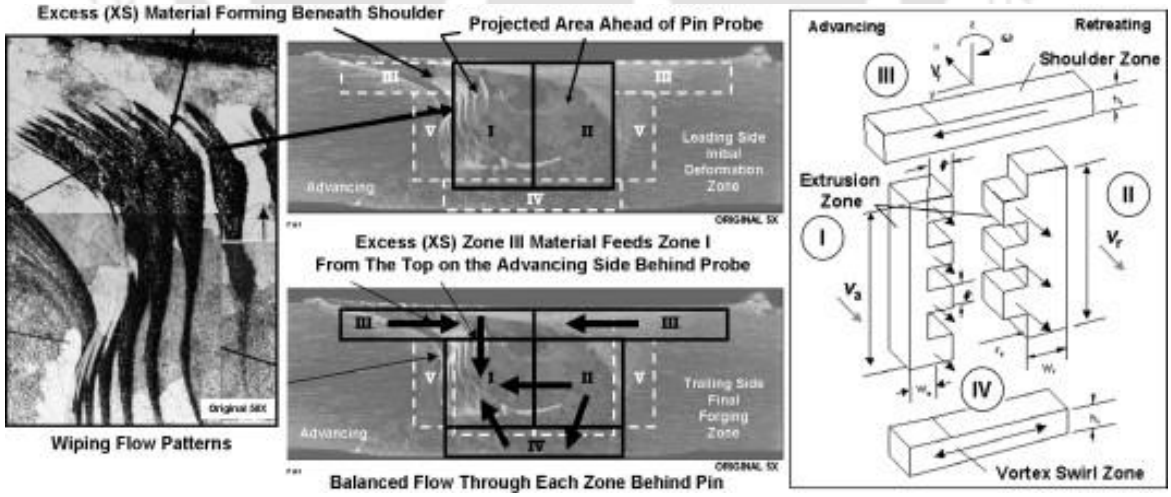

Figure 2.5. Flow-partitioned deformation zone geometries forming within the extrusion zone [125].

It is worth mentioning that due to the characteristics of this problem, by using fully coupled thermal-mechanical visco-plastic flow models [128-132], good results can be

expected where plastic deformations commonly occur. Ulysse [128] presented a 3D finite element model for determining the temperature profile using visco-plastic flow modeling to determine the effect of tool speeds on plate temperature. He also found that tool forces increase with increasing welding speeds, but it decreases with increasing rotational speeds. Moreover, the presence of high strain rate gradients around the probe along with tool geometric and kinematic characteristics, imposes a high computational demand to solve the problem. Similarly, Colegrove et al. [129] used "CFD package FLUENT" to investigate coupled thermo-mechanical visco-plastic model for aluminum workpiece and obtained good results with respect to material flow distribution. They modeled the 3D metal flow around a threaded tool assumed that the material is completely sticking to the tool. However, their model captured many of the real process characteristics, but its result shows higher estimated temperature and size of the weld zone. Badarinarayan et al. [130] also performed the thermo-mechanical simulation of AA5083-H18 using the CFD code under the unsteady condition to analysis the effect of pin geometry on material flow and joint strength. Nandan et al [131, 8] developed a 3D visco-plastic flow model of FSW for two different materials (Al alloy 6061T6 and 304 stainless steel), and estimate thermal history and material flow stress considering strain rate, temperature and temperature dependent material properties. The estimated temperature and velocity fields compared with experimentally measured values and found good agreement with the corresponding values. In both cases the viscosity was found to be a strong function of both strain rate and temperature, while strain rate was found to be the most dominant factor.

The modelling of material flow of the FSW process is challenging due to the generation of high strains at plasticized temperature with highly non-linear stress field. Therefore, the complex material flow analysis was deals with an Arbitrary–Lagrangian–Eulerian (ALE) formulation. Grujicic et al. [132] applied the ALE formulation to analysis the material flow of FSW of aluminum AA5059. They considered the FSW tool as a Lagrangian component while the workpiece material as an Eulerian component and studied the effect of process parameters including weld pitch, tool tilt-angle, and shoulder/pin diameter, on the material flow, by tracking the movement of an initial sub-volume of the workpiece. Pashazadeh et al. [133] developed a 3D ALE numerical model to obtain hardness

values. They assumed a rigid–visco-plastic material model for the workpiece, whereas the FSW tool and the backing plate were considered as rigid body. The numerical results showed good agreement with the experimental hardness result. Schmidt and Hattel [78] also developed a localized thermo-mechanical model considering Johnson-Cook's material model to analysis material flow during FSW of aluminum 2xxx. They utilized coupled temperature-displacement dynamic explicit methodology with ALE technique to obtain solution. The authors found that higher cooling rate leads to faulty deposition of material behind the tool pin. Zhang and Zhang [134] used an approach similar to that of Schmidt and Hattel [78] to study the effect of welding parameters on material flow and residual stresses in friction stir butt weld of Al 6061-T6. The material flow around the FSW tool was investigated using tracer nodes.

It is not easy to establish a model considering plastic deformation and heat transfer simultaneously. Even though the modelling is possible through ALE, a tremendously large amount of simulation time is required. To solve this problem by considering eularian domain for workpiece. The usefulness of this approach is that it involves no distortion of the mesh and the Eulerian formalism leads to satisfactory computation times [135]. Therefore, Al-Badour et al. [136] developed a coupled eularian lagrangian finite element model to study effect of process parameters on material flow during FSW. Workpiece was generated as localized Eulerian region, while the FSW tool was consider as lagrangian. During analysis they considered the effect of the coefficient of friction, welding speed, and mass scaling. The result shows that by controlling the welding force joint quality can be improved through minimizing the weld defect size. Bendzsak et al. [137] used the Eulerian code Stir3D to model the flow around a FSW tool, including the tool thread and tilt angle in the tool geometry and obtaining complex flow patterns. The temperature effects on the viscosity were neglected. They used the finite volume method to predict the flow field in the fully plasticized region of a friction weld. Similar and dissimilar welds were analyzed. In the similar welds the viscosity was found from a heuristic relationship, which was independent of temperature. The dissimilar welds used a transient thermal model, a complex viscosity relationship and an Eulerian-Lagrangian mesh. A fluid dynamic, or Eulerian, scheme is also an often used alternative, for example the recent work by Pal and Phaniraj [138], and although this approach is good for calculating material flow, it has difficulty computing free

evolving surfaces and tracking material history. In addition, the assumption that the workpiece is a viscous fluid is difficult to justify, given FSF is a solid-state process. Particle methods on the other hand, are able to inherently track material surfaces and particle history without the need for any additional algorithm. The need for remeshing is also alleviated as the particles are not explicitly inter-connected. With this in mind, a number of modellers in various fields have begun to apply particle based numerical methods to solid mechanics problems [139].

2.3 Hybrid friction stir welding

Industries have shown remarkable interest in the hybrid welding process due to its sheer advantages when compared with the fundamental processes of welding. Hybrid friction stir welding is a quite innovative joining technique. It has vast potential for extending its application to different fields of industrial application. This technique, which is considered as a derivative of the more common friction stir welding process, was developed mainly to overcome hindrance of FSW. As an outlying benefit, it provides significant improvements in weld quality and efficiency of processes in manufacturing applications.

It is commonly observed that welding of high plasticization temperature and harder alloys is difficult as compared to aluminum and other soft alloys through FSW. This indicates that if additional heat is given to harder alloys before and during welding process would reduce the amount of work required by FSW tool. This additional heat reduce resistance offer by workpiece material to FSW tool and thus would improve the tool performance, tool life, FSW process window, welding efficiency and weld quality. The additional heating of the high melting temperature material in FSW can be achieved by applying additional heat source or mechanical plasticization mechanism on the workpieces. Based on the mode of assistance, these processes may be classified into two categories: thermal energy assisted FSW and mechanical energy assisted FSW. Thermal methods used for this purpose are electricity, [140–147] induction, [5, 148–150] laser, [151, 156] plasma, [57, 160] arc, [161–167] hot gas stream, [20] gas torch, [168] etc. Electricity and induction are used for resistance heating of the workpieces. Laser, gas and arc/plasma are applied for direct preheating. Ultrasonic energy is the only mechanical energy employed for this

purpose. Ultrasonic vibrations directly soften the material without much variation in the process temperature.

2.3.1 Electrically assisted FSW (EAFSW)

Electrically assisted FSW process utilized electric current for enhancing metal softening before mixing and plastic deformation. Electrical current provides additional heat to soft material by the inevitable resistance heating and the electro-plastic effect. These additional heating effects complement the actual heat generated during the FSW process and reduce the flow stress required to continue plastic deformation. There are two ways to integrate electrical current with FSW as shown in **Fig. 2.6**; generally exerted on the workpieces directly **(Fig. 2.6a**) or via the FSW tool (**Fig. 2.6b**). In the electro-plastic phenomenon, the resistance heating softens the material or reduce the deformation resistance during the plastic deformation without substantial increase in temperature [140].

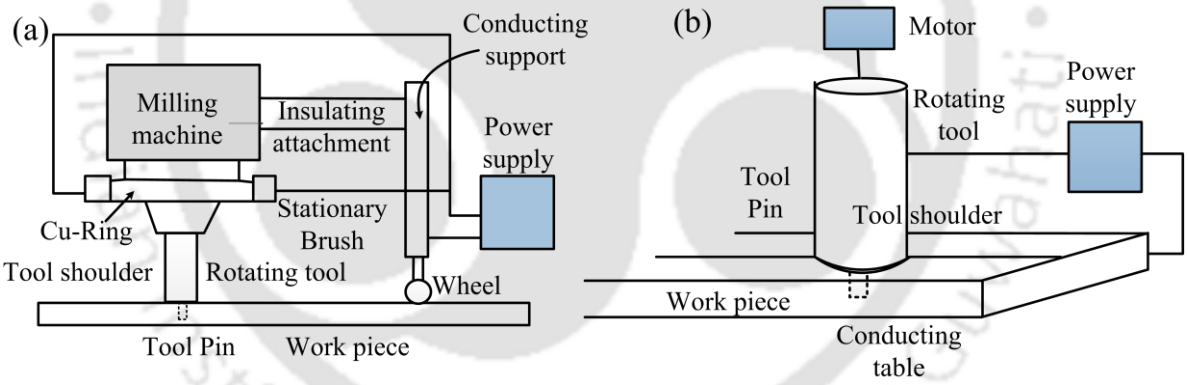

Figure 2.6. Schematic illustration of electrically assisted FSW process.

Ferrando et al. [141] developed a circuit including tool and workpiece for heating the metal of the workpieces immediately adjacent the rotating stir tool with electrical resistance occurring between the stir tool and workpieces. Local heating produces better material softening and adversely affect the weld quality. Similarly, Long et al. [142] also used electric current for local heating and passes electric current from the welding tool into the workpiece through the contact area in the welding region. This local electrical resistance heating reduced the plunge force significantly during the pin plunge stage and subsequently tool wear, whereas the welding speed of the EAFSW process increased by two times than

conventional FSW. Luo et al. [17, 143] developed EAFSW which is based on electric resistant heating of some softer and harder alloys to increasing heat generation during welding. The resistant heat source promoted significant improvement in plasticization of the materials that leads to grain refinement and hardness improvement in the nugget zone. Santos et al. [144-145] utilized electrical joule effect in development of conventional friction stir welding with the ability to eliminate or minimize the root defects caused by lack of penetration. This innovative feature enables to increase the temperature in the weld root by Joule effect and improve material visco-plasticity in this region. Potluri et al. [146] applied the concept of electrically-assisted manufacturing (i.e., passing high direct electrical current through a workpiece during processing) to the conventional friction stir welding process. The expected benefits are reduction in the feed force and torque, which allow for improved processing productivity as well as the possibility for deeper penetration of the weld. Liu et al. [147] utilized a local electrical current field which is moving with the FSW tool. Axial welding force can be effectively reduced with application of current due to improve material visco-plasticity. This phenomenon is more pronounced under a lower rotating speed and a smaller tool offset into aluminum.

2.3.2 Induction assisted FSW (IAFSW)

Induction heating occurs when an electrically conductive material is placed in a varying electromagnetic field. The magnetic field induces an electric current inside the material and thus causes resistive heating of the material. Therefore, this resistive heating is utilized during FSW to plasticize the workpieces and thus reduces the plastic deformation resistance. In the experimental setup, the weld zone of the workpieces should be inside the electromagnetic field of the induction coil and coil moves linearly along the weld line in close proximity just ahead of the welding tool to avoided heat loss. It is most advantageous to provide non-contact heating of workpiece but the workpieces has to be electrically conductive material. Oeystein et al. [15] investigate the effect of induction coil preheating on joining of aluminum alloy Al 6082 T5 and ferrous alloys with induction assisted FSW process. The result shows that the forces on the tool reduced to 50% with the increase in welding speed. This ensures the increase in productivity and improvement in joint mechanical properties. It's also more efficient during joining thick sections without any

significant change in the mechanical properties of joint. Grant et al. [148] solved the issue of tool wear during welding of cast iron by using induction heating system while tool made up of W-Re and PCBN material. They applied induction heating system just ahead of the FSW tool to plasticize the workpiece. They found great reductions in the welding forces. The reductions of forces minimize the tool wear with improvement in material flow.

Sinclair et al. [149] utilized the heating system during the joining of AA 6061-T6 aluminum plate of 0.25 inch thick. The heating system was controlled by thermostat to obtained programmed desired temperature. The aluminum alloy was heated to initial material temperatures up to 300°C which result in slight increase in material flow with increasing temperatures. The result also shows the significant reduction in welding forces up to 43% with even moderate heating. Alvarez et al. [150] studied the microstructure changes and the mechanical properties of a friction stir welded super duplex stainless steel along with induction coil preheating. Preheating technique allows welding with a reduction in forge forces close to 31% at the same welding speed, or doubling speed (200 mm/min) at the same axial force, obtaining sound welds.

2.3.3 Laser assisted FSW (LAFSW)

LAFSW is a hybrid welding process which uses a laser heat source to preheat a workpiece before joining. The commonly used laser sources are Nd:YAG fibre optic laser, diode laser and CO2 laser. A schematic of the LAFSW is shown in **Fig. 2.7**. LAFSW introduces additional non-contact local heating immediately ahead of the weld zone so that the tool will be imposed with a lower amount of mechanical energy. Palm [151] used CO_2 Laser as additional heat source. The heat source is used to heat the region immediately in front of the rotating probe. Similarly, Kohn et al. [18] applied laser energy to preheat the work piece at a localized area ahead of the rotating tool, thus softening a volume of the work piece ahead of the tool. In the FSW of AZ91D Mg alloy, the application of laser preheating lowered the resistance of the material to tool penetration and forward motion. Therefore, the need to apply large forces on both the tool and the workpieces is lowered.

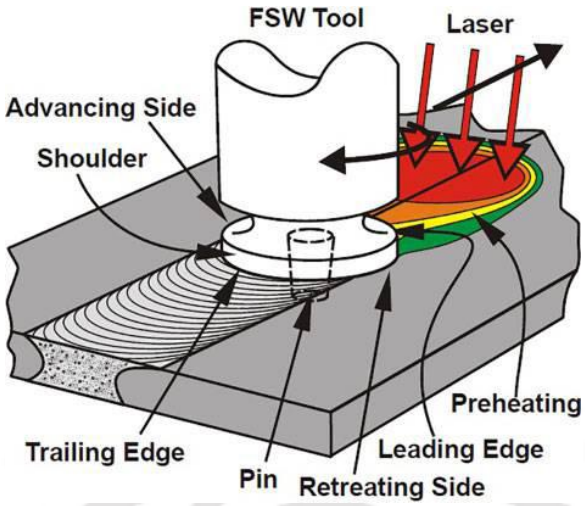

Figure 2.7. Schematic illustration of principle of laser assisted friction stir welding [151].

Song et al [152] carried out laser-assisted hybrid friction-stir welding of Inconel 600 to evaluate the effect of preheating on microstructure and mechanical properties. The investigation was performed at a constant speed (400 rpm) with 2-kW YAG laser preheating was used in front of the rotating tool. The local increase in the temperature of workpieces by laser preheating induces plasticization of the workpieces ahead of the welding tool that leads to reduction in resistance of material. They found the LAFSW is 1.5 times faster than conventional FSW with grain refinement led to 30% and 10% improvements in micro-hardness and tensile strength, respectively. Similarly, Campanelli et al. [153] also conducted test on similar joint of 6 mm thick 5754-H11 aluminum alloy plates in butt joint configuration. They studied the effect of process parameters, such as laser power and temperature gradient on the changes in microstructure, micro-hardness, residual stress, and tensile properties. It was found that the hybrid process improves welding efficiency in term of tool wear, higher welding speeds, and lower clamping force.

For the purpose of improving the strength of dissimilar joint, Chang et al. [154] carried out laser assisted hybrid welding of Al6061-T6/AZ31 alloy plates using third material between the faying edges. They achieved defect-free joint by using a laser power of 2 kW with reduction in brittle Ni-based intermetallic phases. The tensile strength of the joint was increased by 66% of the Mg base metal tensile strength in the case of hybrid welding with Ni foil and showed higher hardness value than that of the friction stir welded join with

and without the third material. Merklein et al. [155] carried out an experimental study of laser assisted FSW of steel and aluminum sheets to increase weld feed and reduce tool wear. In their paper, a parametric study was performed in order to determine process parameters guarantying best mechanical properties of the welded parts. Tensile tests were performed to achieve mechanical properties of joints, which were welded by systematic variation of process parameters. Finally, deep drawing tests are conducted to demonstrate the formability of laser assisted friction stir welded steel aluminum joints. Bang et al. [156] investigated the laser assisted FSW joint of Al6061-T6 aluminum alloy to SS400 low-carbon steel for weldability and mechanical characteristics. They reported laser or GTA assisted friction stir welding of steel to aluminum alloy. The joint strength was achieved ~ 90 –93% with reference to Al alloy as compared to ~ 60 – 78% without the effect of external heat source. Furthermore, it was demonstrated that tool life and decrement of applied load was expanded during joining of dissimilar materials with the aid of external heat source.

2.3.4 Arc assisted FSW (AAFSW)

Electric arc is a most efficient and cheap preheating source used in manufacturing process to improve process efficiency. It may be a plasma arc source or a tungsten inert gas (TIG) welding arc. First attempt to utilize electric arc during FSW was performed by Kou and Cao [157]. It was found that joint strength was improved due to enhanced plastic flow of material by using a secondary heat source of GTAW. Furthermore, it was revealed that tool life is improved due to decrease of load between the tool and material during welding. Bang et al. [158-159] utilized GTAW preheating heat source during FSW of dissimilar materials of Al6061-T6 aluminum alloy and STS304 stainless steel, shown in **Fig. 2.8**. It reduced the tool wear and enhanced material flow during welding. The results indicated that the tensile strength was approximately 93% of the aluminum alloy base metal strength. Similarly, Joo [160] performed hybrid FSW of magnesium alloy (AZ31B) and mild steel (SS400), using a GTAW preheating heat source to the mild steel plate surface. The tensile strength of the hybrid welds was approximately 91% of that of the magnesium alloy base metal but higher than that of the normal FSW welds. This is due to the enhanced material plastic flow and partial annealing effect in the magnesium alloy and mild steel materials by GTAW preheating of the mild steel side.

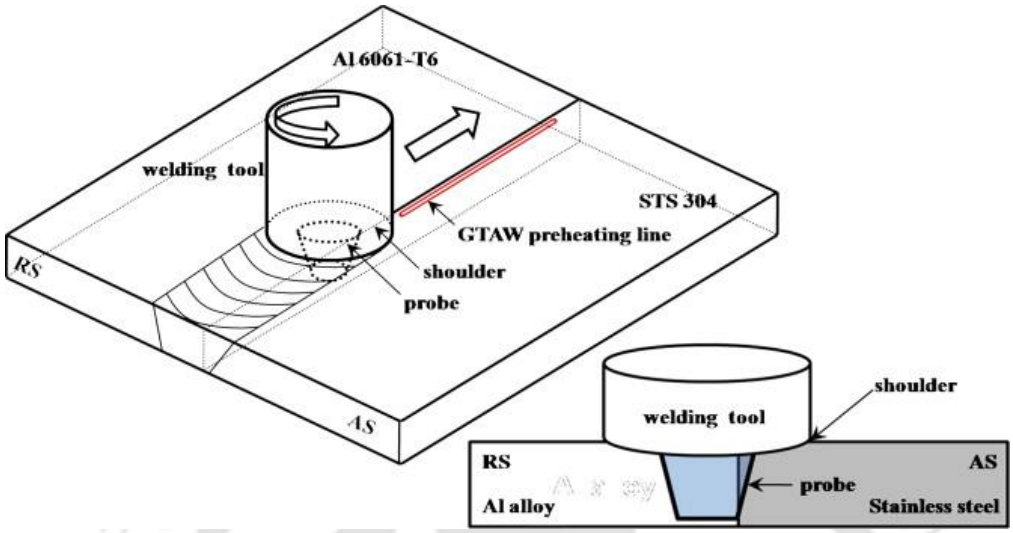

Figure 2.8. Schematic illustration of principle of dissimilar hybrid FSW process using GTAW as preheating source [158].

2.3.5 Ultrasonic vibration assisted FSW (UAFSW)

High frequency vibrations such as the ultrasonic vibrations are applied on a static load that softens the metallic materials without much significant heating. The ultrasonic energy reduces the yield strength of the material and produce similar effect as thermal softening. Therefore, ultrasonic vibration has been widely used in metal forming process to study plasticity of metals and results revealed that ultrasonic vibration decreased the yield stress and flow stress of the metal during plastic deformation [161]. Recently, the implementation of ultrasonic energy in FSW process shows remarkable potential to improve joining efficiency. Lai et al. [162] applied ultrasonic vibrations directly on the tool to improve weld performance during FSW of 1.8 mm 2024 aluminum alloy as shown in **Fig. 2.9(a)**. However, transfer of vibration through the tool may also affect the physical properties of the tool material by acoustic effects. In such a transfer, there is an issue of energy loss and there may be tool wear due to the load of the bearing. Results show the impact of the ultrasound's vibrations on the temperature field is less obvious at lower welding speeds. However, at higher welding speeds, it can provide the additional heat to keep sufficient welding temperature.

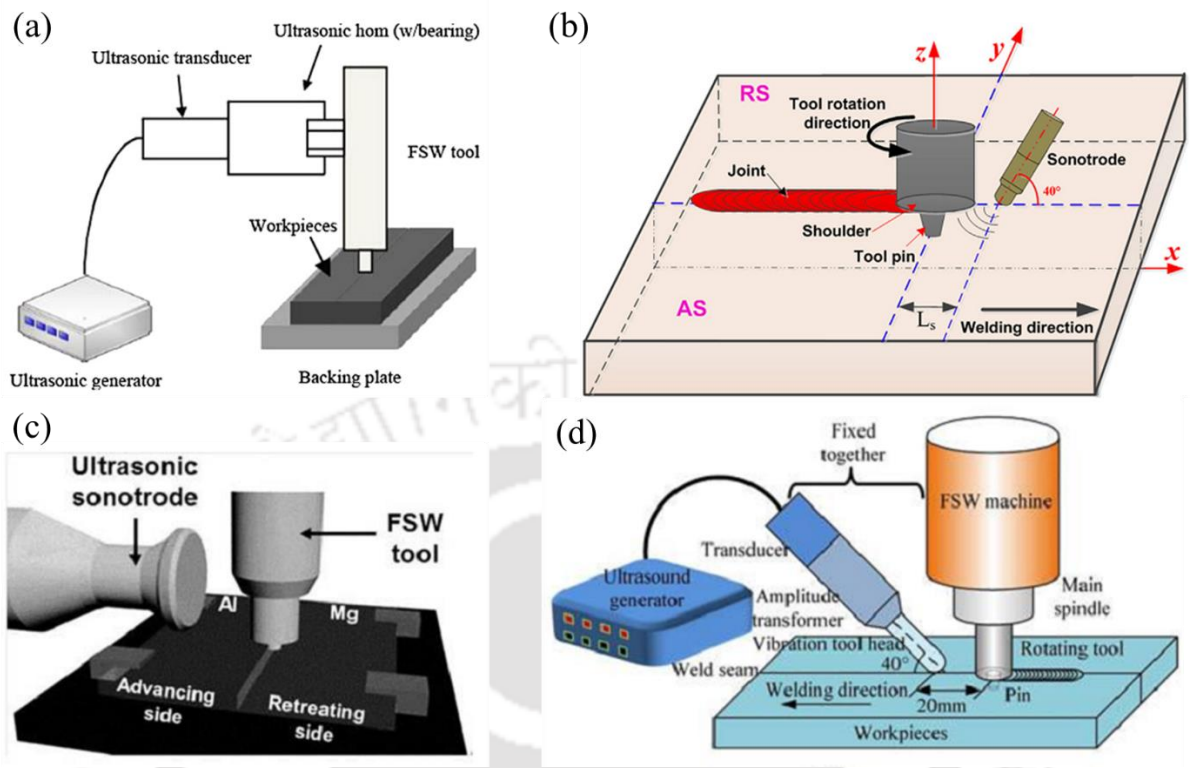

Figure 2.9. Different method to apply ultrasonic vibration during FSW process [162-165].

Shi et al. [163] developed a system to apply the ultrasonic vibration during FSW welding of aluminum alloy 6061-T6. The ultrasonic vibration is directly transmitted into the plastically deformed material layer near the FSW tool by a sonotrode, as shown in **Fig. 2.9 (b)**. It produces an enhanced plastic material flow, increase the welding speed and welding efficiency, and also improve the weld quality by enhancing the plastic material flow near the tool. Strauss et al. [164] performed comparative study of conventional FSW and ultrasound supported friction stir welding (US-FSW) of dissimilar Al/Mg joint. They applied ultrasonic vibration parallel to the welding direction either through the workpiece directly or through the backing plate as shown in **Fig. 2.9(c)**. They found that the US-FSW-joints strength is increased up to 30% in comparison to conventional FSW. However, the ultrasonic vibration is applied in Al side and energy transfer to workpiece is far away from the weld zone. This may affect the beneficial transfer of energy to the weld zone due loss of heat. Liu et al. [165-167] developed a new hybrid FSW system which transmits ultrasonic vibration directly into the localized area of the workpiece near and ahead of the rotating tool. The ultrasonic energy is transmitted onto the weld centre line of the joints at an angle 40^{o} as illustrated in **Fig. 2.9(d)**. The ultrasonic vibration is transmitted to workpiece through sonotrode which travels

at a distance 20 mm ahead of the tool and it's very close to weld zone. Therefore, this method is appearing to be the most efficient method of transmitting the ultrasonic energy because the energy is transmitted directly into the weld zone. The result shows that the assisted FSW process produced good weld joint with improved mechanical properties in a wider process parameters window than the FSW process due to the softening effect of the ultrasonic vibration.

2.3.6 Other thermally assisted FSW

The plasticization and cooling rate of workpiece material can be controlled by external heat source such as gas torch and hot gas stream. This heat source provides thermal assistance before and after the FSW process to improve joint efficiency. Lotfi and Nourouzi [20] used the hot gas stream such as a nitrogen stream to preheat the workpieces slightly ahead of the FSW tool as shown in **Fig. 2.10**. The preheating system comprises a heating element (3 mm diameter and 40 m length) embedded within a ceramic tube. The tube is then casted by ceramic, and the system is subsequently provided with thermal insulation to prevent heat loss. A nitrogen gas stream driving at a constant flowrate via the hot element and the nozzle onto the weld seam produces the preheating effect. The temperature is controlled to ensure that the weld seam temperature is lower than the A1 critical temperature, precipitate dissolution temperature and the aging temperature of the workpiece. Choi et al. [169] developed a gas torch hybrid FSW process, in which material is post heated directly by using a gas torch after the welding. During the process, gas torch was artificially moved behind the welding tool at a fixed distance in order to control the cooling rate during welding. This controlled cooling enabled the formation of duplex structure of ferrite and cementite in weld zone.

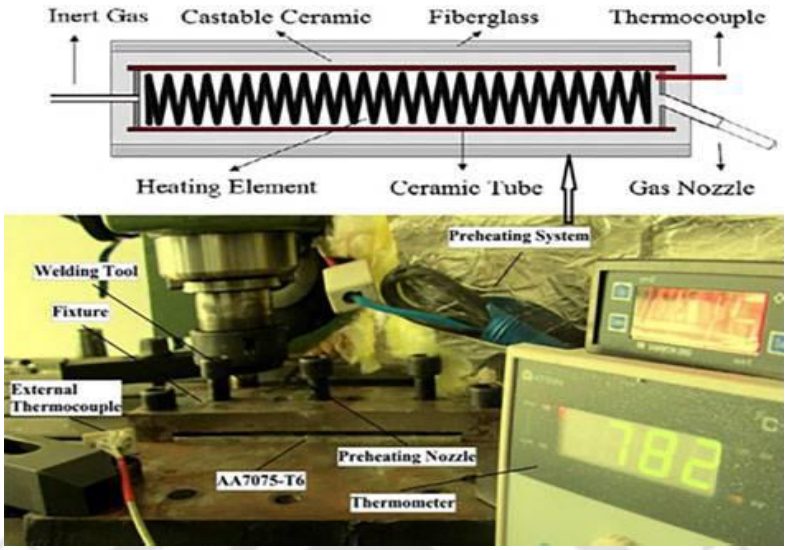

Figure 2.10. Hot gas stream assisted FSW setup using a nitrogen stream to preheat the workpieces [20].

2.4 Design and performance of FSW tool

A FSW tool is obviously a critical component to the success of the process. The tool typically consists of a rotating round shoulder and a straight, threaded or conical cylindrical pin that heats the work-piece, mostly by friction, and moves the softened material around it to form the joint [12]. There are three types of FSW tools namely, fixed, adjustable and self-reacting, as illustrated in **Fig. 2.11**. The fixed pin tool is made of single material and it's able to weld constant thickness workpiece. While, Ding and Oelgoetz [169] developed the adjustable pin tool which have separate shoulder and pin part, that allows to adjust or replace the pin when worn or damaged. In this design, the shoulder and pin can be made of different materials to weld harder workpiece to overcome frequent damage of pin. Afterward, Skinner and Edwards [170] developed self-reacting tool which have additional tool shoulder in bottom to support and generate additional heat. Also, this self-reacting tool can provide some portability to FSW and eliminate some common defects of conventional FSW.

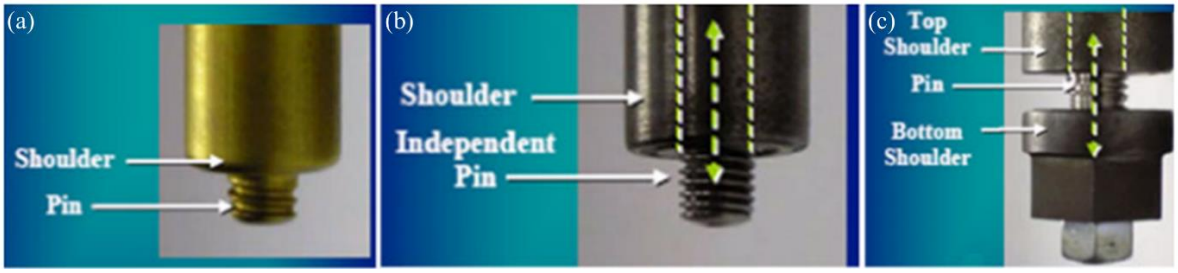

Figure 2.11. Different types of FSW tools (a) fixed, (b) adjustable and (c) self-reacting [12].

Shoulder is important part of FSW tool which generate 70-80% of the total heat and produce the downward forging action necessary for welding consolidation to yield proper material flow during welding. The tool shoulder can also provide confinement for the heated volume of the material [13]. Therefore, tool shoulder end surface inclination with respect to workpiece surface (such as flat, concave and convex) and feature on end surface play vital role to improve performance of tool. Reynolds et al. [171] and Nelson et al. [172] used concave shoulder end surface and restricted material extrusion from the sides of the shoulder. The concave shoulder inclines only a small angle from the flat shoulder end surface. During tool plunging, the material displaced by the probe is fed into tool shoulder cavity. Hence the concave surface profile of the tool shoulder serves as an escape volume or reservoir for the displaced material from the probe. Another possible end shape of the shoulder is a convex profile and it pushes the material away from the probe due to that it is unsuccessful [173].

However, Nishihara and Nagasaka [174] reported that a smooth convex end surface shoulder with a 5 mm diameter was successful to weld 0.4 mm thick AZ31 Mg alloy sheets. Whereas, some researchers [175-176] utilized the shoulder end surfaces with some features to increase material friction, shear and deformation for increased workpiece mixing and higher weld quality. The typical shoulder end styles include flat (smooth or featureless), scrolls, ridges, knurling, grooves and concentric circles, as revealed in **Fig. 2.12**. These features can be applied to concave, flat or convex shoulder ends. Scrolls are the most commonly used shoulder feature. Dawes et al. [177] described the outlined of the tool design aspects of the scroll shoulder concept.

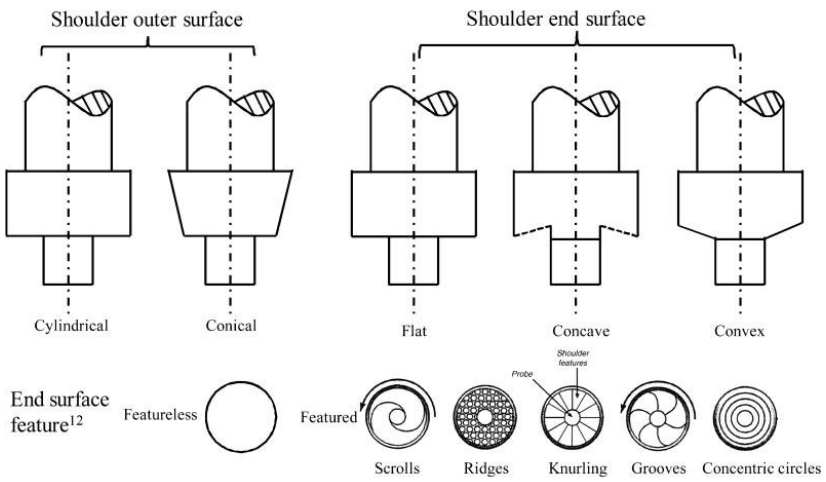

Figure 2.12. Summarizes the typical shoulder outer surfaces, the bottom end surfaces and the end features [176].

An important parameter in FSW is the ratio of dynamic volume (volume swept by the pin during rotation) to static volume (volume of the pin itself). Increasing this ratio results in a reduction in the formation of voids in the welds and allows the surface oxide to be more effectively disrupted and dispersed within the microstructure. In conventional FSW, the dynamic/static ratio can be increased via the use of re-entrant features, flutes, threads and or flats machined into the pin as shown in **Fig. 2.13** [176]. Dawes and Thomas [177] found that the addition of flat features can change material movement around a probe. This is due to the increased local deformation and turbulent flow of the plasticised material by the flats acting as paddles. Elangovan et al. [178] investigated the effect of axial force and tool pin profiles on FSP zone formation in AA6061 aluminium alloy. Five different tool pin profiles (straight cylindrical, tapered, cylindrical, threaded cylindrical, triangular and square) were used to fabricate the joints at three different axial force levels. They found that the square tool pin profile produces mechanically sound and metallurgically defect free welds compared to other tool pin profiles. Chowdhurya et al. [179] studied the effect of pin tool thread orientation right-hand thread (RHT) and left-hand thread (LHT)) in the clockwise rotation on the fatigue resistance of friction stir welded (FSWed) AZ31B-H24 Mg alloy butt joints. They found that the fatigue strength was higher in the joints made with the LHT pin tool than with the RHT pin tool due to the elimination of the welding defects near the bottom surface via a downward material flow. Similarly, Zhao et al. [180] and Schnider and Nunes [121] made FSW joints using right hand thread (counterclockwise) tool profile and

left hand thread (clockwise) tool profile respectively to observed occurrence of welding defects. The combination of the thread orientation with the rotation of the pin tool increased an extra downward force and heat generation that would be beneficial to accelerate the flow of plasticized material to ensure good mechanical bonding.

On the other hand, Cao and Jahazi [181] recently observed some noticeable defects at the bottom or root of the welded joints with a right hand screw threaded pin in the clockwise rotation. These observations indicated that the material flow pattern during FSW is a function of pin tool thread and direction of rotation. But little is known of the effect of the left hand thread (LHT) and right hand thread (RHT) pins on the microstructure and mechanical properties of the FSWed. Zettler et al. [182] welded 4 mm thick 2024-T351 and 6056-T4 Al alloys using three different tapered probe designs: non-threaded, threaded and threaded with flats. It was found that the non-threaded probe produced voids, while the two threaded probes produced fully consolidated welds. The flats on the probe act as the cutting edge of a cutter. The material is trapped in the flats and then released behind the tool, promoting more effective mixing. The addition of the flats was also shown to increase the temperature and nugget area. Mishra and Mahoney [183] conducted experimental studies FSW of aluminum alloy using tool which contains three flutes cut in to the helical ridge. The flutes reduce the displaced volume of a cylindrical pin by approximately 70% and supply additional deformation at the weld line in addition it increases the tool travel speed and it can be used advantageously to welding thick-section aluminum alloys.

The fundamental requirement of the FSW tool is high resistance to wear, high strength and hardness at both room and elevated temperatures, and effective heat-dissipation ability with respect to welding material. However, due to extreme load condition tool experience excessive wear which changes the tool shape, thereby increasing the probability of defect generation, and possibly degrading the weld quality. The exact wear mechanism depends on the interaction between the workpiece and the tool materials, the selected tool geometry and the welding parameters. Liu et al. [184] analyzed the effect of welding speed which has a decisive effect on radial wear rate of the pin. The FSW tool was made of a WC-Co hard alloy and the tool pin possessed right handed threads. A series of tool photographs

was obtained and the variations in tool geometry were accurately calculated in a computer system. Thompson and Babu [185] used three tungsten-based tool materials namely material A (99% W-1% La_2O_3), material B (75% W-25% Re), and material C (70% W-20% Re-10% HfC) to join high strength steel. They identified the tool degradation mechanisms by studying the pre- and post-weld microstructures of the tool. They found that the grain deformation was the most significant source of tool degradation. The primary degradation mechanism of material A was deformation, for material B it was twinning and for C it was inter-granular failure. The shoulder size and pin length are changed slightly and the radial wear of the pin is most severe for the whole tool. The radial wear of tool is different at different locations of the tool and maximum wear is produced at a location of about one-third pin length from the pin root. The welding speed also effect on radial wear rate of the pin that is lower the welding speed, higher the wear rate and the maximum wear rate is produced in the initial welding.

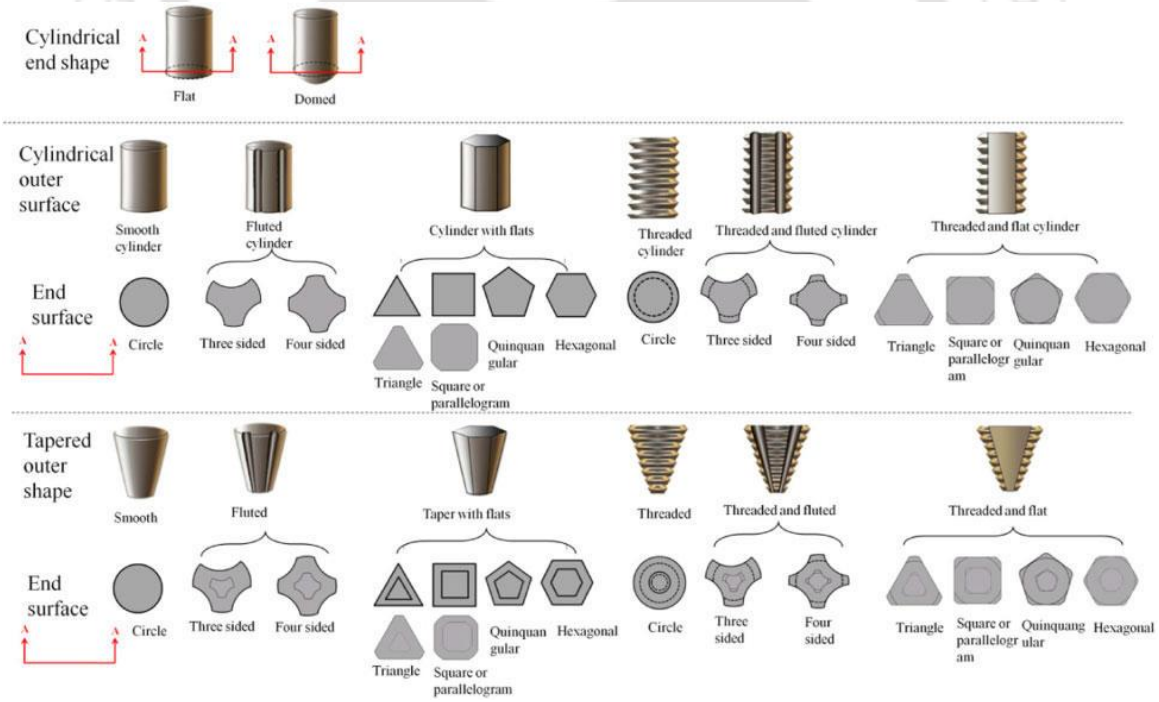

Figure 2.13. Different re-entrant features, flutes, threads and or flats on pin surface [184-185].

Prado et al. [186] studied the tool wear and the rate of wear in the FSW of Al 6061 aluminum alloy with respect to different welding speed. They observed that the tool shape is

changed with increase of welding speed and suggested that the tool wear and shape change are due to counter motion of solid-state flow regimes which depend upon both tool rotation speed and actual weld traverse speed. Plane tool shape was more sustainable than threaded tool which continues to produce excellent welds but without any additional tool wear. The self-optimized shape changed with increase in weld speed and at a constant tool rotational speed of 1000 rev/min. Lienert et al. [187] studied tool deformation and wear by comparing critical tool dimensions for a given tool before and after each weld using an optical comparator. Metallographic and metrology techniques suggested changes in tool dimensions resulted from both rubbing wear and deformation of the tool. The greatest changes in dimensions occurred during the initial plunging stage. Wu et al. [188] investigate tool wear at different travel distances of polycrystalline cubic boron nitride (pcBN) tool at rotation rates of 400, 800 and 1200 rpm during FSW of Ti–6Al–4V alloy. They found that at high rotation rates of 800 and 1200 rpm, the greatest tool wear, including mechanical and chemical wear, occurred at the initial tool plunge point.

Park et al. [189] conducted a detailed study on the tool wear in FSW of stainless steel using pcBN tool. They reported that apart from mechanical wear, chemical wear is also occurred and Cr-rich borides formed through the reaction between the workpiece and the pcBN tool. These Cr-rich borides have adverse effect on the tool strength during welding. Zhang et al. [190] succinctly reported tool wear of pcBN during FSW of pure titanium using electron microprobe analysis (EMPA) and energy dispersive spectrometer (EDS) and they inferred that tool might have reacted with titanium. They had not identified the FSW parameters which influenced tool wear and the nature of the wear products. However, Pilchak et al. [191] showed that millimeters of bands consisted of sub-micro-sized tungsten-rich particles as the result of tool wear were deposited in the stir zone. Tool wear not only reduces the lifetime of the tool but also probably affect the material flow and the properties of the welds. Agrawal et al. [192] studied tool wear during FSW of AA6063 aluminum alloy and pure copper. The rubbing action with high strength alloys such as brass and AA6063 materials at a higher rotational speed may result in wear of the tool. Additionally, the sticking of Cu–Al mixed material on the surface of the tool after every welding run is a big issue which causes defects and tool wear. However, this problem can be avoided by

inserting the FSW tool into the fresh Al material after every experiment. Insertion of tool in fresh material helps to react Cu–Al mixed material with fresh Al material which in turn clean the tool pin and prevent the defects.

2.5 Dissimilar material joint

In some industrial application, the complementary characteristics of different materials are required, such as increased strength, lowered mass and cost in aerospace industry. So, the joining of dissimilar materials for industrial application to be solved. However, it is difficult to obtain sound dissimilar welds because of the great differences in their thermo-physical performance of materials [193-194]. To solve this problem, special welding methods had been reported to join different materials such as pressure welding, diffusion bonding etc. Friction stir welding (FSW) which is a potential candidate for the joining of dissimilar materials due to its advantageous lower processing temperature over conventional fusion welding [1]. Dissimilar friction stir welding which included welds between the different series of aluminum alloys, aluminum to magnesium, steel, titanium and event composites has been successfully produced by many researchers [5].

2.5.1 Mechanical properties and process parameters

It is reasonable to believe that the location of the materials in FSW of dissimilar alloys could lead to more severe temperature asymmetry. This asymmetry in temperature, stress and materials flow between the advancing and retreating sides could significantly affect the dissimilar joint quality and properties, which mainly depends on the properties of the two materials and the welding parameters such as tool rotation speed, travel speed, tool offset and positions of the materials. The variation of process parameters affects heat generation and leads to diffusion of copper particles into aluminum, increase the intermetallic compositions (IMCs) and the number of micro cracks formation [195]. Sundaram et al. [196] investigated the effects of various process parameters namely, tool pin profile, tool rotational speed, and welding speed on mechanical properties of the dissimilar joints between AA2024 and AA5083 Al alloys. They reported that dissimilar joints fabricated using tapered hexagon tool pin profile have the highest tensile strength and tensile elongation, whereas the straight cylinder tool pin profile have the lowest tensile strength and tensile elongation. Palanivelet et al. [197] examined the influence of tool rotational speed

and pin profile on the microstructure and tensile strength of the dissimilar friction stir welded aluminum alloys AA5083-H11 and AA6351-T6. The welds fabricated using straight tool profiles had no defects while the tapered tool profiles caused a tunnel defect at the bottom of the joints under the experimental considered conditions. Furthermore, three different regions namely unmixed region, mechanically mixed region and mixed flow region were observed in the weld zone.

Aonuma and Nakata [198] studied the weldabilities of Ti/2024, Ti/7075, Ti-6Al-4V/2024 and Ti-6Al-4V/7075 butt joints by FSW. The weldability of the Ti and 2024 Al alloy was better than of the Ti and 7075 alloy, and the tensile strengths of the Ti/2024 joints were higher than the other joints under the same joining conditions. Dehghani et al. [199] investigated the effects of various parameters of FSW on intermetallic and defect formation in joining Aluminium alloy (Al 5186) to Mild Steel. The thickness of MS and Al sheet was 3 mm. The tool rotation speed for all samples was fixed at 355 rev/min The welding speed, pin size, tool plunge depth, tool tilt angle and pin geometry were changed to find the optimum welding condition in which the tunnel defects were prevented and formation of IMCs was restricted. Watanabe et al. [200] studied butt-welding of aluminum alloy to mild steel by FSW, and observed the effects of pin rotational speed and position of the pin axis on the tensile strength and the microstructure of the joint. They found sound joint with minimal intermetallic compounds at tool rotation speed of 250 rev/min.

Recently, the range of combinations of the dissimilar metals used in industrial application are increasing greatly. Tanaka et al. [201] analyzed the effect of rotation speed on temperature rise and joint strength of 7075-T65 aluminum alloy and mild steel at constant welding speed, and the effect of heat input on the formation of intermetallic compounds and resultant tensile strength was investigated. Kim et al. [202] reported that the large defect formation is a result of excess heating and insufficient mixing of plasticized material. Akinlabi et al. [203] carried out investigation on FSW of 5754 aluminum alloy and C11000 Copper. The welds were produced at a constant rotational speed of 950 rpm and the traverse speed was varied between 50 and 300 mm/min while all other parameters were kept constant. Better mixing and metallurgical bonding were improved at the lowest traverse speed. The average UTS of the welds decreased as the welding speed increased due to low

downward vertical force and high heat input [204-205]. Chen and Kovacevic [206] studied the feasibility of joining Al 6061 to AISI 1018 steel. They reported the effect of pin position on the temperature distribution and microstructure of weld zone at constant tool rotation and traverse speed.

Xue et al. [207-208] successfully achieved sound FSW of Al–Cu joints by offsetting the tool to the aluminum side and controlling the FSW parameters. They found sound defect free joints under larger pin offsets with hard Cu plate at the advancing side. Good tensile properties were achieved at higher rotation rates and proper pin offsets of 2 and 2.5 mm. Similarly, Song et al. [209] studied the effect of probe offset distance during dissimilar FSW of titanium alloy Ti6Al4V and aluminum alloy A6061-T6 of 2 mm thickness. Their results indicated that at lower probe offsets the defects formed inside the joints, and at higher values of probe offsets the amount of brittle intermetallic compounds increased which caused to lower mechanical properties. Also, they revealed that in a suitable range of probe offset distance, defect free joints can be produced, which have reasonably better tensile strength. Elrefaey et al. [210] investigated experimentally the influences of welding parameters such as rotating speeds and traveling speeds on the joint strength during friction stir lap welding of pure aluminum plate to low carbon steel plate with the thickness of 2.0 mm and 1.2 mm respectively. Saeid et al. [211] investigated the feasibility of lap joining of 1060 aluminum alloy and commercially pure copper using FSW. They found that welding speed affect tensile strength of joint with respect to change in effective influence on the plastic flow and consequently the heat input with welding speed. Furthermore, lower welding speed caused more vertical transport, while a higher welding speed caused less vertical transport on the retreating side. Kimapong et al. [212] studied the effect of welding parameters on the friction stir lap welding of steel and aluminum. They found that the shear strength of the joint could not be improved by increasing the tilt angle or pin diameter, but the inter-metallic compounds could be reduced and a sound joint could be obtained by increasing the pre-hole diameter.

2.5.2 Formation Mechanism of IMCs

During FSW of dissimilar metals, the IMCs are easily formed in the nugget zone due to severe plastic deformation and thermal exposure. Similar to other joining methods, when IMCs are excessively generated, the dissimilar FSW joints usually exhibit poor mechanical

properties due to the inherent brittle nature of the IMCs. Therefore, preventing the formation of excessive IMCs is extremely important in FSW of dissimilar materials. The formation mechanisms of intermetallics were investigated by few researchers. At the beginning of the FSW process, due to the frictional heating, the weld is heated to a certain temperature, which is higher than the equilibrium solidus temperature of the eutectic structure. The plastic deformation and high-temperature induced the grain boundary diffusion and the interfacial diffusion, thus local melting occurred. During the sleeve retraction period, the "solid-liquid" phase material experienced further diffusion and dynamic recrystallization [213-214].

The intermetallic formation rate at the interface is diffusion-driven and is a function of time, temperature and alloying element [215]. Satisfactory mechanical properties can be achieved by reducing the thickness of intermetallic compound layer [216]. The thickness of intermetallic compound layer can be reduced by controlling the process parameters and composition of weld metal, controlling the heat flow into weld [217] and by using an interlayer which exhibits improved diffusion resistance to both Al [218] and Fe [219]. Hyung et al. [220] investigated how the interfacial intermetallics compounds were formed in the Al–Cu bonds. The study revealed that the thickness of the intermetallic compound layer is a function of temperature and holding time. The atomic diffusion of Cu and Al through the intermetallic compound is the main controlling process for the intermetallic compound growth. Recently, Akbari et al. [221] introduced a new material (anodized Al-MIL-A-8625 F containing coating of anodic sulfur with a layer of Cu thickness of 23 mm) as an intermediate layer between AA6060 and Cu base materials. This intermediate layer has prevented the formation of brittle IMCs and 25% increase in shear strength was reported than the joint without the use of the intermediate layer. The same technique is employed by Elrefaey et al. [222] for dissimilar pure Cu and AA1100-H24 FSW system by using 50 μm thick Zn intermediate layer. They have reported improved joint performance by limiting the formation of hard and brittle IMCs. Different processing parameters were affecting the size and amount of the formed IMCs at the nugget zone.

Galvao et al. [223] looked into the influence of the welding parameters on the establishment and distribution of brittle intermetallic phase during aluminum–copper FSW.

The study concluded that varying the tool travel speed alters the heat input available in the weld region. Since heat is the predominant factor influence the diffusion of dissimilar materials, the thickness of the intermetallic layer along the aluminum/copper interface can be controlled by varying the tool travel speed. On the other hand, Shojaeefard et al. [224] concluded that rotational speed contributes overall 40% in dissimilar Cu–Al FSW system. Rotational speed is an important process parameter of FSW, because it influences the large amount of frictional heat generation, plastic deformation of material, and forces on the tool which consequently influences the formation of IMCs, material flow, defect generation, the size of the stirred zone, and tool wear in the dissimilar FSW system. A mutation in a frictional heat generation also affects the formation of IMCs in dissimilar Cu–Al FSW. Higher rotational speed forms the large amount of IMCs because of higher heat input. Therefore, decreasing the welding speed at constant rotational speeds led to similar trend to increasing the rotational speeds at constant welding speeds [205]

The thickness of the intermetallic layer and its composition at the weld interface is mostly induced by tool offset as shown in **Fig. 2.14**. Okamura and Aota [225] investigated the technique of shifting the tool pin toward the aluminum side in FSW of 8mm thick plates of 6061 aluminum alloy to oxygen-free copper. It reduced the base materials mixing and, consequently, reduced the formation of brittle Al/Cu intermetallic phases during welding. Which improve friction plastic flow and produce less defective welds with improved surface appearance relative to welds obtained with no tool offset. However, in spite of this, welds with offset displayed very poor tensile properties. Genevois et al. [226] also used tool offsetting in friction stir welding of 4mm thick 1050-H16 aluminum alloy to commercially pure copper plates. These authors used full offsetting, with the pin fully displaced to the aluminum side, working tangent to the copper plate. No mechanical mixing between the base materials was observed in these conditions. The authors reported that frictional heating promoted thermally activated inter diffusion at the Al/Cu interface, giving rise to the formation of a very thin layer of intermetallic compounds (about 200 nm).

Xue et al. [208] studied the morphological, structural, and mechanical properties of 5 mm thick friction stir welds between 1060 aluminum and pure copper with different degree of tool offset in aluminum side. They observed that small amount of tool offset (from 0 to 33 % of the pin radius) gave defective joints with poor surface finishing. With small tool offset,

the amount of material interaction is more which result in brittle cracking incidence, due to the formation of high amounts of brittle intermetallic phases. Also, generate unsuitable material flow which produce macro-defects in weld zone. However, larger tool offset (between 67 % and 83 % of the pin radius) improve the weld quality and surface finishing. Still, most of the welds failed at the aluminum/copper interface for very low bending angles. Galvao et al. [227] concluded that the amount of material interaction is controlled by tool offset. When the probe offset was larger, only few Cu pieces with relatively small size were scratched from the Cu bulk. It is easy for the small Cu pieces to mix and react into the Al base in the nugget zone, and therefore sound metallurgical bonding would be obtained at the nugget zone.

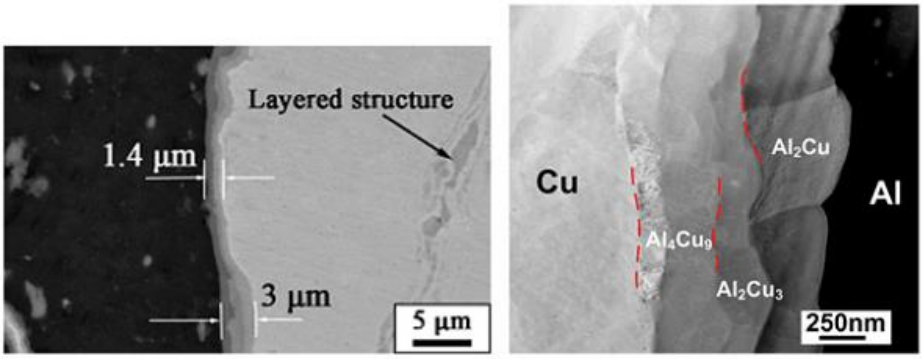

Figure 2.14. SEM image of Cu-Al interface layer and IMCs [228].

2.6 Microstructural study

FSW achieves solid phase joining by locally introducing frictional heat and plastic flow by rotation of the welding tool with resulting local microstructure changes. The local microstructure determines the weld mechanical properties. Therefore, it is important that details of microstructural evolution during the severe thermo-mechanical conditions imposed by FSW be well-defined. Also regardless of the material in which the friction stir weld is performed, the resulting microstructure has three distinct zones that result from the welding process i.e. nugget zone, thermo-mechanically affected zone and heat affected zone as shown in **Fig. 2.15**. All three constituents of the weld zone have distinct features which determines the properties of FSW joints and it can be characterized by using optical micrographs, X-ray diffraction, and TEM. The shape, size, and distribution of precipitates in

weld zones, and the strength and ductility of welds were seen to correlate directly with peak temperatures in weld nuggets and heat affected zones.

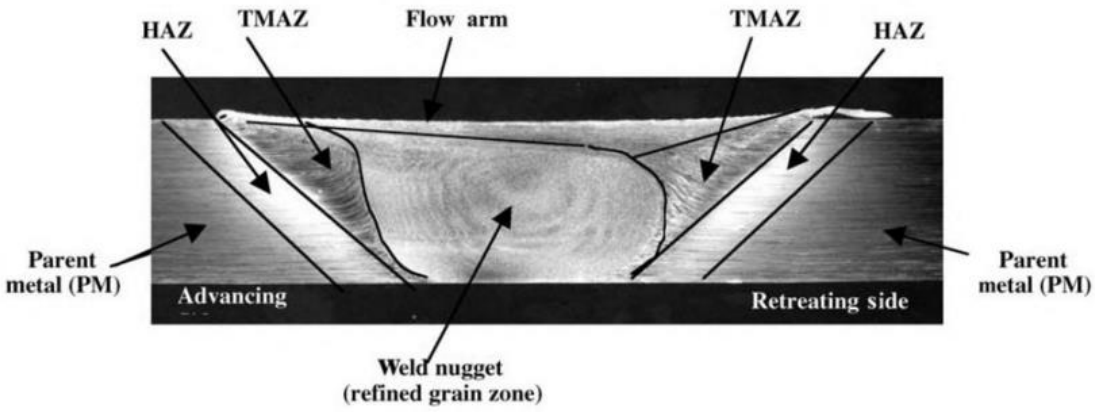

Figure 2.15. Transverse section of friction stir weld showing different regions of the weld. HAZ, heat-affected zone; TMAZ, thermos-mechanically affected zone and weld nugget [1, 4].

The FSW process involves several complex stages that are difficult to visualize during the joining. The various phases of the FSW process and the microstructure and metallurgy of the resultant weld depend on the material of the workpieces, tool material, tool geometry and process parameters such as tool rotation speed, tool tilt angle, welding speed and target depth that affect the heat generation and material flow in the process. The three zones pose distinct mechanical properties but TMAZ has been often documented as being the weakest part of the joint [4]. Adamowski and Szkodo [229] observed softening of the material in the weld nugget and heat affected zone i.e. the hardness of both the heat affected zone and the weld nugget is lower than that of the base metal. The weld zone is not symmetrical due to the rotational movement of the tool, thus moving material from advancing side to retreating side [4]. Mishra et.al [1] observed basin shaped nugget zone and elliptical shaped nugget zone in low rotational speed and higher rotational speed, respectively. The NZ is relatively small, and is characterized by a shape loosely resembling the FSW tool used. The zone is characteristic of all friction stir welds, and has several qualities that are significantly different from the surrounding microstructures. In the NZ, the dynamically recrystallized grains are frequently an order of magnitude smaller than the grains of the base material.

The microstructure of the friction stir welded joints also depends on base materials. Aluminum alloys contain a wide variety of microstructures which is hardly surprising when the extreme range of strains, strain rates and thermal cycles to which different regions of the weld are exposed is considered. Murr et al. [230] reported textural gradients associated with FSW and dynamic recrystallization in pure Al 1100 and suggest that the fine grain structure formed within the center of the welded zone. Whereas, Sato et al. [231] presented microstructural study of an ARBed Al 1100 alloy joint with ultrafine grained microstructure and higher hardness. They found that the grain size gradually increased locally from the base material region toward the center of the stir zone. The microstructure evolution and mechanical properties of friction stir processed pure aluminum was studied by Yadav and Bauri [232]. They found refined grain size of 3 μm in a single pass from the starting coarse grain size of 84 μm and grain are equiaxed fine grains with well-defined grain boundaries. In FSW, the material is generally subjected to high strain rate and aluminum is normally subjected to continuous dynamic recrystallization that leads to steady state grain size in nugget zone with a huge difference with respect to base material grain size.

In FSW, tool geometry plays a fundamental role in obtaining desirable mechanical properties and microstructures in the welded zone. Scialpi et al. [233] investigated the effect of three different shoulder geometries on the mechanical and microstructural properties of the joints. They found light influence of shoulder geometry on the nugget grain dimension, this is due to the different heat power generated by the three shoulders. Fujii et al. [57] investigated the effect of columnar tool probe with and without threads and triangular prism cross-section. There was no significant effect on the microstructures and mechanical properties of the joints as compare to process parameters. But, different pin profile and welding parameters induced significant changes in the material flow pattern and microstructure of NZ during welded joint of AA6016-T4 [234]. Wei and Nelson [235] used a convex scrolled shoulder step spiral tool. They found a linear relationship of heat input with ferrite grain size and bainite lath size. Pseudo heat index, power and advance per revolution exhibit nonlinear relationships with post-weld microstructures. Ramanjaneyulu et al. [236] joined 5 mm thick AA2014-T6 aluminum alloy using tools with non-circular pin profiles. They found finer microstructure in the weld nugget and thinner TMAZ in joints

produced with hexagonal pin tools. Non-circular tool pin flats generate pulsating action and relatively higher temperatures throughout the microstructure across the weld joints. Elangovana et al [237] studied the influences of tool pin profile and welding speed on the formation of friction stir processing zone in AA2219 aluminum alloy. The joint fabricated using square pin profile tool contains finer grains compared to other joints. The higher number of pulsating action experienced in the stir zone of square pin profiled tool produces finer grained microstructure with uniformly distributed precipitates and in turn yields higher strength and hardness. Therefore, tool pin profile plays major roles in deciding the weld quality.

Yeni et al. [238] reported recrystallized fine grain structured at the NZ. The grain sizes increased from the weld region to the base metal. Radisavljevic et al. [239] reported that the thread shape (regular and rounded) strongly influence the cross section morphology and hardness distribution during FSW. However, Ikuta et al. [240] used pins with different thread depths in FSW and concluded that the thread has limited influence on the weld mechanical properties. Fonda and Bingert [241] studied the microstructure across the weld zone of friction stir welded aluminum alloy 2195. They found that the sub-grains were form within the TMAZ with boundary misorientations through continuous dynamic recrystallization by sub-grain rotation. This mechanism describes the generation of sub-grains and their evolution into grains through a dynamic recovery-dominated process. Sun and Fujji [242] analyzed the effect of SiC particles on the microstructure and mechanical properties of the pure Cu joints during the friction stir welding process. The particle-rich region has an average grain size of less than 2μm, much smaller than that of about 8μm in the particle-free region. Microstructural observation confirmed that the SiC particles can act as the heterogeneous nucleation site in the dynamic recrystallization of Cu grains.

The thermal history during FSW influences the cooling phenomena of the weld. In addition, the mechanical and metallurgical properties of the joints depend on the interatomic forces, which are influenced by the additional heat source. Therefore, the microstructure of HFSW joints would be significantly different from their FSW counterparts. Sun et al. [19] developed a laser heating system which was used as a preheating source during the FSW of 3.2 mm thick S45C steel plates. Although the appearances of the welds are quite similar, the

phase constitutions in the stir zone are different from each other due to change in cooling rate caused by leaser preheating. Song et al. [243] studied the microstructure and mechanical properties of a laser–FSW hybrid welding joint of Inconel 600, and found that HFSW improvements grain refinement and dynamic grain recrystallization caused the average grain size to decrease 58 % in the stir zone of the welded specimen. While, Luo et al. [17] found that with increasing the electric current, led to increase in grain size during dissimilar electrical current aided FSW process. Campanelli et al [244] conducted a comparative study on FSW and LAFSW of aluminum alloy. They observed that the microstructures are not affected by laser preheating while the nugget shape is sensitively altered. The grain size appears smaller and with an equiaxic and regular shape just under the weld surface with a laser power of 2 kW. Strass et al. [245] used ultrasonic vibration to reduce the development of the intermetallic phases of Al/Mg-joints significantly during dissimilar joint. Microstructures show that the shape of the boundary of FSW and UAFSW are different. In addition, the vortex like weld nugget becomes unobvious in UAFSW.

There is a prominent feature observed in the nugget region such as the appearance of a series of circular or elliptical features which is often termed as 'onion rings'. Biallas et al. [246] studied the effect of FSW parameters on tensile properties and ductility of 2024Al-T4. They suggested that the formation of onion rings was due to the reflection of the material flow from the cooler walls of the heat-affected zone. The induced circular motion led to circles that decrease in radii and formed the tube system. Threadgill [247] suggested that the formation of onion ring was associated with the forward motion of the tool in one revolution, but they have not studied the effect of the onion ring formation process on the properties of the weld joint. Based on the above studies, Krishnan [123] has been made an attempt to explain the formation of the onion rings, the practical significance, and their likely effect on properties. He conducted FSW using differently colored clays, which made up the band structure. However, these techniques do not clearly explain how the material flows, as they do not consider continuous phenomena during FSW. He suggested that the FSW process could be thought to be simply extruding one layer of semicylinder in one rotation of the tool, and a cross-sectional slice through such a set of semicylinders resulted in the familiar onion ring structure. However, Chen and Cui [110] conducted experiments

using an aluminum alloy and pin–workpiece couples to determine the formation mechanism of banded structures. They provided more direct evidence for material flow adjacent to the pin, and suggested that the spacing of the onion rings was equal to the tool advance per rotation due to geometrical restriction. Similarly, Cui et al. [248] studied onion ring pattern formed in the weld zone during FSW of aluminum alloy. They observed that the formation of onion ring is attributed to the mechanical shaking effect caused by the variation in the stress state of the deformed metal due to the tool rotation. In addition, they suggested that the spacing of the onion rings is equal to the advance of the tool per revolution. Recently, Yoon et al. [249] suggested different theory for formation mechanism of typical onion ring structures and void defects in friction stir lap welded dissimilar aluminum alloys. The results revealed that the threaded probe was significantly correlated to typical onion ring structure and the onion structure formed as soon as it touched the probe.

During dissimilar FSW, onion ring structure and the intercalated microstructure were responsible for formation complex flow pattern in the weld zone [250]. This structure in the weld nugget is variable in shape and layer thickness of the onion ring due to uneven flow abilities of the two alloys. Khodir and Shibayanagi [251] conducted investigation on friction stir butt welding of 2024-T3 Al alloy and AZ31 Mg alloy of 3mm plates. The nugget zone decreased its size and became rounder shape with higher welding speed. They found lamellar-like bands where either 2024 Al alloy related region or AZ31 Mg alloy is lying one on another. Other characteristics of the rings include texture effects and variations in dislocation density was influence by process parameters also. While, Leonar et al. [252] have shown for alloys 7075 and 2014A that the ring patterns are an etching response to variations in grain size between the rings. Yong et al. [253] investigated FSW between AA 5052 and AZ31 Mg alloy. They observed that the microstructure of the base metal was replaced by equiaxed and fine grains in the stir zone. Furthermore, at the top of the stir zone, 5052 and AZ31 alloys were simply bonded, while onion ring structure which consisted of aluminum bands and magnesium bands was formed at the bottom of the stir zone.

Unlike FSW of similar materials, typical cross section of FSW dissimilar joint is difficult to be divided into different regions. Moreover, the nugget zone does not exhibit the classical onion ring structure due to different materials flow patterns and formation of

intermetallic compound [254]. Zadpoor et al. [255] studied the global and local mechanical properties and microstructure for two friction stir welded aluminium alloys namely, 2024-T3 and 7075-T6. They found heterogeneous texture in NZ. Large intermetallic particles were observed in the HAZ and NZ. The yield strength and plasticity parameters drastically vary around the weld centerline. Jiang and Kovacevic [256] joined 6061 Al alloy and AISI1018 steel and found defects free joints. The high joint strength was observed from tensile failure location which is at the boundary between the NZ and TMAZ. The average NZ hardness was found to be higher than base Al alloy. Fine Al-Fe intermetallics and coarse steel pieces were observed in the SZ. Li et al. [257] was investigated the friction stir welding of pure copper/1350 aluminum alloy sheet with a thickness of 3 mm. Complex vortex-like pattern and lamella structure are formed in the dissimilar FSW joint. The lamella structure in the bottom of the nugget is more homogeneous and finer than other regions. Also, Murr et al [258] investigated the microstructures of Cu-6061Al FSW joints, and found that a complex intercalation microstructure consisting of vortex-like and swirl features was formed in the joint. Although many researchers reported that intermetallic compounds existed in the FSW CuAl dissimilar joints.

2.7 Summary

From the literature, it is observed that many researchers have studied about the effect of process parameters like shoulder diameters, pin profile, tool rotational speed, welding speed, axial force, and tool tilt angle on the material flow, defects formation in the joints, microstructural changes, and mechanical properties in various similar and dissimilar materials. From the published works, it is noticed that each parameter has its own significance in changing the joints properties. Specifically tool design influences the heat generation, material flow, power required and the uniformity of the welded joints. It creates uniform microstructure and comparable mechanical properties with base material. Along with tool design, the process parameters such as tool rotational speed, welding speed, tool tilt angle and axial force are also affect the microstructure and mechanical properties of the joints. In the previous studies a common conclusion was made for the selection of welding parameters to achieve required temperature and material flow during the welding, and higher

quality mechanical properties in weld joint of similar and dissimilar materials with same or different thickness is obtained from optimum combine of process parameters.

These optimum parameters are obtained from experiments but experiments are often time consuming and costly to identify optimum parameters for FSW. To overcome these problems, different numerical approaches are developed and investigated. Those approaches and their findings are presented in this chapter. Some established numerical modeling techniques can explain and predict heat generation and material flow involved in the FSW. The numerical models cover a broad range of complexity, from the simple conduction heat transfer models to the fully coupled thermo-mechanical models in which the visco-plastic flow and the heat transfer phenomena were used for predicting temperature and residual stress distributions. However, a reliable FSW process modeling depends on the fine tuning of some process and material parameters. The numerical modeling of the FSW process can help to achieve optimal process parameters with less effort and with economic advantages. In addition, several important key problems and issues on numerical analysis of FSW remain unaddressed and there are opportunities for further research.

Although, commercial implementation of FSW to materials beyond aluminum alloys is hitherto limited, and such implementation in the near future would still require higher levels of FSW technology, model based investigations and better design and materials for manufacturing of FSW tools. Many studies have already been focused on improvement and development of new FSW process. In the enhanced process fixed and floating bobbin tool can be implemented. In recent years, new concept of partial or additional softening of the harder alloys before or during the FSW is introduced. It reduces the load requirement on the tool and thus improves the tool performance, tool life, FSW process window, welding efficiency and weld quality. External (or additional) heat sources used for this purpose are thermal energy from electric resistance heating, induction heating, laser, plasma, arc, etc. and mechanical energy in the form of ultrasonic vibration. The immediate objectives of all the additional heat assisted FSW processes converge at achieving sufficient local plasticization of the workpieces ahead of the tool. It is obvious that the more plasticized the material would be, the better the flow characteristics, the joint quality and the tool life would be. However, development of these variants, their experimentation, etc. are still in their

preliminary stage and systematic investigations on the process optimization, weld joint efficiency, weld performance, etc. are limited. More investigations are necessary for their critical assessment. In addition, the current investigations with these variants of FSW are mostly limited to aluminum alloys. The feasibility of each individual variant to harder and complex materials is yet to be testified in greater details.

2.8 Scope of the present work

Friction stir welding process was developed initially for joining aluminum, it was inevitable that interest would emerge in applying it to other materials. An increasing volume of work is appearing on friction stir welding of materials such as magnesium, copper, titanium and steels. Therefore, significant progress has also been made in the fundamental understanding of both the welding process and properties of the welded joints. The understanding has been useful in reducing defects and improving uniformity of weld properties and, at the same time, expanding the applicability of FSW to new engineering materials. So, based on the study of existing work in literature, the scope of present work is outline as follows:

- The fundamental knowledge of asymmetry in heat generation during FSW process with respect to difference in thermal history of advancing side and retreating side. Attainment of this important goal would require new, more reliable and efficient heat source model to describe the evolution of heat during welding. This understanding would be useful in reducing defects and improving weld properties.
- Commercial feasibility of the FSW process depends on development of cost effective and durable tools which lead to structurally sound welds consistently. The ratio of dynamic volume (volume swept by the pin during rotation) to static volume (volume of the pin itself) is important parameter in FSW to improve tool performance and joint efficiency. The dynamic/static ratio can be increased via the use of re-entrant features and threads machined into the pin. Therefore, different threaded FSW tools can be investigated to increase dynamic/static ratio. This addition of features can change material movement around the pin due to the increased local deformation and turbulent flow of the plasticized material by the threads acting as paddles.

- Recently, several hybrid FSW processes have been developed to overcome drawbacks of conventional FSW process. One of these variants is thermal-assisted FSW in which a preheat source is placed before the FSW tool in order to soften the material on or before the stirring action. It is thus obvious that preheating in FSW contributes favorably to improve the weld joint proprieties. Among the possible preheating source, plasma arc provides unique combination of high arc stability, concentrated energy density, and low equipment cost. Therefore, the feasibility of P-FSW for dissimilar and high strength materials joining can be carried out. It is expected that the advantages like faster and better plasticization of the base material, reduced FSW tool wear and clamping forces, faster welding speed with improved weld quality may be achieved.
- Due to the difference in thermo-physical properties, the joining of dissimilar materials pretense more challenging task than joining of similar materials. FSW is a promising technology for joining metals with very different physical properties with optimum combination of process parameters. The different physical and mechanical properties of two different materials contribute to the asymmetry in both heat generation and material flow during FSW. These drawbacks can be overcome by introducing additional local heating to preheat the harder material side up to certain temperature with optimum location of plasma touch. It promotes adequate material flow around the tool and reduces asymmetry in material flow during FSW.
- In dissimilar friction stir welding, two different materials are plasticized and mixed together that may produce intermetallic compounds during the welding. These intermetallic compounds in nugget zone have highest impact on joint efficiency. Therefore, design of material property of the weld zone including the effect of intermetallic compounds is important in thermal analysis. The distribution and resultant properties of intermetallic compounds in weld zone is difficult to predict due to its dependency on many parameters such as flow pattern. Researchers have studied the formation of intermetallic compounds and flow pattern in weld nugget which resembles to functionally graded material in the weld zone. For joining dissimilar material, the concept of time varying functionally graded material (FGM) can be applied to define the welding zone so that the reliability of analysis can be improved.

Chapter 3

Theoretical Background

3.0 Introduction

In friction stir welding, the mechanical energy primarily transforms into heat when the rotating tool contacts with the base metal and secondarily when it deforms around the tool. The primary heat generation occurs on the surface while the deformed material around the tool is the volume of the material where secondary heat generation source appears. Understanding the process of heat generation and quantitative estimation of the same during FSW is complex in nature and is also a challenging task that requires a multidisciplinary approach. Estimation of generated heat during FSW aids in understanding the amount of thermal stress developed during process and its effect on metallurgical changes in base metals inflicted by heat. The amount of heat generation is useful in designing the welding tool as well as in selecting the optimal parameters of FSW (e.g. rotation frequency, travel rate) in respect of minimal thermal stresses and deformations, and energy consumption. Also, the numerical model of the FSW process can assist to achieve such range of feasible parameters with computational cost only. The most general configuration of FSW tool is a solid cylindrical object with a terminating pin. The rotating tool moves along the contact surfaces of two rigidly clamped substrates on a backing plate support. The tool shoulder makes firm contact with the top surface of the work-piece with applied load. Therefore, heat generated by friction occurs on the surface in contact with tool. The tool shoulder experiences large amount of heat than pin surface. The process is also experienced severe plastic deformation surrounding the tool and flow of this plasticised metal rounded from the front of the tool to the trailing edge where it is forged into a joint. This chapter aims at important physical insights into the mechanism of the process in terms of heat generation and heat transfer during conventional and hybrid friction stir welding processes.

In general, the FSW process is carried out by plunging a rotating tool into the interface of two rigidly clamped sheets, until the shoulder touches the surface of the material being welded, and traversed along the weld line. The frictional heat and plastic deformation heat are utilized for the bonding of materials under the applied normal force [7]. The primary heat source is frictional heat from tool shoulder and secondary heat source is deformation heat from the tool pin [259]. While the shoulder is the main source of heat generated during the process, acts as primary constraint to material expulsion and the primary driver for material flow around the tool. The pin is the primary source for material deformation and the secondary source for heat generation in the nugget zone. **Figure 3.1** schematically represents different thermally and mechanically affected zones. In hybrid friction stir welding, the auxiliary heat source is applied to provide additional heat to the workpiece immediately ahead of the weld zone so that the tool imposes with a lower amount of mechanical energy. However, temperature control of the welded zone in hybrid FSW system is critical and several hybrid technology have been developed to preheat the workpiece that may enhance the plasticize state, reduce the tool forces and indirectly affects the tool life.

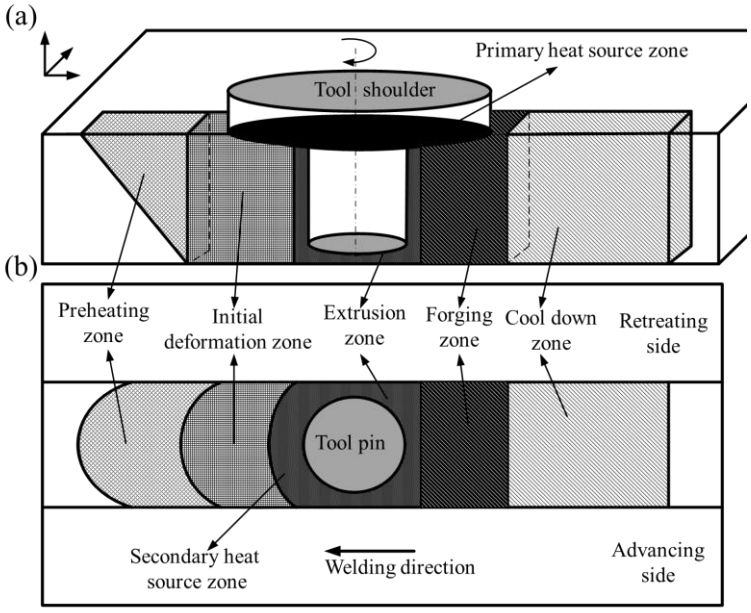

Figure 3.1: Schematic illustration of primary and secondary heat affected zones and mechanical deformation zone: (a) Isometric view (b) Top view.

3.1 Heat transfer model

The heat transfer aspect during FSW can be described into three phases. The first phase is called dwelling period where the material is preheated by a stationary rotating tool in order to achieve a sufficient temperature ahead of the tool to allow for the traverse movement. The second phase is the transient heating when the welding tool begins traversal movement until the pseudo steady-state is reached. Finally, the pseudo steady – state where the system reached effectively constant thermal field around the tool. The relative velocity on a symmetric point of advancing and retreating side is not same due to combination of similar directional rotational and transverse motion of the tool. This actually leads to asymmetry in heat transfer and material flow of the two sides of the weld joint. FSW involves complex synergistic interaction of the physical phenomena during welding of various similar or dissimilar materials combination of practical significance. To explore the underlying physics of the process, a three-dimensional heat transfer model is developed. The temperature dependent thermal properties are considered during simulation. Linear Newtonian convective cooling is applicable to all surfaces open to atmosphere. The materials are considered as isotropic and homogeneous. The interface thermal resistance between two plates is neglected.

In FSW, the workpiece material does not melt and the plasticized material flows with dependence on temperature and strain-rate. The heat generation in FSW is due to friction and plastic deformation that takes place at the tool-workpiece interface and inside the workpiece, respectively. A mathematical model is developed to estimate the generated heat in the welding zone where friction is the major contributor for the heat generation. Recently, several hybrid FSW processes have been developed to provide additional heat in the form of auxiliary heat source. The immediate objectives of all the hybrid FSW processes converge at achieving sufficient local plasticization of the workpieces ahead of the tool. It is obvious that more plasticized the material would be, the better will be the flow characteristics of the material and the tool life. However, due to difficulties of high temperature generation in joining of steel which has an effect of rapid softening and wearing of the tool, this process is not so popular in joining of steel and other hard materials like titanium. However, the hybrid FSW processes exhibit great promise by having numerous advantages over the conventional

FSW in terms improved process window, heat generation, material flow, reduced load on the tools, better mechanical properties of joints and applicable for relatively harder materials [16].

3.1.1 Governing equations and boundary conditions

In P-FSW, the heat generation in solution domain is due to plasma arc as well as friction and plastic deformation by FSW tool. Plasma arc preheat the workpiece ahead of FSW tool to influence the plasticization of material and improves material flow during welding. The heat generated by FSW tool is considered by means of friction and due to plastic deformation where heat is transferred into the work piece following Fourier's law of heat conduction. The transient temperature field T which is a function of time t and the spatial coordinates (x, y, z), is estimated by solving three dimensional nonlinear heat transfer equation. When the FSW tool moves with positive y-direction, the governing heat conduction equation is expressed as

$$\frac{\partial}{\partial x}\left\{k_x \frac{\partial T}{\partial x}\right\} + \frac{\partial}{\partial y}\left\{k_y \frac{\partial T}{\partial y}\right\} + \frac{\partial}{\partial z}\left\{k_z \frac{\partial T}{\partial z}\right\} + \dot{Q} = \rho C_p \left(\frac{\partial T}{\partial t} - V_T \frac{\partial T}{\partial y}\right) \quad (3.1)$$

where ρ, C_p and k refer respectively to density, specific heat and thermal conductivity of the workpiece material, $\dot{Q}$ is the rate of heat generation and V_T is the transverse speed of the tool. However, the interface thermal resistance between two plates is neglected here [30].

Boundary condition for FSW thermal model is specified as surface interaction of the solution domain. At time zero, a uniform temperature in the workpiece is assumed. The initial condition for the calculation is expressed as

$$T(x, y, z, 0) = T_i \quad (3.2)$$

where T_i is the ambient temperature at time t = 0.

The boundary interaction of the solution domain is schematically represented in **Fig. 3.2**. At the free surface of the workpiece natural convective boundary conditions are considered with radiation. Mathematically, the boundary condition is expressed as

P-FSW: $$k\frac{\partial T}{\partial n} = h(T - T_0) + \in \theta(T_0^4 - T^4) - q_s - q_a \quad (3.3)$$

where n is the normal direction vector of boundary, h is the convection coefficient, q_s is heat flux between tool and workpiece, $q_a$is the heat flux from plasma arc, k is the thermal conductivity of workpiece, T is temperature of workpiece, T_o is initial temperature, ∈ is the emissivity of surface and θ is the Stefan Boltzmann constant.

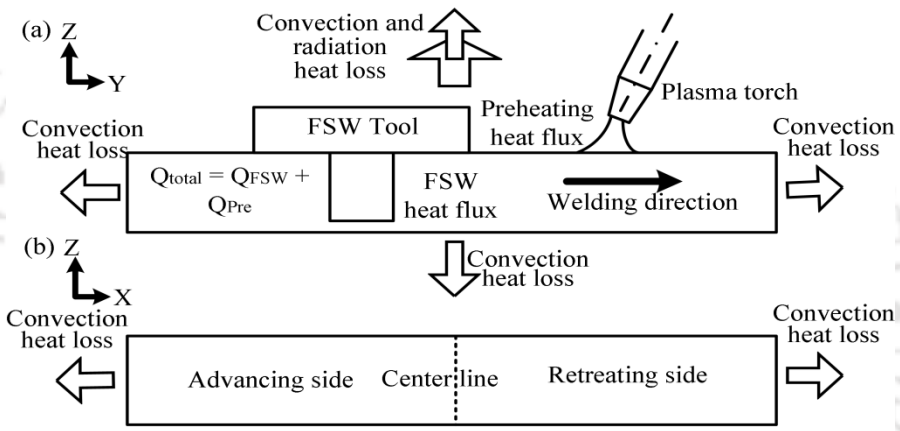

Figure 3.2: Schematic illustration of thermal boundary condition used in heat transfer model.

The heat transfer model of hybrid FSW is a combined effect of heat generation by tool and the surface heat flux from plasma arc. The additional heat source is basically a low power welding system where the primary heat source is due to friction and plastic deformation [40, 260-261]. During the joining of similar materials, the plasma heat source is focused on the weld line. Both the tool and the arc ahead of the tool move at similar speed. In joining of dissimilar materials, preheating is applied on the high thermal conductive material so that the mismatch between the melting points of both the softer and the harder materials can be compensated. In this particular process, the arc is shifted towards the harder material and the tool is slightly offset towards the softer material.

Total heat generation involved in hybrid friction stir welding process (Q_{total}) is equivalent to the combined heat input by plasma arc (Q_{pre}) and FSW tool (Q_{FSW}). Therefore,

$$Q_{total} = Q_{pre} + Q_{FSW} \quad (3.4)$$

The heat input that is transferred to the workpiece by preheating source is determined by

$$Q_{pre} = \eta IV \quad (3.5)$$

where η is the thermal efficiency, I is the welding current, and V is the welding voltage. The heat generated at the interface of tool and work piece due to friction is Q_f and due to plastic deformation is Q_p.

3.1.2 Heat generation model by different tool geometries

Control of heat generation is prerequisite for high quality weld during friction stir welding (FSW) processes. It is important to have an adequate mathematical model capable to precisely describe heat generation during FSW. There are numerous models that explain heat generation and provide results with various degrees of accuracy since these models include numerous approximations and neglect some key parameters. Mathematical model specified in this work describes contact condition, contact pressure, friction, thermal history and points out the dual nature of heat generation process i.e. adhesion and deformation component in total heat generation. It is concluded that adhesion component of total heat dominates than deformation component.

The heat generated at the interface of tool and work piece due to friction is Q_f and due to plastic deformation is Q_p. Therefore, total elemental heat due to friction and plastic deformation is given by

$$dQ_{FSW} = dQ_f + dQ_p \quad (3.6)$$

The material flow and heat generation are characterized by the contact conditions at the interface, and are described as sliding, sticking or partial sliding/sticking condition [262]. The contact condition under the shoulder can be described by sliding friction, using a

friction coefficient μ and interfacial pressure p, or sticking friction, based on the interfacial shear strength at an appropriate temperature and strain rate. It is convenient to define a contact state variable δ, which relates the velocity of the contact workpiece surface with the velocity of the tool surface. The contact state variable (δ) is assumed to change linearly with the distance from the centre of the pin. Based on these assumptions and geometrical aspects of the deformation zone, the contact state variable can be expressed as

$$\delta = \frac{V_{matrix}}{V_{tool}} \tag{3.7}$$

where V_{matrix} is peripheral velocity of workpiece and V_{tool} is peripheral velocity of tool. A 100% sticking condition at the pin/material interface is assumed i.e. same as tool velocity. The velocity of the material is equal to zero at the outer edge of the deformation. The contact shear stress is then

$$\tau_{contact} = \tau_y = \frac{\sigma_y}{\sqrt{3}} \tag{3.8}$$

If the contact shear stress is smaller than the matrix shear yield stress, the matrix segment volume shears slightly to a stationary elastic deformation where the shear stress equals the 'dynamic' contact shear stress. This state is referred to as the sliding condition. Coulomb's friction law is used to describe the critical friction stress necessary for a sliding condition:

$$\tau_{contact} = \mu p \tag{3.9}$$

The frictional heat generation on an elemental area dA at the tool-work-piece interface is expressed as [8]

$$dQ_f = (1 - \delta)\omega r \tau_{contact} dA \tag{3.10}$$

Physically, δ (<1) accounts the amount of frictional work dissipated into the workpiece, ω is angular velocity of tool and r is radial distance of elemental area dA from axis. The heat generated due to plastic shear deformation Q_p sticking to the tool is given by [263]

$$dQ_p = \delta\omega r\tau_{contact}dA \quad (3.11)$$

The last possible state between the sticking and sliding condition is a mixed state. In this case, the matrix segment accelerates to a velocity less than the tool surface velocity where it stabilizes. The equilibrium establishes when the 'dynamic' contact shear stress equals the internal yield shear stress due to a quasi-stationary plastic deformation rate. This is referred to as the partial sliding/sticking condition. In this model, there is no difference between the dynamic and the static friction coefficients. Therefore, the total heat generation due to sliding and sticking is expressed as

$$Q_{FSW} = \delta * Q_{FSW,sticking} + (1-\delta) * Q_{FSW,sliding} \quad (3.12)$$

Straight cylindrical tool pin

Estimation of the amount of heat generated during FSW is based on analytical expression on active surface of the welding tool. In order to calculate the heat generation in the shoulder surface rotating around the tool centre axis, an infinitesimal segment on that surface is considered. The infinitesimal segment area dA = rdθdr is exposed to a uniform contact shear stress $\tau_{contact}$. This segment contributes with an infinitesimal force of dF = $\tau_{contact}$·dA and torque of dM = r·dF. The angle between shoulder surface and This surface is consider as active surface of tool which takes part in welding process as shown in **Fig. 3.3**. Therefore, the heat energy generated at the contact interface between a rotating FSW tool and a stationary workpiece are subdivided as Q_1, Q_2 and Q_3 i.e. on the tool shoulder's surface, tool pin's side surface and tool pin's tip surface, respectively. The amount of translation heat is significantly smaller than amount of rotational heat and it can be neglected in analysis.

$$Q_{total} = Q_1 + Q_2 + Q_3 \quad (3.13)$$

$$Q_1 = \int_0^{2\pi} \int_{R_{probe}}^{R_{shoulder}} \omega \tau_{contact} r^2 (1 + \tan\alpha)\, dr d\theta \quad (3.14)$$

where α is the angle produced by the conical shoulder (Fig. 3.3). Heat generation from the probe are expressed as

$$Q_2 = \int_0^{2\pi} \int_0^{H_{probe}} \omega \tau_{contact} R_{probe}^2\, dr d\theta = 2\pi\omega\tau_{contact} R_{probe}^2 H_{probe} \quad (3.15)$$

$$Q_3 = \int_0^{2\pi} \int_0^{R_{probe}} \omega \tau_{contact} r^2\, dr d\theta = \frac{2}{3}\pi\omega\tau_{contact} R_{probe}^3 \quad (3.16)$$

Therefore the total heat generation due to sliding or sticking friction is estimated as

$$Q = \frac{2}{3}\pi\omega\tau_{contact}\left(\left(R_{shoulder}^3 - R_{probe}^3\right) + R_{probe}^3 + 3R_{probe}^2 H_{probe}\right) \quad (3.17)$$

For a flat shoulder and straight cylindrical tool, the total heat generation is a linear combination of sliding and sticking condition and is expressed as

$$Q_{FSW} = \frac{2}{3}\pi\omega\left[\delta\tau_y + (1-\delta)\mu p\right]\left\{\left(R_{shoulder}^3 - R_{probe}^3\right) + R_{probe}^3 + 3R_{probe}^2 H_{probe}\right\} \quad (3.18)$$

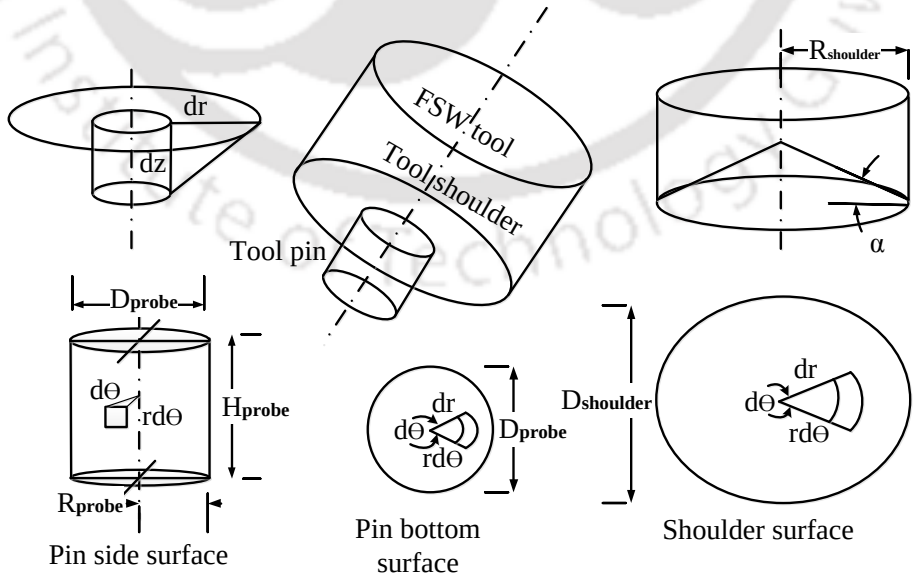

Figure 3.3: Schematic illustration of nomenclature of straight pin tool.

Straight tapered tool pin

An analytical model for heat generation for friction stir welding using taper cylindrical pin profile is developed. The analytical expression is the modification of previous analytical models known from the literature which is verified and well matches with the model developed by previous researchers. **Figure 3.4** describes the typical FSW tool having the geometric shape of a taper cone without any thread along with flat shaped shoulder.

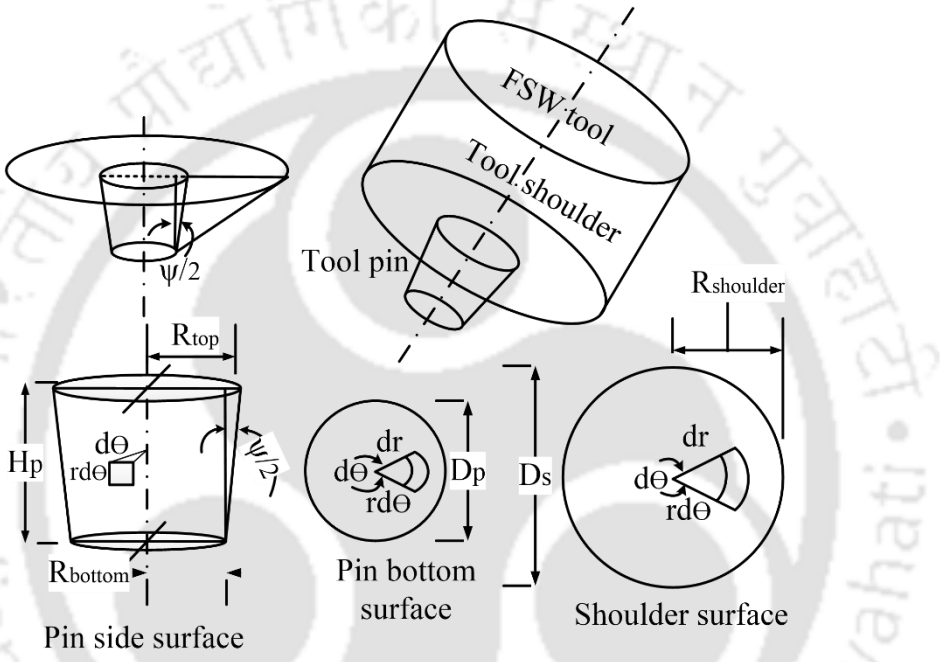

Figure 3.4: Illustration of nomenclature of taper cylindrical pin profile.

The probe consists of a taper cylindrical surface with a bottom radius of R_{bottom}, top radius R_{top} and probe height H_{probe}. The heat generated from the probe is given by Eq. (3.21) over the probe side area

$$Q_2 = \int_0^{2\pi} \int_0^{l} \omega r^2 \tau_{contact} \, d\theta dz \tag{3.19}$$

$$Q_2 = 2\pi\omega\tau_{contact} l \left(\frac{R_{top}+R_{bottom}}{2}\right)^2 \tag{3.20}$$

$$Q_2 = \frac{\pi\omega\tau_{contact}}{2} \frac{H_{probe}}{cos\psi} \left(R_{top} + R_{bottom}\right)^2 \tag{3.21}$$

Different parts of active surfaces of STT pin profile FSW tool result in different amounts of heat generated on them that give different expressions for estimating the amount of generated heat. After the assimilation of Q_1, Q_2 and Q_3, the expressions for the analytical amount of heat generated are, respectively

$$Q_{total} = Q_1 + Q_2 + Q_3 \tag{3.22}$$

Therefore, the total heat generation due to sliding or sticking friction is estimated as

$$Q_T = \frac{2}{3}\pi\omega\tau_{contact}\left(R_{shoulder}^3 + R_{top}^3\right) + 2\pi\omega\tau_{contact}\frac{\pi\omega\tau_{contact}}{2}\frac{H_{probe}}{cos\psi}\left(R_{top} + R_{bottom}\right)^2 + \frac{2}{3}\pi\omega\tau_{contact}R_{bottom}^3 \tag{3.23}$$

3.1.3 Hybrid heat source model

A hybrid heat source model is developed by combining FSW tool and plasma arc. Preheating source is considered ahead of FSW tool with some lead distance in case of joining similar materials. In case of dissimilar joint, the plasma arc is kept offset towards harder material and FSW tool is shifted towards soft material. However, lead distance and offset distance of heat source depends on welding conditions and type of materials. In conventional FSW, tool offset depends on process condition. Heat distribution for plasma arc is exponentially decaying with maximum heat density in the centre.

A moving heat source with heat distribution for plasma assisted friction stir welding of similar and dissimilar materials is illustrated in **Fig. 3.5**. To model the preheating source, a circular surface heat source with effective radius ($\bar{r}$) is considered as shown in **Fig, 3.6**. The effective radius of heat source depends on nozzle diameter of plasma torch and its standoff distance from plate surface. However, the heat flux follows a Gaussian distribution and is expressed as

$$q_a(r) = \frac{3Q_{pre}}{\pi\bar{r}^2}e^{-3\left(\frac{r}{\bar{r}}\right)^2} \tag{3.24}$$

where $q_a(r)$ is the surface flux at radius r and $\bar{r}$ is the effective arc radius over which 95 % energy falls.

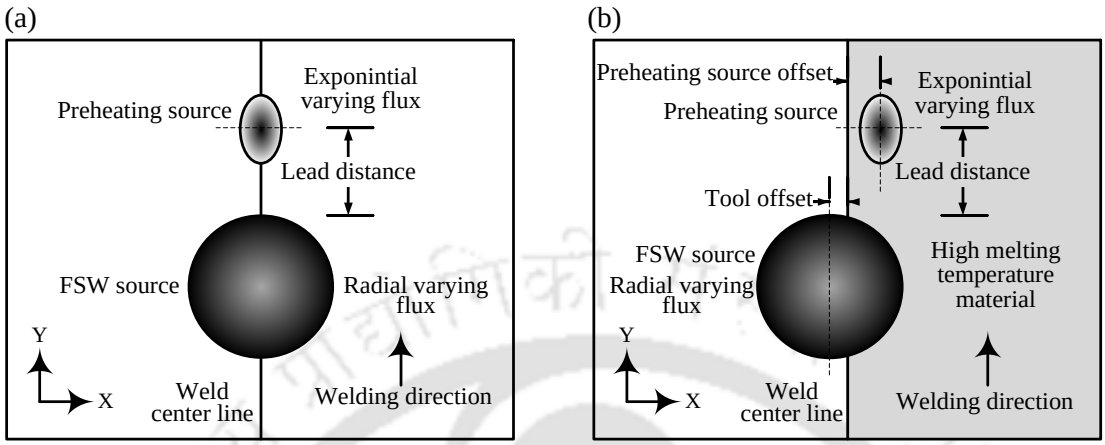

Figure 3.5: Schematic illustration of moving heat source model for P-FSW (a) similar material (b) dissimilar material joining.

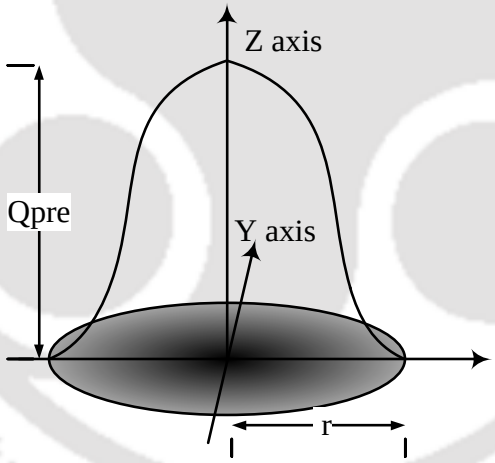

Figure 3.6: Schematic illustration of surface heat flux distribution in moving heat source model for preheating source.

The heat input through boundary is converted as heat flux from heat generation by the tool. **Figure 3.7** illustrates the distribution of heat flux for FSW heat source over the plate surface due to the tool shoulder, on pin-workpiece interface due to tool pin, and due to tool pin bottom surface is given as [264],

$$q_{shoulder} = \frac{3Q_1 r}{2\pi R_{shoulder}^3};\ q_{pside} = \frac{Q_2}{2\pi R_{probe} H_{probe}};\ q_{pbottom} = \frac{3Q_3 r}{2\pi R_{probe}^2} \quad (3.25\text{-}3.27)$$

where $\tau_{contact}$ and δ in the expression of Q_1, Q_2 and Q_3 are applied according to sliding or sticking friction conditions [33]. Therefore, total heat flux from the FSW tool is expressed as

$$q_s = q_{shoulder} + q_{pside} + q_{pbottom} \quad (3.28)$$

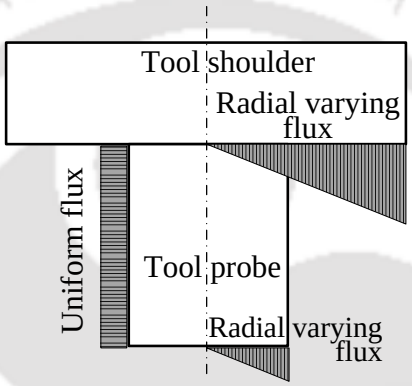

Figure 3.7: Schematic illustration of heat flux distribution in moving heat source model for FSW.

The estimated heat flux acts as input to estimate the temperature distribution by solving the governing heat conduction equation. However, the reliability in calculation of temperature distribution and material flow depends on input model parameters and is difficult to define these parameters from scientific principle alone. The value of the friction coefficient varies mainly with temperature, relative velocity, and surface contact conditions. However, the friction becomes lower at high temperature due to localised softening of material and it also influences the heat generation rate. The simple approach is to modify the coefficient of friction to adjust the heat generation rate. During plastic deformation, the yield strength decreases with temperature and leads to a reduction in the heat generation. The strain rates also diminish rapidly away from the tool and hence most of the heat generation due to plasticity occurs close to the tool–work-piece interface.

3.1.4 Finite element discretization

The governing equations and the boundary conditions are discretization using finite element method over the solution domain. The heat generated at the interface of tool–workpiece is assumed as a direct product of adhesion and deformation of the material around the tool. The heat flux over the boundary is calculated after estimation of total heat generation. The solution domain consists of 8 nodded isoperimetric brick elements. The temperature variable, T, within the element is expressed in terms of nodal temperatures as

$$T = \sum_{i=1}^{8} [N_i] \ \{T_i\} \tag{3.29}$$

The global coordinates can also be interpolated within the element using similar shape functions as

$$x = \sum_{i=1}^{8} [N_i]\{x_i\}; \quad y = \sum_{i=1}^{8} [N_i]\{y_i\}; \quad z = \sum_{i=1}^{8} [N_i]\{z_i\} \tag{3.30-3.32}$$

Applying Galerkin's weighted residue technique to the governing equation yields a general form as

$$\int_{\Omega} \phi \left\{ \frac{\partial}{\partial x}\left(k \frac{\partial T}{\partial x} \right) + \frac{\partial}{\partial y}\left(k \frac{\partial T}{\partial y} \right) + \frac{\partial}{\partial z}\left(k \frac{\partial T}{\partial z} \right) + \dot{Q} - \rho C_p V_T \frac{\partial T}{\partial t} + \rho C_p \frac{\partial T}{\partial y} \right\} d\Omega = 0 \tag{3.33}$$

where ϕ is a weighting function and Ω refers to the volume of the solution domain. Using thermal boundary conditions and substituting the weighting function as shape function in Eq. (3.33), it is possible to obtain for any specific element 'e' as

$$[H^e]\{T\} + [S^e]\left\{ \frac{\partial T}{\partial t} \right\} + [\bar{H}^e]\{T\} + [\bar{S}^e]\{T\} - \{f_{\dot{Q}}^e\} - \{f_q^e\} - \{f_h^e\} = 0 \tag{3.34}$$

where

$$[H_{ij}^e] = \int_{\Omega^e} k\left(\frac{\partial N_i}{\partial x}\frac{\partial N_j}{\partial x} + \frac{\partial N_i}{\partial y}\frac{\partial N_j}{\partial y} + \frac{\partial N_i}{\partial z}\frac{\partial N_j}{\partial z}\right)d\Omega \tag{3.35}$$

$$[S_{ij}^e] = \int_{\Omega^e} \rho C_p N_i N_j d\Omega\,; \qquad [\overline{H}_{ij}^e] = \int_{\Gamma^e} h_{eff} N_i N_j d\Gamma \tag{3.36, 3.37}$$

$$[\overline{S}_{ij}^e] = -\int_{\Omega^e} \rho C_p V_T N_i \frac{\partial N_j}{\partial y} d\Omega \tag{3.38}$$

$$\left\{\left(f_q^e\right)_i\right\} = \int_{\Gamma_1^e} N_i q_s d\Gamma; \quad \left\{\left(f_h^e\right)_i\right\} = \int_{\Gamma_2^e} N_i h_{eff} T_0 d\Gamma \tag{3.39, 3.40}$$

$$\left\{\left(f_{\dot{Q}}^e\right)_i\right\} = \int_{\Omega^e} N_i \dot{Q} d\Omega \tag{3.41}$$

Considering the contribution from all the elements, the final algebraic equation is written as

$$[\bar{\bar{H}}]\{T\} + [S]\left\{\frac{\partial T}{\partial t}\right\} = \{f\} \tag{3.42}$$

where $[\bar{\bar{H}}] = [H] + [\overline{H}] + [\overline{S}]; \quad \{f\} = \{f_{\dot{Q}}\} + \{f_q\} + \{f_h\}$

Equation (3.42) is used within each time step to solve for the unknown nodal temperature field during three-dimensional transient heat transfer analysis. In general, the so-called α-method for time discretization is expressed as [265]

$$[S]\frac{\{T_i^2\} - \{T_i^1\}}{\Delta t} + \alpha[\bar{\bar{H}}]\{T_i^2\} + (1-\alpha)[\bar{\bar{H}}]\{T_i^1\} = \alpha\{f\}^2 + (1-\alpha)\{f\}^1; \quad 0 \le \alpha \le 1 \tag{3.43}$$

The most common values for α are:

$\alpha = 0$, *Explicit Eulers scheme or forward difference scheme*

$\alpha = 1$, Im *plicit Euler scheme or backward difference scheme*

$\alpha = \frac{1}{2}$, *Crank – Nicolson scheme*

$\alpha = \frac{2}{3}$, *Galerkin method*

In time discretization scheme, the Galerkin method i.e. α = 2/3 is unconditionally stable and is generally followed assuming the load vector, {f} is independent of the state of time which is basically explicit scheme. In quasi-steady state analysis, the nodal variable i.e. temperature is independent of time and the elemental matrix equation is expressed as

$$[H^e]\{T\}+[\bar{S}^e]\{T\}+[\bar{H}^e]\{T\}=\{f_{\dot{Q}}^e\}+\{f_q^e\}+\{f_h^e\} \tag{3.44}$$

where $\left[\bar{S}_{ij}^e\right]=-\int_{\Omega^e}\rho C_p V_T N_i \frac{\partial N_i}{\partial y}d\Omega$ (3.45)

The final algebraic equation for the three dimensional pseudo-steady state heat transfer analysis is written as

$$[\bar{\bar{H}}]\{T\}=\{f\} \tag{3.46}$$

where $[\bar{\bar{H}}]=[H]+[\bar{H}]+[\bar{S}]$; $\{f\}=\{f_{\dot{Q}}\}+\{f_q\}+\{f_h\}$ (3.47, 3.48)

Here the algebraic form of Eq. (3.48) is solved in a ramped-up load step for quasi-steady state analysis [12].

3.1.5 Analytical model of strain and strain rate in weld zone

The heat is generated by friction as well as plastic deformation which alters the microstructure and properties. The kinetics depends mainly on the temperature and strain rate and microstructure evolution influence the energy transfer within the system. The phenomenological understanding of heat transfers and material flow demands a strong coupling between thermal, mechanical, and metallurgical aspects. The center of stirred zone (SZ) experiences dynamic recrystallization and is followed by recovered microstructure around the stirred zones at low level of deformation and temperature. A part of the plastic deformation energy is also stored within the thermomechanically affected zone (TMAZ) in the form of increased dislocation densities within the deformed grains. The heat affected zone (HAZ) is affected only by the temperature and the microstructural changes with respect

to base material are insignificant. In FSW, the flow stress is highly dependent on temperature and the stain rate. Thus, the resulting grain structure in the processed zone mainly depends on the resulting strain rate and temperature distributions. In order to achieve a desired microstructure, the strain rate and temperature distributions must be controlled and relates to the grain structure and process parameters. Therefore, the strain rate distribution in friction stir welding in stir zone is determined in terms of process parameters.

To develop the analytical model for strain and strain rate distribution in weld zone, the following assumptions are considered. The velocity field within the stirred zone are determined by considering the effects of both the shoulder and the pin of the tool on the material flow. The state variables by slip condition are introduced to relate the material velocity within the stirred zone. From the velocity fields, the strain rate distribution in the processed zone can be estimated. In the model two incompressible flow fields are combined to describe the material flow such as forced vortex flow and uniform translation. No material movement in the thickness direction are considered.

The relative velocity of the tool surface and workpiece depends on several factors that control this relation including contact condition at the tool/ workpiece interfaces. There are two interfaces between the tool and the sheet: one is at the shoulder and the other is at the pin as shown in **Fig. 3.8(a)**. Two state variables are used for radial and thickness direction respectively to consider the contact conditions between tool contact surface and workpiece material. The first one is denoted by α which relates the material velocity to shoulder velocity and it is defined as a function of z. The same approach is followed to define the second state variable (β) which relates the material velocity to pin velocity. The state variable β is defined in terms of r. Mathematically, the state variables are given by

$$\alpha = Aexp\left\{-B\frac{z}{z_0}\right\} \tag{3.49}$$

$$\beta = Cexp\left\{-D\frac{(r-R_p)}{(R_s-R_p)}\right\} \tag{3.50}$$

where the variables is described by **Fig. 3.8(b)** and the values of state variables like α, β are functions of A, B, C, D that can be determined from friction condition (between 0 and 1), effect of material properties, pressure, and temperature [266-267].

Figure 3.8(b) depicts the schematic view of linear velocity in r and θ direction corresponding to flat tool shoulder and workpiece interface. Assume the workpiece material is having radius r at an angle θ with respect to the direction of tool transverse speed V_T. The material is rotating at an absolute rotational speed of ω. The velocity components on the boundary of the top surface of the tool shoulder is expressed as

$$U_{(s)\theta} = \alpha[\omega r - V_T \cos\theta] \tag{3.51}$$

$$U_{(s)r} = \alpha[-V_T \sin\theta] \tag{3.52}$$

The velocity at tool pin periphery has been defined as

$$U_{(p)\theta} = \beta\left[\omega R_p - V_T \cos\theta\right] \tag{3.53}$$

$$U_{(p)r} = \beta[-V_T \sin\theta] \tag{3.54}$$

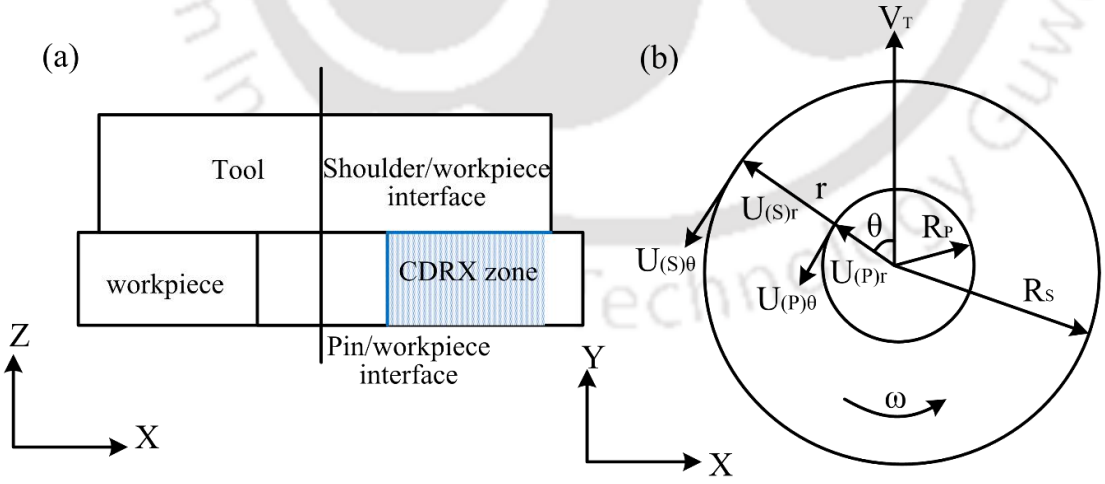

Figure 3.8: (a) Schematic illustration of shoulder and pin interface with workpiece and (b) Velocity presentation in r and θ direction (top view).

To account for how much each of them is responsible for the material flow, weight functions are introduced. Finally, the two velocity fields are combined using the weight functions to yield the overall velocity field. The weight functions for the shoulder and the pin are defined in both r and θ coordinates as given below:

$$\delta_{(s)\theta} = \frac{U_{(s)\theta}}{U_{(s)\theta}+U_{(p)\theta}} \tag{3.55}$$

$$\delta_{(p)\theta} = \frac{U_{(p)\theta}}{U_{(s)\theta}+U_{(p)\theta}} \tag{3.56}$$

$$\delta_{(s)r} = \frac{U_{(s)r}}{U_{(s)r}+U_{(p)r}} \tag{3.57}$$

$$\delta_{(p)r} = \frac{U_{(p)r}}{U_{(s)r}+U_{(p)r}} \tag{3.58}$$

Incorporating the weight function with these velocity fields yields the overall velocity field in the r-Θ-z coordinates as given by:

$$U_\theta = \delta_{(s)\theta}U_{(s)\theta} + \delta_{(p)\theta}U_{(p)\theta} \tag{3.59}$$

$$U_r = \delta_{(s)r}U_{(s)r} + \delta_{(p)r}U_{(p)r} \tag{3.60}$$

$$U_z = 0 \tag{3.61}$$

The velocity-strain rate relation in cylindrical (r-θ-z) coordinates is used to find the strain-rate components. The effective strain rate distribution within the FSW zone estimated by assuming von Mises criteria. The effective strain-rate ($\dot{\varepsilon}_{eff}$) distribution in the friction stir welded zone can be determined as [267]

$$\dot{\varepsilon}_{rr} = \frac{\partial U_r}{\partial r} \tag{3.62}$$

$$\dot{\varepsilon}_{\theta\theta} = \frac{1}{r}\frac{\partial U_\theta}{\partial \theta} - \frac{\partial U_r}{\partial r} \quad (3.63)$$

$$\dot{\varepsilon}_{zz} = \frac{\partial U_z}{\partial z} \quad (3.64)$$

$$\dot{\varepsilon}_{r\theta} = \frac{1}{2}\left[\frac{1}{r}\frac{\partial U_\theta}{\partial \theta} + \frac{\partial U_\theta}{\partial r} - \frac{U_\theta}{r}\right] \quad (3.65)$$

$$\dot{\varepsilon}_{\theta z} = \frac{1}{2}\left[\frac{\partial U_\theta}{\partial z} + \frac{1}{r}\frac{\partial U_z}{\partial \theta}\right] \quad (3.66)$$

$$\dot{\varepsilon}_{zr} = \frac{1}{2}\left[\frac{\partial U_z}{\partial r} + \frac{\partial U_r}{\partial z}\right] \quad (3.67)$$

$$\dot{\varepsilon}_{eff} = \left[\frac{2}{3}\left\{\dot{\varepsilon}_{rr}{}^2 + \dot{\varepsilon}_{\theta\theta}{}^2 + \dot{\varepsilon}_{zz}{}^2 + \dot{\varepsilon}_{r\theta}{}^2 + \dot{\varepsilon}_{\theta z}{}^2 + \dot{\varepsilon}_{zr}{}^2\right\}\right]^{\frac{1}{2}} \quad (3.68)$$

$$\dot{\varepsilon}_{eff} = \left(\frac{2}{3}\dot{\varepsilon}_{ij}^2\right)^{\frac{1}{2}} \quad (3.69)$$

where, $\dot{\varepsilon}_{rr}$, $\dot{\varepsilon}_{\theta\theta}$, $\dot{\varepsilon}_{zz}$, $\dot{\varepsilon}_{r\theta}$, $\dot{\varepsilon}_{\theta z}$ and $\dot{\varepsilon}_{zr}$ (Eq. 3.62-3.367) are the strain rate components in the respective plane of r-θ-z coordinate and $\dot{\varepsilon}_{ij}$ is the strain rate in i direction on the area normal to the j direction.

The strain values are obtained from the strain-rate using rotational speed (N) as,

$$\varepsilon_{eff} = \frac{\dot{\varepsilon}_{eff}}{N} \quad (3.70)$$

However, the significant microstructural evolution takes place during FSW due to continuous dynamic recrystallization (CDRX) phenomena, resulted in a highly refined grain structure in the weld nugget. The analytical models aimed to the determination of the average grain size due to continuous dynamic recrystallization phenomena in FSW processes. Therefore, the CDRX model takes into account with few material constants to predict average grain size in the weld zone [268].

$$D_{CDRX} = C_1 \varepsilon^k \dot{\varepsilon}^j D_i^h \exp\left(-\frac{Q}{RT}\right) \quad (3.71)$$

This initial grain size (D_i), along with the temperature (T), strain-rate $\dot{\varepsilon}$ and strain (ε) values predicted from the analytical models, yields the final grain size distribution in the weld zone using the Eq. (3.71) suitable for dynamic recrystallization. The constants (C_1, k, j,

h) in the equation were obtained by solving the equation at different points of the grain size distribution from Woo et al. [269]. The values of activation energy (Q) and gas constant (R) assumed are 140 kJ/mole and 8.314 J/kg-K.

3.2 Material property for dissimilar materials

In friction stir welding of dissimilar joint, two different materials are plasticized and mixed together that produce intermetallic compound i.e. multi-phase structures in the weld nugget. These intermetallic compounds in nugget zone have highest impact on joint efficiency. Therefore design of material property of the weld zone including the effect of intermetallic compounds is important in thermal analysis. The distribution and resultant properties of intermetallic compound in weld zone is difficult to predict due to its dependency on many parameters such as flow pattern and corresponding temperature. Researchers have studied the formation of intermetallic compound and flow pattern in weld nugget which resembles to functionally graded material in the weld zone [270]. In heat transfer analysis for the joining of dissimilar materials, the concept of time varying functionally graded material (FGM) is applied to define the welding zone [271]. In FSW process, the weld zone increases in size with time when the tool plunges into the workpiece at a fixed position. However, the weld zone size remains almost constant when the tool travels along weld line of the specimen. The size of FGM zone is considered accordingly (**Fig. 3.9**). The growth of the FGM region is estimated from the rotational and transverse speed of the tool.

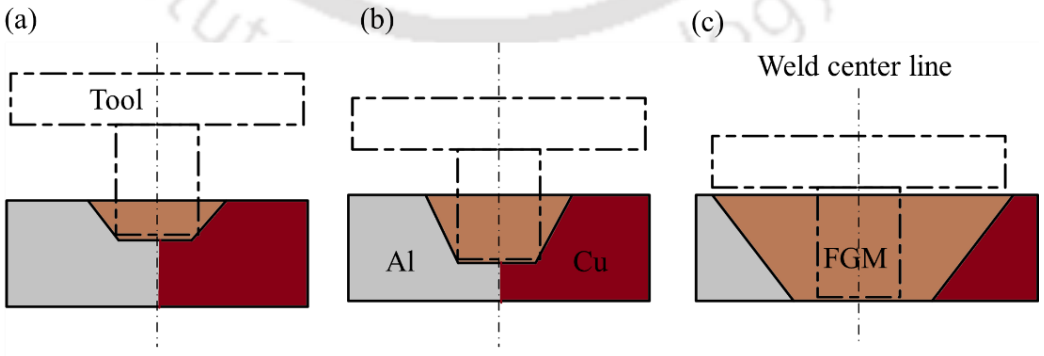

Figure 3.9: Formation of functionally graded material during plunging of tool at (a) 2 mm (b) 3 mm and (c) 5 mm plunging depth.

The workpiece is mainly divided into three zones i.e. advancing side (copper), retreating side (aluminum) and middle trapezoidal zone which is considered as FGM zone. **Fig. 3.10** illustrates three different zone used for analysis which is treated as three different materials. The time varying material properties in the weld zone is applied that depends on position and movement of tool axis and this phenomenon is implemented by "USDFLD" subroutine in ABAQUS. Upgraded material properties such as thermal conductivity, specific heat and density are assigned to location of this region at each time increment during simulation. In the no-weld-region, two different material properties are assigned for different materials.

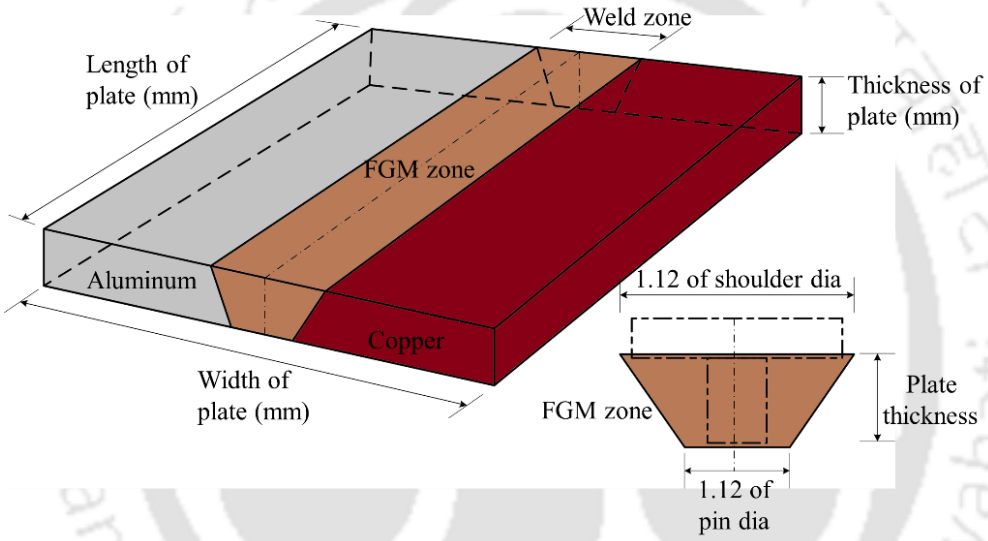

Figure 3.10: Schematic illustration of applied functionally graded material in welding zone of dissimilar material joining.

The weld zone properties are varied according to the mixture rule of FGM [207, 272-273]. The FGM material properties such as thermal conductivity, specific heat and mass density can be estimated by using the following relations

$$k = k_1[1 + (3(k_1 - k_2)\,v_2)/(3k_1\,v_2 + (k_1 + 2k_2)(1 - v_2))] \quad (3.72)$$

$$c = (c_1\,\rho_1\,v_1 + c_2\,\rho_2\,v_2)/(\rho_1\,v_1 + \rho_2\,v_2) \quad (3.73)$$

$$\rho = \rho_1\,v_1 + \rho_2\,v_2 \quad (3.74)$$

where k is thermal conductivity, c is specific heat and ρ is mass density of copper (index 1) and aluminum (index 2). Equation (3.72) represents the thermal conductivity of FGM in

terms of copper, aluminum and the volume fraction of aluminum (v_2). Equations (3.73, 3.74) represent the specific heat and mass density of mixed material. Thermal conductivity and the specific heat are not linear function of the volume fraction while mass density is the linear function of the volume fraction [274]. **Fig. 3.11** illustrates the variation of material properties with respect to normal distance from weld center line. It is noteworthy that there is gradual variation of properties from top of the surface to the bottom. **Fig. 3.11(a)** shows the variation of volume fraction at three different layers in thickness direction. The variation of material properties in FGM zone depends on the volume fraction of aluminum or copper at a particular location. When $v_2 = 0$, it indicates pure copper. If the value of v_2 is between 0 and 1, it implies that the material is within FGM region [275]. The variation of density in FGM is considered as linear whereas the variation of specific heat and thermal conductivity are assumed nonlinear.

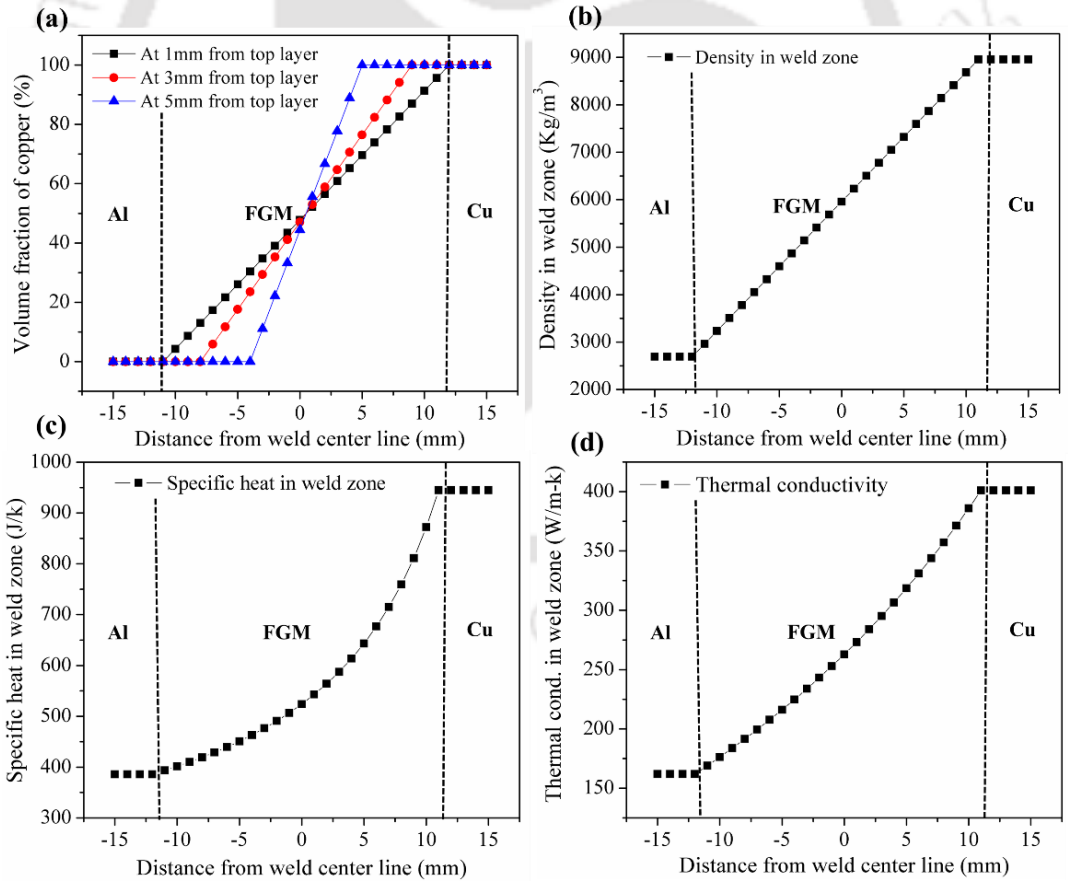

Figure 3.11: Variation of material properties in welding zone (as FGM): (a) volume fraction, (b) density, (c) specific heat, and (d) thermal conductivity.

3.3 Computational aspects

In the present work, three-dimensional heat transfer simulation is carried out for FSW and P-FSW process using commercial FEM software ABAQUS. Simulation of similar and dissimilar joint is performed with or without preheating under different process conditions.

The procedure of modelling is adopted based on the actual experimental welding procedure in order to obtain the numerical solution, such as temperature profile of the welding as shown in **Fig. 3.12**. P-FSW process is divided into six time instants: preheating time, plunge time, dwell time, welding time, final dwell, and plunge out time. In present simulation, 15 sec is considered as initial dwell step and 5 sec as final dwell step. The plunge in velocity of 0.12 mm/s and plunge out velocity of 1.16 mm/s is considered in present simulation.

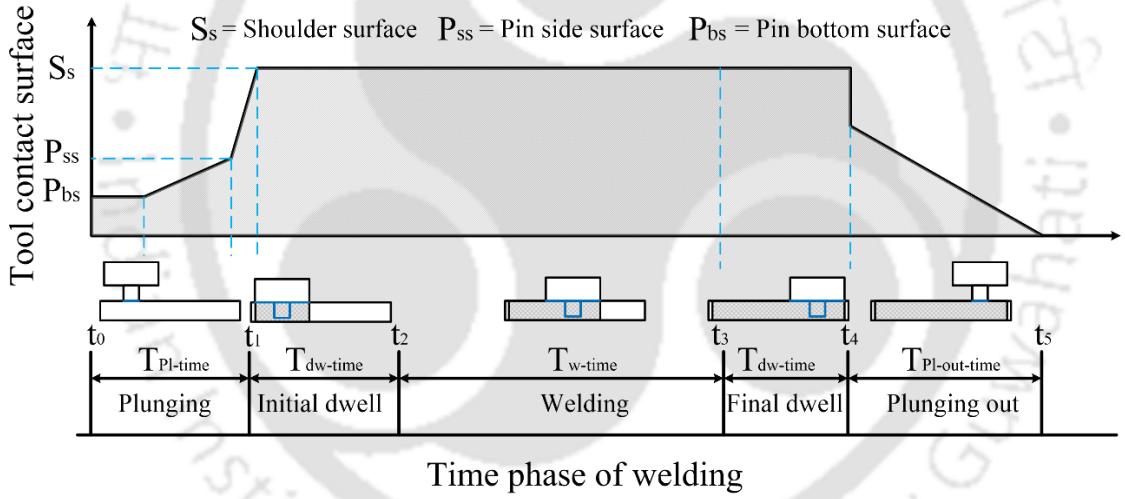

Figure 3.12. Schematic illustration of time phase of welding with respect to change in tool contact surfaces during a complete cycle of welding.

Figure 3.13 illustrates the summary of the general information that finite element software requires to solve heat transfer problem. Few of the significant steps are described as follows:

- First, the solution domain is defined along with number and type of nodes and the elements. The whole domain is discretized to small elements using eight-noded brick

element of type DCC3D8. The temperature is considered as single degree of freedom at each node with fine meshing in the weld zone.

- Next, the temperature-dependent thermal properties are provided. In joining of dissimilar materials, the temperature-dependent thermal properties of both the materials are incorporated in the analysis. In the weld zone, the time variation of material properties is applied by "USDFLD" subroutine for dissimilar weld.
- Boundary and initial conditions are applied thereafter. Initially (t = 0) the workpiece is at room temperature. The convective heat transfer coefficient is used for the top and side surfaces of the workpiece which is typical for natural convection between workpiece and air. However during dissimilar joint, different convective heat transfer coefficients are used for two materials (Cu & Al).
- Similarly, for the loading conditions, the calculated heat flux is applied in solution domain through "DFLUX" subroutine. The "DFLUX" subroutine executes the moving heat source as per the welding process parameters.
- In transient heat transfer analysis, the total weld time including cooling period is applied in step time.
- Finally, the output of the model is the node temperature (NT11) and weld zone isotherm. From these results it can be estimate the cooling rate and weld zone shape and dimensions.

The analytical model to predict the strain rate distribution during FSW is shown in **Fig. 3.14**. The numerical simulations of the FSW processes characterized by the investigated operative conditions permitted to highlight the temperature, strain and strain rate distributions occurring during the processes. The framework of this model is as follows:

• State variables that relate the material velocity to the tool velocity (shoulder and pin) are first introduced.

• Weight functions are also introduced to determine how much the tool shoulder and the tool pin contribute to the net flow of material in the processed zone.

• The velocity fields in the processed zone are then determined as a function of process parameters.

• Finally, the strain rate distribution in the deformed (processed) zone is calculated from the velocity fields.

• Finally, the prediction of average grain size occurring in FSW through CDRX model.

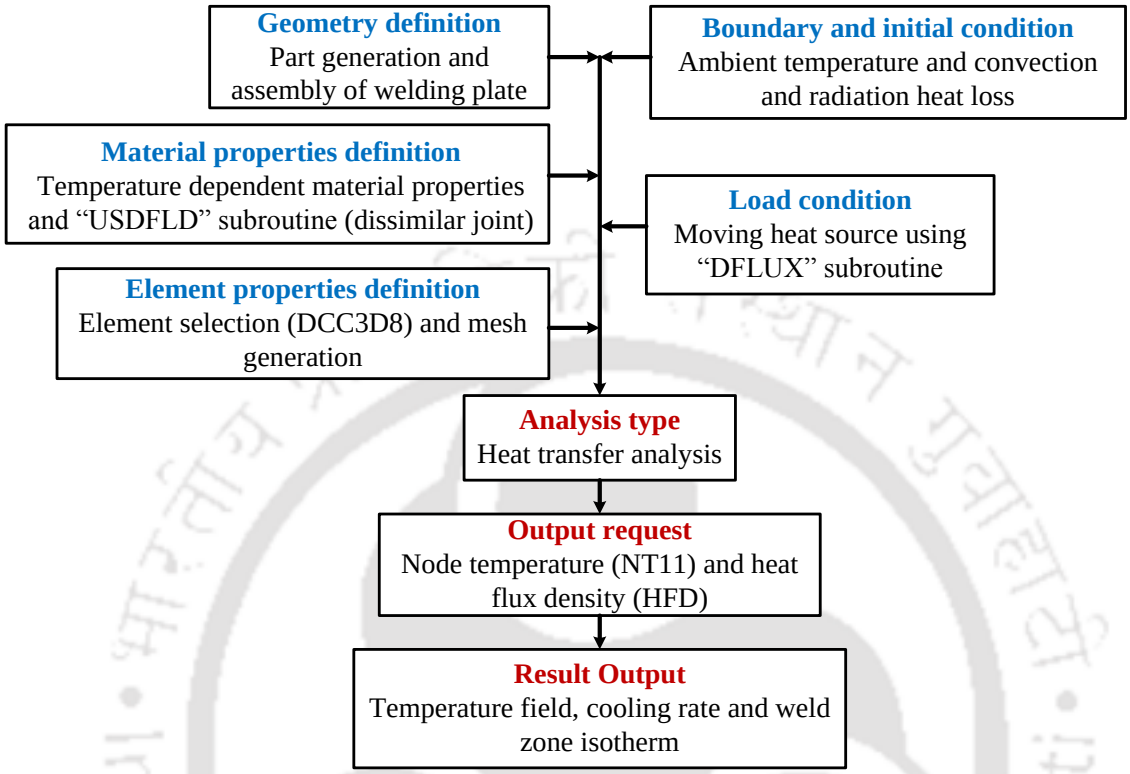

Figure 3.13. Overall procedure followed in heat transfer analysis.

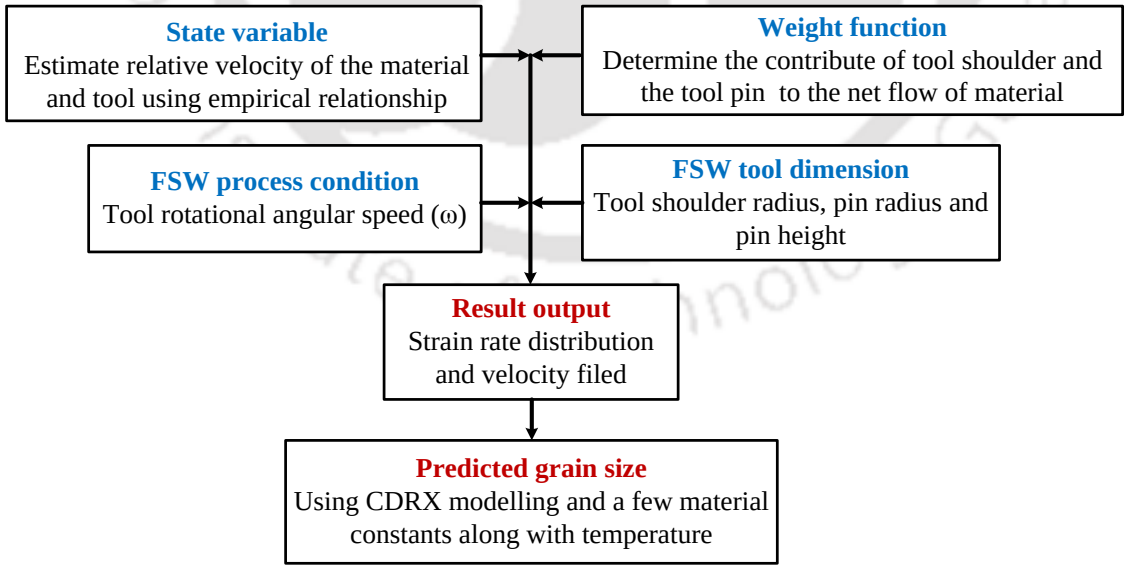

Figure 3.14. Flow chart for strain and strain rate analysis

3.4 Summary

This chapter covers fundamental understanding of heat transfer and material flow mechanism in friction stir welding through mathematical modeling. The important issues related to the topic provide an overall view of the subject by creating individual sections of their own merits. This section presents the governing equations and boundary interactions to demonstrate the physical description of the process. The significant effort is put forward for explicit description of heat generation model. A detail finite element formulation and computational aspects is also included in this section. Hybrid heat source model for plasma assisted friction stir welding of similar and dissimilar joint are presented here. The hybrid heat source model is the combination of a surface heat source by plasma arc and frictional heat by FSW tool. Moreover, this chapter also includes the mathematical background and modeling aspects of strain analysis to predict the strain rate of FSW process. The properties of weld zone for dissimilar materials is based on the time-varying functionally graded material (FGM) that varies with respect to the motion of tool and mixing of material in the weld zone.

Chapter 4

Experimental Investigation

4.0 Introduction

The experimental methods employed during the thesis work are explained in this chapter and can be largely characterized by two parts, conventional FSW and HFSW. The experiments are performed on a vertical milling machine with the help of a specially design fixture which is capable of measuring welding forces by incorporating strain gauge. In Section 4.1, an investigation on nonsymmetrical heat distribution during FSW of aluminum joint is included. Thereafter, six different pin profile tools used to weld aluminum plates at three different rotational speeds with a thickness of 6 mm through FSW process are discussed. The process parameters setting and materials used for welding are discussed next, and finally the post weld preparation and characterization techniques used to measure weld qualities are discussed.

In the following section no. 4.2, the integration of preheating source of plasma arc welding torch with FSW machine using a specially designed torch holding fixture is described. Experiments are conducted under different welding conditions for joining of similar (aluminium alloy) and dissimilar (aluminium alloy -Pure Cu) materials in butt joint configuration. The thickness of workpiece is 6mm and same tool is used for each weld. The effects of preheating source on mechanical and micro-structural properties for welds are studied to identify the industrial potential of P-FSW process.

4.1 Friction stir welding

The experimental work includes investigation of the effects of process parameters on the thermal history, mechanical properties and microstructure of FSW welded joint.

4.1.1 Experimental set-up

The experimental setup used in this work is a vertical milling machine with 7.5 HP motor capacity. Butt welding of commercial grade aluminum alloy was performed in the initial trial experimental where the dimension of test samples was 200 mm × 100 mm × 6 mm. The edges of the test samples are machined to obtain a perfect square butt. They are clamped on the horizontal machine bed without root gap by the help of fixture. The developed fixture has four main components, namely top plate, clamps, backing plate and support plates. Each part has been fabricated individually with all appropriate features required for holding workpiece rigidly against high welding forces. The clamping of the test pieces is done in such a way that the movement of the plates is totally restricted against the welding forces. Several tests were carried out by varying tool rotational speed and feed rate. It was found that the fixture is highly useful for carrying out FSW operations in vertical milling machine. The FSW setup used in this work is shown in **Fig. 4.1**.

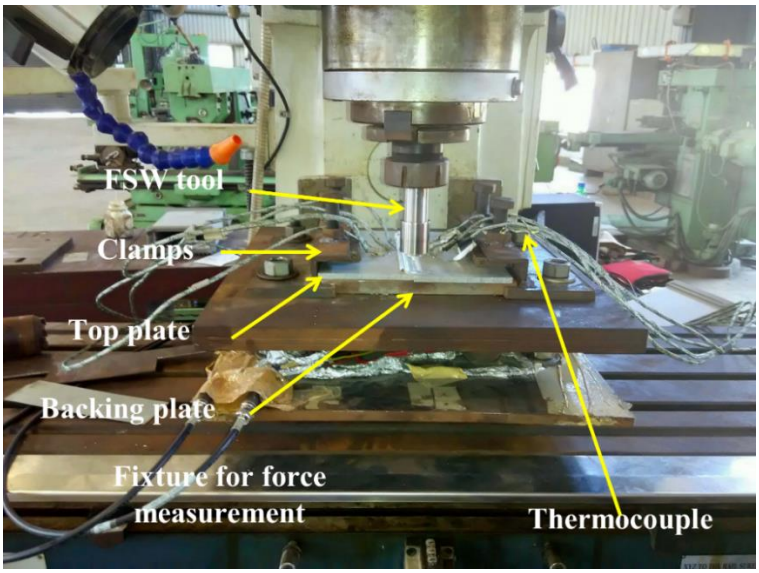

Figure 4.1. Experimental setup for FSW.

Agilent 34970A Data Acquisition system is used in the present work. It is used with multiplexer to acquire temperature data at different thermocouple point with the help of K-type thermocouples having two-core with wire protraction grill outside. The operating temperature is between -200°C to 1260°C for single exposure. The limits of error of thermocouple is conforms to ASTM E230. However, a special fixture has developed for

clamping system and plunging force measurement. It is an instrumented setup for a vertical milling machine for friction stir welding operations and measuring the process forces as shown in **Fig. 4.1.** It is an adjustable fixture to hold workpiece during welding and reduce the chances of gap formation due to lateral and transverse movement of the workpiece. For force measurement, a strain gauge based force dynamometer have been designed, developed, and fabricated. The strain gauges are imbibed on the specially designed four hexagonal supporting members to support the welding plates. During welding, the applied force by tool is transferred to the four hexagonal members and it induces strain in the member. This strain is measured by strain gauges in terms of voltage using a Wheatstone bridge circuit. This voltage is measured by a data acquisition system with amplifier. This voltage signal is calibrated with forces measured by standard dynamometer. Transient temperature is recorded on the top surface at eight different locations using 36 gauge K-type thermocouples. All the temperature measurements are made in four on the advancing side and four on the retreating side of the welds. The location of thermocouple is shown in **Fig. 4.2.** The material used in this work is commercial grade aluminium alloy rolled plate. The chemical composition and mechanical properties of the base metal are presented in **Table 4.1** and **Table 4.2,** respectively.

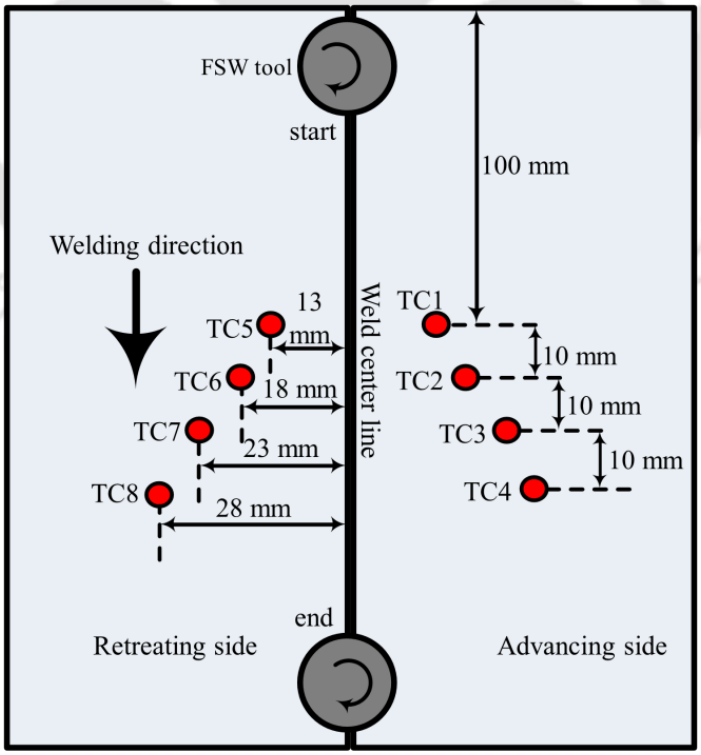

Figure 4.2. Layout of thermocouples for temperature measurement.

Table 4.1: Chemical composition of aluminum alloy (AA1100).

Alloy	Fe	Cu	Si	Ti	Mg	Mn	Ni	Zn	Al
Weight percentage	0.57	0.12	0.13	0.03	0.02	0.013	0.017	0.01	Bal.

Table 4.2: Mechanical properties of aluminum alloys.

Property	Value
Tensile strength (MPa)	150.78
Yield strength (MPa)	118.62
Elastic modulus (GPa)	66.94
Percentage of elongation (%)	13.75
Micro hardness (HV)	48.51
Density (g/cm3)	2710

Once the welding is over, test samples for different mechanical testing are prepared to evaluate quality of weld joints. Transverse tensile test, bending test and hardness test are performed on the specimens. The tensile specimen is cut from the center of the welded joint and prepared as per the dimension provided by ASTM E08 standard [276-277] which is shown in **Fig 4.3**. Tensile test is carried out on a 100 kN capacity electro-mechanical controlled Universal Testing Machine (model: INSTRON-8801) (**Fig. 4.5b**). All the samples are tested at a constant speed of 1.5 mm/min. After the testing it was observed that most of the samples failed inside the welded zone. The 0.2 % offset yield strength, ultimate tensile strength and percentage of elongation are evaluated from test data. The bending sample is prepared along with the tensile sample as shown in **Fig 4.4**. Bending test is carried out using three-point bending test setup attached with the same Universal Testing Machine (**Fig. 4.5a**). The specimen is tested at constant speed of 2.5 mm/min as per ASTM specifications, so that bending specimen undergoes bending load [277]. The bending angle and bending strength are evaluated for each welded joint.

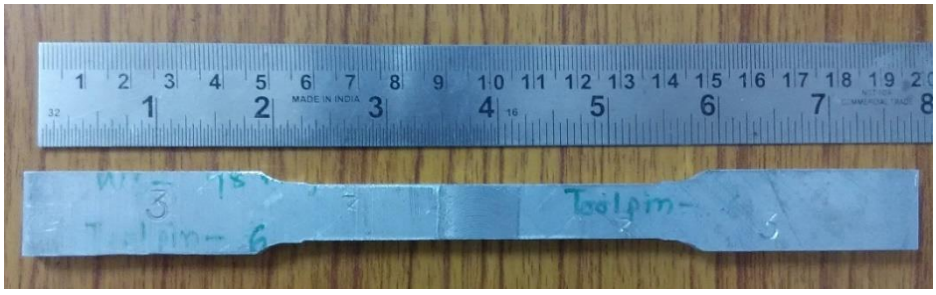

Figure 4.3. Tensile test sample.

Figure 4.4. Bending test sample.

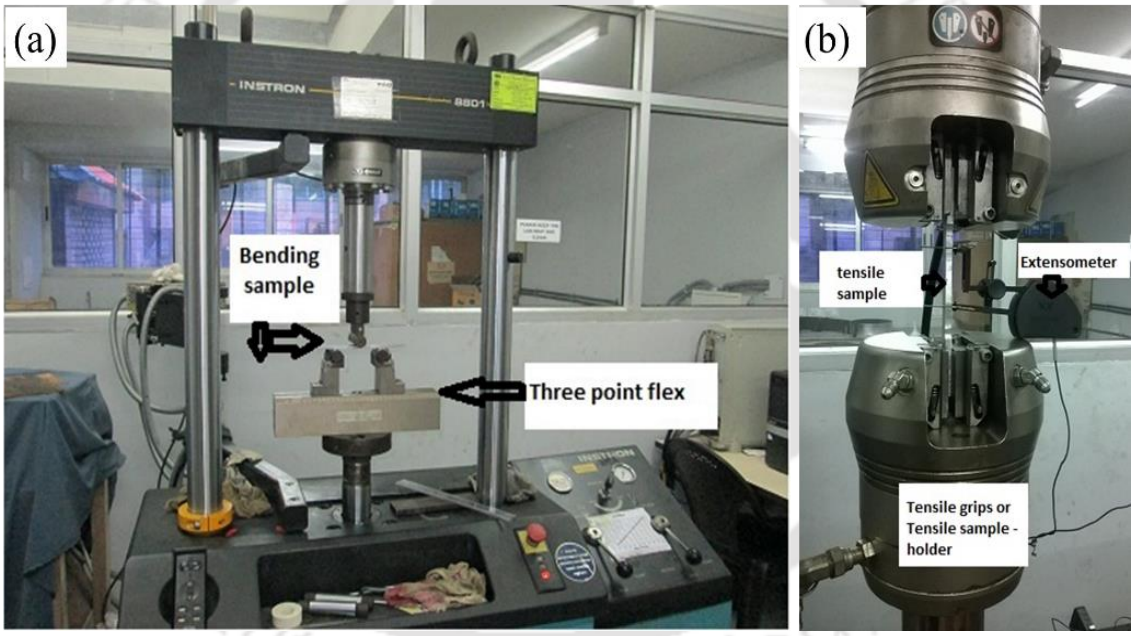

Figure 4.5. (a) Three-point bending test setup (b) Tensile test setup with extensometer.

The hardness distribution in the weld zone is measured by using an Akashi AAV-500 Vickers indenter as shown in **Fig 4.6 (a)** with a load of 100 gf and dwell time of 10 s, according to the ASTM: E384-11 [278]. Hardness is measured both in across the welding direction and in through the thickness direction from top to bottom at the center of weld zone. Micro-hardness is measured in three lines at 1, 3, and 5 mm from top surface with 1 mm of space between two indents as shown in **Fig 4.6 (b)**.

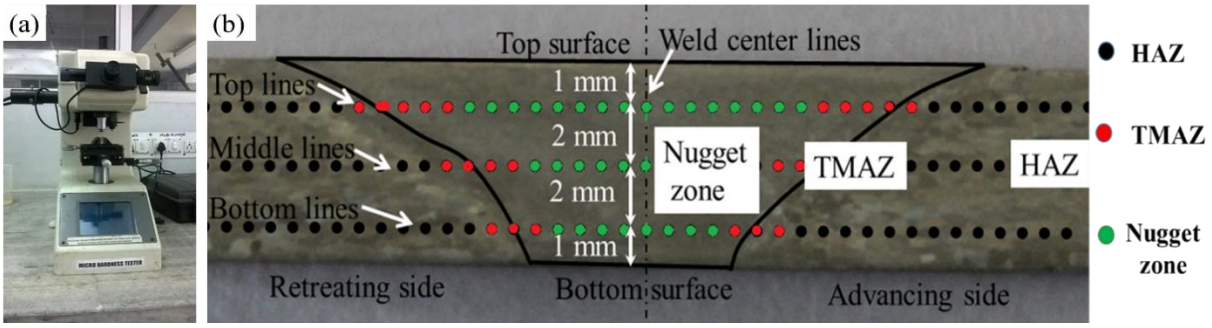

Figure 4.6. (a) Vickers indenter for vickers micro hardness test (b) Schematic illustration of three lines in cross-section of different weld zone for hardness at 30 points in 1 mm of spacing.

Microstructural examination is carried out using an optical microscope (MEJI, Japan; model MIL-7100) incorporating image analyzing software (Aixo Vision 4.2) as shown in **Fig 4.7(a)**. The specimens are ground with silicon carbide papers of 240, 400, 800, 1000, and 1200 grades followed by polishing on a rotating wheel with 1 and 0.3 μm alumina suspension. Furthermore, the optical microscope is used for microstructural study of polished specimens. All polished specimens are etched with a solution comprising 25 ml methanol, 25 ml HCl, 25 ml HNO_3, and HF of one drop to expose grain boundary [279]. A detailed microstructural observation is conducted for each welded specimen using optical microscopy to determine the variation of grain size and presence of any weld defect. After obtaining the grain structure the same sample is used to obtain the macrograph using the optical microscope (Leica S6D) at two different resolutions 1.0X and 1.25X as shown in **Fig. 4.7(b)**.

In stirred zone, two different materials are plasticized and mixed together that produce intermetallic compound within the matrix of two base materials. Therefore, it is quite difficult of get clear microstructure of stirred zone due to presence of three different materials (Cu, Al and IMC). There is no common etchant available to reveal clear microstructure in stirred zone after polishing of the sample. Modified Poulton's reagent is used to reveal the microstructures of copper while Killer's etchant is used for aluminum. However, Poulton's reagent is more reactive for aluminum and Keller's etchant is less reactive for copper. It is followed in sequence i.e. first Keller's etchant is applied and then Poulton's reagent. As a result, the desired image from stirred zone is obtained.

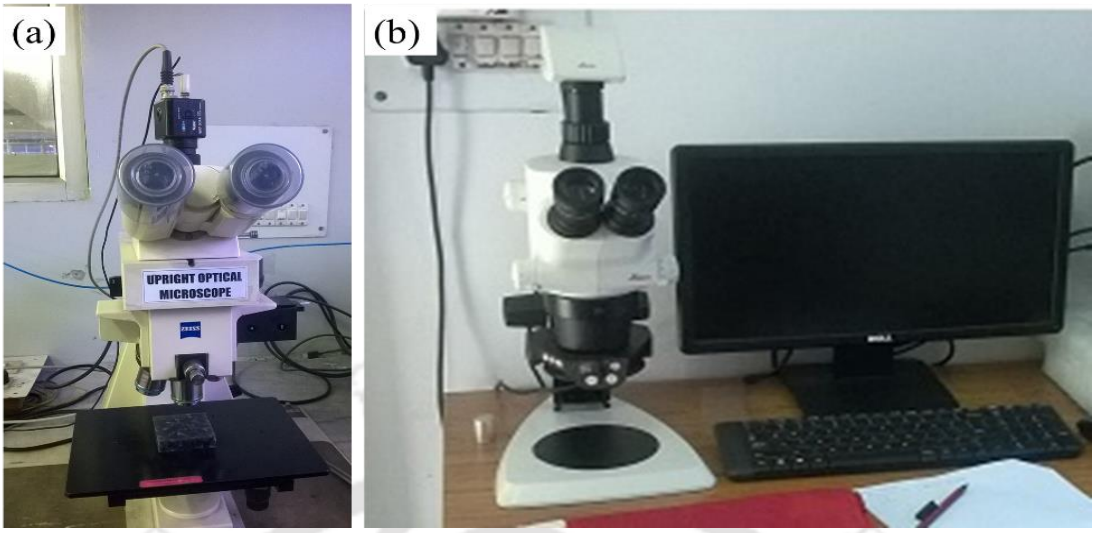

Figure 4.7. (a) An optical microscope (MEJI, Japan; model MIL-7100) for microstructure (b) An optical microscope (Leica S6D) for macrograph.

4.1.2 Non-symmetry in thermal history during FSW

In this study, experiments are carried out to test and validate the developed numerical model for calculating the thermal history of FSW process on aluminum alloy. The tool is made of SS304 with the shoulder and pin diameters of 20 mm and 6 mm, respectively. The welding tool is perpendicular to the plate. The shoulder has a flat profile. The pin length is slightly less than the thickness of work-pieces, i.e. 5.75 mm. The chemical composition of the aluminum alloy is depicted in **Table 4.1**. The melting temperature of aluminum alloy is considered as 933.15 K. Four experimental conditions are described in **Table 4.3**. The location of thermocouples placed at eight different points on the top surface of workpiece is described in **Fig. 4.2**.

Table 4.3: FSW process parameters for aluminum alloy.

Exp. no.	Process parameter		
	Transverse speed (mm/min)	Rotational speed (RPM)	Average plunging force (kN)
Exp. 1	63	600	6.79
Exp. 2	98	600	6.23
Exp. 3	63	815	5.72
Exp. 4	98	815	5.25

The transient temperatures recorded from the thermocouples corresponding to Exp. 1, 3, and 4 in **Table 4.3** are shown in **Figure 4.8, 4.9** and **4.10**, respectively in which each profile corresponds to a specific location indicated in **Fig. 4.2**. The temperature profile of each point corresponds to the welding time and displacement of the tool from the starting point. The maximum values of the temperature on advancing and retreating side is depicted in **Table 4.4**. Since the thermocouple TC1 is closest to the joint line, its peak temperature is higher than that of the others. It is also obvious from **Figs. 4.8 – 4.10** that there is delay of measuring points to reach peak temperature away from the centre line and a systematic trend is observed. This is due to location of thermocouple points. So the contemplation comes from all experimental data that in a defect free welding, the peak temperature is between 597.55 and 643.25 K at 3 mm away from shoulder edge on thermocouple point TC1. It is also obvious that the temperature on the advancing side at all four points is higher than the retreating side although the temperature is measured in similar locations. As it moves away from centre line, the temperature difference reduces and came to equilibrium at certain distance. This temperature difference is the cause of asymmetric heat generation and flow of plasticized material owing to difference in relative velocity between advancing and retreating sides [24]. However, the temperature in advancing side close to the weld centreline is higher than that of the retreating side.

Table 4.4: Maximum temperatures at different thermocouple points corresponding to experimental conditions of **Table 4.3**.

Thermocouple points	Maximum temperature (K)			
	Exp. 1	Exp. 2	Exp. 3	Exp. 4
TC1	617.65	597.55	643.25	621.75
TC2	574.75	562.85	593.45	578.35
TC3	533.85	523.75	553.55	538.55
TC4	499.15	487.15	504.35	501.75
TC5	595.35	583.25	623.25	601.15
TC6	555.25	550.85	578.55	562.75
TC7	519.65	513.75	543.85	525.35
TC8	489.95	478.15	495.05	488.95

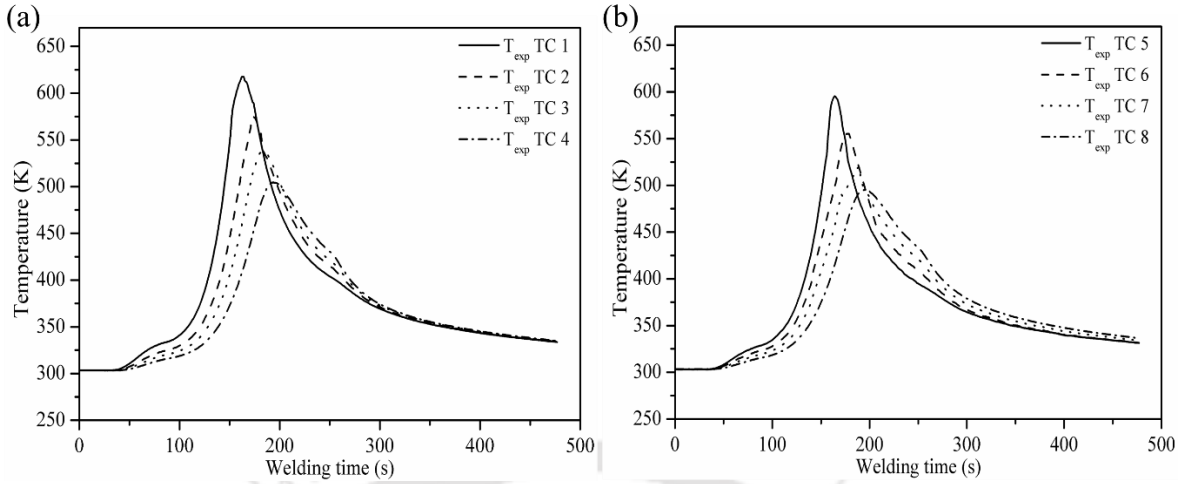

Figure 4.8. Thermal history of Exp. 1 in **Table 4.3** (a) Advancing side (b) Retreating side for aluminium alloy.

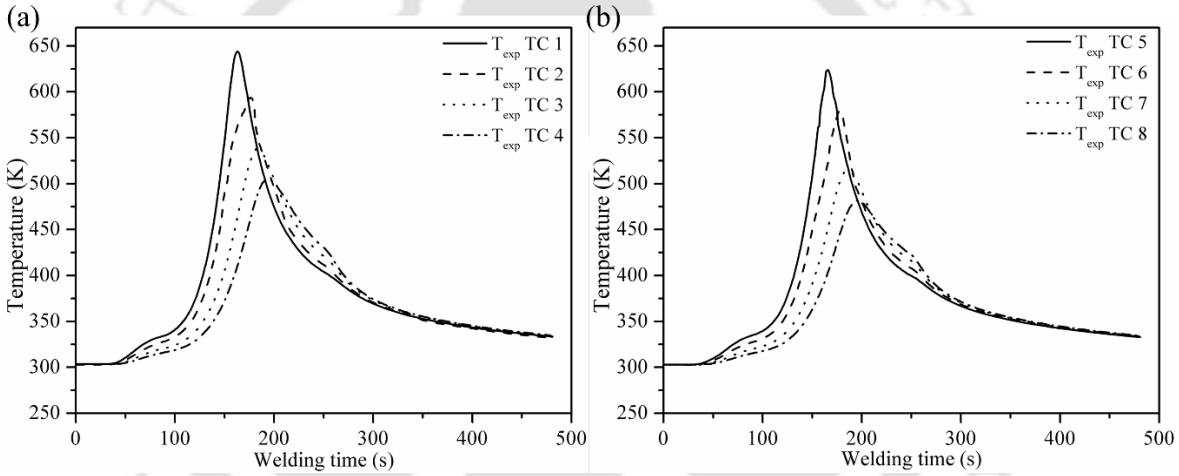

Figure 4.9. Thermal history of Exp. 3 in **Table 4.3** (a) Advancing side (b) Retreating side for aluminium alloy.

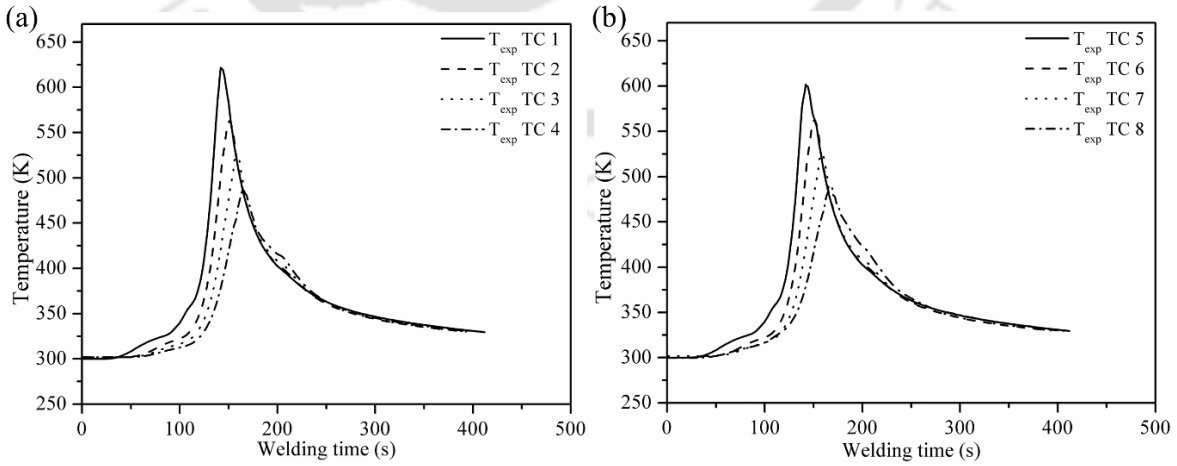

Figure 4.10. Thermal history of Exp. 4 in **Table 4.3** (a) Advancing side (b) Retreating side for aluminium alloy.

It is observed from the experiments that the temperature in advancing side close to the weld centre line is higher than that of the retreating side. However, the temperature difference of two sides is small as getting away from the weld centre line owing to similar rate of heat loss. **Figure 4.11** depicts the comparison of peak temperature between advancing and retreating sides for all experimental conditions. The right hand side of **Fig. 4.11** indicates the percentage of melting point temperature for aluminium alloy with reference to maximum peak temperature of a thermocouple point. The melting point of aluminium alloy is considered as 933.15 K [280]. The percentage of melting point at different location varies between 52.2 to 56.1%. The maximum temperature is decided by the combined factor of welding speed, rotational speed, and plunging force during welding. It is obvious that as tool rotational speed increases, heat generation rate increases whereas with increase in welding speed the rate of heat input decrease and these phenomena are confirmed by the nature peak temperature depicted in **Fig. 4.11**.

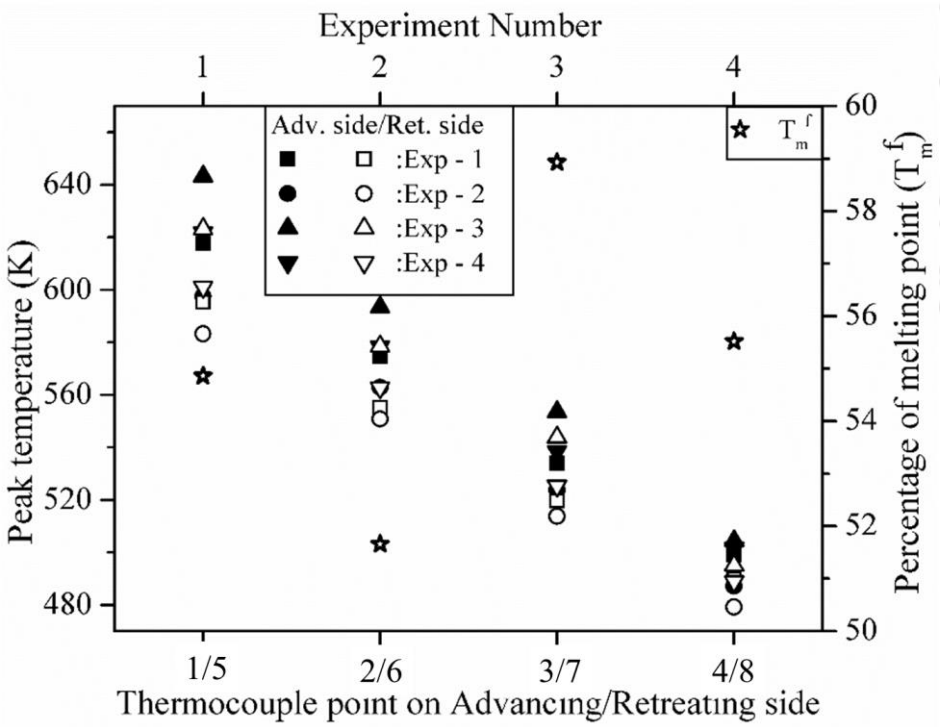

Fig. 4.11: Comparison of peak temperature of four experimental conditions at four points in advancing side and four points in retreating side for aluminum alloy.

4.1.3 Effect of tool pin profile during FSW

As mentioned earlier, the tool has two primary functions: (a) localized heating, and (b) material flow. In initial stage of tool plunge, heat is generated primarily from friction between the pin and work piece. However, some additional heating can be generated through plastic deformation by using featured pin profile. But, the biggest component of heat generation is friction between the shoulder and work piece. Therefore, from the aspect of heat generation, the relative size of the pin and shoulder is important. The second function of the tool is to 'stir' and 'move' the material. Therefore, six various FSW tool geometries are considered by varying the tool pin profile to investigate its effect on weld joint. The contact surface area of the pin side surface is increased by threads that help in providing intensive mixing and localized heating of material. Three types of pin profiles (plane, v-thread and square thread) are selected for the experiments. Whereas, the tool shoulder diameter and pin height (16 mm and 5.75 mm respectively) are kept fixed. **Figure 4.12** shows the six tools with different pin profile and the detailed configuration of FSW tool geometry and **Fig. 4.13** shows schematic illustration of tool profile which is given in **Table 4.5**. Tool rotational speed are considered as 600, 1100 and 1500 rpm while welding speed is kept constant at 98 mm/min. Design of experiment is obtained by considering the process parameters within the above mentioned levels is shown in **Table 4.6.**

Table 4.5. The detailed configuration of the designed FSW tool geometry

Tool dimensions	Unite	C	CS	CV	T	TS	TV
Shoulder diameter	mm	16	16	16	16	16	16
Pin top diameter	mm	6	6	6	6	6	6
Pin bottom diameter	mm	6	6	6	4	4	4
Pin height	mm	5.75	5.75	5.75	5.75	5.75	5.75
Thread pitch	mm	0.75	0.75	0.75	0.75	0.75	0.75
Helix angle	degree	30	30	30	30	30	30
Cone angle	degree	-	-	-	7.5	7.5	7.5

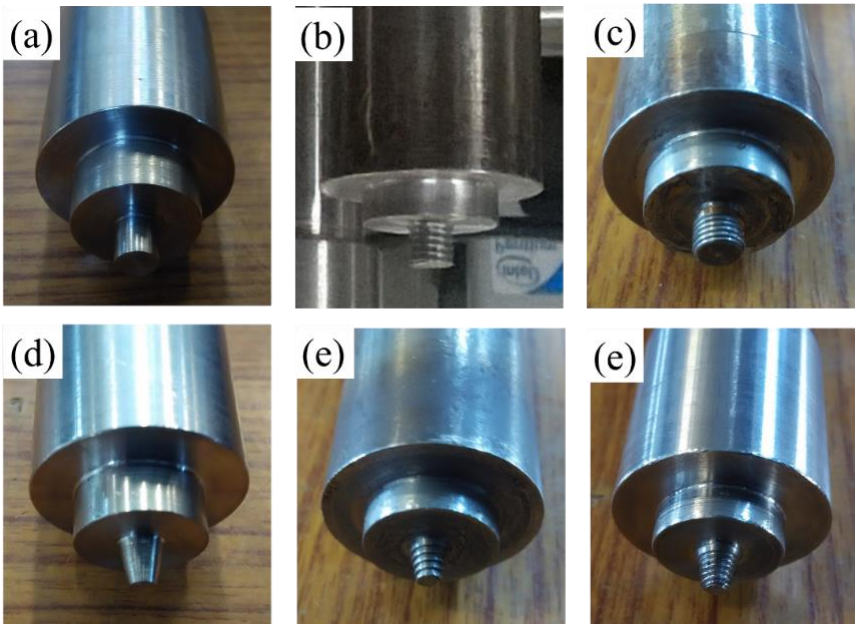

Figure 4.12. (a) Straight cylindrical pin tool C, (b) Straight cylindrical square thread pin tool CS, (c) Straight cylindrical V-thread pin tool CV, (d) Taper cylindrical pin tool T, (e) Taper cylindrical square thread pin tool TS and (f) Taper cylindrical V-thread pin tool TV.

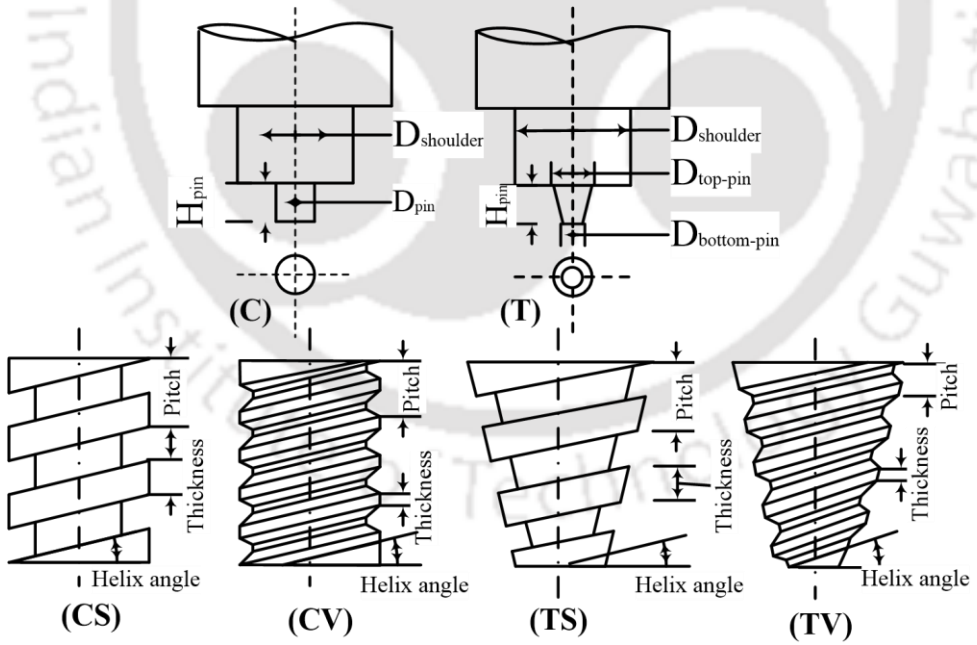

Figure 4.13. Schematic illustration of tool profile (C) Straight cylindrical pin tool, (T) Straight cylindrical square thread pin tool, (CS) Straight cylindrical V-thread pin tool, (CV) Taper cylindrical pin tool, (TS) Taper cylindrical square thread pin tool and (TV) Taper cylindrical V-thread pin tool.

Table 4.6. Design of Experiment of similar FSW joints.

Exp. No.	Tool rotational speed (RPM)	Welding speed (mm/min)	Tool pin profile
1	600	98	C
2	1100	98	C
3	1500	98	C
4	600	98	CS
5	1100	98	CS
6	1500	98	CS
7	600	98	CV
8	1100	98	CV
9	1500	98	CV
10	600	98	T
11	1100	98	T
12	1500	98	T
13	600	98	TS
14	1100	98	TS
15	1500	98	TS
16	600	98	TV
17	1100	98	TV
18	1500	98	TV

The time–temperature history of advancing and retreating sides at 1100 rpm and CS pin profile tool is depicted in **Fig 4.14**. The temperature profile of each thermocouple point corresponding to the welding time relates the displacement of the tool from the starting point. It observed that the temperature on the advancing side at all four locations is higher than the retreating side, although the temperature is measured in corresponding similar points. This temperature difference is the cause of asymmetric heat generation and plasticized flow of hot material from retreating side to advancing side. As moves away from the weld center line, the

temperature difference is reduced and reaches equilibrium at certain distance due to similar rate of heat diffusion. However, the temperature in advancing side close to the weld center line is higher than that of the retreating side. It can be concluded that variations in dimensions and tool geometry of FSW tools along with tool rotational speed have prominent effects on thermal history [180].

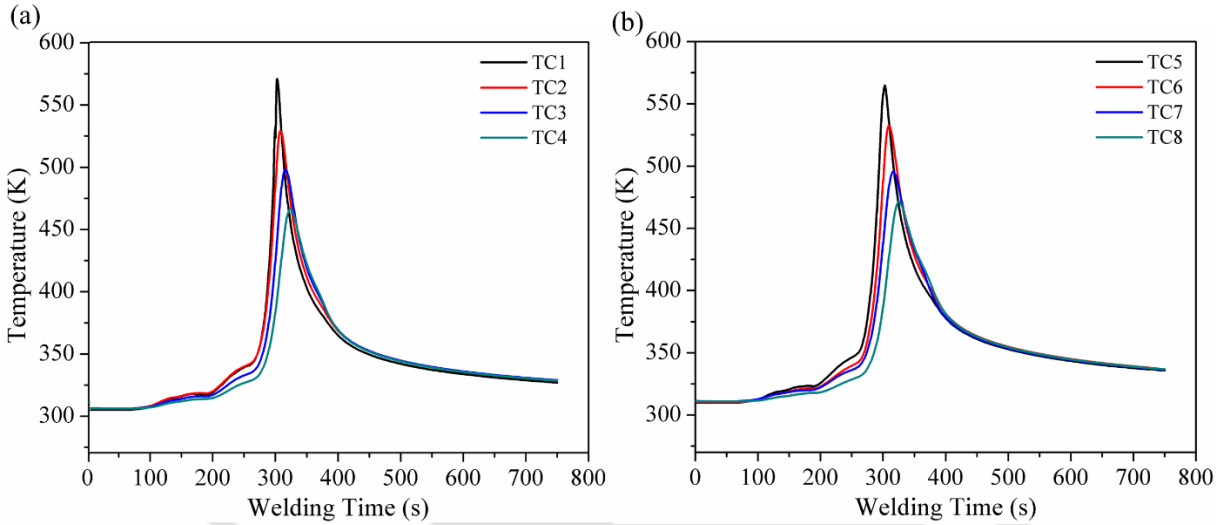

Figure 4.14. Thermal history at 1100 rpm and CS pin profile tool (a) advancing side (b) retreating side.

Figure 4.15 illustrates the comparison of peak temperature between advancing and retreating sides for the experimental conditions shown in **Table 4.6**. It's observed that the peak temperature obtained at 1500 rpm is higher than 600 and 1100 rpm due to increase in rate of heat generation with increase in tool rotational speed (from 600 to 1500 rpm). Similarly, increase in surface area of pin promotes (threaded pin) the heat generation rate due to that peak temperature obtained at TC1 and TC5 in case of threaded pin is 10 to15 K higher that straight pin. These threaded pins are more effective in weld zone to enhance heat generation through plastic deformation and material flow. Cylindrical pin with square thread FSW tool produce maximum peak temperature at TC1 and TC5 due to high surface area as compare to other. However, the effect of tool rotation is more prominent in heat generation than tool geometry [12].

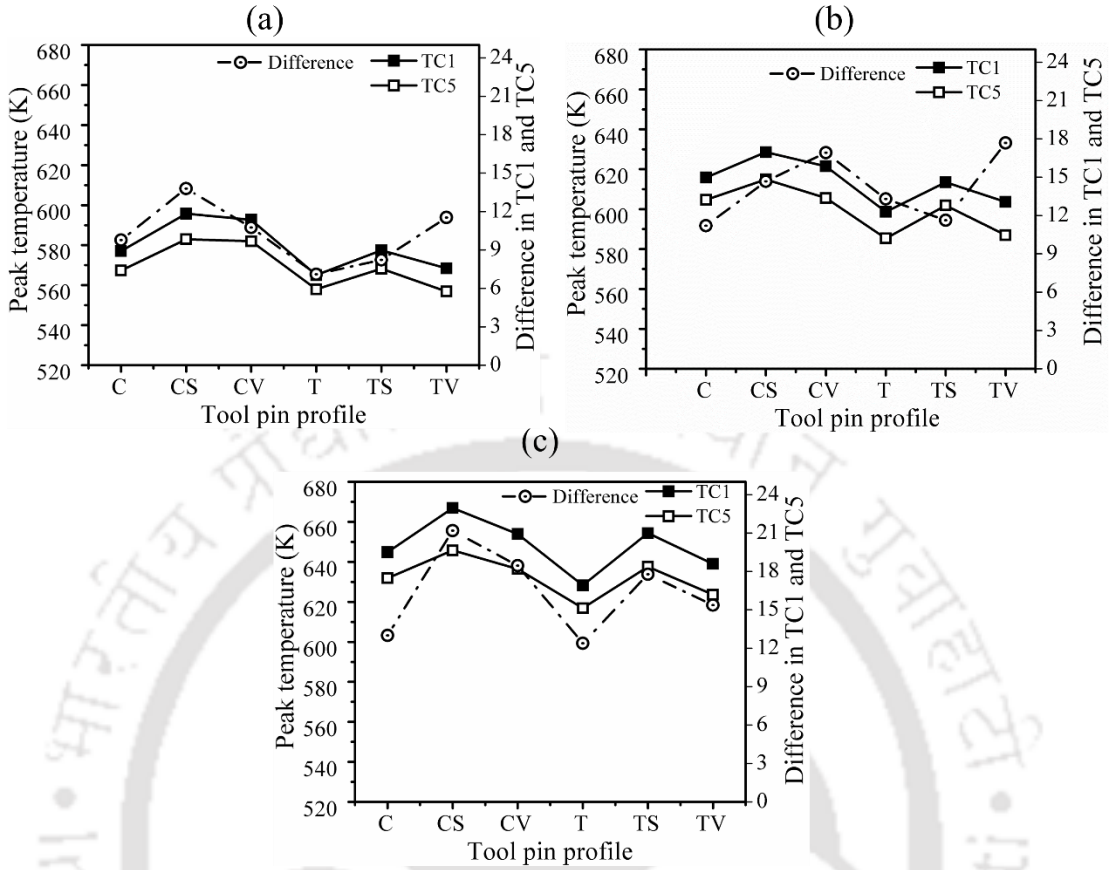

Figure 4.15. Comparison of peak temperature of different experimental conditions at TC1 advancing side and TC5 retreating side for experimental condition (a) 600 rpm, (b) 1100 rpm and (c) 1500 rpm.

Figure 4.16 shows the axial force on the tool with respect to welding time at 1100 rpm, 98 mm/min welding speed and CS tool pin profile. There is a significant variation in the axial forces with respect to different phases of welding. The peaks of axial force is identified the pin plunge and shoulder plunge regions during plunging phase. During plunging heat is generated by the pin due to frictional and plastic deformation which drops the axial force and afterwards rises again when the shoulder of the tool is plunged into the hard and cold workpiece. When the tool has plunged into the workpiece and stayed for 45 seconds during dwell phase to preheat the workpiece the axial force again drops. During welding period axial force is approximately constant around 4 kN. The axial force continues to decrease as the tool plunge-out of the weld seam. The variation of force is attributable to the resistance offered by un-welded and colder material to tool movement. Therefore, this axial force data provides useful information about weld joint to estimate weld defect and quality [281].

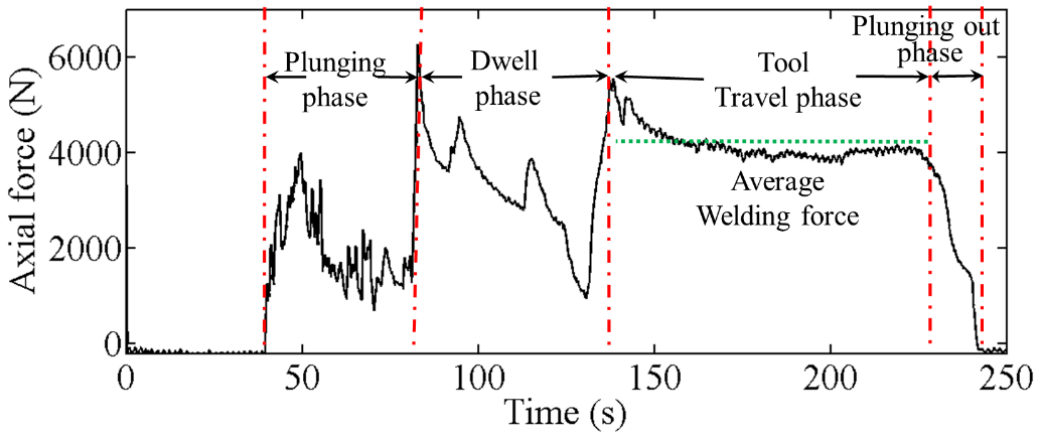

Figure 4.16. Variation of axial force at experimental condition of 1100 rpm, 98 mm/min welding speed and CS tool pin profile.

Figure 4.17 show the influence of FSW parameters on the average welding force. It's found that, with increase in tool rotation speed there is a decrease in the axial force due to increase in heat input during welding. With an increase in heat input, the contact area below the shoulder and in the stir zone, the workpiece material becomes softer and reduces the resistance offered by workpiece in this region. Whereas, the effect of tool pin geometry is low as compare to tool rotational speed and welding speed. While it's observed from **Fig. 4.16**, the variation is 0.5 to 0.8 kN between straight and threaded tool due to increase in material flow and heat generation than straight pin tool [282].

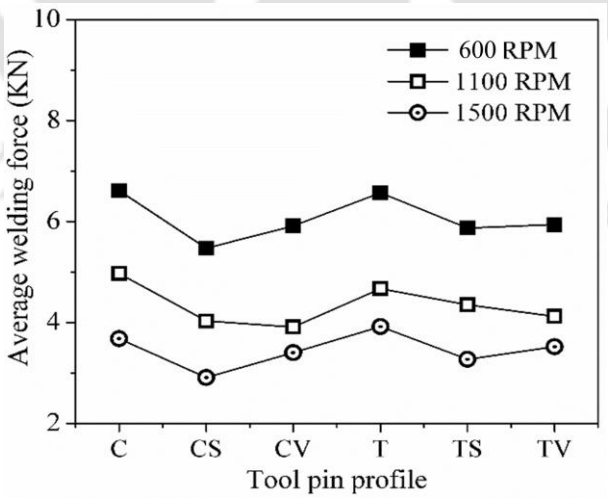

Figure 4.17. Comparison between average welding forces at various welding conditions.

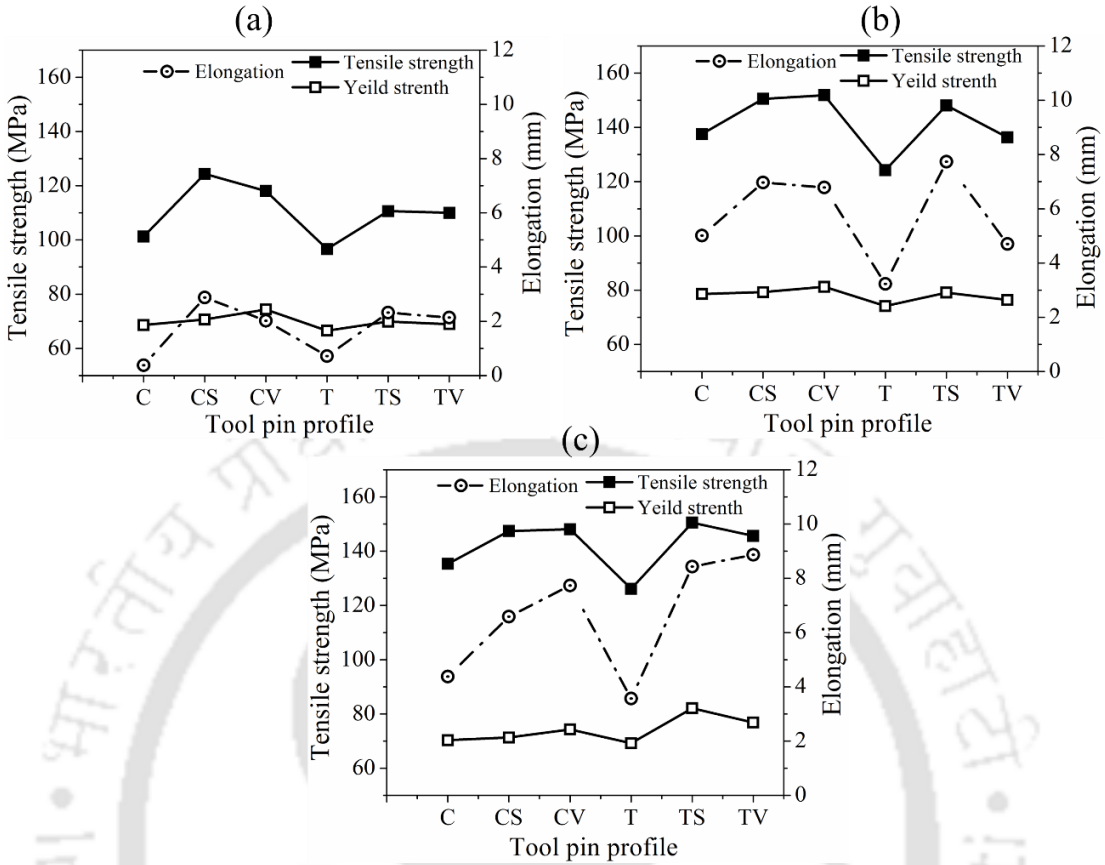

Figure 4.18. Tensile strength, yield strength and % of elongation of welded joint at various welding conditions (a) 600 rpm, (b) 1100 rpm and (c) 1500 rpm.

Figure 4.18 illustrate the tensile strength, yield strength and % elongation of welded joints corresponding to welding condition shown in **Table 4.6**. For these range of parameters, the tensile strength of weld in case of threaded pin is 2% higher than that of base material (base material tensile strength is 148.1 MPa). The maximum tensile strength of welds obtained at the rotational speed of 1100 rpm, welding speed of 98 mm/min, and with cylindrical pin with square thread FSW tool is 151.2 MPa which is 102 % of base material. The effect of rotational speed is concerned, the joints fabricated at a rotational speed of 1100 rpm are showing superior tensile properties compared to other joints, irrespective of tool profiles. Pin profile plays a crucial role in material flow and in turn regulates the welding speed of the FSW process [283]. In addition, the V-thread and square thread pin profiles produce extra stirring action in the flowing material due to thread in pin side surface. There is no such extra stirring action in the case of cylindrical and tapered plane pin profiles. This results in higher tensile

strength. In case of threaded pin profiles irrespective of rotational speed, the tensile strength is higher.

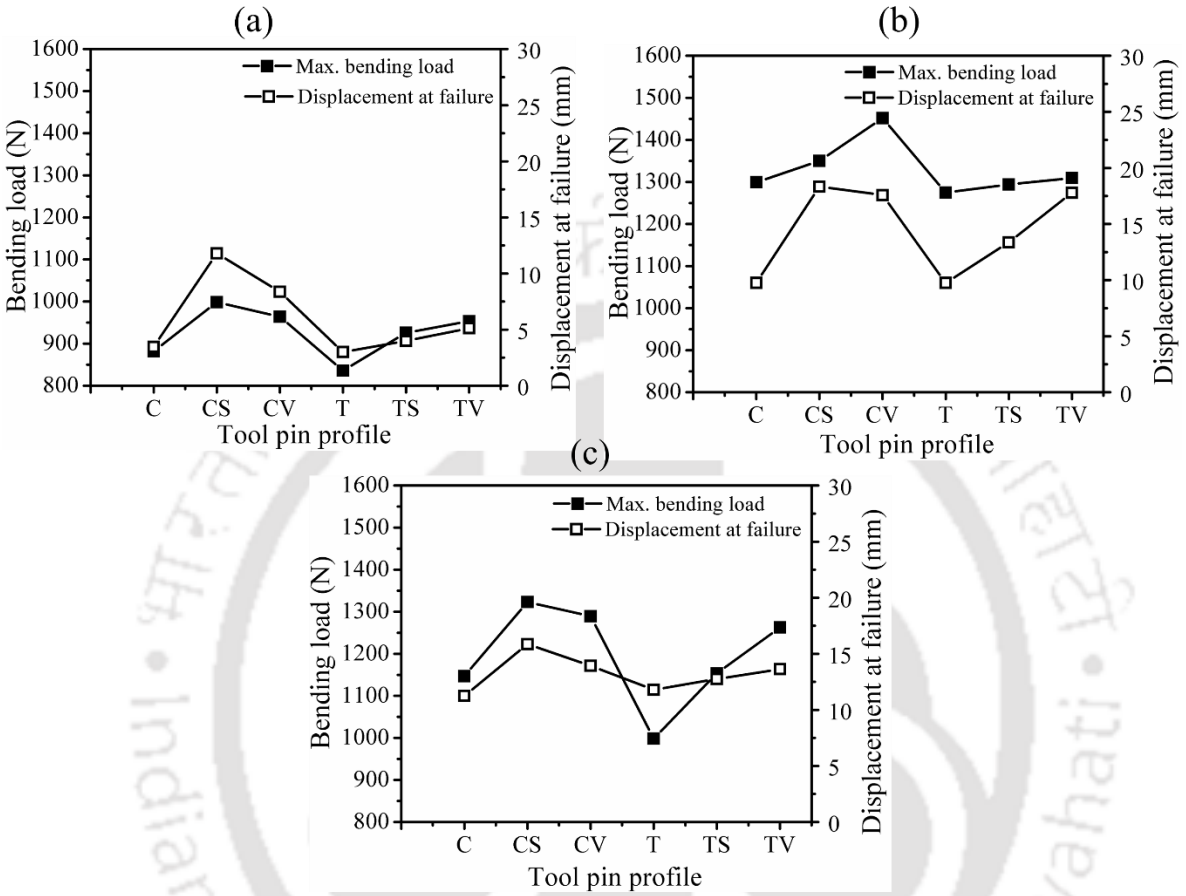

Figure 4.19. Comparison between ultimate bending loads of various welding conditions (a) 600 rpm, (b) 1100 rpm and (c) 1500 rpm.

The fracture toughness of a specimen can also be determined using a three-point flexural test. This test is very sensitive to defects near the surface of the weld bead, such as root flaws. During the test a 1 mm/min cross-head speed is used and one specimen for each type of weld and base materials are tested. No root flaws or other defects are detected in most of the joints. From the **Fig. 4.19(b)** it is observed that at tool rotational speed of 1100rpm, with the straight cylindrical threaded tool, the temperature and material stirring increase enough, so the higher bending strength joint is produced. Since the temperature at the welding speed of 400 rpm is not enough to soften the base material, the materials were not sufficiently plasticized to be stirred and forged easily for all the pin profiles resulting lesser bending

strength as shown in **Fig. 4.19(a)**. Defect was in the root for all the joints fabricated. This defect is known as the tunnel-hole defect. Though the appearance of the welded surface seems to be good, tunnel defects could be observed at the advancing side and in the stirred zone of the weld. The plasticized metal under the shoulder cannot flow sufficiently during the welding process due to insufficient heat generation [284].

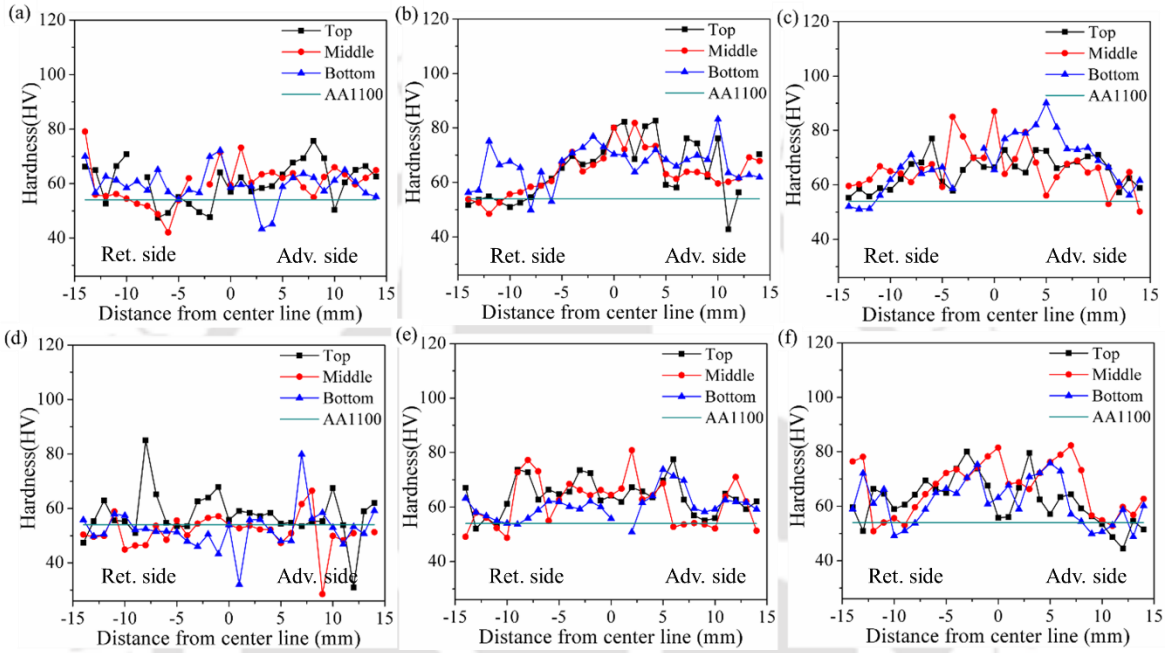

Figure 4.20. Hardness distributions on the transverse cross-section for joints fabricated at a rotational speed of 1100 rpm and 98 mm/min welding speed for different pin profiles (a) C, (b) CS (c) CV (d) T (e) TS and (f) TV.

Micro hardness distributions on the transverse cross-section of the joints for different tool pin profiles are shown in **Fig. 4.20**. It has been investigated that the hardness influenced by the tool pin profile due to the dominant influence on the plastic flow and deformation during welding. It's also illustrates that, for the same welding parameters, the highest hardness increase was achieved in the nugget and TMAZ of the welds produced with the threaded tool, i.e., about 30% more of base material hardness. The increase in hardness is attributed to the formation of fine grains in the stir zone, and in addition, the reduced size of weaker regions, such as TMAZ and HAZ regions, results in higher tensile properties. Similarly, the weld region of the joint fabricated using square threaded pin profile tool contains finer grains compared to other joints. The higher number of stirring action experienced in the stir zone to

produce finer grained microstructure and in turn yields higher strength and hardness. Therefore, the complex intercalated microstructure and the orbital stacking of materials in the stir zone results in the fluctuation of hardness values in the stir zones which is influenced by tool pin profiles [285].

Figure 4.21 shows the macrographs of the welded joints with low magnification. **Figures 4.21(C)** and **(T)** are fabricated using straight cylindrical and tapered cylindrical pin profiled tool, respectively, are having void defects. This is due to insufficient flow of plasticized material around the tool pin during welding process. In the case of threaded cylindrical and taper pin tool, the joints are found defect free as shown in **Figs 4.21(CS), (CV), (TS)** and **(TV)**. Under these welding conditions, the heat generation is almost the same for tool shoulder. The screw thread will be beneficial to the heat generation, under the same weld parameter, the pin with screw thread will generate more heat than the pin without screw thread. More heat input can improve the flow of the plastic material [179]. On the other hand, the screw thread on the pin exerts an extra downward force that will be beneficial to accelerate the flow of the plastic material. In addition, the pin profile has greater effect on the material flow behavior. This concluded that the heat input decides the formation and location of defect in the stir zone. In spite of the same heat input range, the different pin profiles alter the material flow, defect formation and its location [180].

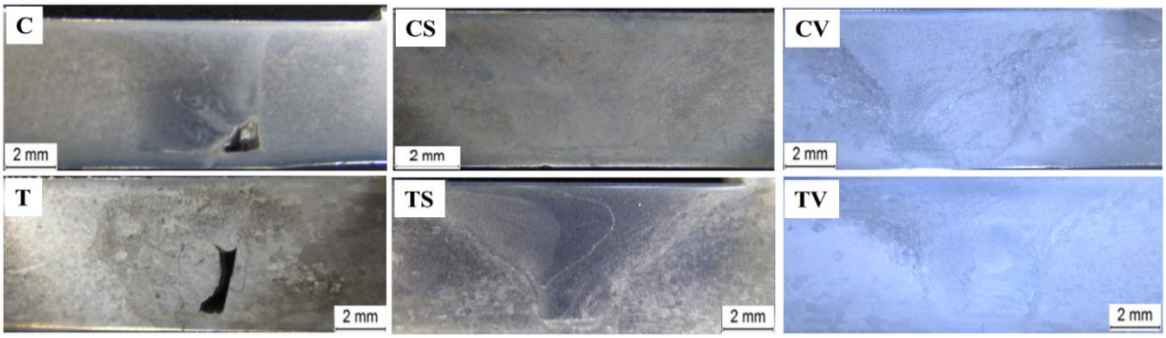

Figure 4.21. Macrographs for weld joints in longitudinal cross section at 1100 rpm for different pin profile (a) C, (b) CS (c) CV (d) T (e) TS and (f) TV.

The grain size and its orientation for various tool pin profiles at 1100 rpm are analyzed using optical microscope and shown in **Fig. 4.22**. The grain size in nugget zone at six different

tool pin profiles is 21.4 µm, 14.2 µm, 15.3 µm, 22.2 µm, 16.1 µm and 17.5 µm for C, CS, CV, T, TS and TV respectively at constant 1100 RPM and welding speed. The increase in degree of deformation during FSW results in the reduction of grain size according to the general principles of recrystallization. It is noted that the recrystallization grain size is reduced by threaded pin tool at constant tool rotational speed. The combination of lower temperature and shorter excursion time at the nugget bottom effectively retards the grain growth and results in smaller recrystallized grains [286].

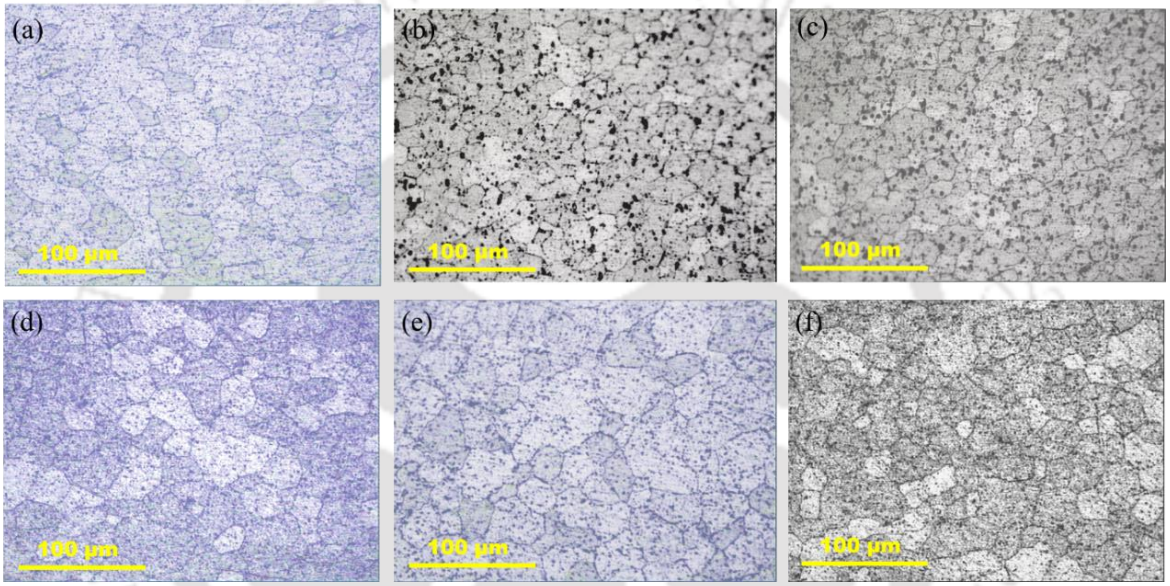

Figure 4.22. Microstructure of nugget zone for joints fabricated at a rotational speed of 1100 rpm and 98 mm/min welding speed for different pin profiles (a) C, (b) CS (c) CV (d) T (e) TS and (f) TV.

The variation of average grain size in the stir zones under the various tool pin profiles and rotational speed are shown in **Fig. 4.23**. It's observed that lower rotational speed resulted in lower peak temperature and consequently the reduction in grain size due higher plastic deformation and strain rate at low temperature [287-288]. During this process, the material experiences severe plastic deformation and thermal exposure which normally leads to formation of fine recrystallized grain structure. Similarly, at different tool pin profile average grain size decreases with increase in threaded profile in both straight and taper cylindrical pin. At the circumference of the pin, the material flow is shown to be governed by the simple shear deformation induced by the rotating pin, which led to the formation of a fine equiaxed grains.

Therefore, threaded pin generate higher degree of plastic deformation than straight and taper cylindrical tool which lead smaller grain at comparatively equivalent temperature [289].

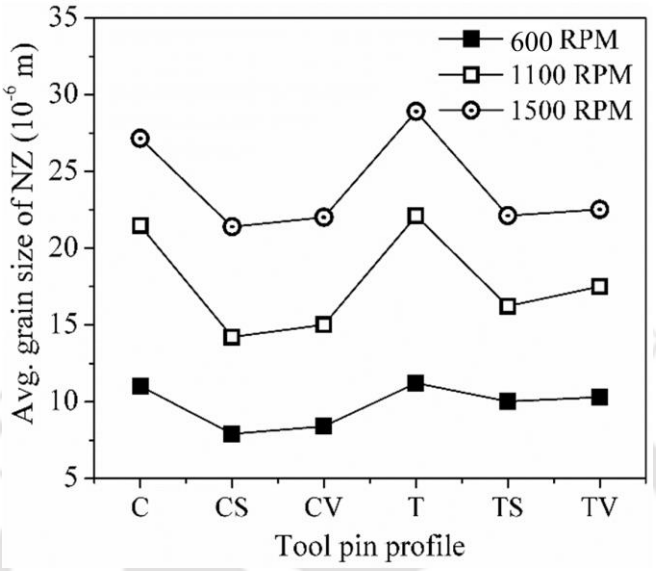

Figure 4.23. Comparison between average grain sizes of nugget zone at various welding conditions.

4.2 Hybrid FSW

Plasma assisted FSW (P-FSW) of similar and dissimilar materials is investigated on the aspects of thermal behavior and mechanical properties of welded joints. In thermal analysis, thermal history and variation of cooling rate are included to understand effect of preheating phenomena in FSW. Whereas, for mechanical properties, the joint strength, hardness, microstructure and fractography analysis of weld joint is carried out on the basis of the effect of preheating.

4.2.1 Experimental set-up

Experiment is conducted under different welding conditions for joining of similar (aluminium alloy) and dissimilar (aluminium alloy-Pure Cu) materials in butt joint configuration. First, similar material hybrid FSW of aluminium alloy is discussed. The chemical composition, in weight percentage of the aluminium alloy used for present work is described in **Table 4.7** which is found from the EDX test. The mechanical properties of the base material are concluded in **Table 4.8** after performing different tests. Two rectangular plates of 200 mm x 100 mm size with 6 mm thick are butt joined by P-FSW process. The plate

surface is cleaned by acetone prior to welding. The same FSW setup is used with additional fixture to hold plasma torch at an appropriate position as described in **Fig. 4.24**. The welding tool is made of stainless steel 304 for similar joint with flat shoulder and straight cylindrical pin having diameter of 20 mm and 6 mm, respectively. The pin length is slightly less than the thickness of work-pieces i.e. 5.70 mm. The rotating tool axis is perpendicular of the plate with zero degree tilt angle. The edges of the test pieces are machined to obtain a neat square butt. They are clamped to the horizontal bed with zero root opening. As shown in **Fig. 4.24 (a)**, the preceding plasma torch is placed 13 mm in front of the shoulder edge with an angle of 60 degree adjacent to the joint which ensure less effect of arc on tool and enhanced the material flow during welding. The layout of thermocouple on advancing and retreating side for similar Hybrid FSW is similar to **Fig. 4.2**.

Table 4.7. Elemental compositions (in wt %) of aluminum alloy used in the present experiment.

Element	Cu	Fe	Si	Mn	Mg	Zn	Cr	Ti	Al
Weight percentage	0.15- 0.40	0.70	0.40-0.80	0.15	0.80-1.20	0.25	0.01-0.35	0.15	Bl.

Table 4.8. Mechanical properties of the aluminum alloy.

Property	Value
Tensile strength (MPa)	142.781
Yield strength (MPa)	112.452
Elastic modulus (GPa)	61.94
Percentage of elongation (%)	13.758*
Micro hardness (HV)	42.02
Density (g/cm3)	2690

*gauge length = 57 mm

In case of dissimilar joint, the aluminum workpiece is located on the retreating side and the copper plate is on the advancing side (**Fig. 4.25**). The PAW torch preceding to the FSW tool is used as preheating source with an off-set towards the copper plate by 5 mm as shown in **Fig. 4.24(b)**. The torch is kept 13 mm away from the shoulder edge with an angle

of 60° with reference to the normal of work piece surface. The optimum location of the plasma torch ensures less effect of arc on FSW tool and enhances the material flow during welding. The tool is made of H13 with the shoulder and pin diameters of 20 mm and 6 mm, respectively. The welding tool is perpendicular to the plate. The shoulder has a flat profile. The pin length is slightly less than the thickness of work-pieces i.e. 5.70 mm. The chemical composition and mechanical properties of the copper used in present investigation are depicted in **Table 4.9** and **Table 4.10** respectively. Whereas, chemical composition and mechanical properties of the aluminum alloy already shown in **Table 4.7** and **Table 4.8** respectively. The melting temperature of pure copper and aluminum alloy is considered as 1336.15 K and 913.15 K, respectively.

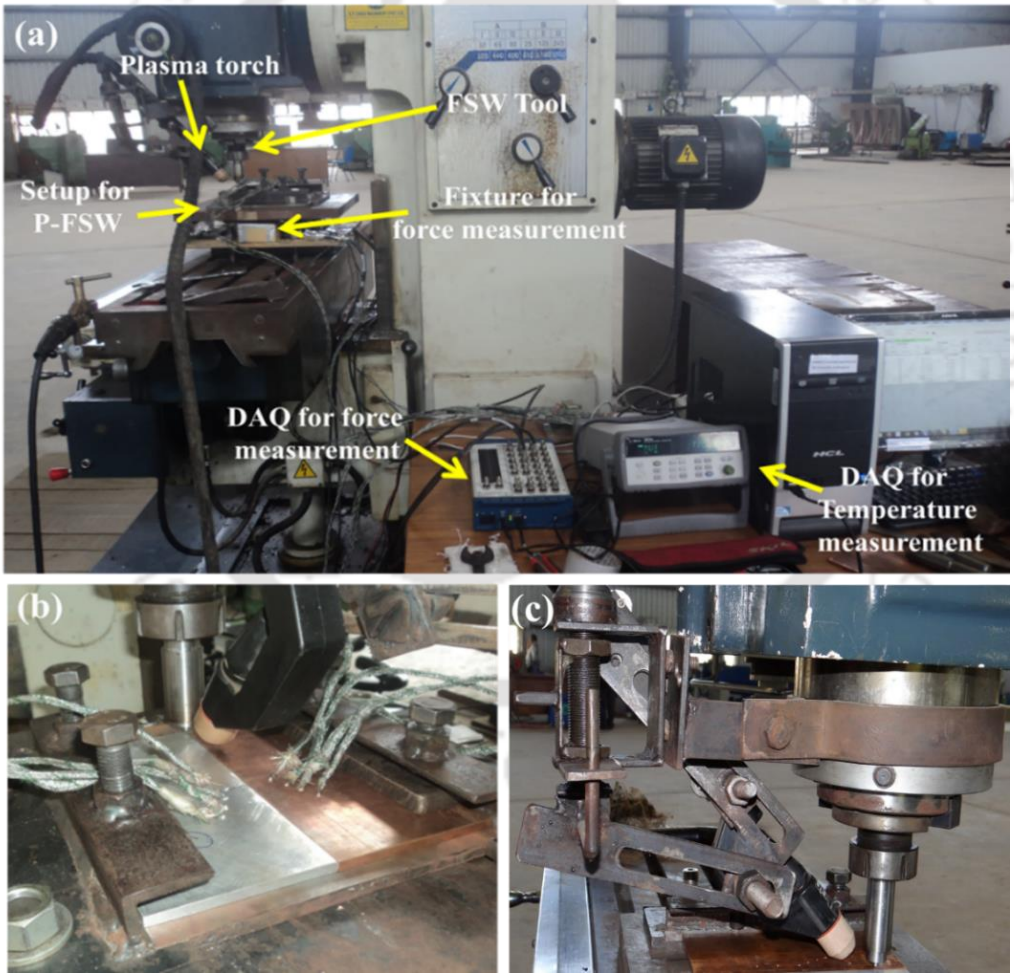

Figure 4.24. (a) Experimental setup for P-FSW; (b) Front view of P-FSW setup; (c) Side view of P-FSW setup.

Transient temperature is recorded on the top surface at eight different locations using 36 gauge K-type thermocouples (**Fig. 4.25**). The location of thermocouples is decided by the position of offset distance of FSW tool and the welding torch. The size of workpiece is 200 mm long and 100 mm wide taken from 6 mm thick copper and aluminium plates.

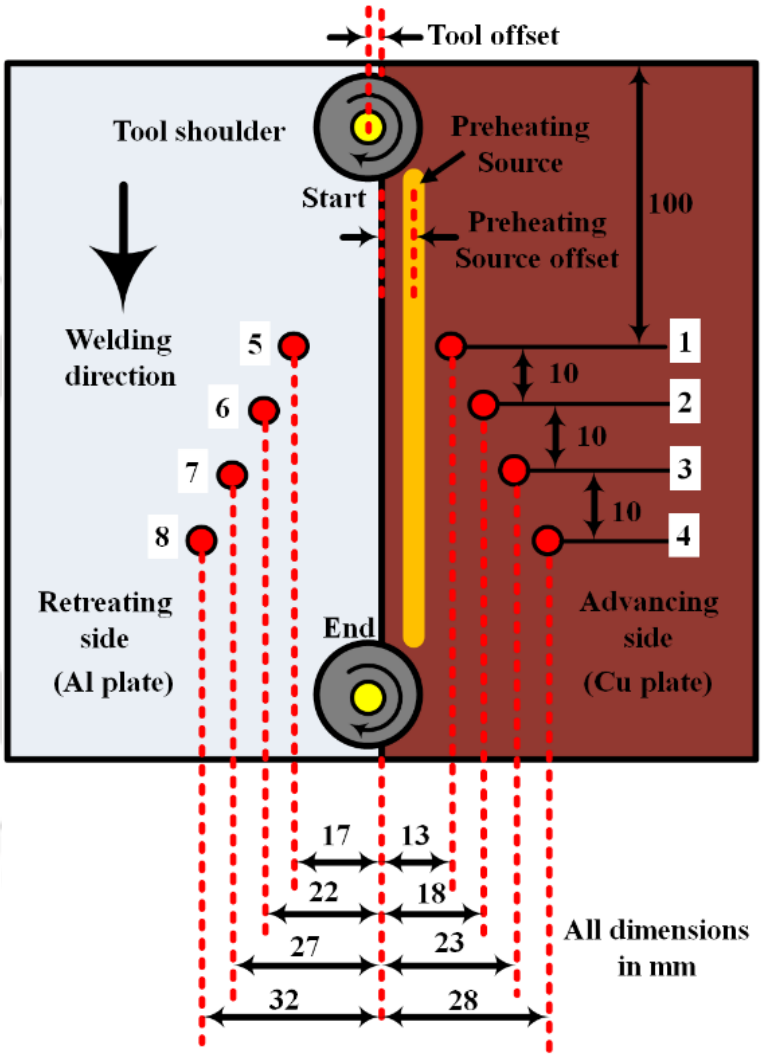

Figure 4.25. Layout of thermocouple points during welding for dissimilar material joint.

Table 4.9. Chemical composition of pure copper (wt%).

P	Bi	Sb	As	Fe	Ni	Pb	Sn	S	Zn	O	Cu
—	0.001	0.002	0.002	0.005	—	0.005	—	0.005	—	—	Balance

Table 4.10. Mechanical properties of the pure copper base material.

Property	Value
Tensile strength (MPa)	374.7841
Yield strength (MPa)	35.010
Elastic modulus (GPa)	108.94
Percentage of elongation (%)	5.758
Micro hardness (HV)	80.51
Density (g/cm3)	8245

The test samples are prepared in transverse direction with respect to welding direction for metallographic analysis. The modified Poulton's reagent is used to reveal the microstructures of copper [290] while the aluminium side is etched with Keller's etchant [291]. The distributions of the constituents of two base alloys in the nugget zone is analysed by a scanning electron microscope (SEM) equipped with an energy dispersive X-ray spectroscopy (EDS). The Vickers hardness distribution of the joint is measured with a load of 200 gm and dwell time of 10 s, according to the ASTM: E384-11 standard [292]. Hardness is measured on the cross-section both in transverse direction of the weld and in the thickness direction. The tensile tests of the joint are performed using samples prepared according to ASTM E8M-04 standard [293]. The tensile load is perpendicular to the welding direction as explained in previous section. Scanning electron microscopy is used for factography analysis of tensile fracture surfaces. Bending test is carried out using three-point load system. The specimen is tested at constant speed of 2.5 mm/min as per ASTM specifications as explained in previous section [294].

4.2.2 Effect of preheating on thermal and mechanical properties of similar joint (Al-Al)

In this section, a comparative study between FSW and P-FSW is investigated on the aspects of thermal, mechanical, and microstructural properties of welded joints. In thermal

analysis, preheating phenomena in FSW include several aspects such as thermal history and variation of cooling rate. In mechanical properties, the preheating effect is carried out on the basis of tensile strength, hardness, and fractography analysis. The characterization of microstructure evolution in welded aluminum alloy is also carried out to understand the effect of preheating. The rotational speed of the tool, welding speed, and the axial pressure are the principal process variables. The process parameters for the experiment are described in **Table 4.11**.

Table 4.11. Process parameters for FSW and P-FSW

Experiment No.	FSW		P-FSW
	Welding speed (mm/min)	Rotational speed (RPM)	Current (amp)
Case 1	63	600	25
Case 2	63	815	35
Case 3	98	600	35
Case 4	98	815	25

The effects of preheating on thermal history at 13 mm from weld centre line in advancing and retreating sides are shown in **Figs. 4.26(a)-(b)**. In advancing side, the temperature is higher than retreating side and confirms the non-symmetric heat generation. The area under the curve of thermal history represents total heat input during welding which is higher in case of preheating. This additional heat input, due to plasma arc, makes an effect on rate of change of temperature during welding that may improve the weld joint properties. This additional heat also increases the temperature of material around the weld zone so that material tends to lose some of its mechanical strength and facilities the ease of welding. The experimental method reveals that the peak temperature reached in the case of the hybrid welding is around 405 K - 425 K at a distance of 13 mm from weld centre line It is obvious from **Fig. 4.27** that the peak temperature in P-FSW is about 25 to 35 K more than FSW in all cases. The material around the weld becomes much hotter than the case of no preheating. So the material tends to lose some of its mechanical strength and increases the plastic flow of material.

Figure 4.28 depicts the rate of change in temperature i.e. the cooling rate consequence of the time temperature profile described in **Fig. 4.24**. The cooling rate is estimated by change of temperature with respect to change of time $(\sim dT/dt)$ for a fixed thermocouple location. It is obvious form **Fig. 4.28** that there is wide variation of cooling rate when the FSW tool is nearer to thermocouple location and asymptotically approaches to zero value when the tool is away from the fixed point. The preheating effect due to plasma arc decreases the variability and magnitude of cooling rate as compared to conventional FSW process. Preheating builds up heat in the metal and it takes little longer time for it to cool down. Since the maximum cooling rate is less than 17 K/s, the diffusional transformation will occur and this transformation is more stable for P-FSW process due to less variation of cooling rate [295]. However, this much variability in cooling rate may influence the grain coarsening rate in this temperature range [296]. Since the average cooling rate or temperature gradient $(\sim dT/dx)$ from the top surface to the bottom surface decreases, it may influence the hardness distribution. Less variability of hardness distribution is expected for P-FSW process than FSW process.

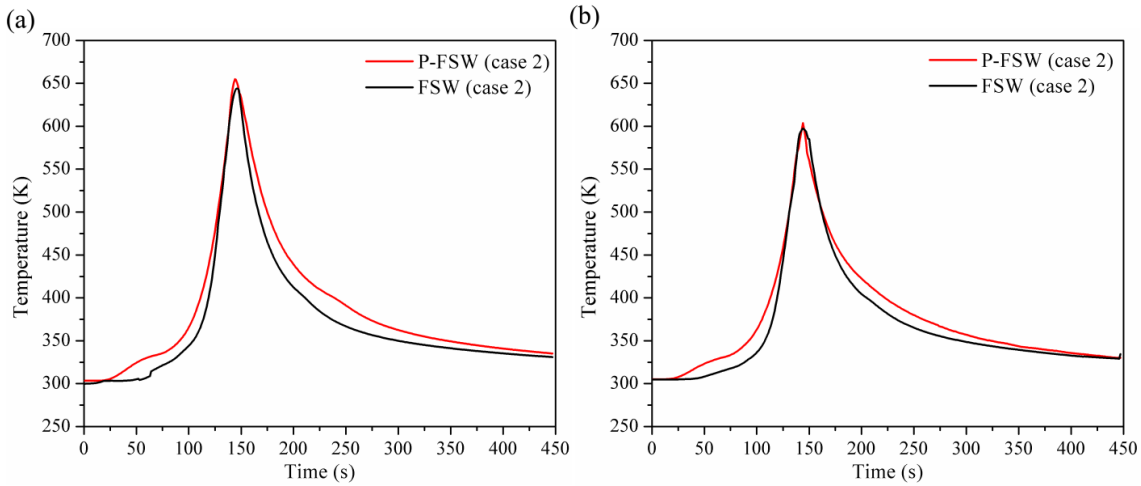

Figure 4.26. Comparison between temperature profiles of case 2 at 13 mm from weld centre line: (a) Advancing side and (b) Retreating side.

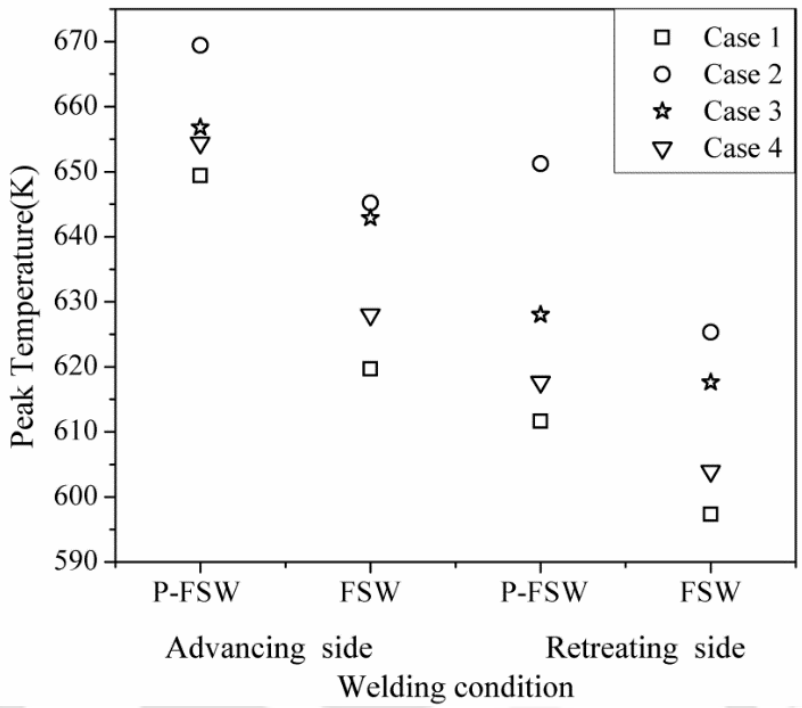

Figure 4.27. Comparison between peak temperatures of different welding conditions at 13 mm from weld centre line in both sides for FSW and P-FSW.

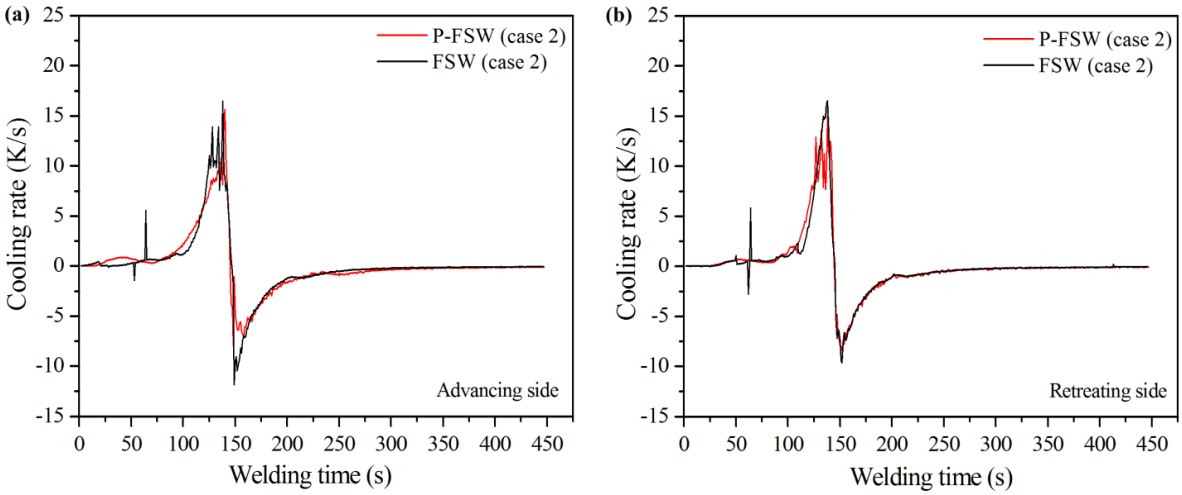

Figure 4.28. The estimated cooling rate for case 2 of **Table 4.11**: (a) Advancing side and, (b) Retreating side.

Figure 4.29 shows typical plunging force signal for case 2 of Table 4.11 at different welding conditions. The average magnitude of plunging force is low in P-FSW (**Fig. 4.29b**) as compared to FSW process (**Fig. 4.29a**) for case 2. It is expected that the preheating of the workpiece would reduce the axial forces during dwell period and welding phase due to the

preheating of workpiece. It is observed from **Fig. 4.30** with increase in peak temperature of P-FSW there is reduction of plunging force around 20 to 28 % with similar process parameters.

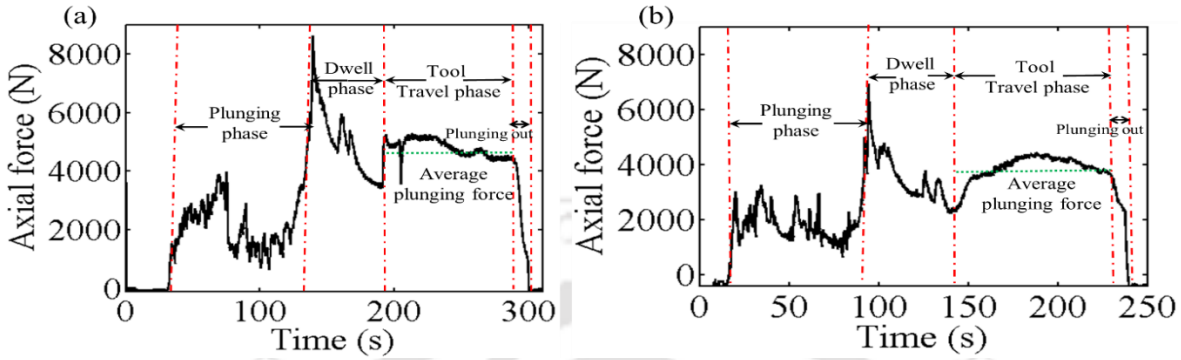

Figure 4.29. The axial (plunging) force signals of case 2 of Table 4.11: (a) FSW and (b) P-FSW.

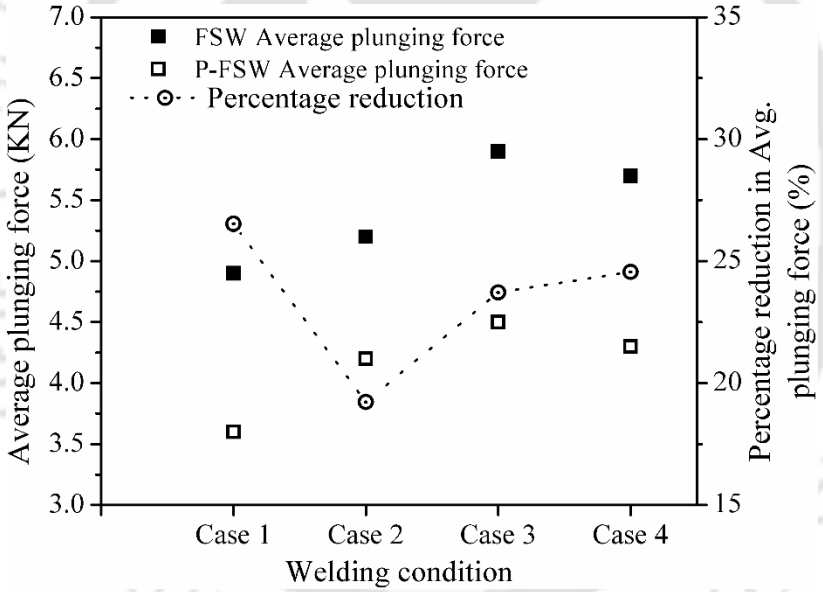

Figure 4.30. Comparison between average plunging force of different welding conditions during tool travel phase.

The effect of preheating is more prominent in mechanical performance of welded joints. The characterization of mechanical properties is done by ultimate tensile strength, elongation, and micro-hardness of the welded joints. The comparison of tensile strength between FSW and P-FSW welded joints corresponding to welding condition of **Table 4.11** is described by **Fig. 4.31**. For these range of parameters, the tensile strength of P-FSW weld is ~ 8 % higher than that of FSW welds. The maximum tensile strength of P-FSW welds obtained

at the rotational speed of 815 rpm, welding speed of 63 mm/min and preheating current of 35 A is 134 MPa which is ~ 95% of base metal tensile strength. Whereas the maximum tensile strength of 122 MPa is achieved for FSW with similar welding conditions and is ~ 89 % of the base metal tensile strength.

It is obvious that the tensile strength of welded joint with preheating increases significantly as compared to conventional FSW. This is mainly due to strain aging by plastic deformation and dispersion strengthening by fine Al_2O_3 particles at stirred zone. Although with the Al_2O_3 particle addition, the ultimate tensile strength increases marginally, further increase of tensile strength is attributed to the grain structure difference and the Orowan strengthening due to stirring of finely dispersed aluminium oxide particles. Overall, the recovery and continuous dynamic recrystallization for aluminium refine the grain size over the base material with the expense of heavily deformed work hardened material [297].

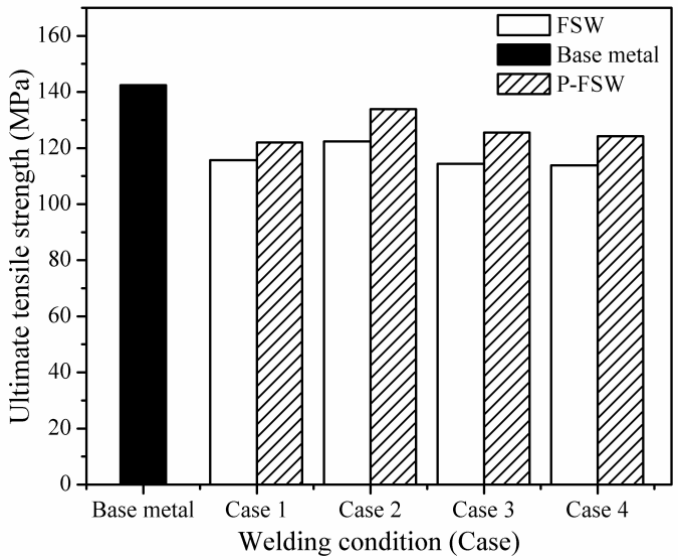

Figure 4.31. Comparison between tensile strength of various welding conditions.

Figure 4.32 depicts the percentage of elongation for tensile test specimens. There is markedly difference in elongation of friction stir welded specimens as compared to base material. This is due to the fact that in FSW, the material undergoes continuous dynamic recrystallization and as a result a fine grain structure is produced with Al_2O_3 particles at stirred zone. There is slight decrease in elongation for P-FSW welds as compared to base metal. The deformation in coarse-grain aluminium is known to have steep strain gradient in the vicinity of grain boundary and the centre of the grain. As the grain size decreases and strain increases,

the deformation becomes more homogeneous. Therefore, the preheating does not improve its elongation much and the elongation is around $\sim 10\ \% \pm 2\ \%$ for all cases. The effect of preheating works quite homogeneously throughout the structure although there is application of surface heat flux from the plasma arc. This happens in case the base metal has high thermal conductivity and thermal diffusivity which leads the intuition that the effect of preheating may work quite homogeneously for highly thermal conductive materials.

Fracture in the tensile test specimens of FSW and P-FSW welds occurred mostly at heat affected zone of the advancing side due to inhomogeneous grain size distributions. The maximum plastic deformation occurs only in a narrow region of the advancing side which subsequently forms necking at the fracture locations of the joints. It can be observed that the controlling of weld temperature distribution by preheating improves the ultimate tensile strength of the welded joint and promotes the brittleness. It is thus obvious that preheating influences the strengthening mechanisms by the pinning effect of Al_2O_3 particles that retarded grain growth following continuous dynamic recrystallization during P-FSW and thus led to more pronounced reduction in grain size and relatively brittle fracture during tensile loading of welded joint.

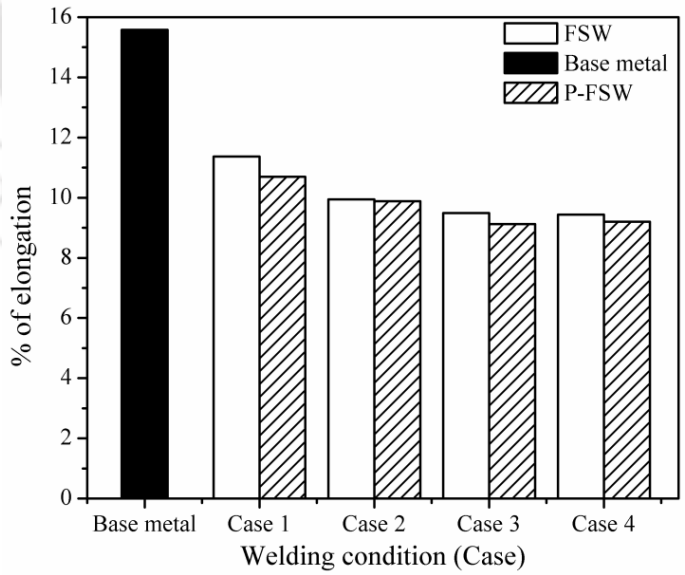

Figure 4.32. Comparison between percent of elongation of various welding conditions.

In FSW, the joint efficiency is defined by the ratio of the strength of a joint to the strength of the base metal and is expressed as

$$\eta = \frac{joint\ strength}{base\ metal\ stermgth} \times 100\ \% \quad (4.1)$$

Figure 4.33 represents the efficiency of the welded joint with reference to the base metal joint efficiency as 100 %. It is observed that the joint efficiency for welding condition of case 2 (P-FSW of **Table 4.11**) is much close to the base metal. The highest joint efficiency of 95.93 % was obtained in this case. **Figure 4.34** indicates tensile stress-strain curves for the FSW and the P-FSW process corresponding to welding condition of case 2 in **Table 4.11**. The tensile strength of the P-FSW joint are greatly increased due to the application of preheat. It is obvious that the yield and ultimate tensile strengths of the P-FSW joint increases, however, they are lower than those of the base material. The elongation of P-FSW weld decreases as compared to FSW joint. From **Fig. 4.34,** it is concluded that the strain-hardening rates of P-FSW welds are higher than that of the FSW welds which is approximately 2 times at 3 % and 5 % strains.

Figure 4.33. Comparison between joint efficiency of various welding conditions.

Figure 4.35 shows the hardness profiles measured along the transverse cross section of welded specimen at three different lines along centre, bottom, and top of the weld zone corresponding to welding condition of case 2 in **Table 4.11**. Similar qualitative trend is

observed in the hardness profiles in all three lines of the weld zone in other cases also. In FSW of aluminium alloy, the hardness is slightly less in the thermo-mechanically affected zone (TMAZ) at retreating side that is attributed probably due to work hardening and grain coarsening caused by thermo-mechanical effect due to the dynamic recovery, recrystallization and grain growth. The minimum hardness is located around 9–11 mm from the weld centres in retreating side.

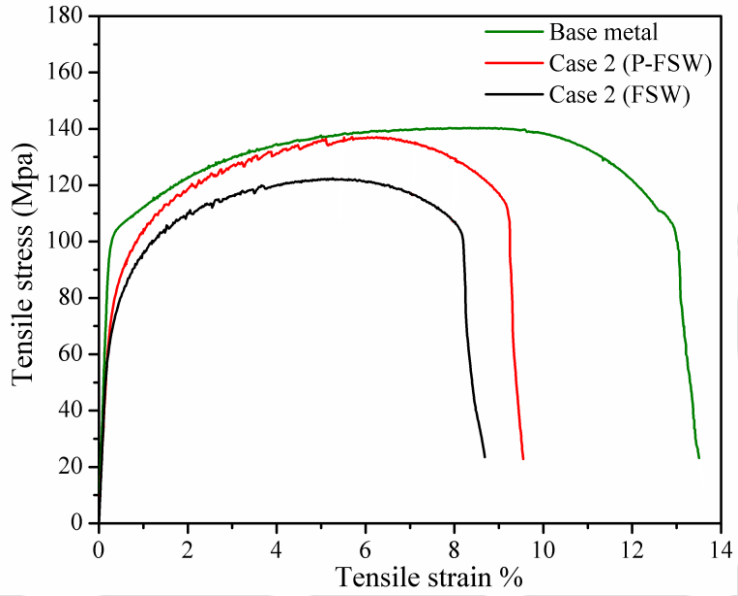

Figure 4.34. Comparison between the stress-strain curves of the case 2 in **Table 4.11** under two different welding conditions.

In the case of FSW welds, hardness profile is strongly affected by work hardening rather than grain size in the weld and it is dominantly governed by the grain boundary strengthening and the dislocation strengthening. This hardening mechanism leads the case of irregular profile of hardness depicted in **Fig. 4.35(a)**. In the case of P-FSW welds as shown in **Fig. 4.35(b)**, the hardness profile is relatively uniform and comparatively less variation is observed. There is significant differences in the hardness distribution between retreating side (RS) and advancing side (AS). The hardness within the stirring zone is higher on the AS than the RS i.e. the hardness distribution in the NZ is asymmetric with respect to the tool rotation axis. Moreover, in the transition zone between the unaffected zone and the stirring zone, the hardness variation was more drastic on the AS than on the RS, as shown by hardness profile. The weld nugget has an average hardness value of about 45 HV, which is higher than that of

base metal. Overall, the higher hardness value at the TMAZ and nugget zone of advancing side is observed due to pronounced effect of continuous dynamic recrystallization. It is attributed by the fact that the strain-rate change due to the high-temperature deformation of pure aluminium is depends on stress and temperature [298-299]. This determines the steady-state deformation during process due to the effect of preheating and left more uniform finer grain throughout the structure.

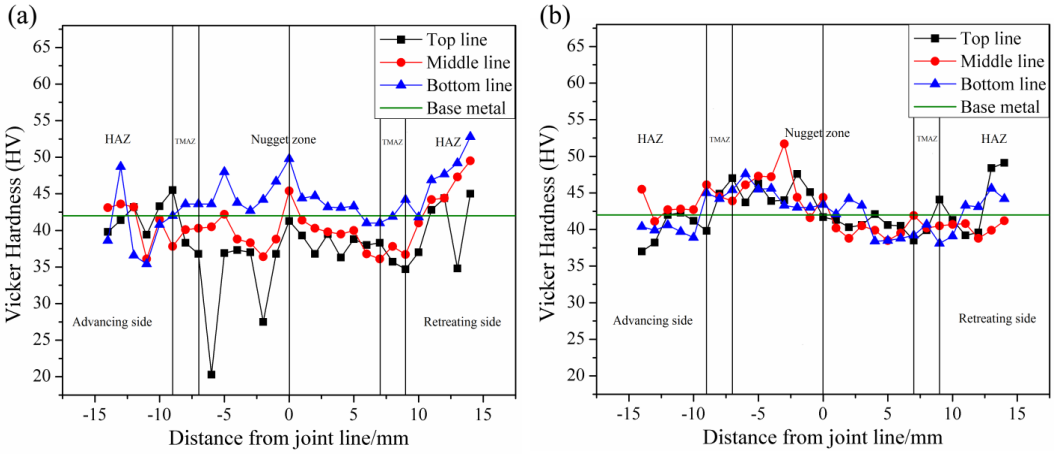

Figure 4.35. Hardness distributions on the transverse cross-section for case 2: (a) FSW and (b) P-FSW.

The morphological study of welded joints is performed using optical microscope on two different scales such as macro-level and micro-level. The macrograph of the FSW and P-FSW joint is verified and is shown in **Fig. 4.36(a)** and **4.36(b)** respectively. It reveals all three regions i.e. nugget, TMAZ, and HAZ in the weldment. The preheating of the welding material does not affect the final outlook of weld zone cross section. In P-FSW, extreme strain rate is developed at more elevated temperature (less flow stress) and recrystallization of material in the weld nugget occurs after the tool passes through it that result in a dispersion of finer grains in this area. The nugget zone is slightly larger than the pin diameter. The thermo-mechanically affected zone slightly reduces with increase in additional heat input but heat affected zone is increased with additional heat input (**Fig. 4.36)**. The stirred zone in P-FSW has the highest degree of deformation that takes place at elevated temperature and it is characterized by fine recrystallized grain structure. This recrystallized grain structure in the nugget zone is contributed to strength and toughness of weld joint. Such contribution would be expected to

be proportional to the grain size in nugget zone. In general, the macrostructure of P-FSW weld is quite similar to FSW welding but HAZ in P-FSW is much higher than FSW.

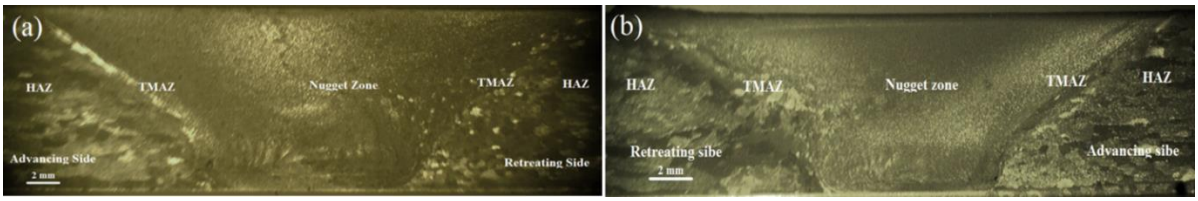

Figure 4.36. Macroscopic cross section with the four characteristic regions of the weld indicated of case 2: (a) FSW and (b) P-FSW.

Different micrographs of the FSW and P-FSW joint is investigated in four microscopically distinct regions, i.e. base material, HAZ, TMAZ, and nugget zone with reference to previous macrograph. **Fig. 4.37** illustrates microstructures of the nugget zone corresponding to welding condition of case 2 in **Table 4.11**. Grain structures in the nugget zone are investigated at same location on centre line to reveal the effect of preheating on microstructural evolution using optical microscope. Average grain size in the case of FSW is ~ 9 μm (**Fig. 4.37a**) whereas it is ~ 7 μm for P-FSW (**Fig.4.37b**). It is obvious that the dynamic recrystallization at a higher temperature in P-FSW yields lower grain growth of the aluminium substrate due to pinning effect of aluminium oxide formed mainly on the top surface which is stirred into the whole volume of weldment by FSW tool and thus increases the number of grain boundaries in nugget zone. Also, there is the possibility of larger number of nucleation site in case of P-FSW and hence there is not much difference in average grain size between FSW and P-PSW. It is noteworthy that the grain refinement in the FSW of aluminium alloy occurs due to continuous dynamic recrystallization in which a continuous introduction of strain is coupled with rapid recovery and migration of sub-grain/grain boundaries [300-302].

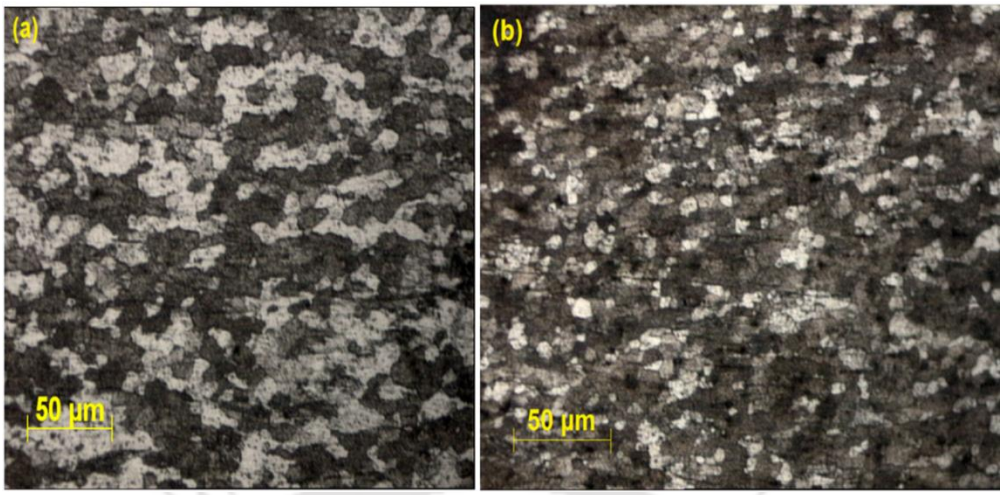

Figure 4.37. Comparison of optical microstructures of the nugget zone for case 2: (a) FSW and (b) P-FSW.

On the other hand, TMAZ and HAZ are not much affected by preheating in microstructure level but width of these zones is changed. The grains of aluminium alloy in the TMAZ in FSW is slightly coarse and elongated differently in the radial direction of base metal as compared to P-FSW due to the mechanical force and heat caused by friction of a rotation tool shoulder. The average grain size in these two regions is around ~ 13 µm. The HAZ is unaffected by any mechanical deformation and only the thermal effects act due to frictional heat generated by the shoulder and tool pin rotation. Therefore, owing to preheating there is no change in microstructure but there may be increase in thermal stress in HAZ due to higher temperature difference.

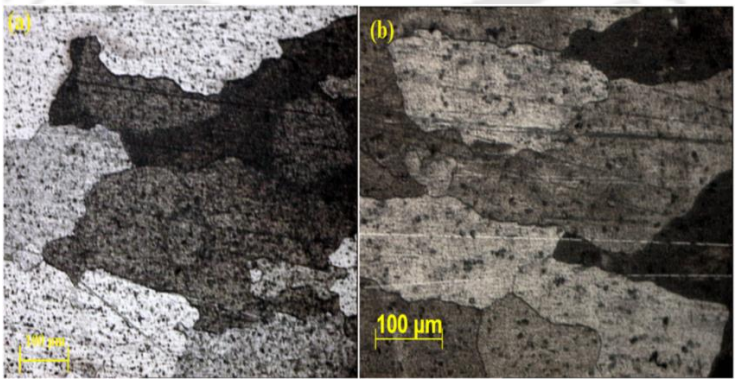

Figure 4.38. Optical micrograph of microstructure of cross-section for case 2: (a) FSW and (b) P-FSW joints welded at HAZ.

Fractured surface of the tensile test specimens are characterized by using scanning electron microscope to understand the failure pattern. All the fracture surfaces consist of dimples which indicates failure pattern during tensile test. **Figure 4.39** shows a comparison of the tensile fracture feature of FSW and P-FSW welded aluminium specimens corresponding to case 2 in **Table 4.11**. Deeper and lower population dimples are found in FSW case while shallow and large populations of dimples are observed on the fractured surface in P-FSW which is indicative of relatively higher fracture energy. Meanwhile, the bigger second phase particles presence in FSW, results in the bigger dimples during the tensile test shows in **Fig. 4.39 (a)**. From an enlarged SEM photograph, the dimple pattern indicates ductile fracture and the porosity in the matrix. **Fig. 4.39 (b)** shows the photograph of dimple patterns and some defects which cause fracture to initiate. These two fracture surfaces invariably consist of dimples, which is an indication of ductile fracture. The fracture surfaces of the FSW tensile specimen (**Fig. 4.39a**) show larger dimples than the P-FSW (**Fig. 4.39b**). The ductile fracture phenomena are found in FSW welded specimens whereas relatively brittle fracture is found in P-FSW joints. It is observed that the crack tends to occur initially at the upper region of the joint and propagated towards the bottom region due to more prominent preheating effect on the upper surface of the specimen.

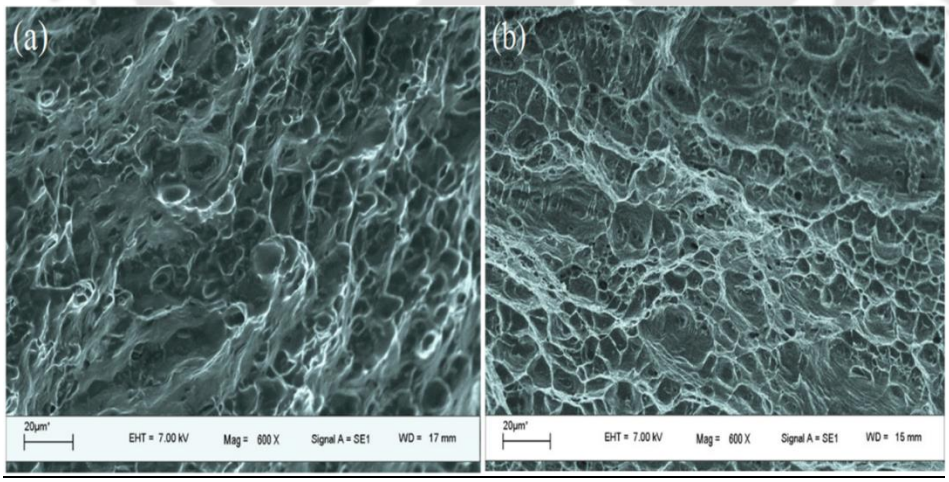

Figure 4.39. Comparison of fractured surface of the tensile test specimens of case 2: (a) FSW and (b) P-FSW.

The EDX analysis of fracture surface resulted from tensile test specimens is obtained for the welding condition of case 2 in **Table 4.11** and is depicted in **Fig. 4.40**. After the preheating, agglutinated aluminum oxide are observed at the fracture surface. On the other hand, a dimple pattern which is observed in FSW is a feature of the ductile fracture. According to the EDX analysis results, after the preheating, the oxygen is detected on the fracture surface. The ratio of the oxygen content at the fracture surface is high due to the effect of preheating. This indicates that the oxide layer formed at top surface in stirring zone is getting mixed and causes the brittle fracture. It is concluded that the fine distribution of Al_2O_3 particles in the local region does not affect much, but agglutination of the aluminum oxide affects the bulk mechanical properties of the weld joint.

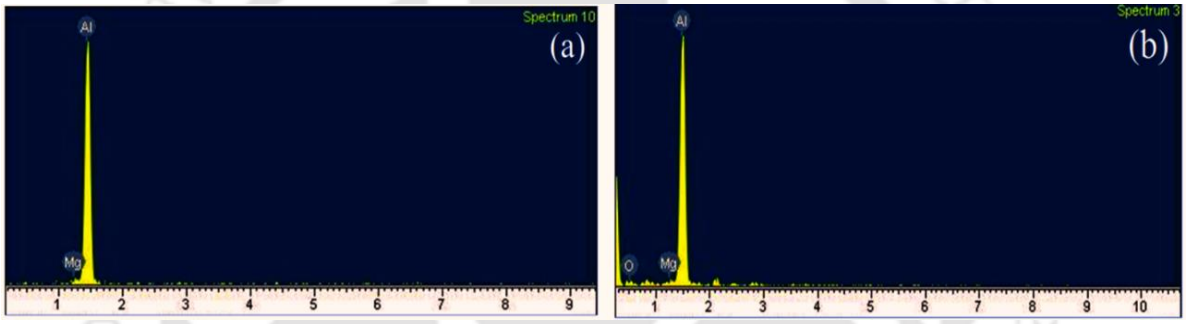

Figure 4.40. Fracture surface EDX analysis results of tensile test specimens of case 2: (b) FSW and (a) P-FSW.

4.2.3 Dissimilar welding

The experimental investigation of dissimilar Hybrid FSW of pure copper and aluminium alloy with a thickness of 6 mm in butt joint configuration is discussed in this section. The chemical composition, in weight percentage of the aluminium alloy and pure copper used for present work is described in **Table 4.1** and **Table 4.11** respectively. The mechanical properties of the aluminium alloy and pure copper are represented in **Table 4.2** and **Table 4.12** respectively. The plasma arc is focused on the copper plate at 13 mm in front of FSW tool shoulder edge with an angle of 60˚ with respect to the FSW tool axis. Argon is used as a plasma gas with constant flow rate of 2.5 l/min and is also used as shielding gas. An offset of the FSW tool towards the aluminium side is followed here. The copper plate is placed on advancing side as shown in **Fig. 4.23(b)**. To conduct the experiments, the range of

rotational speed is varied from 440 to 1100 rpm, tool offset 0.5 to 2.75 mm in aluminium side and the welding speed varies from 63 to 200 mm/min as illustrated in **Table 4.12**.

Table 4.12. Design of experiments for welding of aluminum and copper dissimilar joint.

Exp. No.	Rotational speed (rpm)	Transvers speed (mm/s)	Preheating current (A)	Tool offset (mm)
1	815	98	0	2
2	815	98	35	2
3	815	98	45	2
4	815	98	55	2
5	815	98	65	2
6	815	98	55	0.5
7	815	98	55	1.25
8	815	98	55	2.75
9	815	63	55	2
10	815	132	55	2
11	815	200	55	2
12	440	98	55	2
13	600	98	55	2
14	1100	98	55	2

Figure 4.41 shows the temperature history measured at TC1 (advancing side) and TC5 (retreating side) for two different preheating conditions (by plasma current) i.e. 0 and 55 A at welding condition of 815 rpm, 98 mm/min welding speed and tool off-set of 2 mm. Without preheating, marginal temperature rise is observed (~ 5 K) in the aluminium side due to high thermal conductivity of copper. However, the maximum temperature in P-FSW welds acquired in the copper side is significantly higher than the aluminium side. The difference of maximum temperature in the copper side between P-FSW and FSW welds is approximately 313–383 K (40 - 110˚C). It is very likely that a very low welding temperature leads to some defects like channels and voids near the interface, especially in the Cu side. Adequate heat

generation during the welding process shows good mixing of both materials due to reduced thermo-plastic state temperature difference [205]. Additionally, it is observed that increasing the process temperature reportedly leads to considerable amount of copper particle diffusion to the aluminium side and increases the intermetallic compositions [303]. Further increase in process temperature results in formation of micro cracks due to decrease in solubility and formation of insoluble intermetallic compounds. Therefore an optimum temperature rise is desirable for dissimilar weld to obtain the maximum strength.

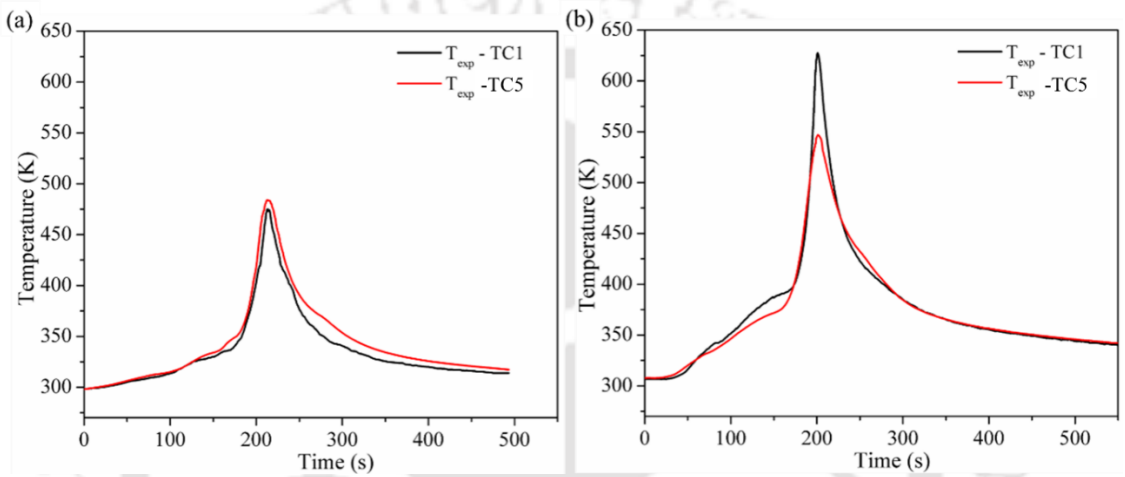

Figure 4.41. Thermal history at experimental condition of 815 rpm, 98 mm/min welding speed and 2 mm tool off-set - (a) without preheating and (b) with preheating current of 55 A.

There is a significant variation in the axial forces with the variation in preheating. The axial force during the welding process is much higher in case of zero preheating, as shown in **Fig. 4.42(a)**. It is observed that when 20-30% of pin length plunge into the workpiece, it reaches the first peak [304]. The heat generated by the pin due to frictional and plastic deformation makes the drop of axial force and afterwards rises again when the shoulder of the tool is plunged into the hard and cold workpiece. It is expected that the preheating of the workpiece would reduce the axial forces during dwell period but the temperature development is not optimum to soften both the materials. **Figure 4.42(b)** shows the variation of the axial force with preheating at constant rotational and translational speed. The variation of the axial force comparatively same as **Fig. 4.42(a)** during plunging phase. In dwell phase, the axial force drops due to additional heat input into the copper side from plasma arc. In welding phase

(tool travel), there is 30-35% reduction in axial force due to preheating which enhances the stirring action of relatively softer materials and may reduce the tool wear.

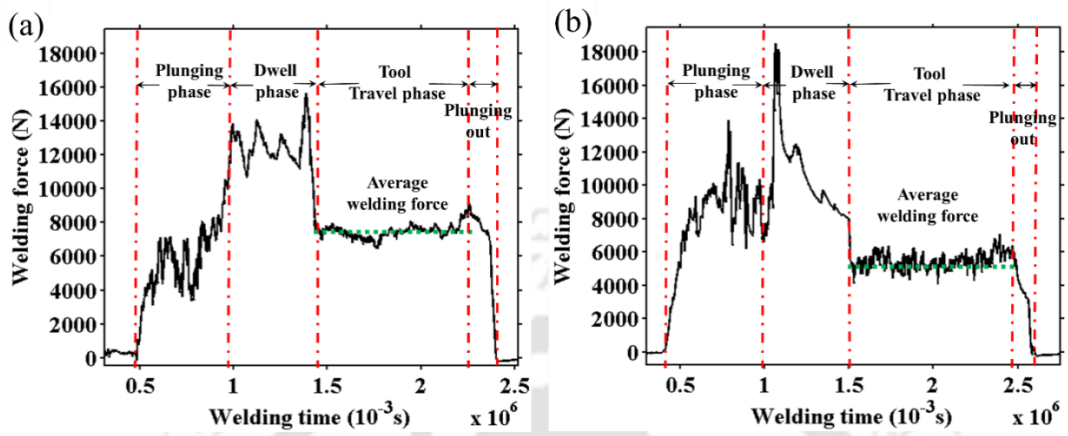

Figure 4.42. Variation of axial force at experimental condition of 815 rpm, 98 mm/min welding speed and 2 mm tool off-set - (a) without preheating and (b) with preheating of 55 A plasma current.

Figure 4.43 depicts the influence of different process parameters on difference in flow stress and temperature, and average welding force with respect to reference parameters of 815 rpm rotational speed, 98 mm/min welding speed, 55 A preheating current and 2 mm tool offset. It is more beneficial to maintain high temperature difference between TC1 and TC5 during dissimilar joint. With increase in temperature difference along with increase in preheating current reduces the flow stress (plasticized state) difference of two materials as shown in **Fig. 4.43(a)**. The average welding force reduces significantly with increase in preheating current. The tool offset does not produce any significant effect on average welding force (**Fig. 4.43b**). However, the optimum location of tool offset is significant to control intermetallic compound formation. **Fig. 4.43(b)** indicates that too much of tool offset is not beneficial since the peak temperature difference is minimum (or the flow stress difference is maximum) at tool off-set of 2.75 mm. The flow stress difference and the average welding force increases with increase in welding speed which may not be desirable for joining dissimilar materials. Hence the minimum welding speed is beneficial with reference to other welding parameters. The difference in flow stress as well as average welding force reduces with increase in rotational speed due to increase in heat deposition rate. Overall, the variation in flow stress value with respect to preheating current is more impactful as compared to

welding speed and rotational speed. Therefore, preheating current is more dominating factor to control the dissimilar weld joint for present set of parameters.

It is obvious from **Fig. 4.43** that the preheating current and tool rotational speed have great impact on average welding forces. The response of axial force is associated with plunge depth and is related to the physical contact between the tool and the workpiece. If the area of contact is more, the resulting axial force is more. Preheating provides additional heating to copper side which reduces the resistance for tool movement. Tool offset towards aluminium side reduces the welding force (**Fig. 4.43b**) as compared to high resistance at copper side. It is obvious that the location and intensity of preheating current to relatively harder material influences the variation of the axial forces in case of dissimilar P-FSW process [305]. Therefore, the sensitivity analysis of present set of welding parameters may be beneficial to find optimum domain of parameters to get successful weld joint for dissimilar materials using P-FSW process.

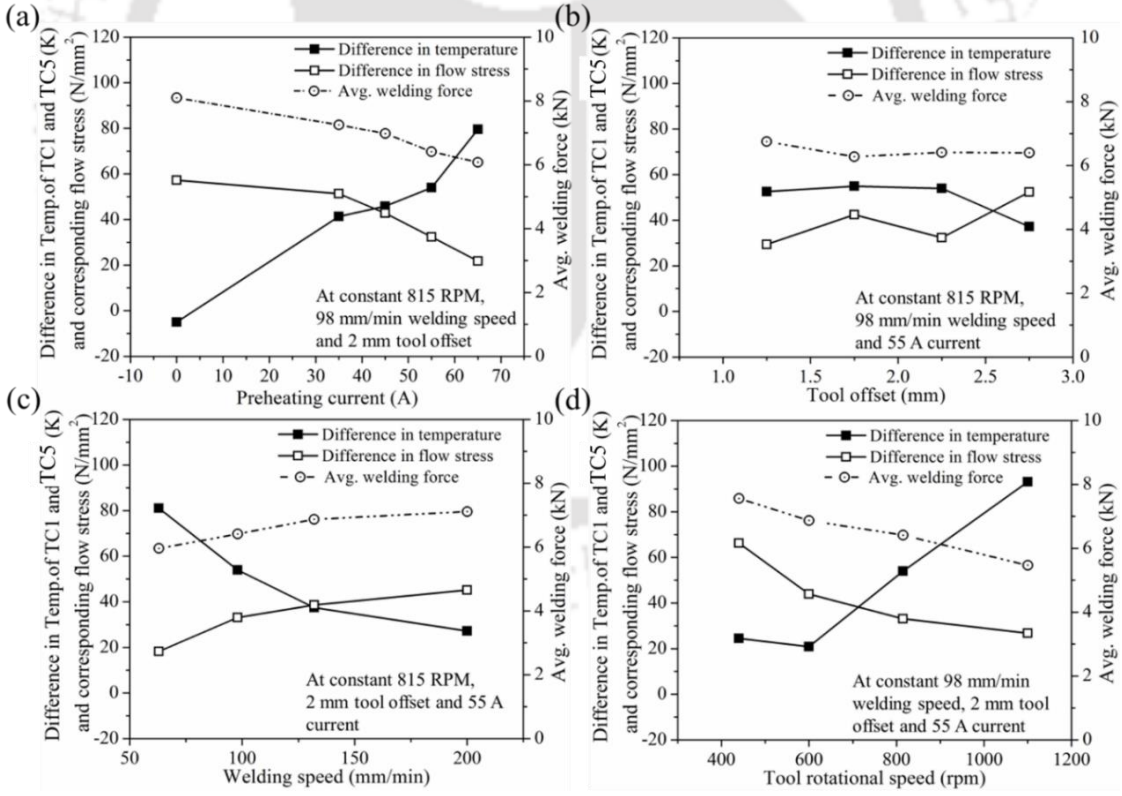

Figure 4.43. Difference in peak temperature and corresponding flow stress difference with average welding force for: (a) preheating current (b) tool offset (c) welding speed and (d) tool rotational speed.

Figure 4.44 shows that the tensile strength of welds under different preheating conditions at 815 rpm and 98 mm/min welding speed with 2 mm of tool offset as compared to base materials (Cu and Al). The ultimate tensile strength of 139 MPa in P-FSW weld is obtained at 55 A indicating about 95% of the base metal (Al alloy) and its elongation to fracture is 4.67% while the strength is 52% at zero preheating (~ 74.21 MPa) with elongation to fracture is only 1.8%. The maximum tensile strength of P-FSW weld is ~ 47% higher than zero preheating case under the same tool rotational speed and welding speed. Fracture in the tensile specimen of P-FSW weld occurs at the interface of two materials or at the nugget region of aluminium. It is thus obvious that the sufficient interaction of the material at the interface due to improved stirring action at the optimum temperature generated by preheating in copper side contribute significant improvement in elongation and joint strength [306].

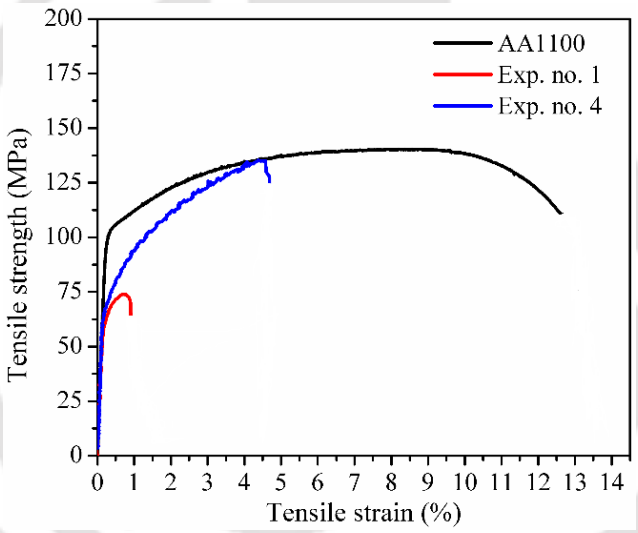

Figure 4.44. The stress-strain profile at welding condition of 2 mm tool offset, rotational speed of 815 rpm and 98 mm/min welding speed along with base materials.

Figure 4.45 depicts the tensile strength and elongation at different welding conditions corresponding to welding condition of **Table 4.12**. The tensile strength and elongation is improved due to preheating at copper side (**Fig. 4.45a**). Further increase in plasma current to 65 A promotes the formation of more brittle intermetallic compound that affects the elongation and joint strength. A large number of voids are observed without preheating due to lack of proper material flow caused by insufficient stirring and heat generation. However, the optimum joint strength is obtained at 55 A plasma current. **Figure 4.45(b)** reveals the fact

that the joints produced at 98 mm/min welding speed with preheating of 55 A exhibits lower tensile properties at ~ 400 – 600 rpm. Many defects in the nugget zone are identified within this range of rotational speed that is probably insufficient interaction between Cu bulk pieces and Al matrix. However, at higher rotational speed i.e. 815 ~ 1100 rpm, decent joint strength is achieved. At 1100 rpm, the increasing heat generation leads to higher amount of copper particles diffused to aluminium matrix and favours the formation of high amount of intermetallic compositions. This actually leads to formation of micro cracks and subsequently decreases the joint strength and elongation. There is formation of high amount of micro-cracks in the nugget zone below this welding speed whereas at higher welding speeds, the cavity defects are produced. All these defects reduce the tensile strength of dissimilar joint. In P-FSW the joint efficiency is defined with respect to the strength of aluminium base material. The maximum joint efficiency is achieved ~ 96% for optimum welding condition at 55 A plasma current, 815 rpm, 98 mm/min and 2 mm tool offset with reasonable yield strength and elongation of ~ 77.15 MPa and 7 % respectively. The lowest joint efficiency of 42 % is obtained at 400 rpm due to insufficient heat generation and improper mixing of dissimilar materials. However, preheating by plasma prevents the accumulation of a large amount of brittle intermetallic compounds in the weld zone. Literature indicates that the FSW of dissimilar materials produces poor weld joint using this traditional procedure and the pin offset towards softer material is usually adopted to achieve the defect-free joints [307-308]. **Figure 4.45(d)** illustrates that the tool offset at 2 mm produce optimum weld joint strength since the formation of intermetallic compounds as well as its distribution is well controlled at this welding condition. The maximum tensile strength is obtained at welding speed of 98 mm/min (**Fig. 4.45c**).

In P-FSW, the bending properties are tested to determine the flexural strength and ductility of the dissimilar joint as per ASTM E08 standard. The bending load of dissimilar joint is more than Al but less than copper in case of plasma current of 55 A. Bending load of 1023 N with 5.5 mm of extension is observed at 55 A preheating while 815 N compressive loads with 4.3 mm extension is observed is case of zero preheating. It is obvious from **Fig. 4.46(a)** that the bending strength of joint increases with increase in preheating current up to 55 A. Plasma current allows weld joint to bend at high angle that is due to increased plastic flow of the material and attributed to the sufficient interaction between two materials. When the

generation of temperature is not enough to soften the base material (Cu) at low plasma current or without any external heating, the materials are difficult to flow easily (get forged) due to lack of sufficient plasticized state and results in lesser bending load. Tool offset plays an important role on bending strength. The offset deviation from 2 mm in either side shows decrease in load (**Fig. 4.46b**). Literature indicates that 1.5 to 2 mm pin offset is preferred to achieve good quality dissimilar Cu–Al joint. However, the optimum tool pin offset assist in making good metallurgical bonding between copper particles and aluminium matrix at proper tool design and thickness of the workpiece [208, 309]. **Fig. 4.46(c)** and **(d)** illustrate that the bending load changes due to variation of heat generation at different welding speed and rotational speed. Decreasing the welding speed at constant rotational speed leads to similar trend of increasing the rotational speed at constant welding speed [205].

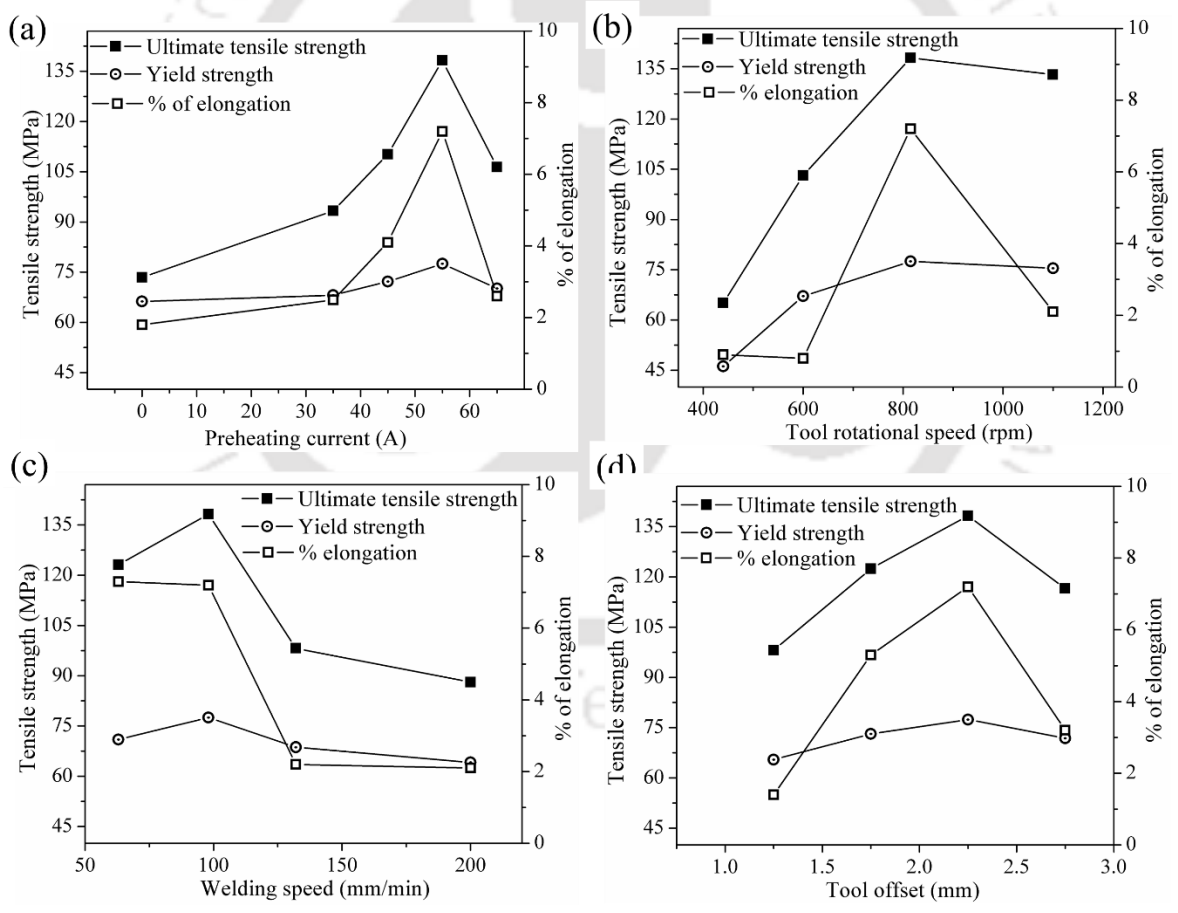

Figure 4.45. Comparison of tensile strength and percentage of elongation for: (a) preheating current (b) tool rotational speed (c) welding speed and (d) tool offset.

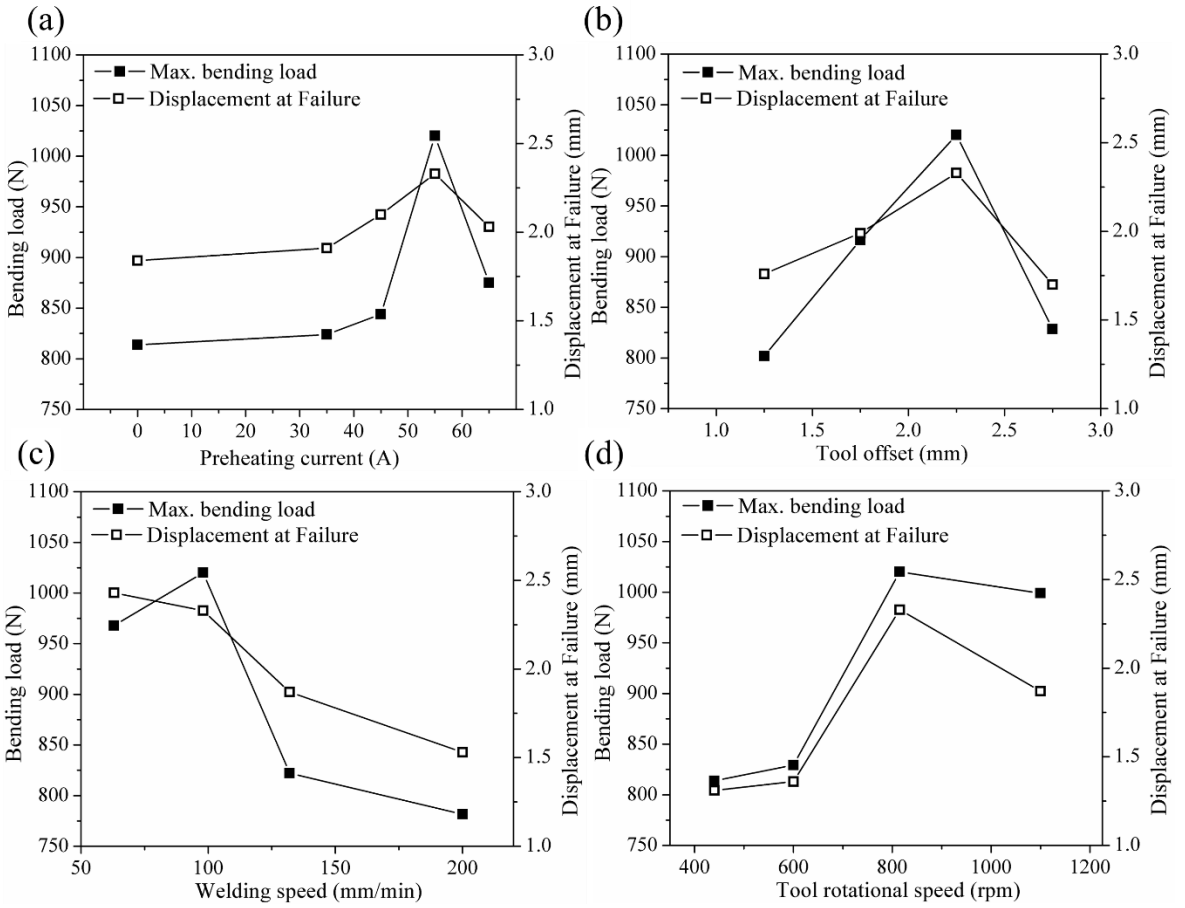

Figure 4.46. Comparison of bending strength and displacement at failure for: (a) preheating current (b) tool offset (c) welding speed and (d) tool rotational speed in **Table 4.12.**

Fig. 4.47 depicts the hardness profile at three distinct line of weld joint which is measured along the transverse cross section of the welded specimen. Approximately similar qualitative trend is observed in the hardness profiles at the HAZ and TMAZ except weld interface. The maximum value of hardness reaches to 137 HV at zero preheating current whereas it reaches to the maximum of 179.3 HV in case of 55 A preheating current. The intermetallic layer is very thin that appears like cold lap joint and there is no bonding of two materials. However, in the preheated weld (**Fig. 4.47b**), the hardness is higher at the interface which is attributed to the formation of intermetallic compound and their distribution caused by improved stirring at high temperature. An inhomogeneous distribution of hardness values is observed in the nugget zone. The higher hardness value in the nugget zone is primarily associated with the formation of very fine recrystallized grains and the Cu-rich dispersed particles.

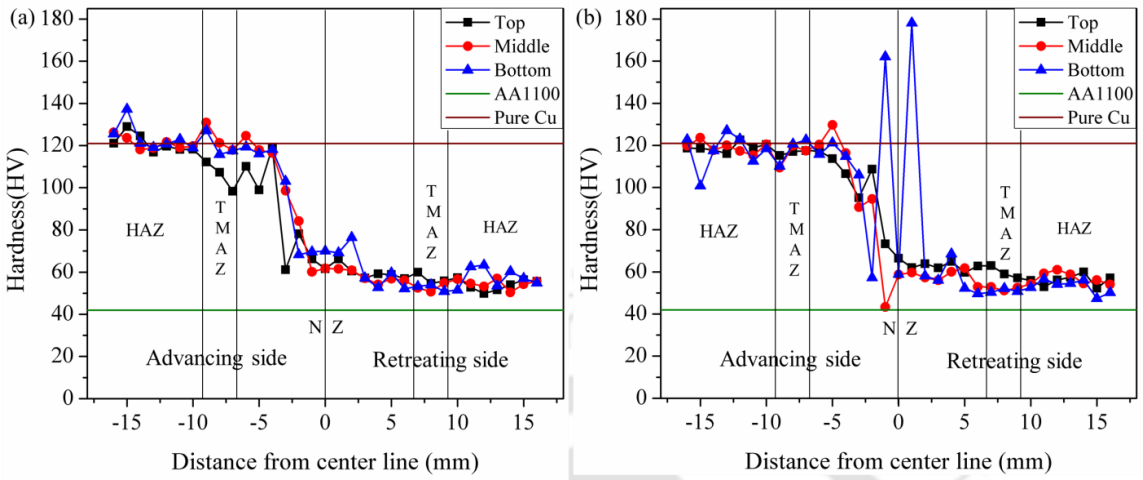

Figure 4.47. Hardness distributions on the transverse cross-section for: (a) without preheating and (b) with preheating of 55 A current at 2 mm of tool offset, 815 rpm and 98 mm/min welding speed.

Hardness distribution at the interface in dissimilar joint shows the interaction of two materials which is attributed to the joint quality viz. visualization of material flow and fraternization of two different materials. **Fig. 4.48** shows the variation of average hardness over the area marked by yellow colour in the figure. The area is defined at 4 mm on both side of tool pin centre line along the transverse cross section of the welded specimen. Temperature and material flow control the interaction of materials which also defines solubility of one material in other. Solubility of copper in aluminium is the maximum at 821 – 863 K (548 - 590˚C) with 5.8 weight % of copper [310]. It accredits the formation of the intermetallic compounds ($CuAl_2$, CuAl, Cu_9Al_4) due to high temperature associated with strong stirring of Al and Cu. These intermetallic compounds lead to hasty and inhomogeneous hardness distribution in the nugget zone. It is observed that average hardness in nugget zone is increased with increase in preheating current (**Fig. 4.48a**) that is credited to improved interaction caused by external heat input on harder material side and improved solid solution solubility of the material. Tool offset doesn't have much effect, but offset changes further from 2 mm (for 3 mm radii tool pin) decrease the interaction (**Fig. 4.48b**). **Fig. 4.48(c)** shows that the average hardness decreases with welding speed due to decrease in heat input whereas it increases with tool rotational speed (**Fig. 4.48d**) due to increase in heat generation.

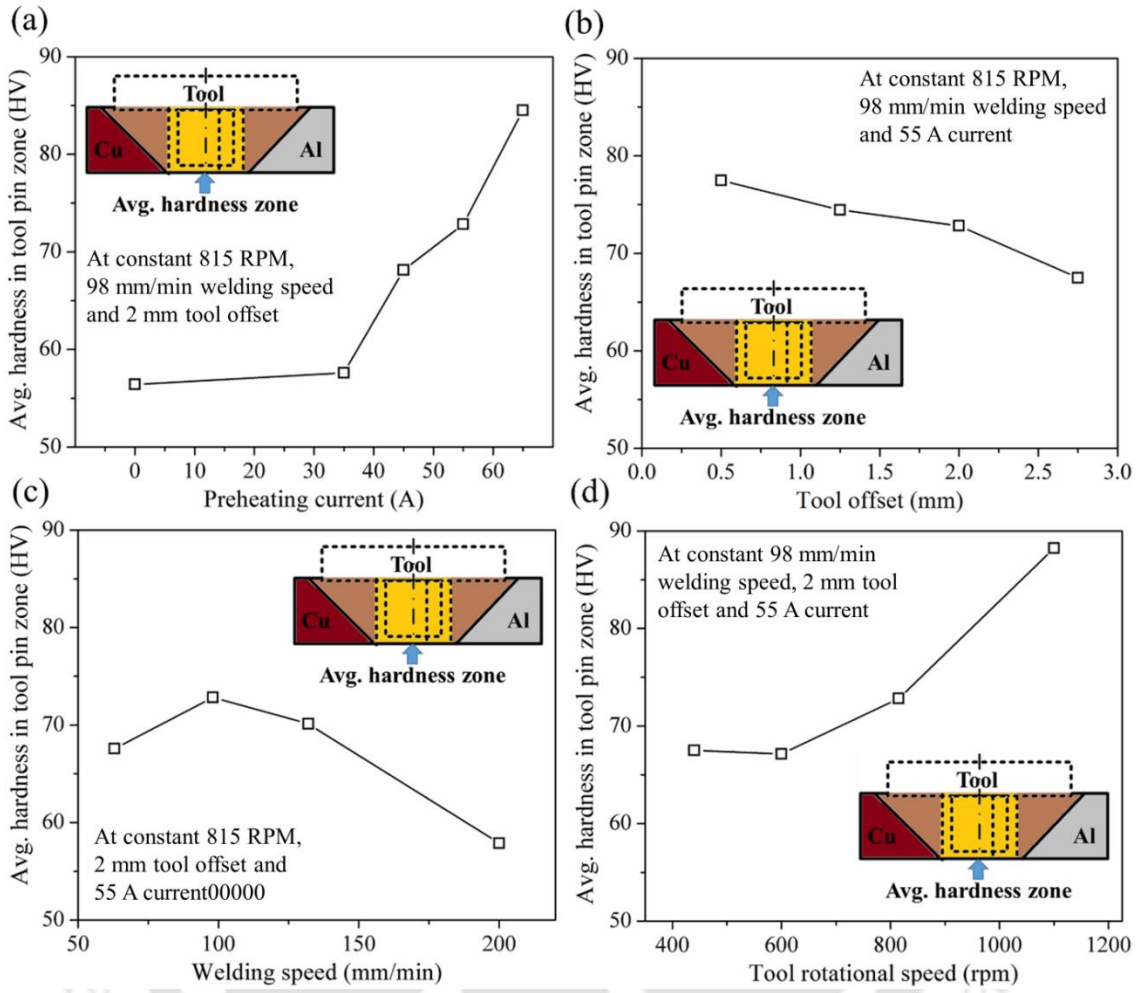

Figure 4.48. Average hardness distribution extend upto 4 mm on both side of tool pin centre line on the transverse cross section of welded specimen: (a) preheating current (b) tool offset (c) welding speed and (d) tool rotational speed.

To apprehend the variation in joint efficiency, the tensile fracture surface is analysed using SEM method**. Figure 4.49** shows the appearance of tensile fractured surface at 815 rpm, 98 mm/min welding speed and 2 mm offset. The patterns of tensile fracture surface shows locally layered flat surface with very few dimples. Therefore, this pattern indicates brittle fracture mode with some ductility. It's due to the lack of interaction caused by insufficient stirring and less amount of brittle intermetallic compound formation at the interface. On the other hand, features of brittle fracture mechanism like flat surface are observed in **Fig. 4.49(b).** This result indicates that there is sufficient plastic flow of material that improve material interaction and formation of intermetallic compounds. Layered flat surfaces can be clearly seen which

indicate that the brittle fracture mechanism is involved. However, layered flat surfaces have covered more region than the flat dimples on fractured surface. The fracture with very little plastic deformation before failure occurs is initiated from minor defects like voids, tunnel and cracks. The causes of these defects may be attributed to the generation of insoluble brittle intermetallic compounds. The presence of intermetallic phases such as Cu_9Al_4 and $CuAl_2$ were likely be present at different fractured locations that provides brittle fracture mechanism.

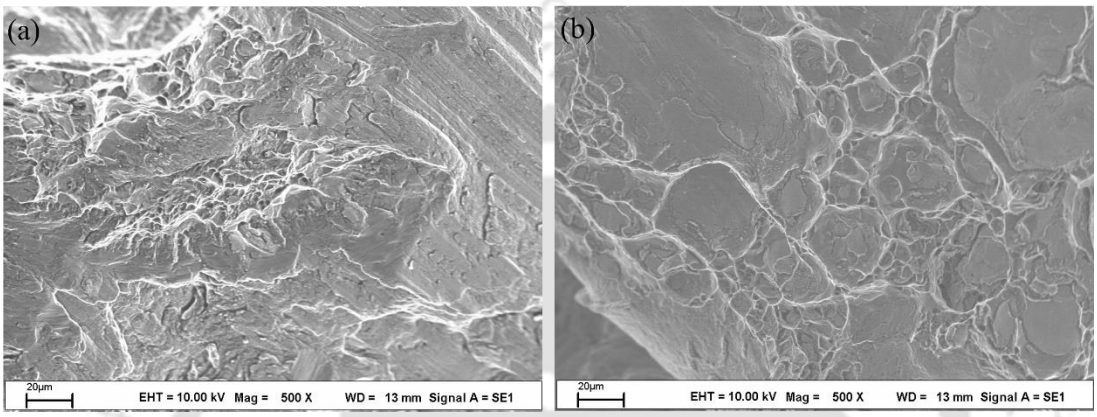

Figure 4.49. Fracture surface morphologies of joints at different welding condition: (a) without preheating and (b) with preheating of 55 A at 2 mm of tool offset, 815 rpm and 98 mm/min welding speed.

At different range of preheating condition, rotational speed and welding speed, the surface morphology of the welds are produced without causing any surface defects except few cases where welds are obtained without preheating and low rotational speed. **Figure 4.50 and 4.51** shows the cross-section and crown appearance of the weld joints. The un-welded zone at the bottom region of the weld interface due to the insufficient plasticization caused by lack of heat generation in copper side is obvious. The stirred zone cross-section reveals some voids during mixture of aluminium alloy and coarse copper particles scattered away from the copper surface by the stirring action of the tool pin. Few dispersed copper particles at retreating side are induced to deteriorate the joint strength of the weld. The cracks are initiated from these copper particles scattered in the weld nugget. Also the un-welded zone acts as the cracking initiate source and degrades the tensile strength of weld during tensile test [205]. **Figure 4.50 and 4.51** shows good weld joint using preheating by plasma where no dispersed copper particles in the weld are observed. However, at tool rotational speed over 815 rpm, dispersed fine copper particles is observed due to the sufficient plasticization of copper by preheating

resulting from almost equally distributed temperature both in aluminium and copper side [311].

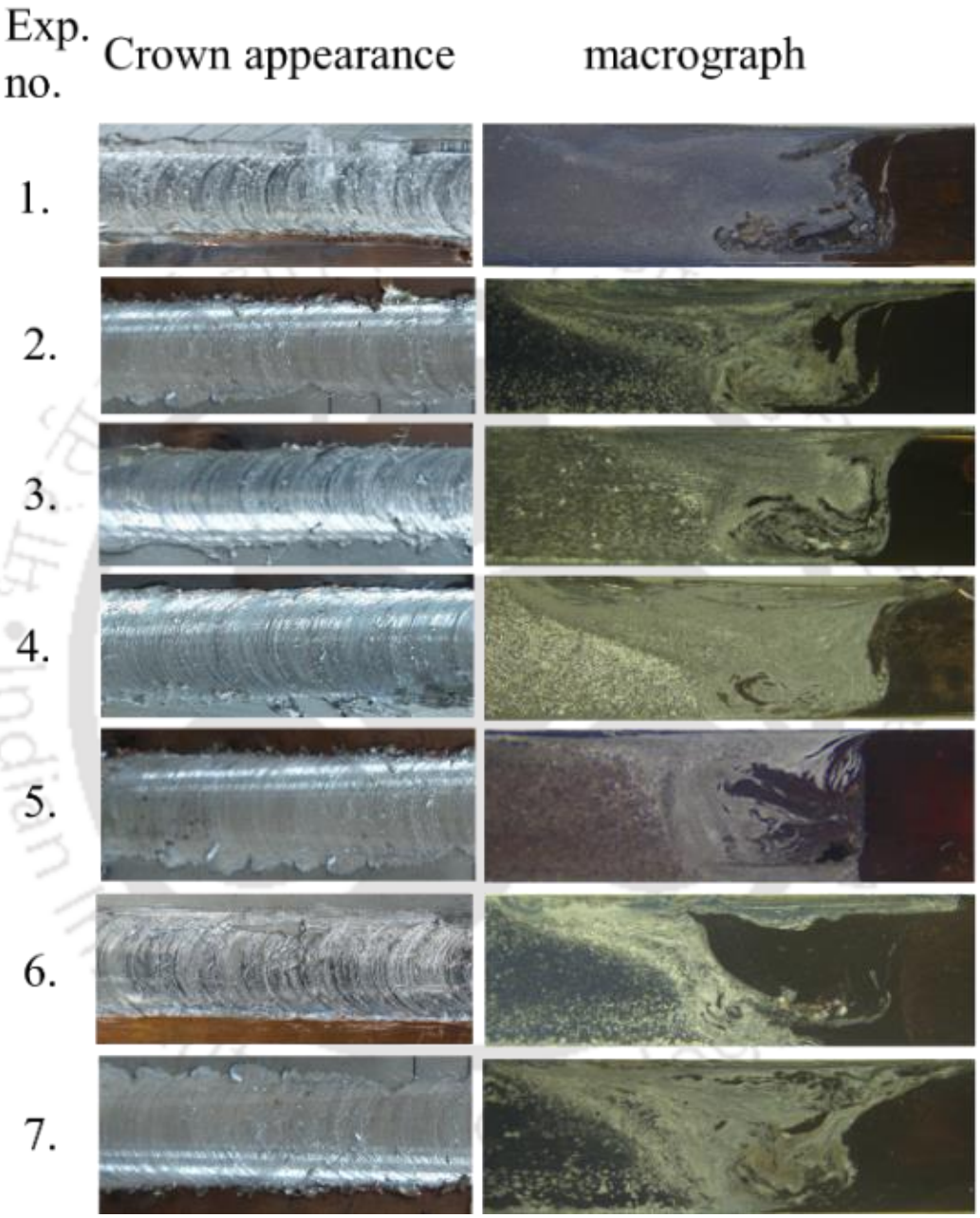

Figure 4.50. Crown appearance and macrograph of weld joint corresponding to welding conditions of **Table 4.14** from Exp. 1 to Exp. 7.

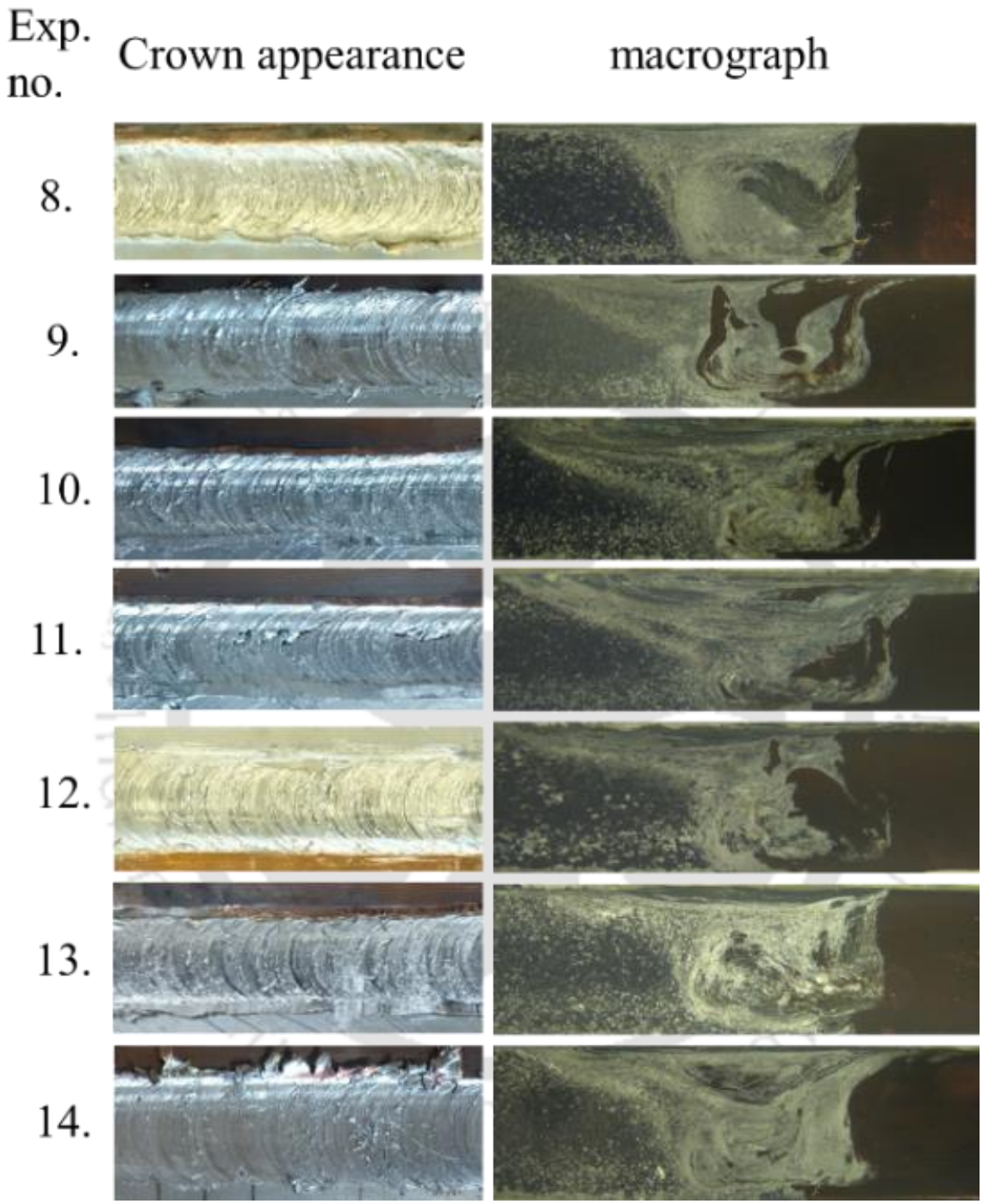

Figure 4.51. Crown appearance and macrograph of weld joint corresponding to welding conditions of **Table 4.14** from Exp. 8 to Exp. 14.

Figure 4.52 shows the macrostructure of the distinct regions of nugget zone and the flow pattern at welding condition of 815 rpm and 98 mm/min speed. The nugget zone consists of a

mixture of the aluminium matrix and Cu particles. At comparatively low temperature, the defects like voids and channels along with weak interface bond are observed (**Fig. 4.52a**). **Figure 4.52(b)** indicates that the distribution of the Cu particles with irregular shapes and various sizes is inhomogeneous in the nugget zone. The presence of the copper particles in the aluminium matrix attributes to the stirring action of the tool pin that worn out the Cu pieces from the bulk copper, breaks up and scattered them during the FSW process (**Fig. 4.52c**). Under low heat input condition, no important mixing patterns are found in the nugget zone. The formation of interface morphology performed in friction diffusion bonding is observed here [312].

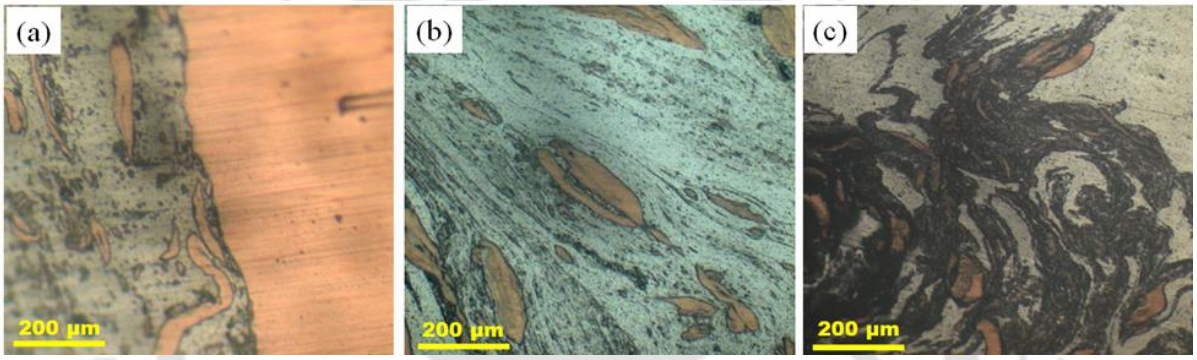

Figure 4.52. Material flow pattern and types of bond formation during welding at 2 mm of tool offset, 815 rpm and 98 mm/min welding speed and without any preheating in the weld nugget zone.

Figure 4.53 shows the flow pattern at the cross-section which indicates good mixing of both the materials due to adequate heat input during welding. By increasing the heat input, increased amount of both Cu and $CuAl_2$ are dragged by the shoulder into the inner shear layer surrounding the pin where chemical and thermo-mechanical conditions for the formation of Cu_9Al_4 exist (**Fig. 4.53a, b**). All these intermetallic formation is confirmed by EDX analysis of the weld sample. **Figure 4.53(c)** and **(d)** indicates that the shear layer dimension depends on heat input and stirring of tool while the upper aluminium layer tends to disappear. However, the optimum ultimate strength of the weld joint is achieved from a proper material flow and metallurgical bonding through a narrow intermetallic layer at the interface in addition to the occurrence of lamellar composite structure in the stirred zone [312].

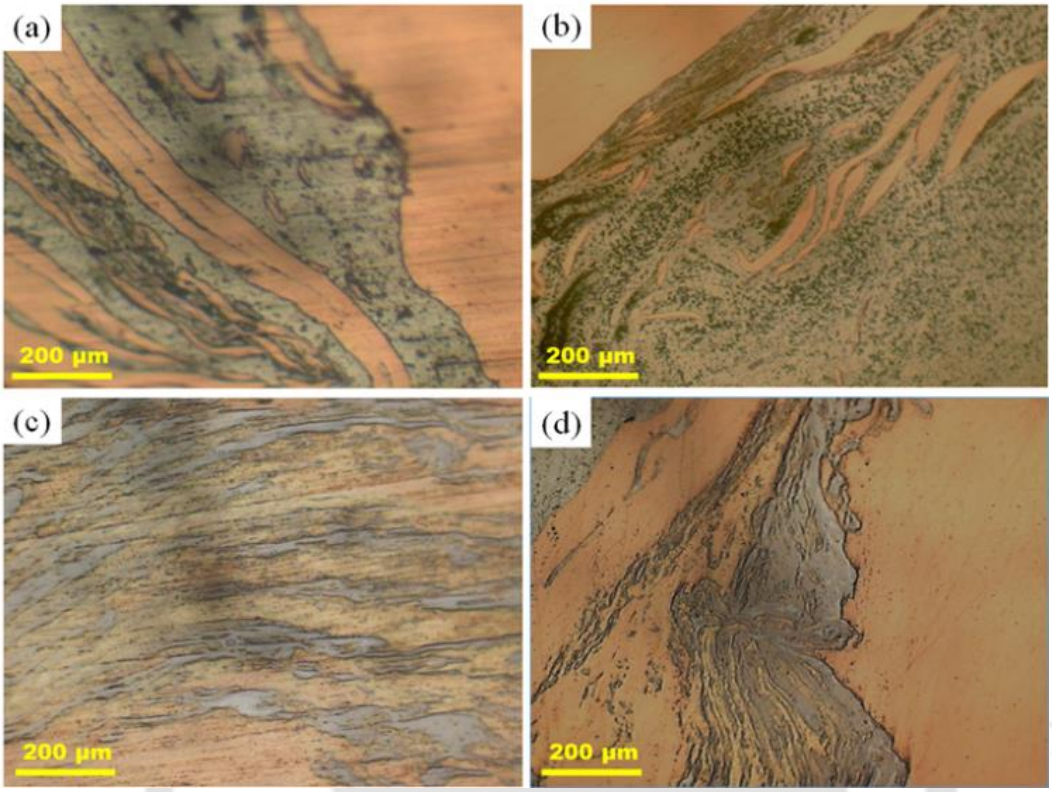

Figure 4.53. The material flow pattern in the weld nugget zone at welding condition of 55 A preheating current, 2 mm of tool offset, 815 rpm and 98 mm/min welding speed.

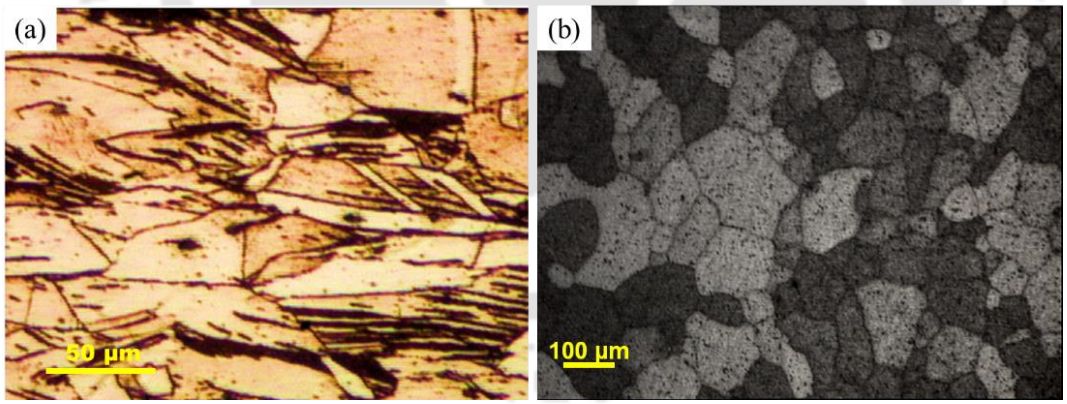

Figure 4.54. Microstructure of base material (a) copper and (b) aluminium.

Figure 4.54 shows the microstructure of the base materials like pure copper and aluminium alloy, respectively. The aluminium has annular type structure whereas copper has elongated type structure. Average grain size of pure copper is ~38 µm and aluminium alloy is 98.72 µm. **Figure 4.55(a)** shows the distinct regions of weld without any preheating at welding condition of 815 rpm and 98 mm/min welding speed with 2 mm of tool offset. **Figure**

4.55(b) shows the microstructure of the HAZ in the Al alloy at retreating side that is slightly coarse but very similar structure to the base material. The grains of Al alloy in the TMAZ (**Fig. 4.55c**), at retreating side are fine and elongated differently in the rolling direction. The average grain size in the nugget zone is decrease to 17.1 μm (~ 19-20 % of base aluminium alloy). In weld nugget zone (**Fig. 4.55e**), the discontinuous copper particles scattered at the interface due to insufficient plasticization of copper. These fragments of copper are distributed randomly in the aluminium substrate near the interface with various sizes and structures. **Figure 4.55(f)** and **(g)** illustrations microstructure of TMAZ and HAZ of copper respectively which are similar to base material due to low process temperature and lesser degree of plastic deformation for copper.

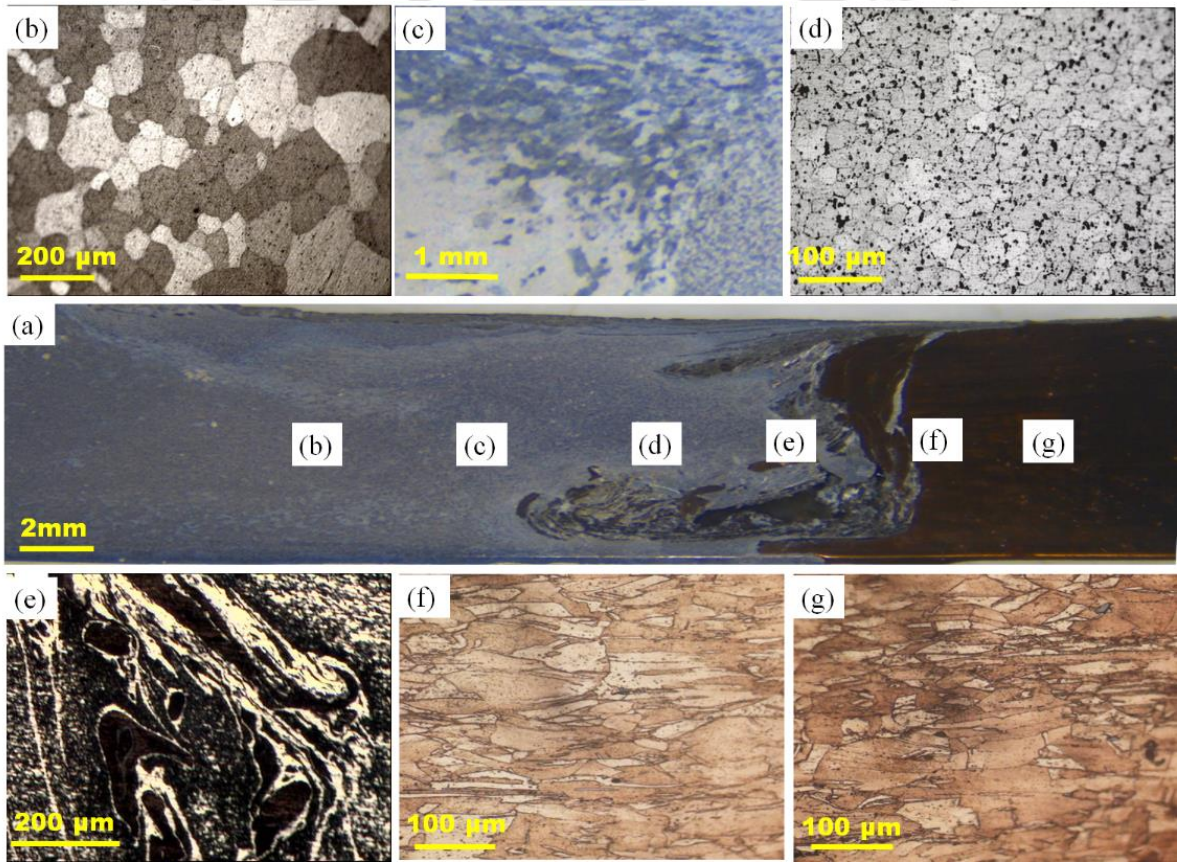

Figure 4.55. Microstructures of different zone at welding condition of 2 mm of tool offset, 815 rpm, 98 mm/min welding speed and without any preheating: (a) macrograph of weld zone, (b) HAZ in the aluminium side, (C) TMAZ in the aluminium side, (d) SZ in the aluminium side, (e) SZ in the copper side, (f) TMAZ in copper side and (g) HAZ in the copper side.

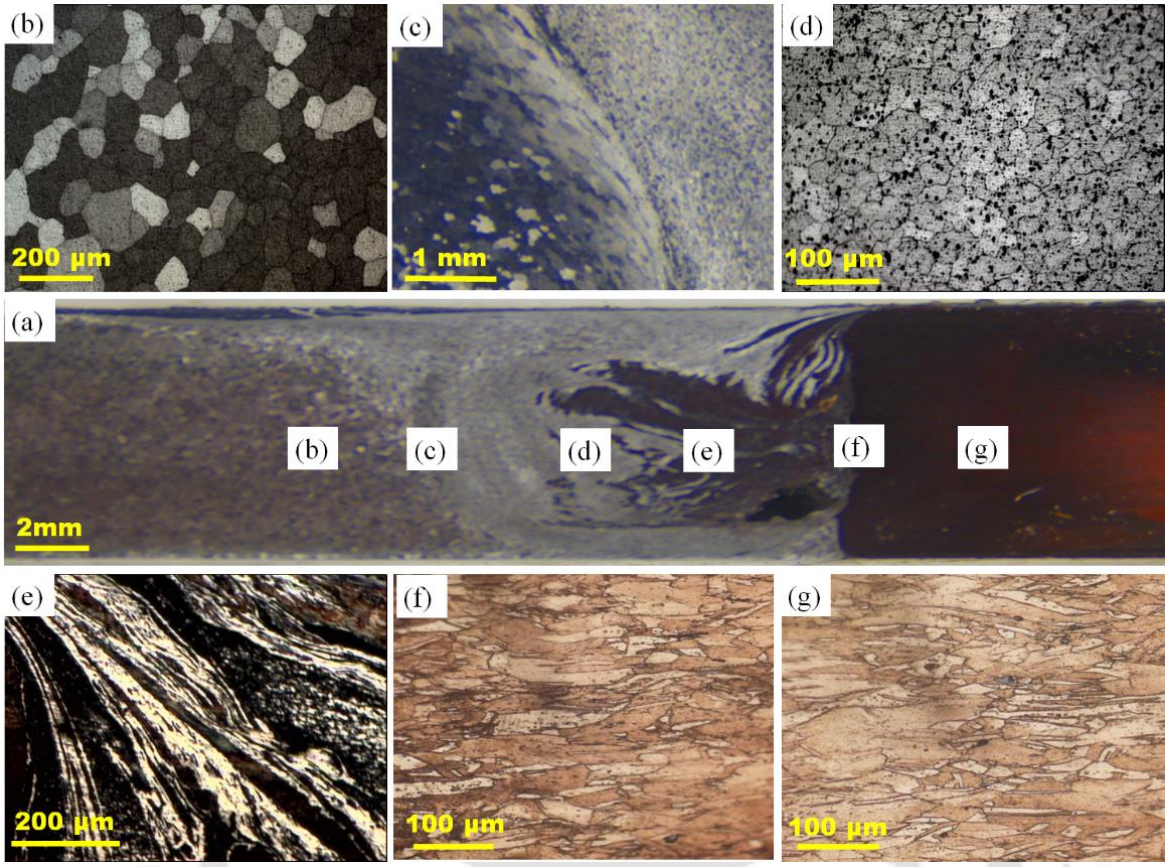

Figure 4.56. Microstructures of different zone at welding condition of 2 mm of tool offset, 815 rpm, 98 mm/min welding speed and with preheating current of 55 A: (a) macrograph of weld zone, (b) HAZ in the aluminium side, (C) TMAZ in the aluminium side, (d) SZ in the aluminium side, (e) SZ in the copper side, (f) TMAZ in copper side and (g) HAZ in the copper side.

Figure 4.56 illustrates the microstructures of distinct regions of weld zone at 815 rpm and 98 mm/min welding speed with 2 mm of tool offset and 55 A preheating current. Microstructural evaluation of the joint interfaces showed good mixing of both materials due to adequate heat input into the weld during the welding process. The microstructure of the HAZ in the Al alloy at retreating side showed slightly coarse but very similar structure to the base metal (**Fig. 4.56b**). The grains of Al alloy in the TMAZ (**Fig. 4.56c**), at retreating side are slightly fine and elongated due to the mechanical stirring by tool shoulder [313]. It is observed from **Fig. 4.56 (d)** that the average grain size in the stirred zone is finer (~88 % decrease) at retreating side than base metal (Al). This grain refinement during FSW process

leads to greater hardness in the stir zone in comparison with base metal. The weld nugget has a composite structure of slightly finer recrystallized grains of aluminium alloy and the copper particles scattered away which shows fully mixed structure at interface between aluminium and copper [207]. **Figure 4.56 (e)** indicates a continuous intermetallic layer in Al-Cu interface and is different from **Fig. 4.56(e).** As shown in **Fig. 4.56(f)**, little elongated grains are observed due to improvement in plastic flow of the material but similar to base material (Cu). **Figure 4.56(g)** illustrate microstructure of HAZ (Cu side) similar to base material that is not affected by low peak temperature for copper.

Figure 4.57 shows the intermetallic compound layer formed at the interface between Al and Cu in weld nugget zone. The thickness and continuity of intermetallic layer depends on the temperature and flow of material for joining of dissimilar materials. Weld made without any external heating or low preheating, the intermetallic layers at the interface are mostly non-uniform and there are some areas at the interface which are not having completely metallurgical bond similar to a cold lap defect [314] as illustrated in **Fig. 4.57(a)**. A thin continuous intermetallic layer with laminate structure is observed at the interface in case of sufficient preheating by plasma arc. This type of laminated structure between Cu and Cu–Al intermetallic layer has been observed in previous studies during lap welding of dissimilar metals [210-315]. It is thus obvious from the characterization of the interface for dissimilar weld that the good quality weld is obtained by the hook-like feature and metallurgical bond (evidenced by intermetallic and laminate structures of Cu and Cu–Al at the interface) with optimum preheating and tool off-set condition.

The presence of intermetallic compounds in the weld joint is evaluated by X-ray diffraction (XRD) analysis of the nugget zone and is illustrated in **Fig. 4.58**. The XRD analysis detected that Al_2Cu, CuAl, and Cu_9Al_4 intermetallic phases are formed at the bond interface of the joint. The effect of preheating has also been investigated with the growth of intermetallic compounds. It is clarified that the apparent activation energy for growth behaviour of CuAl and Cu_9Al_4 is lower than $CuAl_2$. Preheating affects the thickness of $CuAl_2$ and bond strength of aluminium-copper joint. However, the intermetallic compound formed has a dual effect i.e. strengthening in very thin layer but lead to brittle behaviour in thick layer [316]. From XRD analysis (**Fig. 4.58**), the weld nugget contains $CuAl_2$ intermetallic

compounds that is observed for preheating case and provides sufficient reason for the strength of this zone. These intermetallic compounds are found as continuous non-linear layer in the Al side and worked as dispersed particles which provide a reinforcing effect in this zone.

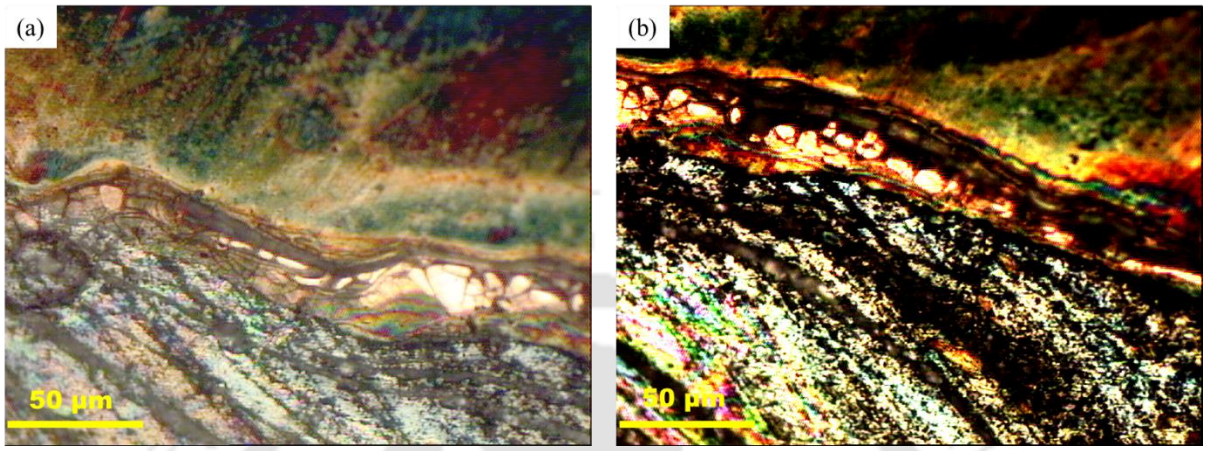

Figure 4.57. Microscope images of intermetallic layer for different preheating conditions: (a) without preheating and (b) with preheating current of 55 A at 2 mm of tool offset, 815 rpm and 98 mm/min welding speed.

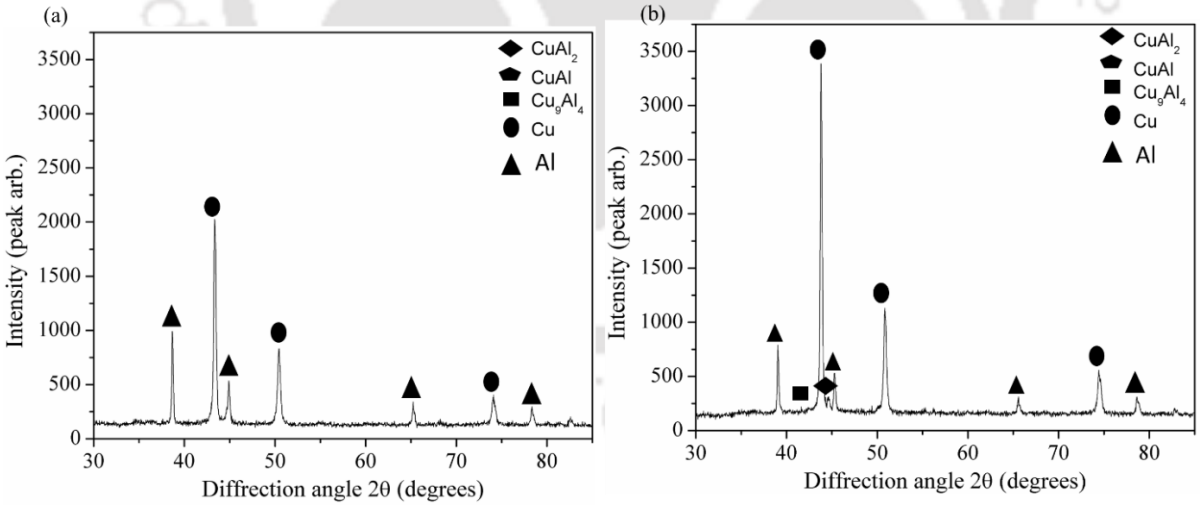

Figure 4.58. XRD patterns of dissimilar aluminium 1100 and pure copper welds at transverse sections: (a) without preheating and (b) with preheating of 55 A at welding conditions of 2 mm of tool offset, 815 rpm and 98 mm/min speed.

Different intermetallic compounds are formed in distinct region of weld zone under the influence of high temperature and plastic deformation. **Figure 4.59** shows XRD patterns of weld zone to distinguish intermetallic compounds at three different cross sectional locations that are at 4 mm away from the weld centre-line. More intensities peak of aluminium and copper are detected with less predominate intermetallic compound peaks. Thus, the emergence of the corresponding intermetallic compounds and their location and quantity depends on inter-diffusion through extreme deformation and intense stirring under preheating temperature (which is less without any preheating). **Figure 4.59(b)** is associated with the strong stirring action of tool pin with improved mixing of Al and Cu at higher temperature than zero preheating. Therefore, the formation of intermetallic compounds $CuAl_2$, CuAl, and Cu_9Al_4 is more predominant in preheating condition. Moreover, XRD analysis revealed the existence of distinct characteristic diffraction peaks of Al_2Cu and Al_4Cu_9. Therefore, it is clear that Al_2Cu and Al_4Cu_9 were generated around the larger Cu particles and there growth rate is determined by inter-diffusion through extreme deformation and intense stirring which is effected by preheating.

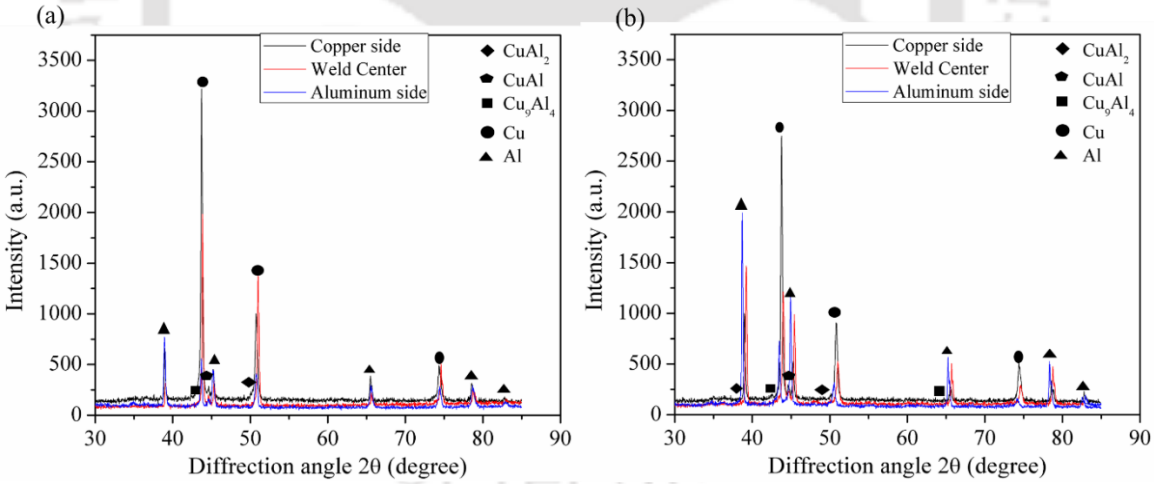

Figure 4.59. XRD pattern of dissimilar joint at three different longitudinal sections of 4 mm from the weld centre-line to both copper and aluminium side and the weld centre-line: (a) without preheating and (b) with preheating of 55 A at 2 mm of tool offset, 815 rpm and 98 mm/min welding speed.

4.3 Experimental data taken from literature

Song and Kovacevic [31] were conducted FSW experiment to find out thermal history and weld zone microstructure of aluminum 6061/T6 plate with 12.7 mm thick. The diameter of the tool shoulder was 50 mm and the diameter of the tool pin was 12 mm. The tool rotational speeds were 344, 637 and 914 rpm and welding speed was 95 mm/min. Eight K-type thermocouples were embedded in the workpiece to measure the temperature history. The locations of measuring points 1, 2, 3 and 4 were 2.0 mm beneath the upper surface and 8, 12, 16 and 25 mm from the joint line respectively. **Figure 4.60** shows the measured thermal history of the points 1, 2, 3 and 4 at rotational speed of 637 rpm and welding speed of 95 mm/min. It's found that the measured temperature peaks at points 1, 2 and 3 at all rotational speeds was close to the material melting point (855 K). All these measuring points were 2.0 mm beneath the tool shoulder/workpiece interface so, the peak temperature was expected to be even higher at the tool shoulder/workpiece interface.

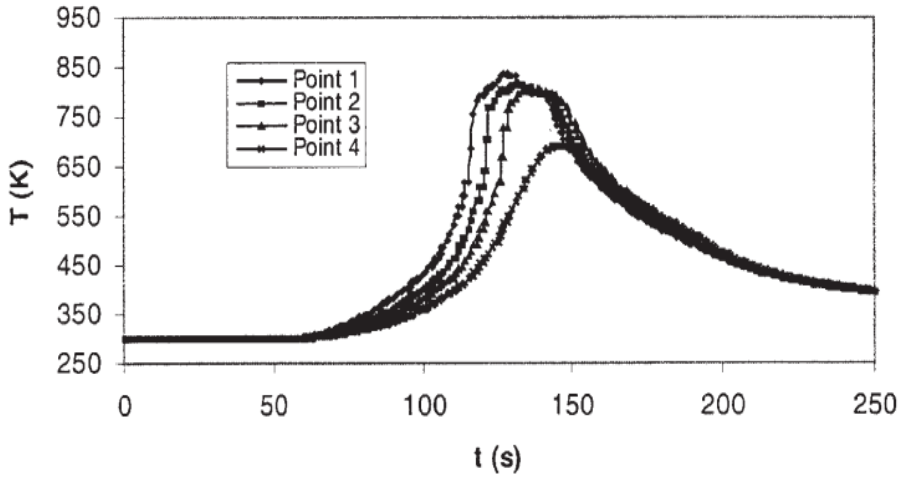

Figure 4.60. Experimental thermal history of weld joint at rotational speeds of 637 rpm and welding speed is 95 mm/min [31].

Figure 4.61 shows typical FSW microstructural morphology consists of the weld nugget, the thermal-mechanical-affected zone (TMAZ), the heat-affected zone (HAZ) and the base material at rotational speed of 637 rpm and welding speed of 1.59 mm/s. The microstructure morphology of weld zone is related to the local thermal history measured during welding.

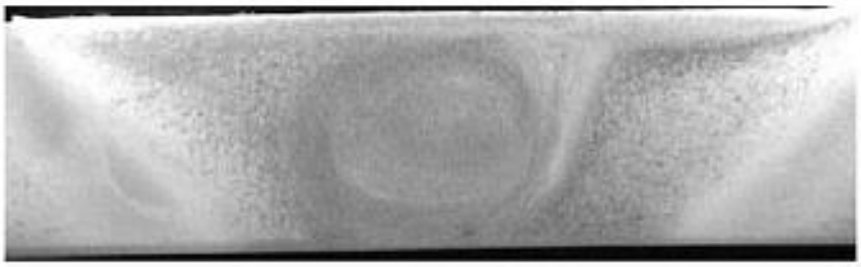

Figure 4.61. FSW microstructural morphology consists of the weld nugget, the thermal-mechanical-affected zone (TMAZ), the heat-affected zone (HAZ) and the base material [31].

4.4 Summary

The work presented in this chapter focuses on experimental investigation of conventional FSW and P-FSW conducted on an indigenously developed FSW setup. Initial investigation is conducted to study the transient thermal history during FSW. It is observed from experiments that the temperature on advancing side close to the weld centre line is higher than corresponding location of the retreating side. This temperature difference is due to dragging of material (hot and plasticized) by the shoulder from the retreating side of the weld around the rear of the tool and deposited on the advancing side. Thereafter, evaluate the effect of six different tool pin profiles on the mechanical and microstructural properties of friction stir welded aluminum alloy butt joints. FSW tools having fixed shoulder diameter, pin tip diameter and pin length with six different pin profiles namely, straight cylindrical, taper cylindrical, cylindrical with v-thread and square thread and tapered cylindrical with v-thread and square thread were experimented at three different welding speeds. From this investigation it is found that tool geometry has a great influence on resulting mechanical properties of the weld. It provides intense heating, stirs base material, and thus creates weld. FSW can be performed with tool of a simple geometry yet having good mechanical properties. Threaded tool design provides intensified material flow in the stirred zone and better weld quality.

The primary deed of the present work lies in the development and investigation of a P-FSW setup is presented in this chapter. This setup is capable of measuring welding force and thermal history during welding process and has fixture to introduce additional preheating source (plasma torch) ahead of FSW tool. Introduction of additional heat source along with

conventional FSW tool (principal process) to preheat the material ahead of FSW tool to improve joining efficiency of FSW. A comparative study of mechanical and macro-microstructural characterizations of weld joint by FSW and P-FSW has been performed. The effect of preheating enhances material flow and dissolution of fine oxide particles by plasma arc results in increase of strength and marginal modification of deformation behavior. Overall, the influence of preheating acts quite homogeneously throughout the structure as compared to conventional FSW during joining aluminum alloy. Thereafter, the plasma assisted friction stir welding is used to join aluminum alloy AA1100 to pure copper. The copper side is preheat up to 500 K with optimum location of plasma arc and less mechanical energy is delivered by the tool that converted into heat. Preheating temperature can make up the lost heat due to high thermal conductivity of copper and improves the material flow during the FSW process. The investigation indicates that P-FSW with optimum offset of preheating source towards copper side not only improves the joining efficiency; but also provides high quality defect-free weld over a range of process parameters.

Chapter 5

Results and Discussion

5.0 Introduction

This chapter presents primarily the computed results of temperature distribution in conventional FSW and hybrid FSW processes as obtained from finite element based thermal model developed in the present work. The computed thermal history in the weld zone and its surrounding area are used next to calculate the evolution of cooling rate that are significant to predict final microstructure and mechanical properties of the similar and dissimilar weld joint. The calculated results from the heat transfer model were validated with corresponding experimental results using in-house developed set-up.

The selection of solution domain, calibration of numerical model, computational aspects and temperature dependent material properties are envisaged as preliminary work towards the development of numerical model. Thereafter, a comparative study among the computed results from different heat generation models are presented with annexation of various welding process conditions and parameters. The heat transfer analysis includes geometrical, kinematic and physical phenomena of heat generation during FSW and hybrid FSW processes. It also recognizes the dominant parameters that affects heat generation process and uses them to estimate how much mechanical power is transformed into heat. The result of temperature distribution and computed macrograph is validated with literature as well as experimental data. Subsequently, the result of analytical model is presented that can predict the strain rate distribution and the deformation zone in the friction stir weld zone as a function of process parameters. The result of strain-rate and strain are incorporated by analytical models of CDRX phenomena to predict average grain size in weld zone with the effect of preheating condition by plasma arc. Finally, heat transfer model for hybrid FSW incorporates the additional heat source which is applied for joining similar and dissimilar

materials along with predefined tool offset. The calculated thermal cycles in and around the tool are utilized to estimate the evolution of cooling rate. Further validation of cooling rate and influence of it on microstructure of weld joint is reported in this work.

5.1 Observation from experimental investigation

As welding is mainly governed by the method of heat transfer between heat source and work piece, it is essential to understand the process through a mathematical system of equations and their solutions to develop a reliable heat transfer model. The experimental study of heat transfer mechanism provides useful information about thermo-mechanical heat generation phenomena during the process and the consequent effect of microstructural development. With this objective, the detail experimental investigations are reported in **Chapter 4**. Hence, the summary of the experimental observations are presented to facilitate the development of phenomenological model and their consequent effect on numerical results. The investigation on transient temperature at several specific locations was used for checking the temperature field gained by numerical simulation. The temperature measurement by thermocouples indicates that there is an obvious asymmetric temperature distribution between the advancing side (AS) and the retreating side (RS). As the tool moves away from the center-line, the temperature difference is reduced and reaches equilibrium at certain distance due to similar rate of heat diffusion. Asymmetry in temperature distribution is due to the differential heat generation and difference in relative velocity between AS and RS. It is also observed that as tool rotational speed increases, heat generation rate increases whereas increase in surface area of pin promotes (threaded pin) the heat generation rate and these phenomena are obvious by the nature of the peak temperature. The recovery, recrystallization and grain growth kinetics depend mainly on the temperature and strain rate, and the microstructure evolution is influenced by the energy transfer within the system.

The controlled energy input into the system by introducing an extra heat source to enhance the material flow along with reduction of the plunging force remains a potential area of considerate for the development of hybrid friction stir welding (FSW) process. In case of P-FSW, the material around the tool in case of preheating becomes much more plasticized than the case of without preheating. This additional heat input due to plasma arc makes an effect on rate of change of temperature during welding that improve the weld joint

properties. The temperature is ~20-50 K higher in case of preheating by plasma arc for joining similar materials. However, tool rotation and welding speed influences more on heat generation rate than the preheating for this range of welding parameters. With the application of external heat source, the plunging force reduces significantly ~ 22 to 28 %. The location and intensity of preheating source in relatively harder material influences the variation of the thermal history in case of P-FSW process for dissimilar materials (Cu-Al). The Maximum temperature obtained in copper side at the nearest thermocouple location is ~316 –378 K higher than the aluminium side that aims to reduce the difference in plasticized state temperature. It is beneficial to increase the temperature of the harder workpiece in front of the tool pin during dissimilar material joint, making the material easy to be welded, and possibly reduces tool wear due to difference in flow stress value. The difference of flow stress between copper and aluminium ~ 60 MPa without any preheating is reduces to ~ 10 MPa with optimum preheating condition and tool offset. This actually facilitates the improved stirring action of material by FSW tool and enhances the weldability between copper and aluminium. The grain size in nugget zone is accredited by combined effect of peak temperature and strain rate as compared to low cooling rate in FSW. The microstructural study for dissimilar joint between aluminium and copper indicates that the stir zone consists of typically functionally graded materials.

5.2 Numerical model and material properties

Numerical study of heat generation and heat transfer during FSW is important criteria to apprehend a highly complex process comprising several coupled physical phenomena. However, heat transport process in FSW requires understanding several other physical processes such as material flow around the welding tool, contact pressure inflicted by the welding tool, the friction coefficient, wear, change of thermo-mechanical properties and heat transfer coefficients etc. Numerical analysis includes the effect of all these parameters to evaluate heat transfer during welding whereas the reliability of numerical model is greatly depends on temperature dependent material properties, optimum mesh size and other calibrated model parameters. The present section describes the model geometry; mesh size selection, time step and load step selection for the development of numerical

model. Thereafter, the thermal and mechanical properties of aluminum and copper are described which has considered in the present work.

5.2.1 Model geometry

The heat transfer analysis of the FSW and P-FSW process is performed using commercial software ABAQUS. The solution domain of the model is assumed as rectangular plate. The element of workpiece domain is meshed using eight-nodded brick element of type DCC3D8. The temperature is considered as single degree of freedom at each node with fine meshing in the weld zone. The size of the welding plate for the simulation is considered as same as experimental condition. The welded workpiece have dimensions 200 mm length and 200 mm width, while the thickness of the workpiece is 6 mm. In the present work, non-uniform meshes are used and shown in **Fig. 5.1**. The finer mesh is considered near and along the weld center line to capture high temperature gradient of the simulated results and the mesh size increases for rest of the zone in order to reduce the computational time. However, in case of dissimilar joint the solution domain is partition in three section and each section assigned different material properties. The weld zone is designed as functionally graded material. Other two sections are assigned with thermal properties of copper (advancing side) and aluminum (retreating side). In this case, the model geometry and type of mesh and size is similar to **Fig. 5.1** except weld zone material property.

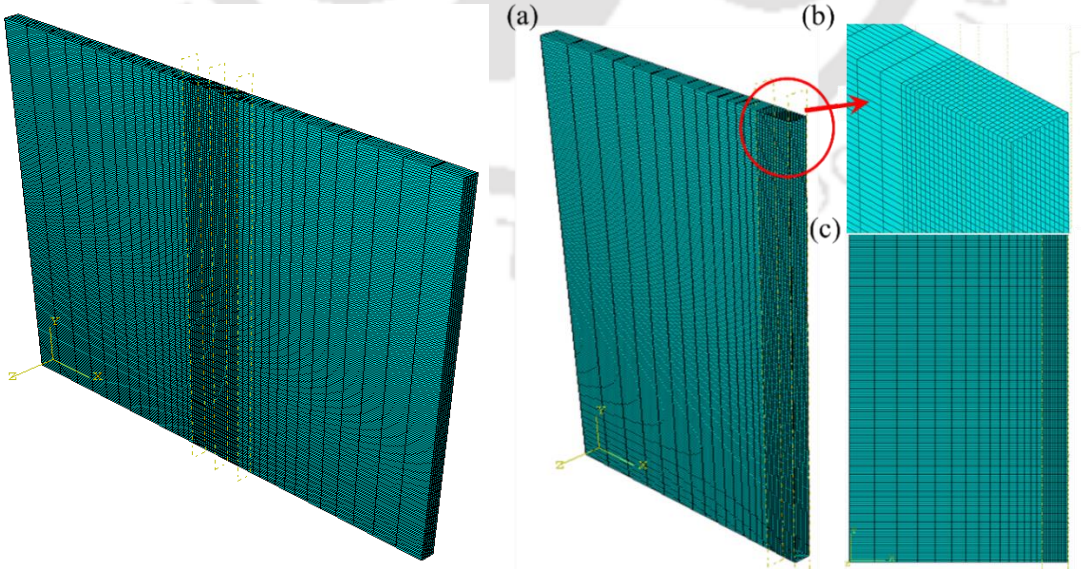

Figure 5.1: Finite element mesh for model geometry.

5.2.2 Calibration of numerical model

This solution of finite element based numerical model depends on the selection of the number of elements, number of time steps, number of non-linear iterations per time step and the time required for each non-linear iteration. Therefore, the computational time can be reduced by proper and optimum selection of these parameters. Also the accuracy of numerical model depends on assignment of proper material properties. The computed thermal cycles and weld zone isotherm of finite element heat transfer model are sensitive to the element size and the distribution of elements within the model geometry. The accuracy of the predicted result is directly proportional to element size: finer the mesh sizes higher the precision of the model.

In FSW, the plastic deformation of material is occurred at the tool-workpiece interface and creates a shear layer. It is assumed that total frictional heat generated in the whole FSW process is attributed solely in the shear layer thickness [313]. Therefore, to apply volumetric heat flux on boundary shear layer, the size of mesh should be finer than that of mesh in the weld zone. The typical estimate of boundary shear layer thickness is 0.25 mm [78, 314].

To comply with this small size of boundary layer, it considerably increases the element number and consequently the computational time. Hence application of surface heat flux eliminates the complexity arises from the restriction of mesh size due to boundary shear layer thickness. Mesh sensitivity analysis is conducted to select a proper element size to accurately simulate the FSW process to minimize the computational cost. **Figure 5.2** indicates that three different meshes are considered in the weld zone. The peak temperature obtained at a thermocouple point is estimated using these three types of meshes and is compared with the experimental value. Finite element model using coarse mesh was found to overestimate the experimental peak temperature at the thermocouple location by more than 12%. On the other hand, the peak temperatures predicted by using fine and very fine mesh are comparable with their experimental counterparts and a maximum difference around ~ 3 % is observed. No improvement in numerical result has observed from the use of fine mesh to very fine mesh. Therefore, fine mesh is used in all subsequent simulations.

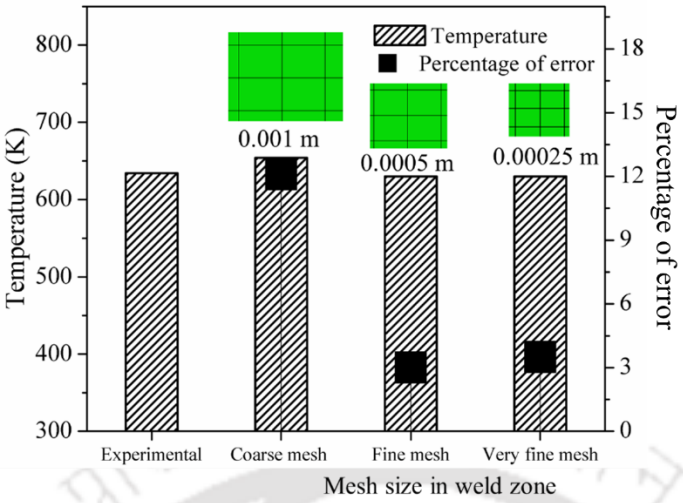

Figure 5.2: Peak temperature obtained at a thermocouple point (TC1) using different meshes.

Published literatures indicates that the selection of backing plate have a significant influence on the thermal history of the workpiece, as the backing plate with high thermal conductivity would allow more heat loss than the plate with low thermal conductivity [32]. It was found that including a proper thermal boundary condition for the backing plate is critical for accurate simulation results. The objective was to minimize the difference between the experimentally measured temperature and the temperature obtained using a 3D FE model [103]. The workpiece backing plate contact conductance is one the uncertain aspect of the thermal model as it cannot be determined accurately with experiments. The contact conductance value is assumed in the most of the previous thermal models as a fixed uniform value. The heat loss to the backing plate, which is essentially contact conduction, is accounted by using an equivalent convection coefficient at the bottom of the plates.

A convective heat transfer coefficient of 25 W/m^2-K is used for the top and sides of the work-pieces which is typical for natural convection heat transfer between aluminum and air [315]. However, the higher convective heat transfer coefficient is used for the bottom surface, which is equivalent to the surface film conductance between the workpiece and the backing plate. In the present work, convective heat transfer coefficient of 300 W/m^2-K is assumed at the bottom of the workpiece [316]. For the radiation heat loss, the emissivity (ϵ) of 0.4 is considered whereas Stefan–Boltzmann constant is 5.6703 10^{-8} W/m^{2}K^4. In

dissimilar joint, the different convective heat transfer coefficient is used for both the workpieces (Cu & Al) which is typically for natural convection between work-piece and air. At bottom surface high heat transfer coefficient (500 W/m^2-K) is considered due to presence of highly conductive backing plate in copper side.

The procedure of physical modelling is adopted according to the actual experiment where the numerical solution returns the temperature profile in special domains. FSW process is divided into five time instants: plunge time, initial dwell time, welding time, final dwell, and plunge-out time. However, total simulation time depends on welding speed that also includes the cooling period.

5.2.3 Material properties

There are four different types of materials used in numerical analysis of FSW process such as Aluminum 6061, aluminum 7075, aluminum 1100 and pure copper. **Figure 5.3** illustrates the temperature dependent thermal conductivity and specific heat of AA 6061 and AA 7075 [27, 317]. Both the thermal properties vary linearly with temperature for AA 6061. The thermal conductivity of AA 7075 remains constant after 500 K. Presence of second phase particles and their distribution in aluminum alloy, and the change of microstructure over temperature and strain rate in real FSW process is accommodated by variation of thermal properties.

Figures 5.4 shows the temperature dependent thermal properties of AA 1100 and pure copper, respectively that are used for finite element simulation [35, 318]. For AA 1100, the value of the thermal conductivity and specific heat increases almost linearly with respect to temperature. However, the thermal conductivity of pure copper is decreased linearly with temperature. **Figure 5.5** shows the temperature dependent yield stress of AA1100 and pure copper. The yield strength of both materials is decreased with increase in temperature but yield strength of copper is much higher than aluminum at room temperature.

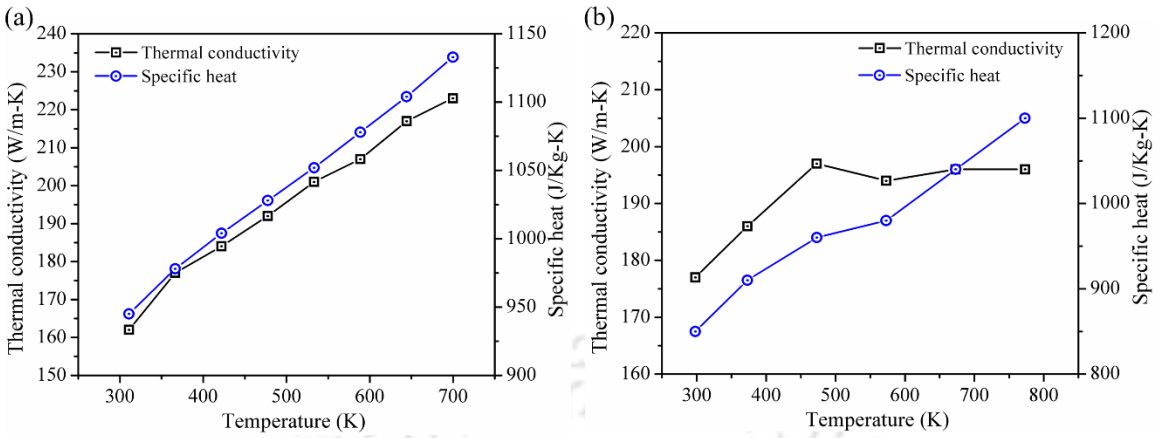

Figure 5.3: Temperature dependent thermal properties used in the present numerical work: (a) AA 6061; and (b) AA 7075.

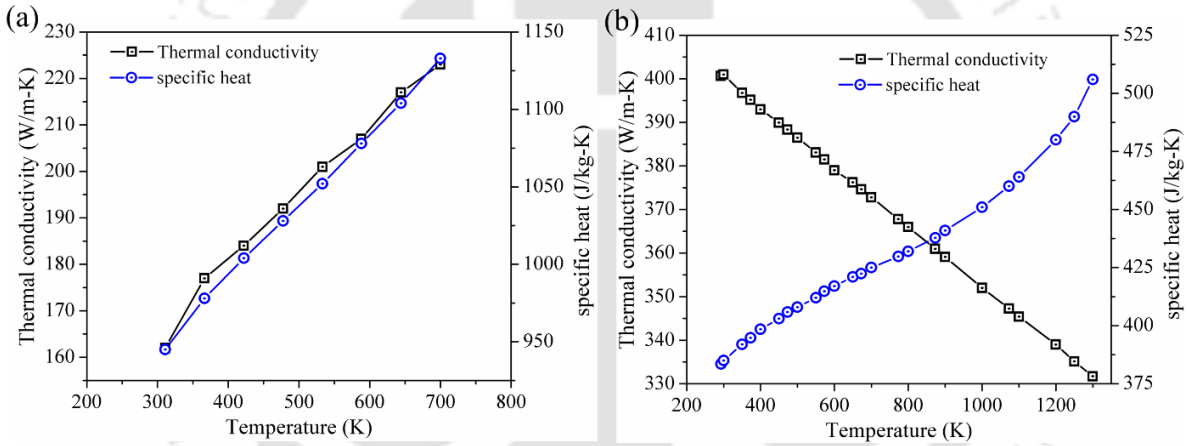

Figure 5.4: Temperature dependent thermal properties of (a) AA 1100; and (b) Pure copper.

Table 5.1 describes the physical properties of material at room temperature of AA 1100, AA 6061, AA 7075 and pure copper utilized in the FE model. The melting temperature of AA 1100 and pure copper is considered as ~ 933 K and ~ 1353 K, respectively. The physical properties like density, young's modulus, poisson's ratio, convection heat transfer coefficient, emissivity and melting temperature of copper and aluminum is described here. It is observed that there is huge difference in physical properties of copper and aluminum at room temperature.

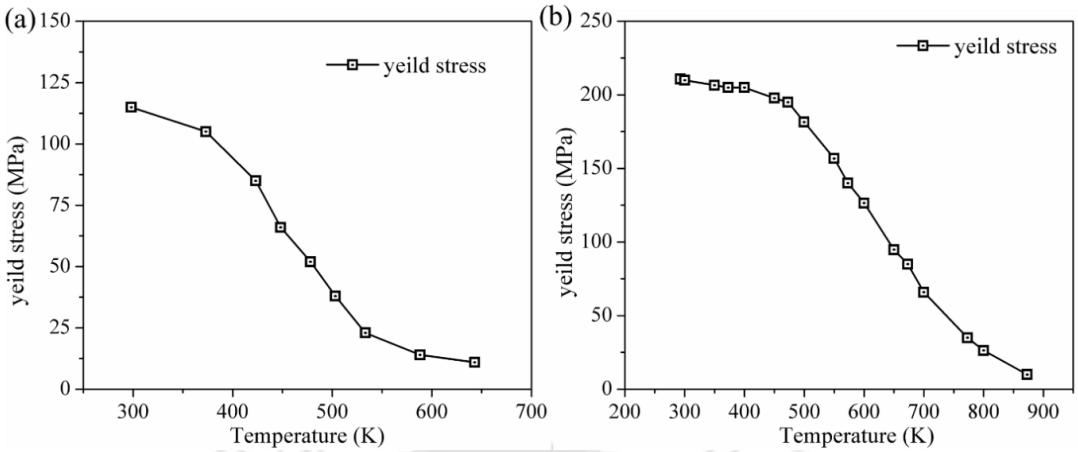

Figure 5.5: Temperature dependent yield stress of (a) AA 1100 and (b) Pure copper.

Table 5.1: Constant material properties of aluminum alloy and pure copper used in numerical simulation.

Material properties	Unit	Aluminium AA1100	Pure copper	Aluminium 6061	Aluminium 7075
Density	kg/m^3	2690	8933	2710	2810
Young's modulus	GPa	75	117	69	70
Poisson's ratio	-	0.3	0.34	0.33	0.33
Convection heat transfer coefficient	W/m^2K	25	100	30	30
Emissivity	-	0.4	0.74	0.36	0.34
Melting temperature	K	933	1353	924	908

5.2.4 Identification of model parameters

In FSW, there are several parameters that cannot be assigned with confidence because of complex thermo-physical interaction during the process. These parameters are the slip between the tool and the workpiece interface and the coefficient of friction that varies with temperature. Due to the complex kinematics of the FSW process, it is difficult to establish a straightforward procedure for estimating the friction coefficient. Previous

research recognizes the friction coefficient as a variable in FSW, but neglects the variation and assumes a constant value throughout the complete cycle of FSW process. During FSW process, the temperature of material ahead of FSW tool is increased due to preheating. So the contact condition is strongly depended on temperature viz. the extent of preheating. The contact state variable or extent of slip is not only temperature dependent; also it depends on process parameters. Based on the variations of the average fraction of slipping with temperature, a model is developed based on a modified Arrhenius equation to present average fraction of slipping between the tool and the workpiece [319]:

$$\delta = 1 - A\ exp\left[-\left(\frac{Q}{RT}\right)^{\beta}\right] \quad (5.1)$$

where A and β are experimental constants, Q is the activation energy for deformation (for 1100-H14, Q = 156 kJ mol^{-1}), R is the universal gas constant (R = 8.314 $JK^{-1}mol^{-1}$) and T is the stir zone temperature (in K). When the experimental data are fitted by equation (5.1) based on least square method, one can obtain A = $4.07x10^7$ and β = 0.89 [121]. Typically a constant friction coefficient model (Coulomb) is used to evaluate the temperature distribution in the work piece during hybrid FSW process. The coefficient of friction in reality is a function of many parameters such as pressure, speed, temperature etc. A stick-slip friction behavior is proposed by Schneider et al. [320] which is a function of process condition such as pressure. In the present work, the variation of friction coefficient in sliding friction condition is depicted in **Fig. 5.6** which is analogous to temperature dependent material property only.

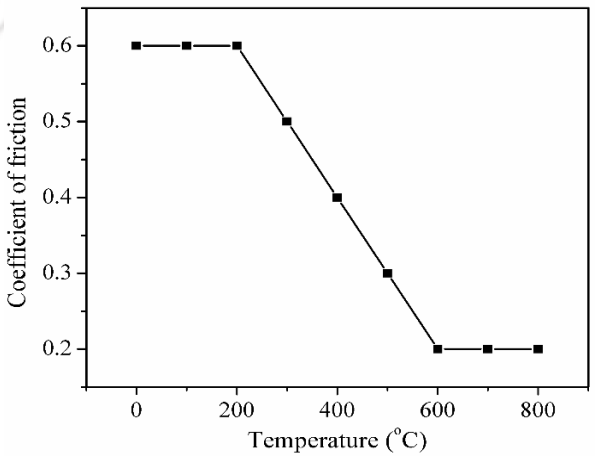

Figure 5.6: Coefficient of friction as a function of temperature.

The plunging force is very important parameter during heat transfer analysis since it is used to estimate heat generation during FSW process. Its magnitude is altered significantly during welding period which is difficult to implement in the mathematical model. **Figure 5.7** depicts the experimental nature of force signal (815 rpm, 63 mm/min and 0 A). The average value during welding phase is used in calculation of heat generation.

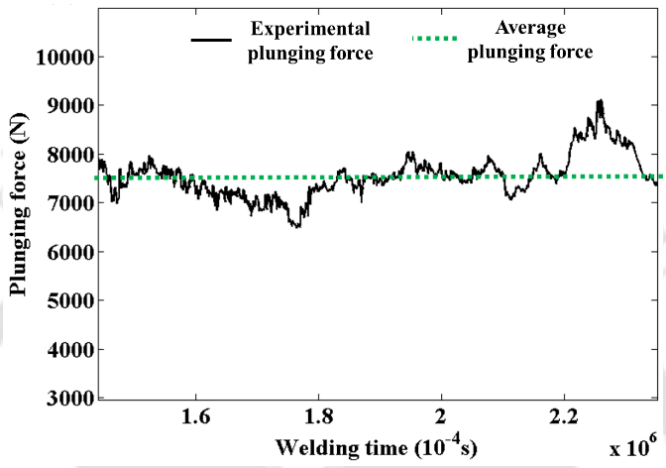

Figure 5.7: Profile of plunging (axial) force vs time during welding phase.

5.3 Heat transfer analysis

This section contains heat transfer analysis of conventional FSW and plasma assisted FSW for similar and dissimilar type of joints. A transient heat transfer analysis is conducted using a moving heat source that resembles the modeling of the moving tool. Heat is generated by friction and plastic deformation between the tool and the workpiece are incorporated. Heat input from both the tool shoulder and the tool pin are considered in the model.

5.3.1 Reliability of the process

The developed heat transfer model for friction stir welding and hybrid friction stir welding process is used to predict the peak temperature of the process. However, the accuracy of the prediction in a complex system has been analyzed through comparative error between predicted and experimental results. It is a way to estimate the level of confidence that can be placed in a simulation-based prediction. The error analysis consists of individual

component errors and relative reliability of the predicted solutions. The relative reliability and error term are defined by [321]

$$\%\, E_{RR} = \frac{|T_{RE} - T_{RC}|}{T_{RC}} \times 100 \text{ and } \%\, E_{RA} = \frac{|T_{AE} - T_{AC}|}{T_{AE}} \times 100 \quad (5.1\text{-}5.2)$$

$$R_s = (1 - |E_{RR}|) \times (1 - |E_{RA}|) \quad (5.3)$$

where E_{RR} and E_{RA} are the non-dimensional predictable errors of peak temperature on retreating and advancing side, respectively, T_{RE} and T_{RC} are experimental and calculated peak temperatures on retreating side, T_{AE} and T_{AC} are experimental and calculated peak temperature on advancing side respectively and R_s is the overall reliability of the system. In this section, the reliability of developed model is first estimated from the experimental data and then from heat transfer model. Thereafter, the reliability of the whole system for similar and dissimilar joint is estimated.

5.3.1.1 Temperature distribution for AA 6061-T6

To validate the numerical model, the experimental data is taken from literature [31] for the material AA6061-T6 [27]. The welding process parameters are depicted in **Table 5.2**. The diameter of the tool shoulder is 50 mm and the diameter of the tool pin is 12 mm. The work piece is 12.7 mm thick butt welded. The numerical simulation of aluminium alloy is performed for three different welding conditions to determine the maximum welding temperatures and temperature profiles during thermal analysis. **Figure 5.8** depicts the time temperature history of 4 selected special points. The location of measuring points 1, 2, 3 and 4 are 2.0 mm beneath the upper surface; points 1, 2, 3 and 4 are 8, 12, 16 and 25 mm from the joint line respectively. In this case, the shoulder diameter is very large so that peak temperature zone is wide in temperature profile. Therefore, maximum temperature during that period sustain for more time. It is also found that the peak temperature during simulation at point 1 in three trials is close to 85% of the material melting point. The temperature profile and peak temperature attained in all cases are almost in similar range because of low transverse tool speed and this resembles the fact of considering symmetric heat source profile. The temperature rise also depends on contact condition. At low rotation and welding speed this contact state variable intensifies fraction of heat generation due to

plastic deformation and this plastic deformation is found to have a significant effect on the resulting temperature especially at low-energy levels.

Table 5.2: FSW process parameters for AA6061-T6 [31].

Exp. no	Process parameter for FSW		
	Transvers speed (mm/mm/min)	Rotational speed (rpm)	Average plunging force (kN)
Exp. 1	95	914	17.5
Exp. 2	95	637	25.0
Exp. 3	95	344	32.0

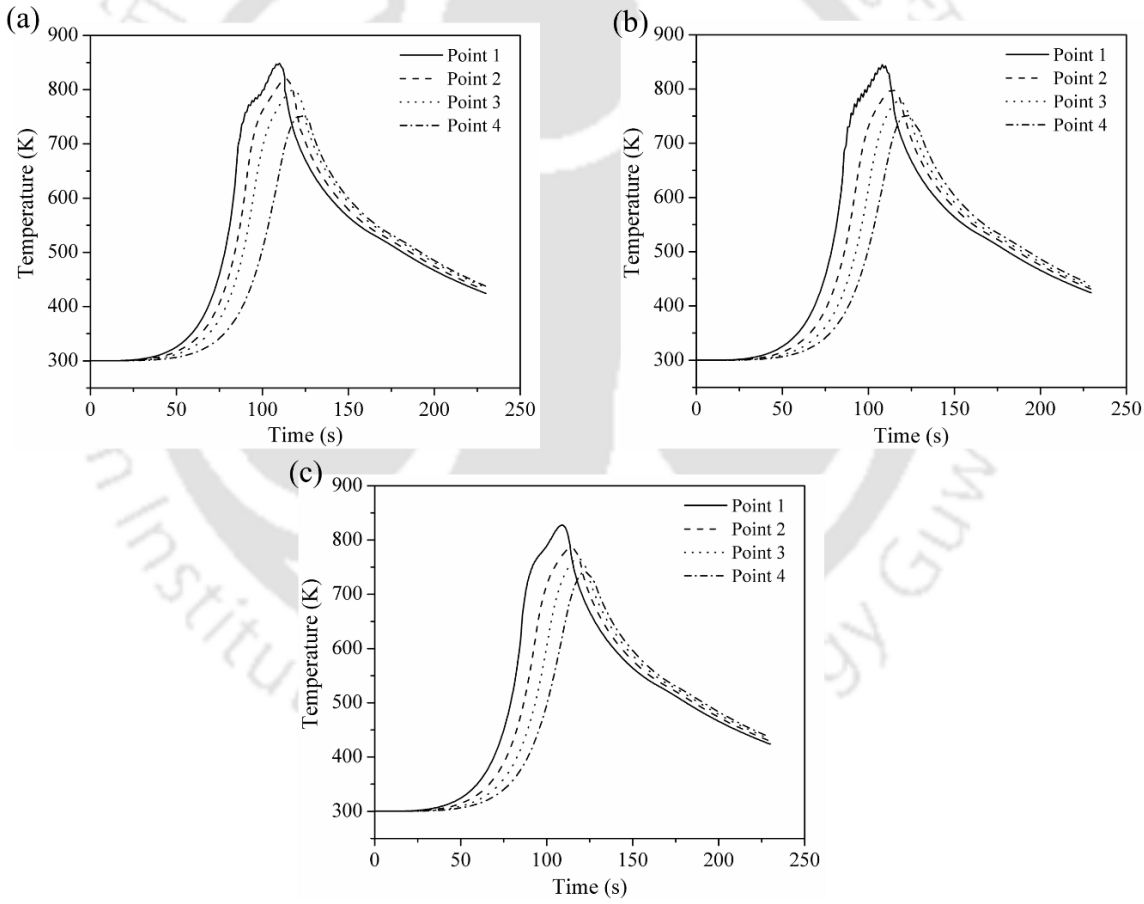

Figure 5.8: Temperature history of three experimental conditions in **Table 5.2** during simulation (a) Exp. 1, (b) Exp. 2 and (c) Exp. 3 for AA6061-T6.

Figure 5.9 shows a comparison between the experimentally measured temperature profiles of Exp. 2 and the model results. Relatively better agreement between the profiles is obtained by optimum heat transfer film surface coefficient of backing plate. It is obvious from **Fig. 5.9** that there is insignificant temperature rise during dwell period and almost zero temperature gradient in that period. However, the stiff temperature gradient is observed before reaching peak temperature.

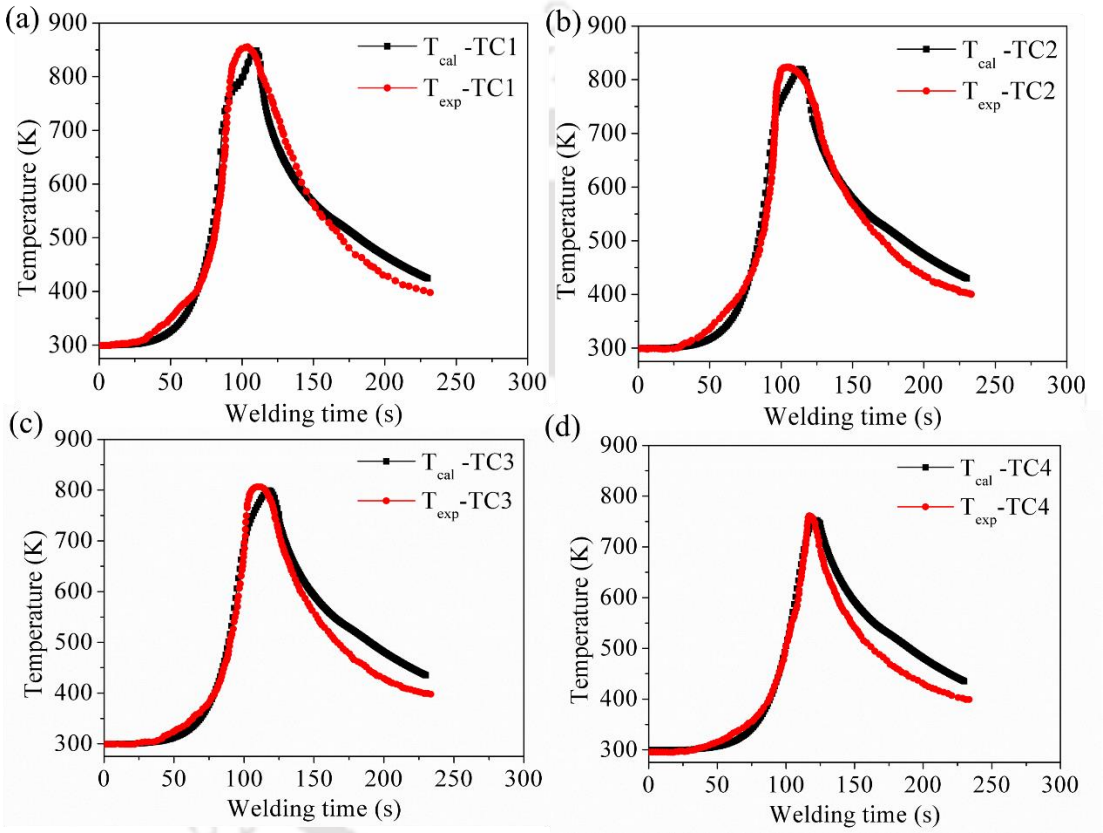

Figure 5.9: Comparison between experimental [31] and calculated time temperature profile on the advancing side of Exp. 2 in **Table 5.2** for AA6061-T6 (a) TC1 (b) TC2 (c) TC3 (d) TC4.

Figure 5.10 depicts the error percentage of peak temperature and reliability of calculated peak temperature during simulation. It is obvious from **Fig. 5.10** that E_{RR} is high at the measurement of temperature specifically for Exp. 3. This point is close to the tool axis that is usually affected by non-symmetric phenomena of heat generation owing to plastic deformation away from tool pin-workpiece interface and convective heat transfer due to

flow of material. As moves away from axis, the error percentage drops due a reduced effect of non-symmetric phenomena of heat generation. It is observed that the overall error in peak temperature is 0.5 ~ 5.5 % and the maximum reliability is achieved as 0.95. So, the developed model is considered to be adequate and predicts the peak temperature without unacceptable error.

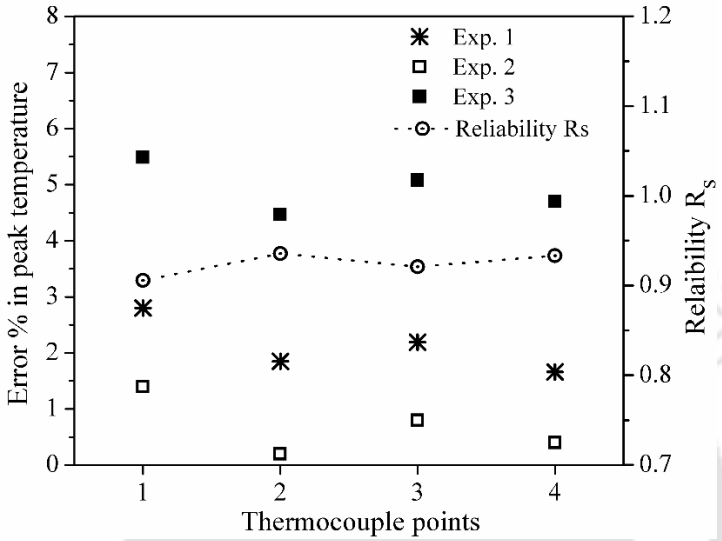

Figure 5.10: Estimated percentage error of peak temperature in comparison between simulated and experiments corresponding to **Table 5.2**.

5.3.1.2 Temperature distribution for AA 1100

The numerical model is also validated with in-house developed experimental setup. Four experiments are carried out to measure temperature history during joining of AA1100. The experimental conditions are reported in **Table 4.5**. A three-dimensional transient thermal analysis is performed using symmetric heat source profile (mechanism of heat generation) to compare the results corresponding to Exp. No. 2. The temperature profile at points TC1, TC2, TC3, and TC4 in advancing side of welding joint is targeted to validate the numerical model results.

A comparison between the estimated maximum temperature obtained using the proposed model and the experimental results is depicted by **Fig. 5.11**. This comparison is corresponding to welding condition of 98 mm/min transverse speed and 600 rpm of tool (Exp. 2 in **Table 4.5**). It is observed that the calculated and measured thermal histories for all thermocouple locations of advancing side of the weld shows decent equivalent result

even if the advancing side temperature values are underestimated and the retreating side values overestimated by the model due to symmetric nature of heat source assumption. The results indicate that the calculated profile and the measured profile are of the same shape and that the maximum temperatures on both curves are of the approximately same value, which implies that the present model can accurately predict the heat transfer process in FSW. Additionally, it can be concluded that use of a moving heat source technique is proved to be a reliable method to simulate temperature profile of FSW process.

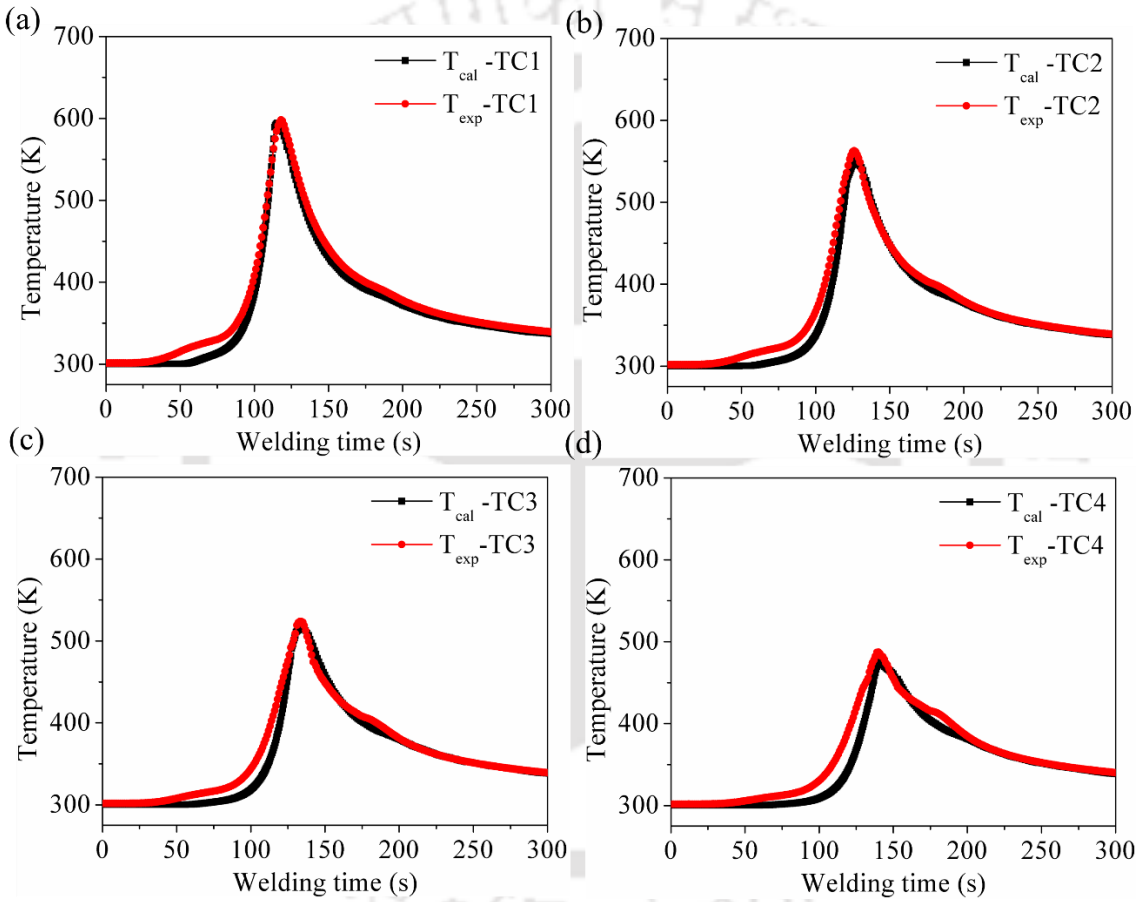

Figure 5.11: Comparison between experimental and calculated time temperature profile on the advancing side at 98 mm/min transverse speed and 1100 rpm of tool (Exp. 2 in **Table 4.5**).

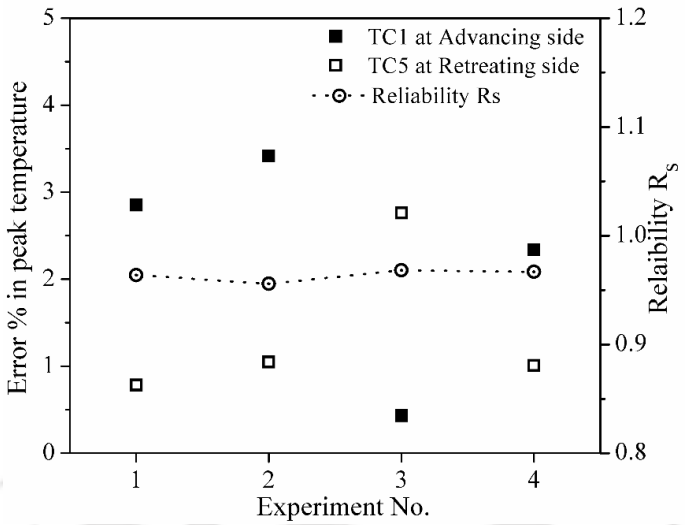

Figure 5.12: Percentage error at TC1 and TC5 thermocouple points with reliability.

Figure 5.12 shows the percentage error between experimental and calculated peak temperature at TC1 and TC5 with reliability for experimental condition explain in **Table 4.5**. Percentage of error in calculated result is between ~1-4 percent of experimental temperature at TC1 which is acceptable for present model. The error could be because of considering some varied parameters such as plunging force as a constant. The maximum reliability attained is 0.95 which shows accuracy of proposed model to predict peak temperature during welding. Therefore, the established mathematical models presented a good agreement between the output of the model and physical experiment, thus improves the reliability and usability of the model.

5.3.1.3 Temperature distribution for P-FSW of AA 1100

The controlled energy input into the system by introducing an external heat source reduces mechanical energy input during FSW. This external heat also improves joining efficiency which is a potential area of consideration for the development of hybrid friction stir welding process. Therefore, the effect of additional heat input on the thermal history of weld joint is evaluated through heat transfer analysis of plasma assisted friction stir welding of aluminum AA1100. In this section, numerical investigation of P-FSW is shown with the combine influence of heat input from preheating and process parameters on thermal history. **Figure 5.13** shows the temperature evolution at thermocouples positions TC1 for

experimental data and numerical results obtained from 3D model. **Figure 5.13(a)** represent temperature profile of Exp. 1 without preheating and **Fig. 5.13(b)** represent temperature profile of Exp. 3 with preheating of 35 A at same process condition shown in **Table 4.11**. A good agreement was observed between experimental data and numerical results. The temperature profile of thermocouple TC1 data is associated to the passage of the tool during welding including cooling period. The temperature at TC1 was more (around 20-30 K) during Exp. 3 due to additional heat input through 35 A preheating. Consequently, the application of preheating (additional heat) in FSW brings down the mechanical load on the tool and improves the welding speeds.

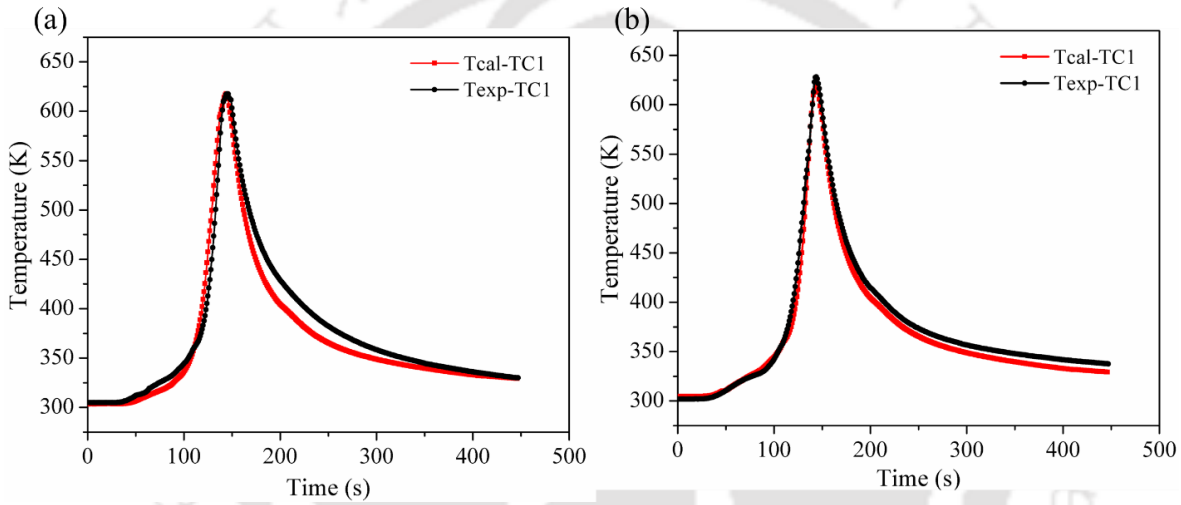

Figure 5.13: Comparison between experimental and simulated thermal cycle at TC1 for: (a) Exp. No. 1, and (b) Exp. No. 3.

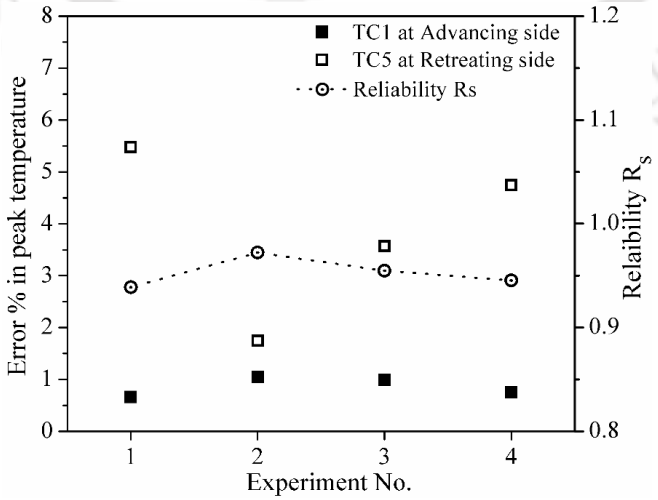

Figure 5.14: Effect of process parameters on error in peak temperature and reliability.

Figure 5.14 illustrates the error percentage in estimation of peak temperature and overall reliability for all the experimental conditions with preheating of **Table 4.11**. Due to nonsymmetrical heat generation during FSW, the overall error in peak temperature is 0.5 ~ 5 % and the maximum reliability is achieved as 0.95. So, the developed model is considered to be adequate and predicts the peak temperature without appreciable error.

5.3.1.4 Temperature distribution for P-FSW of dissimilar copper and AA 1100

The numerous parameters involving transformation of mechanical energy into heat and their complex mutual dependency yield difficulty in exact estimation of heat generation. **Figure 5.15** depicts the comparison between experimentally measured and computed time-temperature history for Exp. No. 1 and Exp. No. 5, respectively in **Table 4.12**. The calculated results are in relatively better agreement with the measured temperature which indicates that the developed heat-transfer model can be applied successfully in predicting the thermal cycles during P-FSW of dissimilar joint. The peak temperature is very high at the nearest thermocouple point (TC1) with plasma current of 65 A (**Fig. 5.15b**).

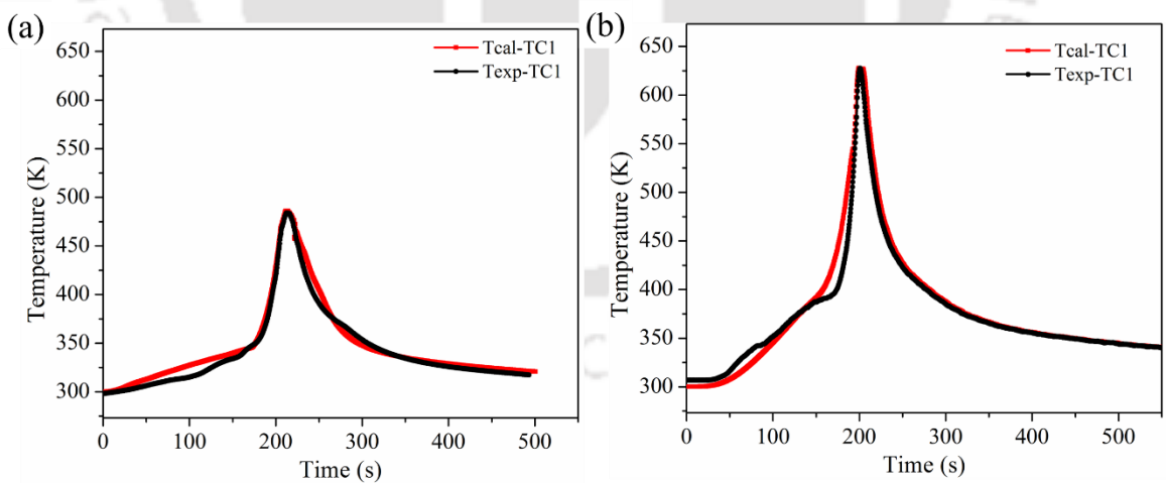

Figure 5.15: Comparison between experimental and calculated thermal cycle at welding condition of 815 rpm, 98 mm/min weld speed (a) without preheating (b) with preheating of 65 A.

It is obvious that the developed heat transfer model for hybrid friction stir welding process is relatively adequate and precise to predict the peak temperature of the process. However, the accuracy of the prediction in a complex system has been analyzed through comparative error between calculated and experimental results. It is a way to estimate the level of confidence that can be placed in a simulation-based prediction. The error analysis consists of individual component errors and relative reliability of the predicted solutions. After estimating the individual component of error percentage in peak temperature (**Eq. 5.1 and Eq. 5.2),** the relative reliability of the predicted solutions is calculated (from **Eq. 5.3**). **Figure 5.16** illustrates the error percentage of peak temperature and overall reliability for all the experimental conditions of **Table 4.7**. The overall error in peak temperature is 5 ~ 12 % and the maximum reliability is achieved as 0.84. The quantitative prediction using the present methodology indicates the reliability and robustness of the modeling approach.

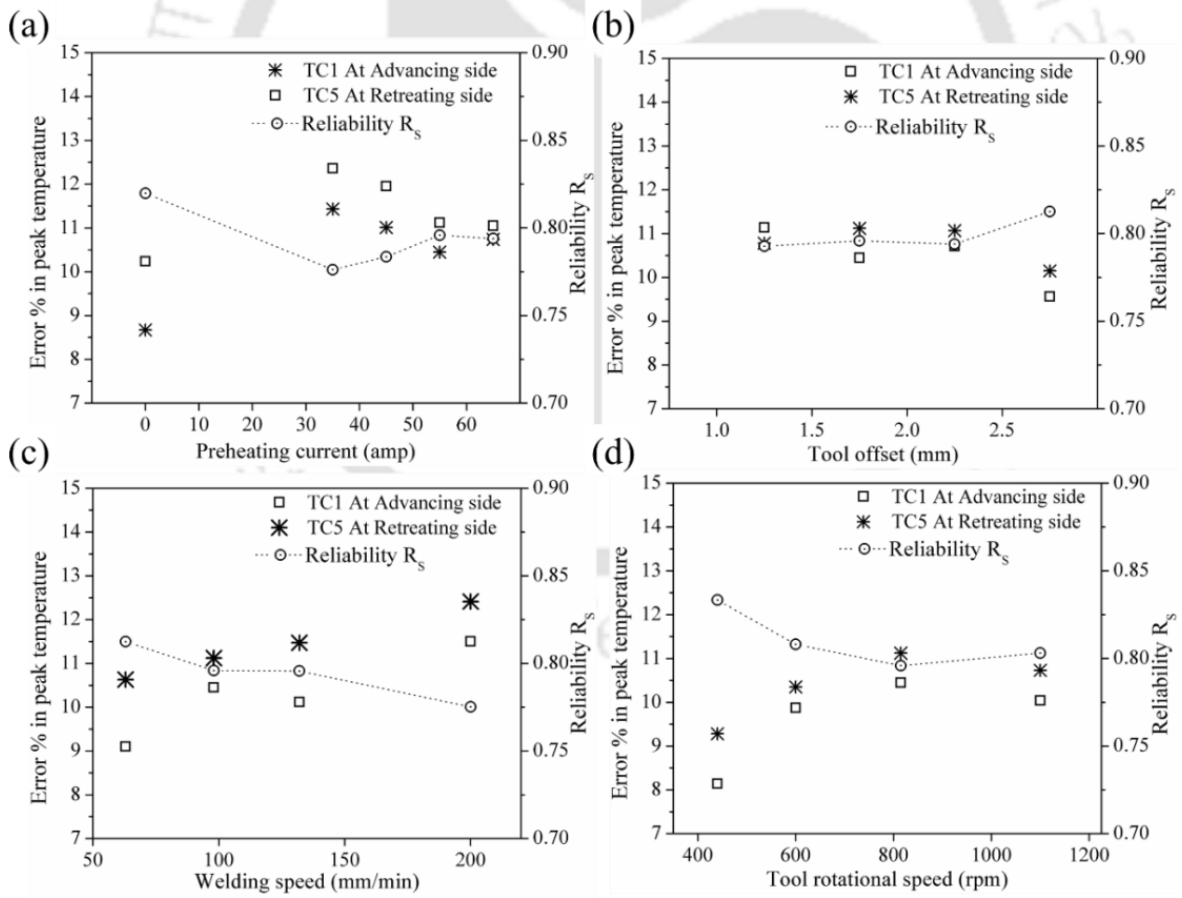

Figure 5.16: Effect of process parameters on error in peak temperature and reliability (a) preheating current, (b) tool offset, (c) welding speed, and (d) tool rotational speed.

5.3.2 Heat transfer for joining similar materials

In this segment, three dimensional temperature distribution is calculated from finite element based numerical model. The 2D computed isotherm is extracted from temperature distribution to validate with experimentally measured macrographs for similar welding conditions. Both literature data as well as in-house developed experimental data for conventional FSW and hybrid FSW are considered here.

5.3.2.1 Friction stir welding of AA 6061-T6

The typical FSW microstructural morphology consists of the weld nugget, the thermal-mechanical affected zone (TMAZ), the heat-affected zone (HAZ) and the base material. The microstructure morphology is related to the local thermal history. The calculated isotherms of the peak temperatures in the welding zone are compared with the experimentally obtained macrograph. Based on shapes and grey levels on the microstructure morphology, the weld cross-section area relates to the local peak temperature experienced in each region and corresponding local peak temperature is compared with calculated isotherms as shown in **Fig. 5.17**. The calculated temperature in center part corresponding to nugget zone is around 836.15 K. In the "V" shape area the temperature range is between 758.15 to 663.15 K that belong to thermo-mechanical affected zone. The temperature range in between 663.15 to 480.15 K corresponds to heat affected zone. The calculated isothermal weld cross-section is nearly equivalent with experimental microstructure morphology that verifies the reliability of numerical model [322].

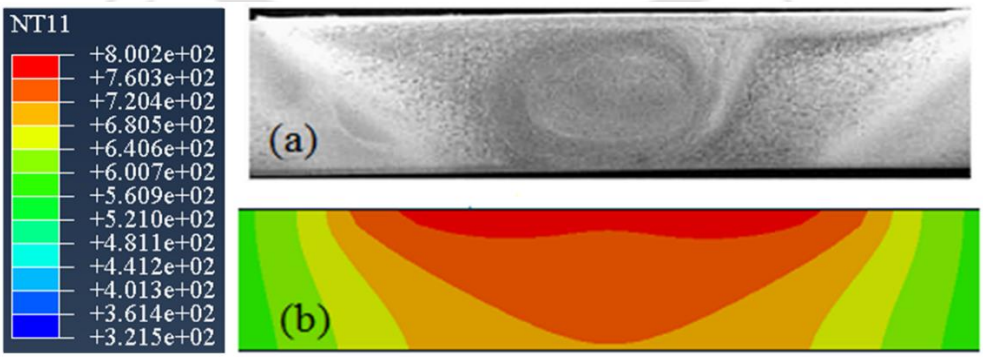

Figure 5.17: Comparison of experimental and simulated weld zone at 95 mm/min welding speed and 637 rpm (a) Experimentally measured macrograph [31] (b) Simulated isothermal temperature profile of AA6061-T6.

5.3.2.2 Friction stir welding of AA 1100

Figure 5.18(a) describes 3D temperature distribution when the rotating tool is moving with welding speed of 98 mm/min. The amount of generated heat can be assumed as direct merchandise product of tool rotation and it is coming directly from sliding and sticking of the material. Simulation result shows that the temperature distributions are not symmetric around welding line and maximum temperature occurs behind the tool pin as observed in **Fig. 5.18(b)**. This temperature difference arises due to plastic deformation and material flow around the rotating tool which moves from advancing side to retreating side with additional heat due to friction that gives higher temperature behind the tool pin. At the same time, the highest temperatures are always found in the workpiece material right below the tool shoulder and the temperature progressively decrease from this region as a function of the distance in the radial and through-the-thickness directions.

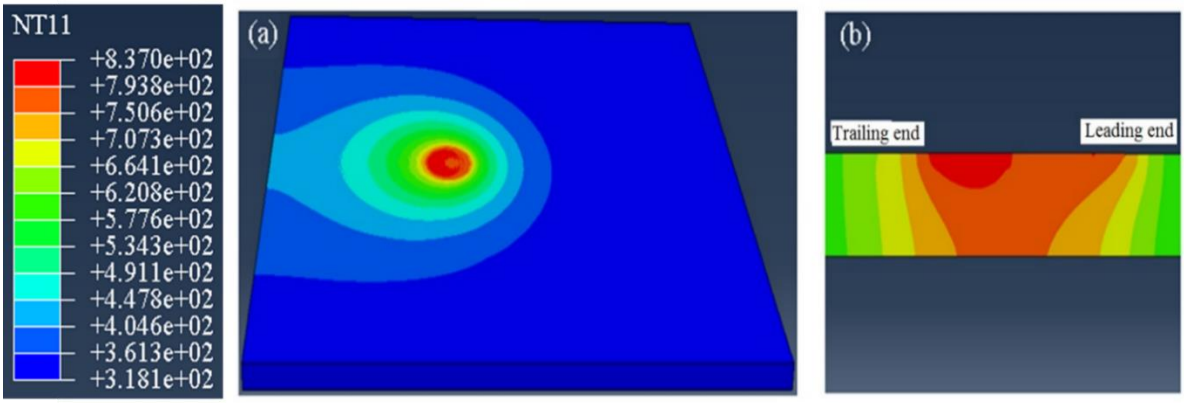

Figure 5.18: Temperature distribution of Exp. 2 in **Table 4.5** during simulation (a) Isometric view (b) Cross-section view for AA1100.

Three-dimensional simulated thermal history within the weld piece of Exp. 2 in **Table 4.5** at different time instants is illustrated in **Fig. 5.19**. The maximum temperature in weld zone was 800.1 K observed during simulation. The red color circular area represents the weld zone and its area is approximately equal to tool shoulder area. The color bar in this figure actually defines the weld zone, and heat affected zone in terms of corresponding isotherms.

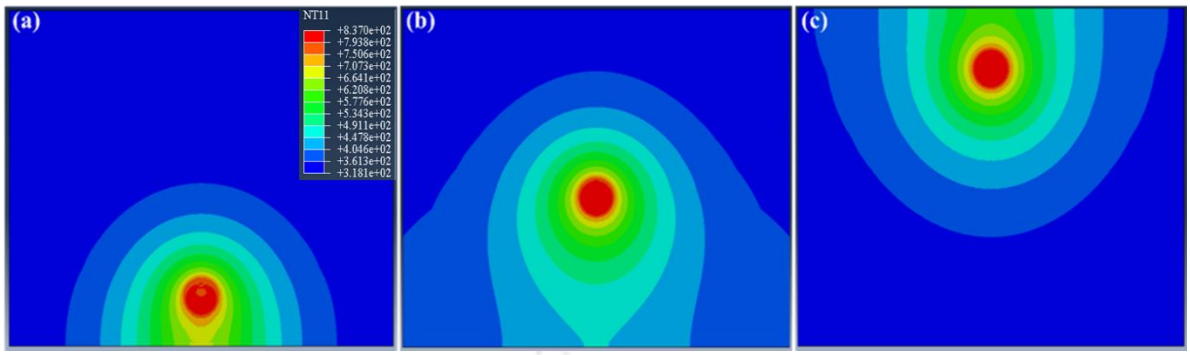

Figure 5.19: Simulated temperature distribution of Exp. 2 in **Table 4.5**.

Figure 5.20 shows the calculated isotherms of the peak temperatures in the welding zone compared to the experimentally obtained microstructure morphology. Weld zone is demonstrated the grains within the stir zone are roughly equiaxed and often an order of magnitude smaller than the grains in the parent material due to high temperature between 800 to 730 K. In thermo-mechanical affected region temperature are lower and the effect on the microstructure is correspondingly smaller so that temperature is between 730 to 716 K and rest of part peak temperature range of 663 to 480 K is heat affected zone. It is obvious that the temperature isotherm provides useful information about various microstructural zones of weld cross-section and this can be linked with dimensions of weld nugget [322].

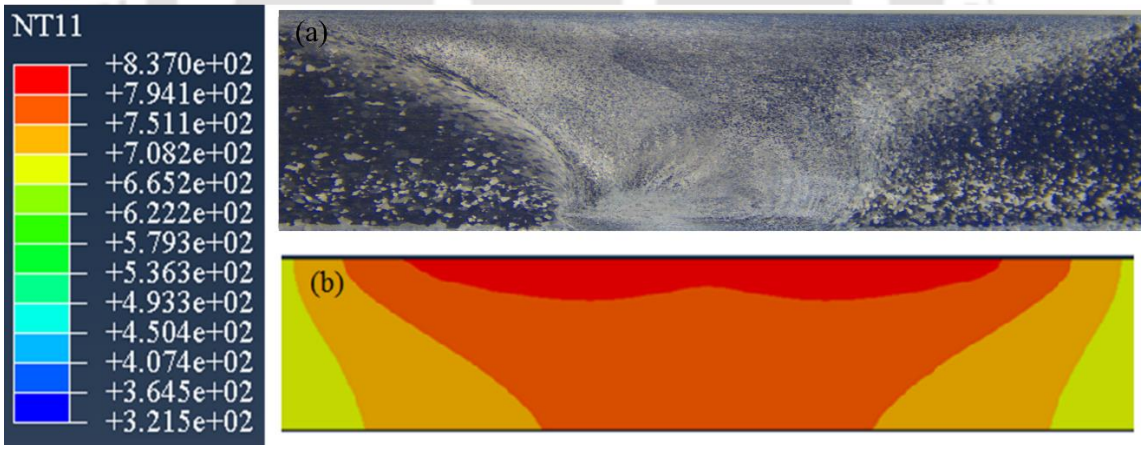

Figure 5.20: Comparison of experimental and simulation weld zone for Exp. 2 in Table 4.5 (a) Experimentally measured macrograph (b) Simulated isothermal temperature profile of AA1100.

5.3.2.3 P-FSW of similar AA 1100

The yield strength of every material decreases with increasing temperature which is important parameter for FSW. Therefore, an investigation is carried out to find the temperature distribution ahead of tool and corresponding flow stress value at different preheating conditions. **Figure 5.21(a)** depicts the temperature distribution at 815 rpm and 98 mm/min weld speed for various preheating conditions. It shows that with the increase in preheating current the temperature ahead of FSW tool is also increased. The temperature dependent flow stress value is depicted by **Fig. 5.21(b)** when the tool shoulder is at the middle of the workpiece. The flow stress value is obtained from literature data for this material [318]. With increase in plasma current, the temperature ahead of FSW tool also increases. The flow stress value (~20-30 MPa ahead of the tool shoulder) at no plasma current is high whereas it decreases upto ~ 10 MPa (~10-25 MPa ahead of the tool shoulder) with increase in plasma current which facilitates the stirring action of material by FSW tool.

Figure 5.22 illustrates the temperature contour without the effect of preheating at three different time steps at welding condition of 815 rpm, 63 mm/min weld speed. During welding a tool shape heat source is applied along the weld centerline to form a joint. This heat source results in an intense thermal gradient in the material which causes inhomogeneous deformation of the workpiece being welded. The highest temperature (~810 K) is always found in the workpiece material right below the tool shoulder. **Figure 5.23** shows temperature contour for with preheating of 35 A at three different time steps at welding condition of 815 rpm, 63 mm/min weld speed. The FSW tool along with plasma arc moves along welding direction and maximum temperature is achieved around ~846 K which is well below solidus temperature of aluminum alloy. Peak temperature is found at leading end of tool due to additional heat input caused by preheating. Preheating enhances plasticization state ahead of tool and improve plastic flow around the tool.

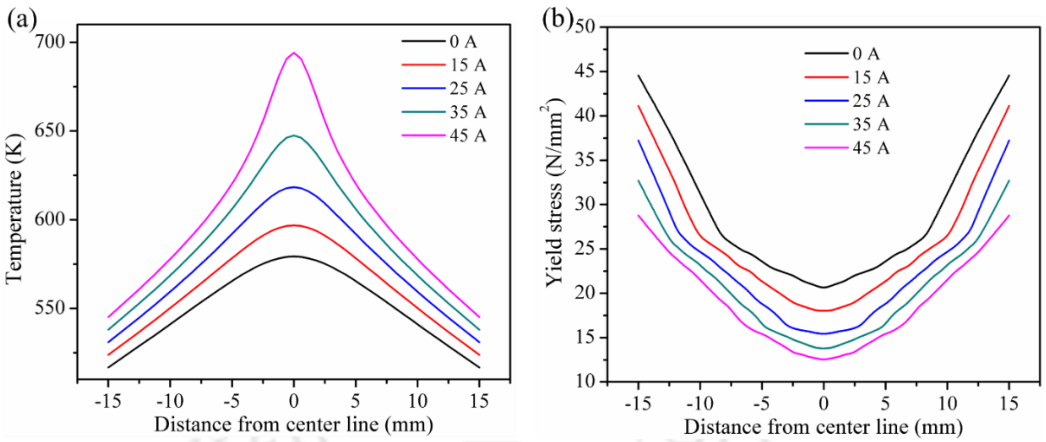

Figure 5.21: (a) Temperature profile and (b) corresponding yield stress at the middle line of the workpiece for different preheating current at welding condition of 815 rpm, 98 mm/min weld speed.

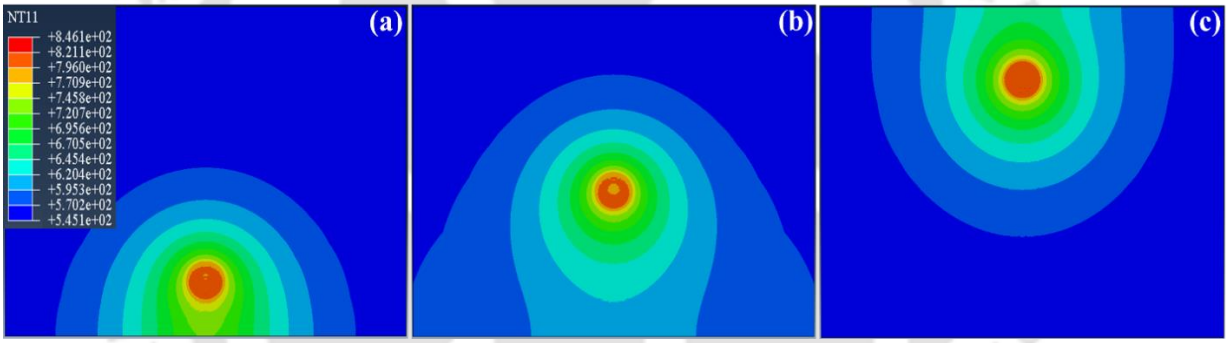

Figure 5.22: Simulated temperature distribution at welding condition of 815 rpm, 63 mm/min weld speed without preheating.

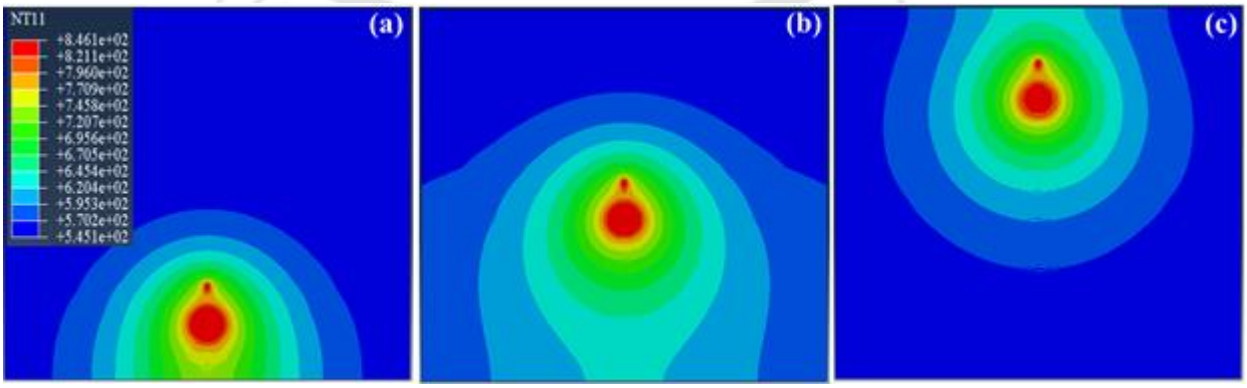

Figure 5.23: Simulated temperature distribution at welding condition of 815 rpm, 63 mm/min weld speed with 35 A preheating.

Figure 5.24 depicts the temperature distribution in longitudinal and transverse direction at welding condition of 815 rpm, 63 mm/min weld speed without the effect of preheating. Peak temperature is found at tailing end of tool due to deposition of hot material from front of tool (**Fig. 5.24a**). The temperature distribution is symmetric in stirring zone due to effectively use of a symmetric heat source in numerical model (**Fig. 5.24b**). **Figure 5.25** depicts the temperature distribution at welding condition of 815 rpm, 63 mm/min weld speed with the effect of preheating of 35 A. This additional heat through preheating provides sufficient local plasticization of the workpieces ahead of the tool. So that, more plasticized material have better flow characteristic to produce quality joints. It reduces the amount of mechanical energy required by the tool to stir the material in weld zone. The temperature distribution was symmetric around weld centerline caused by preheating.

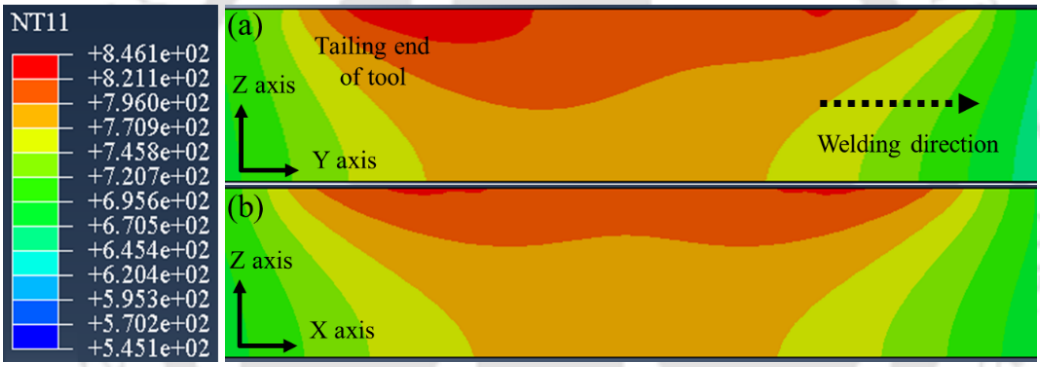

Figure 5.24: Cross sectional view of simulated results at welding condition of 815 rpm, 63 mm/min weld speed without preheating.

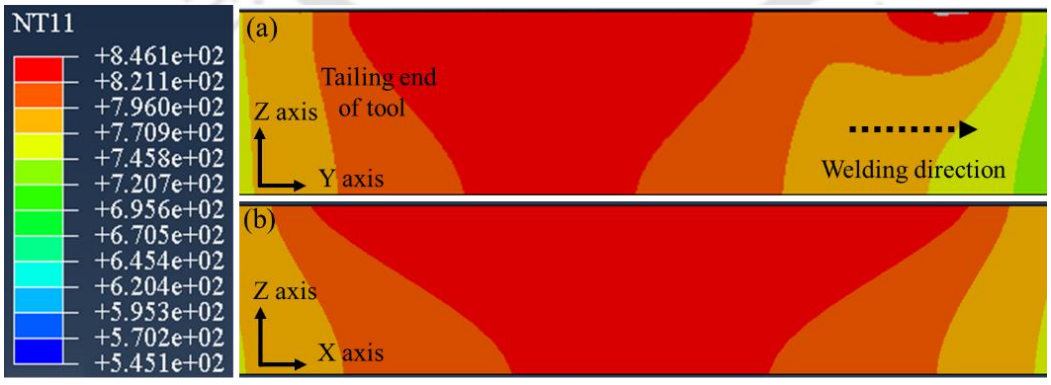

Figure 5.25: Cross sectional view of simulated result at welding condition of 815 rpm, 63 mm/min weld speed with 35 A preheating.

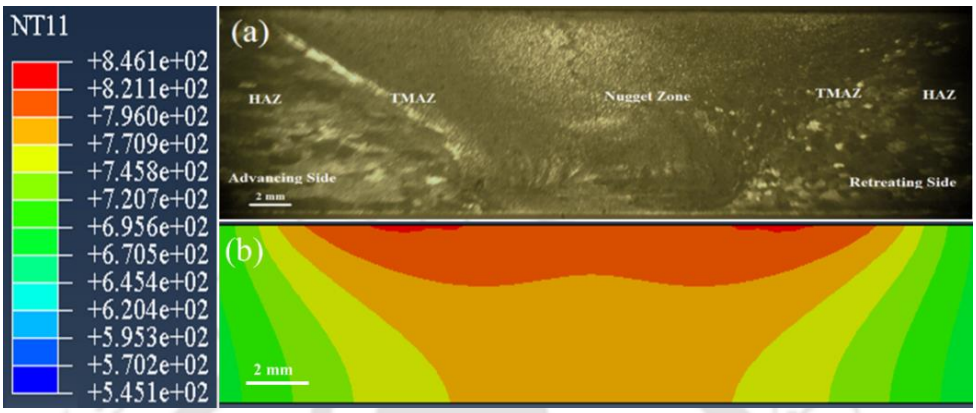

Figure 5.26: Comparison of simulated and experimental measured weld zone at welding condition of 815 rpm, 63 mm/min weld speed without preheating.

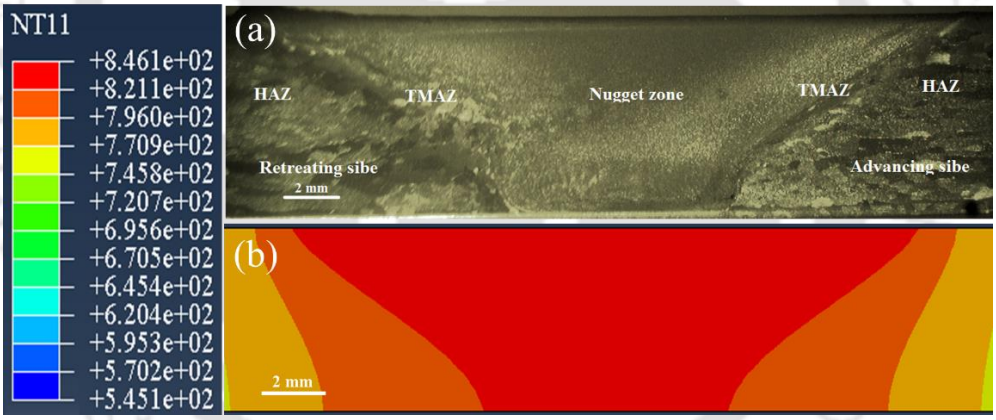

Figure 5.27: Comparison of simulated and experimental measured weld zone at welding condition of 815 rpm, 63 mm/min weld speed with 35 A preheating.

The comparison of experimental and simulated weld zone at 815 rpm and 63 mm/min welding speed without preheating is shown in **Fig. 5.26**. Good agreement is achieved between the computed isotherm and the experimental macrograph results, indicating significant promise for the application of this procedure in predicting thermal history of P-FSW. The maximum peak temperature was recorded at the top surface and at weld center but with increasing distance from the weld centerline, the peak temperature decreased. **Figure 5.27** illustrates the cross-sectional view of experimental and simulated

weld zone at welding condition of 815 rpm, 63 mm/min weld speed with 35 A preheating. The preheating at 35 A current improves weld zone temperature up to ~ 35 K. This improved temperature reduces the resistance of material around the tool. It also overcomes the problem of insufficient weld temperatures, due to low rotational speeds or high traverse speeds.

5.3.2.4 P-FSW of dissimilar pure copper and AA 1100

Figure 5.28 shows the calculated thermal history under the shoulder at various locations of the solution geometry. Time-temperature profile without the effect of preheating is depicted in **Fig. 5.28(a)** whereas **Fig. 5.28(b)** represents the same with the effect of preheating by plasma arc. The temperature difference between Al and Cu without any preheating is found due to two analogous effects. High thermal conductivity or diffusivity of copper promotes additional heat loss to the backing plate and low plastic flow of copper restricts to heat generation by shear energy of copper as compared to aluminum. The preheating source with 65 A plasma arc creates additional 423 ~ 473 K temperature rise in the copper side. The offset position of FSW tool and plasma arc creates high temperature profile in copper side as compared to similar location of aluminum side. The rise of temperature under the tool shoulder in copper side helps to plasticize the material and refine the grains through recrystallization mechanism. Therefore, an investigation is carried out to find the temperature distribution at the interface and corresponding flow stress value. **Figure 5.29(a)** depicts the temperature distribution at 815 rpm, 98 mm/min weld speed and 2 mm tool off-set for various preheating conditions. The temperature dependent flow stress value [323-324] is depicted by **Fig. 5.29(b)** when the tool shoulder is at the middle of the workpiece. With increase in plasma current, the maximum temperature increases in copper side as compared to aluminum side. There is drastic difference in flow stress value (~60 MPa) at no plasma current whereas it decreases upto ~ 10 MPa with increase in plasma current which facilitates the stirring action of material by FSW tool. This increase in temperature enhances the weldability between copper and aluminum. However, the optimum position of tool off-set is significant parameter and almost uniform flow stress value for dissimilar materials near the welding line may enhance the tool life by reducing the wear.

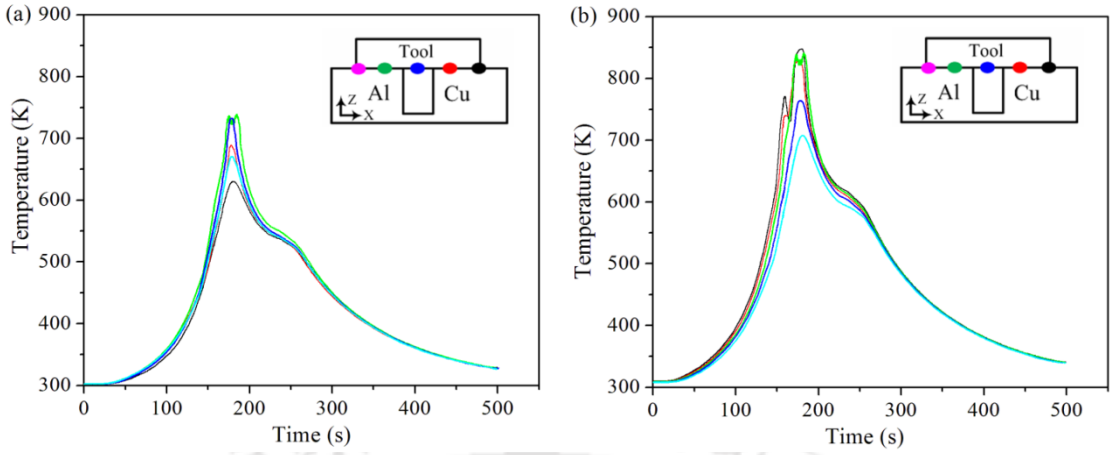

Figure 5.28: Calculated thermal history for (a) Exp. No. 1 and (b) Exp. No. 5.

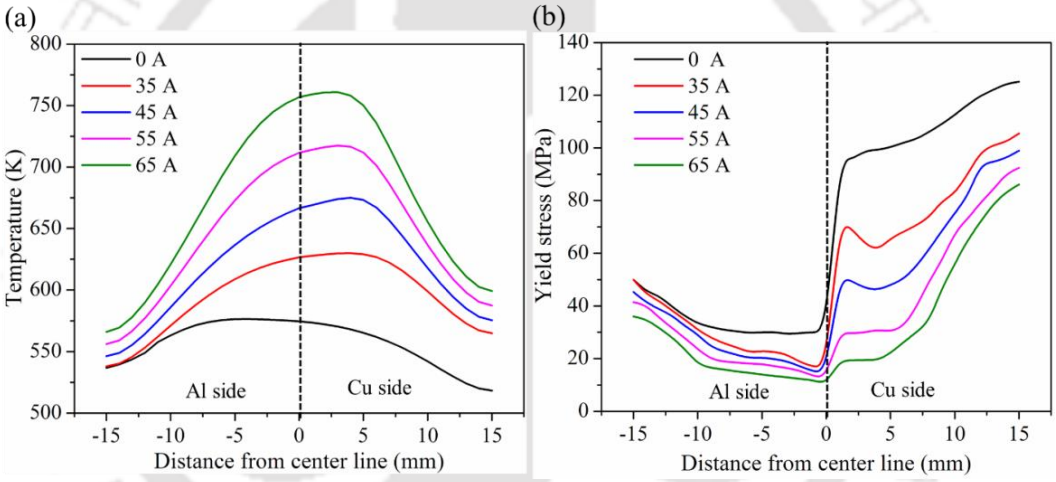

Figure 5.29: (a) Temperature profile and (b) corresponding yield stress at the middle line of the workpiece for different preheating current at welding condition of 815 rpm, 98 mm/min weld speed and 2 mm tool off-set.

Numerical investigation is performed to find out the transient effect of preheating on the plunging stage of FSW process. This is an important phase since thermo-mechanical stirring action develops at this stage and most of the tool wear occurs during this phase [325]. **Figure 5.30** illustrates that the temperature develops in plunging stage gradually over time and is the maximum at the end of the stage. High temperature zone is observed in aluminum side due to more rate of heat conduction by copper. This temperature difference affects the plastic deformation state and having adverse effect on tool wear and tool life.

However, high temperature zone is observed in copper side when preheating by plasma is used (**Fig. 5.31**). At the end of the plunging stage, the temperature develops fully and becomes uniform. Therefore, plasma heating improves plastic state of copper and reduces plastic state difference between copper and aluminum.

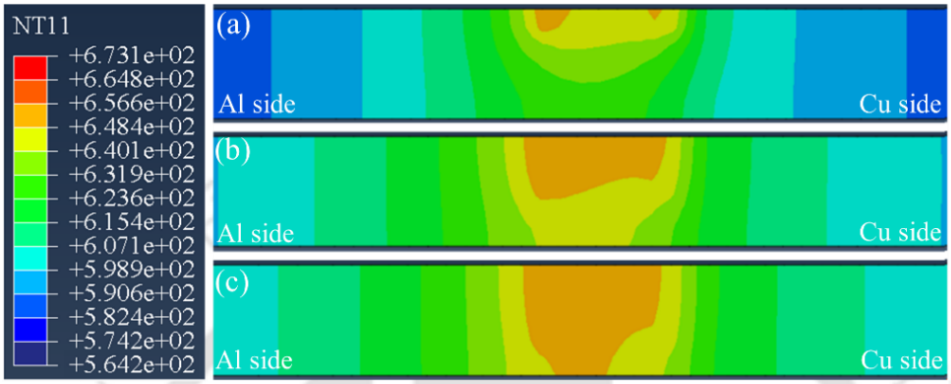

Figure 5.30: Temperature isotherm during plunging stage at zero preheating current corresponding to Exp. No. 1: (a) at 5 s, (b) at 18 s and (c) at 33 s.

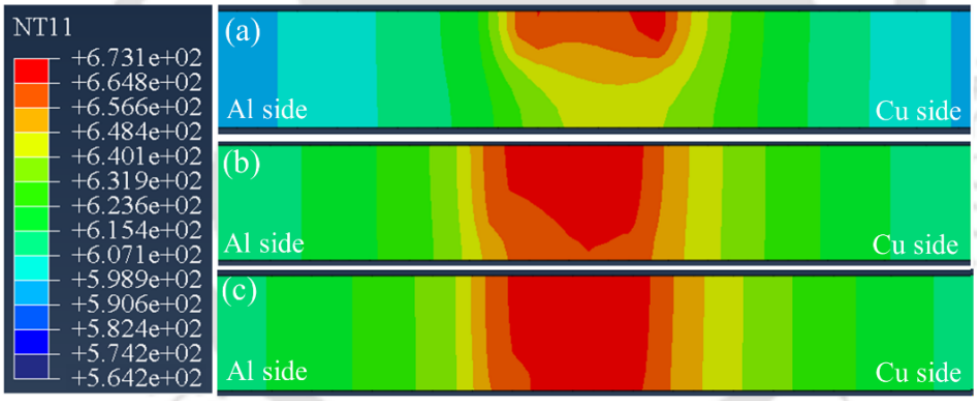

Figure 5.31: Temperature isotherm during plunging stage at 65 A corresponding to Exp. No. 5: (a) at 5 s, (b) at 18 s and (c) at 33 s.

Figure 5.32 illustrates the temperature contour without the effect of preheating at three different time steps. It is observed from temperature data that the maximum temperature is found in aluminum side due to source of heat by tool offset whereas the effect is due to difference in thermos-physical properties. This temperature difference in weld zone is mainly because of heat diffusivity due to different thermal conductivity and specific heat. **Fig. 5.33** shows temperature contour for with preheating of 65 A at three different time

steps. Peak temperature is found in copper side and is significantly different when there is no preheating in copper side. Preheating enhances the temperature in copper side and reduces the effect of heat lost due to high thermal conductivity of copper.

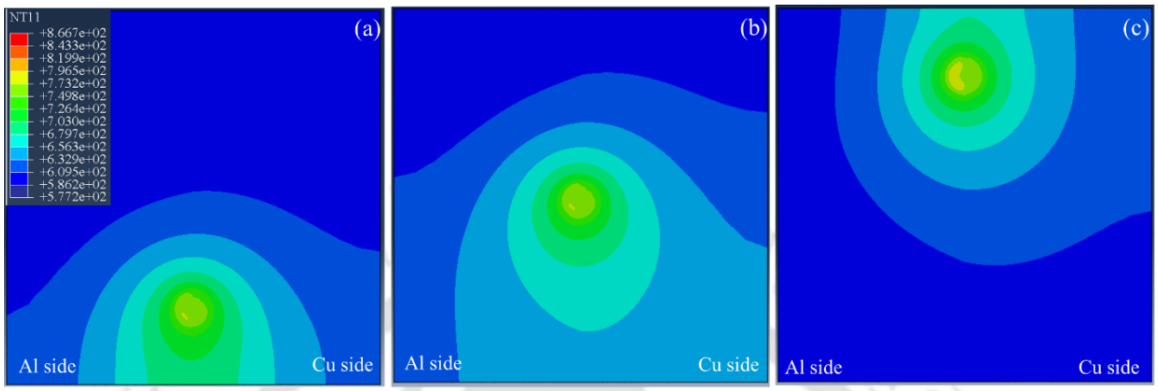

Figure 5.32: Simulated temperature distribution for Exp. No. 1.

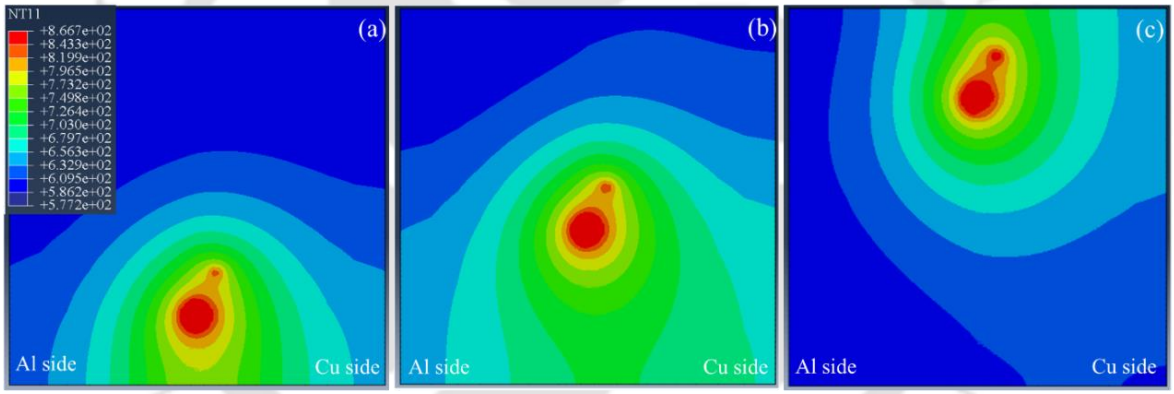

Figure 5.33: Simulated temperature distribution for Exp. No. 5.

Figure 5.34 depicts the temperature distribution in longitudinal and transverse direction for Exp. No. 1. The temperature distribution in stirring zone is not symmetric due to difference in thermal properties of copper and aluminum. Peak temperature is found behind the tool axis on aluminum side. **Fig. 5.35** depicts the temperature distribution with the effect of preheating of 65 A for Exp. No. 5. Temperature distribution in stirring zone is overall symmetric due to application of preheating in copper side. Peak temperature is found around tool axis and in copper side with respect to welding direction.

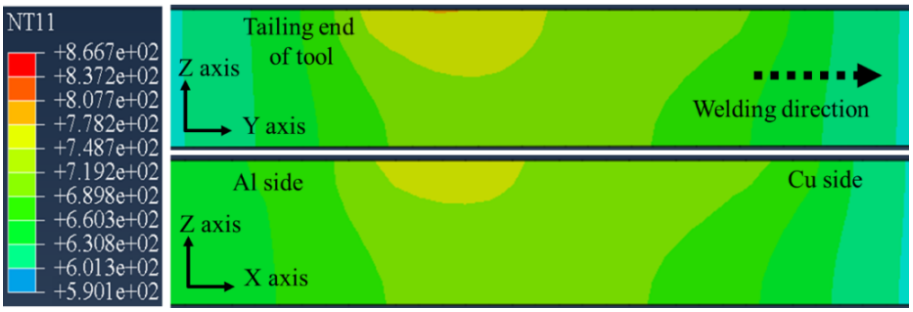

Figure 5.34: Cross sectional view of simulated results for Exp. No. 1.

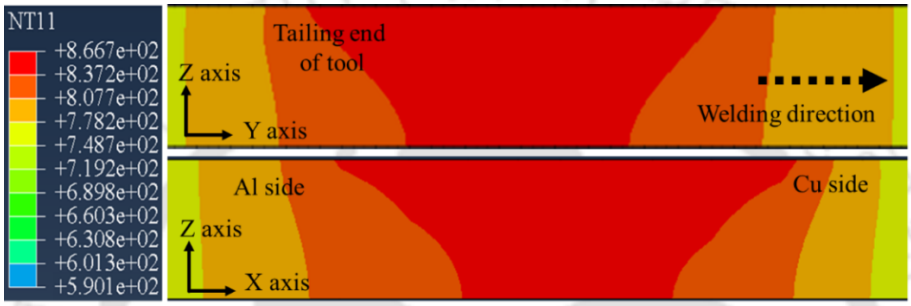

Figure 5.35: Cross sectional view of simulated result for Exp. No. 5.

In P-FSW process, preheating or external heating source aids the material flow and broaden the process window for successful weld joint. The comparison of experimental and simulated weld zone of Exp. No. 1 is shown in **Fig. 5.36**. It shows relatively better agreement between the computed isotherm and experimentally measured macrograph. The attainment of the temperature in copper side is not enough to plasticize the material and it is hard to stir in weld zone. Therefore the probability of formation the defect at the interface is very high. Without preheating, several large Cu pieces are mixed with the Al matrix in the nugget zone, and many voids could be observed (**Fig. 5.36b**). Moreover, the nugget zone does not exhibit the classical onion ring structure due to difference in material flow behavior at the same temperature; rather a lamellar composite structure in the stirred zone is observed [326, 327]. **Fig. 5.37** illustrates the cross-sectional view of experimental and simulated weld zone of Exp. No. 5. It is obvious that the temperature isotherm provides useful information about various weld zones. The preheating source reduces the asymmetry in both heat generation and material flow. **Fig. 5.37(b)** indicates that sound and flaw-less joints are obtained with preheating that reduces the formation of defects.

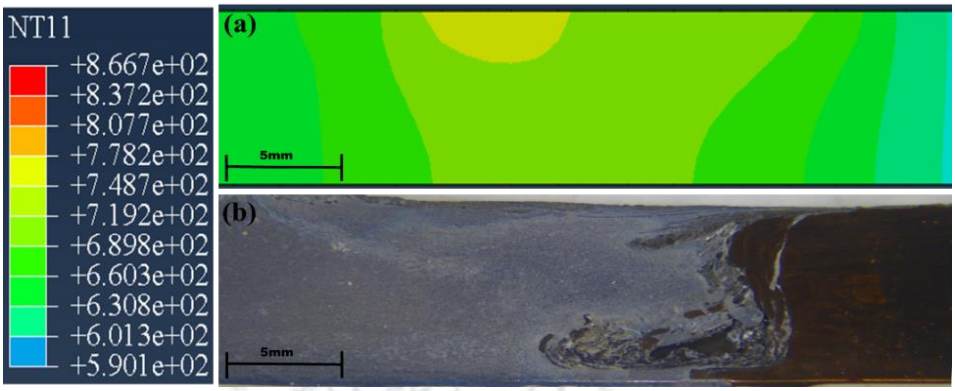

Figure 5.36: Comparison of simulated and experimental measured weld zone for Exp. No. 1.

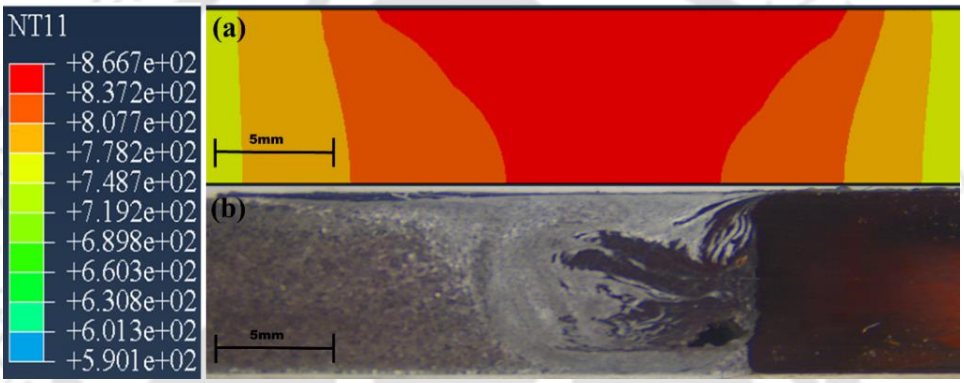

Figure 5.37: Comparison of simulated and experimental measured weld zone for Exp. No. 5.

At low plasma current, voids are observed in weld zone which indicates incomplete mixing between Al and Cu (**Fig. 5.38a**). This defect is usually associated with insufficient material flow in case of zero preheating. With the increase in preheating current, voids size decreases due to improvement in material-flow as observed in **Fig. 5.38(b)**. The difference is induced due to improvement in plasticization state which is improved by performing welds under preheating in copper side and resulted in the formation of mixed material zones with increased dimension and homogeneity. However, it is observed that improved mixing of both materials is better achieved at the highest plasma current that results in proper metallurgical bonding and coalescence during welding process.

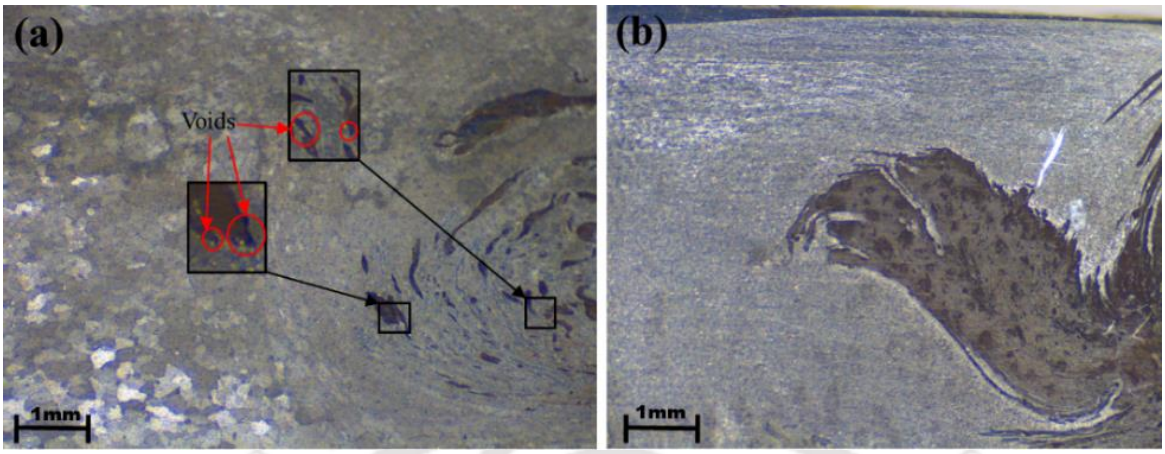

Figure 5.38: Macrographs of Al–Cu joint cross section in aluminum side at joint interface for (a) Exp. No. 1 and (b) Exp. No. 5.

5.3.3 Strain rate and grain size

Knowledge of strain and strain rate is important for understanding the subsequent evolution of grain structure, and serves as a basis for verification of various models as well. The mathematical model described in **chapter 3** is used to predict strain rate and average grain size in the weld zone. The stirring action during FSW is not modelled physically in the present work. The heat flux, strain and strain-rate are given as input through a set of equations in user sub-routine over the frame of finite element based model. The model is validated with the strain rate result of AA 7075 material with 3 mm thick [328]. The straight cylindrical FSW tool is used with pin diameter of 3.0 mm, shoulder diameter of 10.0 mm and 2.8 mm pin height. The calculated result shows good argument with literature data (**Fig. 5.39)**. It was found that non-symmetrical strain rate distribution under tool shoulder is ~ 4.5 s^{-1} around the tool axis. The calculated strain rate is 4.8 s^{-1} which is symmetric about tool axis due to assumption of symmetric velocity and temperature field.

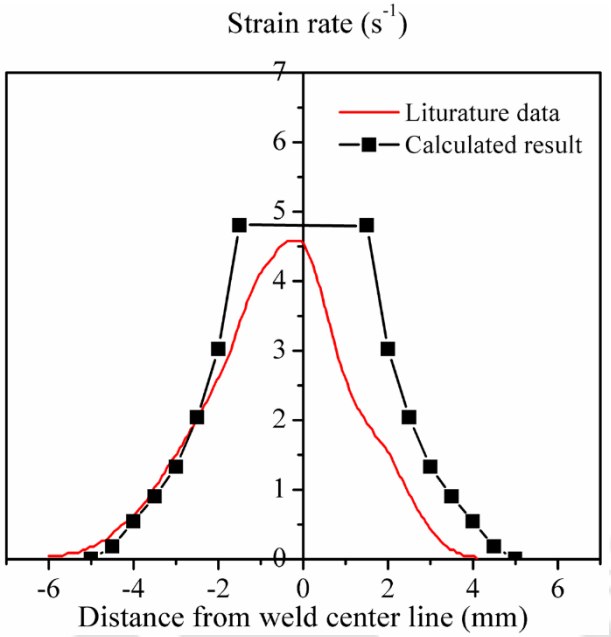

Figure 5.39: Validation of strain rate with Buffa et al. [328].

The strain rate depends on distance travelled by the tool in unit time and contact state condition between the tool and the workpiece. **Figure 5.40** shows the computed strain rate across the weld cross-section at 1 mm under the tool shoulder for different welding condition shown in **Table 4.5**. It shows that maximum strain rate occurs near the surface of the pin where the maximum velocity gradient exists. The strain rate rapidly decreases away from the tool axis due to rapid reduction in velocity gradient below the shoulder periphery. Beyond the periphery, the velocity gradient decreases sharply because of the rapid decay of velocity. The maximum value of strain rate achieved was 6.8 s^{-1} at welding condition of 815 rpm and 98 mm/min welding speed. It is also observed that strain rate in CDRX zone decreases with decrease in rotational speed.

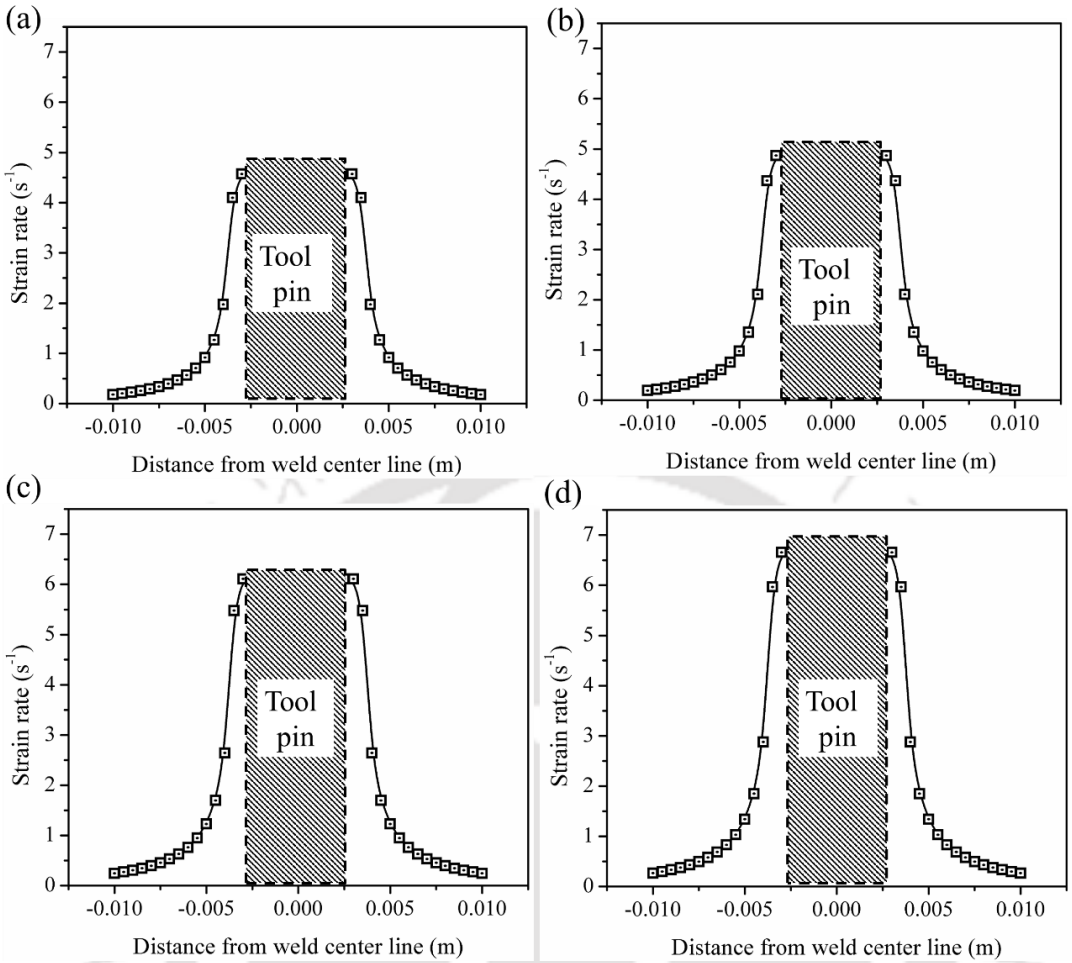

Figure 5.40: Strain rate in weld cross section from 0.001 m of top surface at different welding condition (a) 600 rpm and 63 mm/min welding speed, (b) 600 rpm and 98 mm/min welding speed, (c) 815 rpm and 63 mm/min welding speed and (d) 815 rpm and 98 mm/min welding speed.

Figure 5.41 illustrates the temperature distribution in the FSW joint along the transverse section at 0.001 m under the tool shoulder for different welding condition shown in **Table 4.5**. The temperature histories are symmetric about the weld centerline under the shoulder. The maximum temperature under the shoulder can reach up to ~ 840 K. The maximum temperature occurs at the center of the tool which is due to the large amount of plastic deformation taking place at this region.

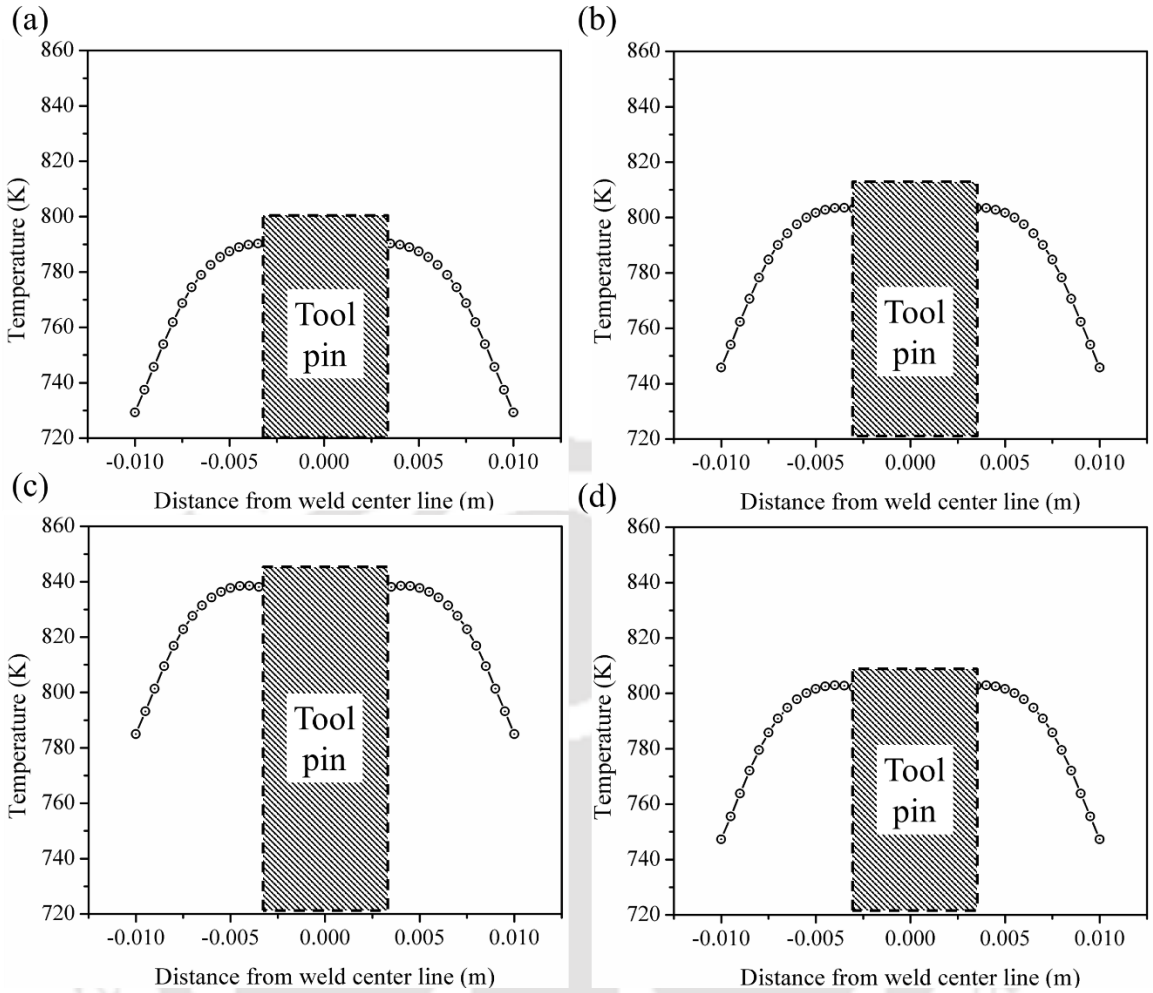

Figure 5.41: Temperature in weld cross section from 0.001 m of top surface at different welding condition (a) 600 rpm and 63 mm/min welding speed, (b) 600 rpm and 98 mm/min welding speed, (c) 815 rpm and 63 mm/min welding speed and (d) 815 rpm and 98 mm/min welding speed.

The initial average grain size (D_i) is approximately ~ 98.42 μm corresponding to base material. This initial grain size, along with the temperature, strain-rate and strain values predicted from the analytical models, yields the final grain size distribution in the weld zone using the following equation suitable for dynamic recrystallization:

$$D_{CDRX} = 55\varepsilon^{-0.145}\dot{\varepsilon}^{-0.282}D_i^{-0.104}\exp\left(-\frac{Q}{RT}\right) \quad (5.3)$$

where the material constant terms are evaluated such that the error between calculated and experimental value is minimized. The constants in the equation were obtained by solving the

equation at different points of the grain size distribution from experimental work as explain in **Fig. 3.14** of section 3.3 computational aspects in chapter 3. The values of activation energy (Q) and gas constant (R) assumed are 140 kJ/mole and 8.314 J/kg K, respectively. **Figure 5.42** shows the final prediction of grain size from analytical model. It shows relatively better agreement with experimental data of welding condition at 815 rpm and 63 mm/min welding speed.

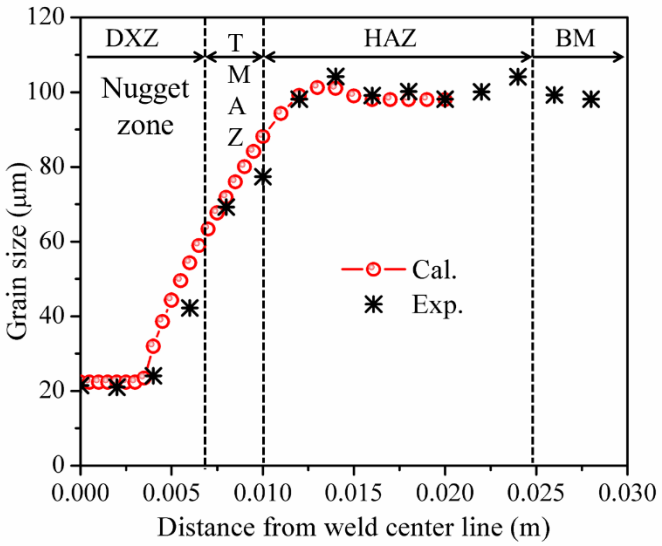

Figure 5.42: Calculated and experimental grain size distribution in different zone during at 815 rpm and 63 mm/min welding speed.

Figure 5.43 shows the predicted grain size in weld zone from Eq. 5.3 by incorporating kinetics of CDRX as a function of temperature and strain rate. The maximum strain occurs close to the tool pin surface and therefore significant refinement in the grain size occurs in the nugget zone. It is indicated that the strain rate increases with increase in velocity field. The grain refinement decreases as move away from tool axis due to the decrease in effect of temperature and strain rate [8]. It's also observed that with increase in welding speed from 63 to 98 mm/min, the average grain size in the nugget has decreased considerably because of lesser heat input. As it is known, an increase in temperature leads to an increase in grain size (815 rpm and 63 mm/min welding speed) and, on the contrary, an increase in strain rate leads to a decrease in grain size (815 rpm and 98 mm/min welding speed) [329].

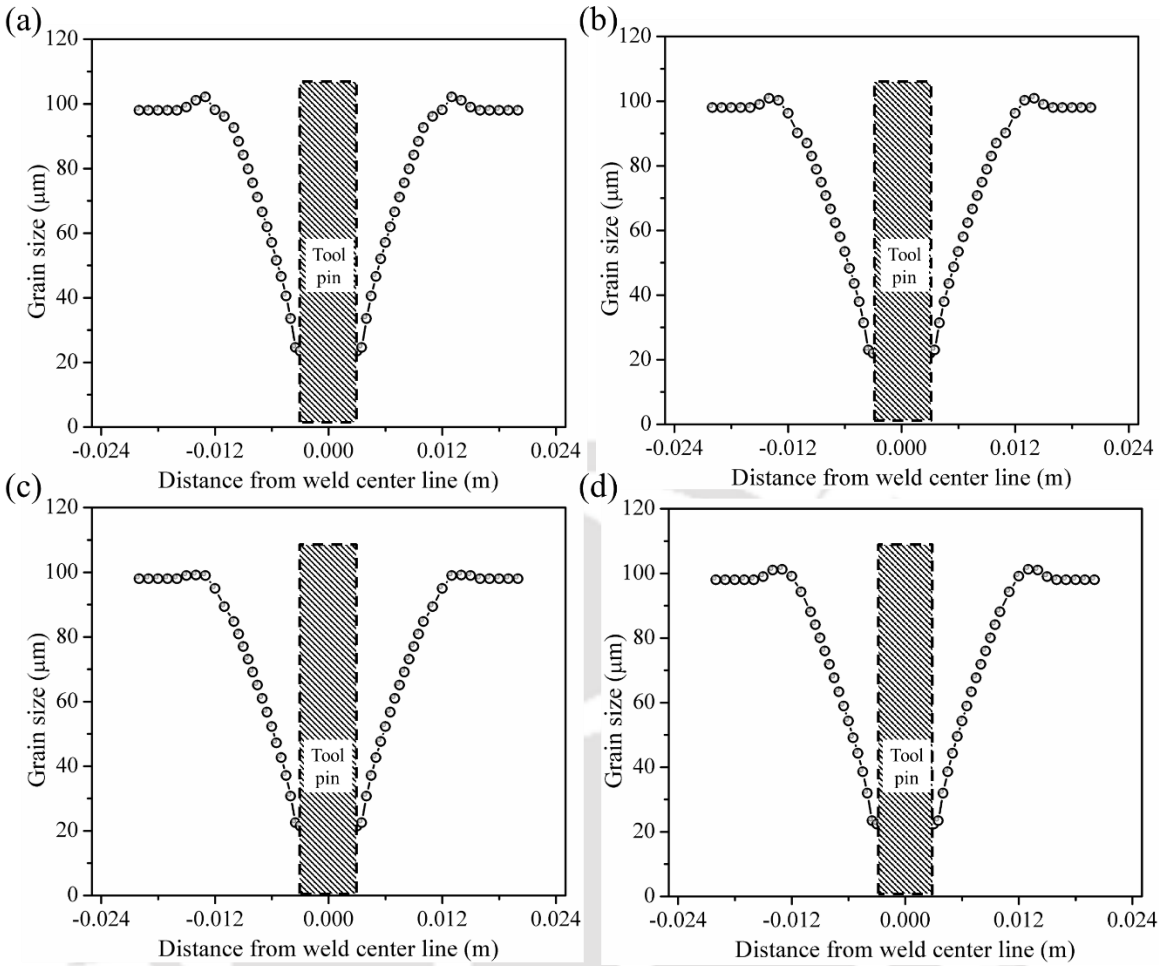

Figure 5.43: Grain size estimation in weld cross section from 0.001 m of top surface at different welding condition (a) 600 rpm and 63 mm/min welding speed, (b) 600 rpm and 98 mm/min welding speed, (c) 815 rpm and 63 mm/min welding speed and (d) 815 rpm and 98 mm/min welding speed.

The grain size during CDRX strongly dependent on material parameters as a function of strain rate and temperature. **Figure 5.44** illustrates the experimental and calculated grain size in nugget zone with percentage of error for welding condition as shown in **Table 4.5**. The experimentally measured grain sizes in the nugget zone ranges ~17 - 23 μm. It can be seen that the grain size of the stirred zone is reduced by increasing the traverse speed. The maximum effect of dynamic recrystallization and the minimum annealing effect on the welding heat input at higher traverse speed are responsible for fine refinement of grains. On other hand, an increase in the peak temperature with increase in rotation speed leads to generation of coarser recrystallized grains. Overall, the percentage error of grain

size between calculated and experimental result is ~ 6 - 16 which is acceptable prediction for present developed model. Although the above constitutive equation of grain size is validated for present material and the analytical model for strain rate will be able to work quite reasonably with different workpiece materials, it may provide an optimal design of process parameters for a target microstructure of FSW process.

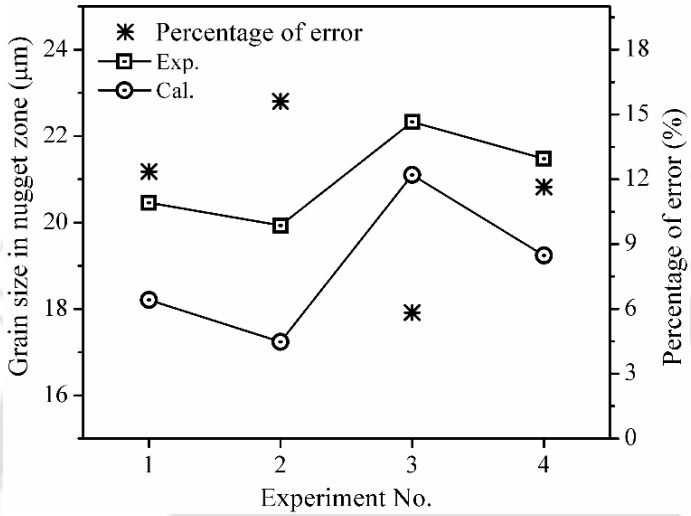

Figure 5.44: Experimental and estimated grain size in nugget zone with percentage of error.

5.4 Process efficiency of hybrid FSW

Preheating the workpiece just ahead of FSW tool can reduce heat generation between the rotating tool and the work-piece caused by friction and plastic deformation. Preheating of workpiece also decreases wear rate of the tool and improve microstructure. Therefore, the additional evaluation is a comparison of the hybrid process with the conventional one while assuming the same process condition of FSW. As the preheating during FSW is increasing the amount of heat generation required by FSW is also reducing to attend the required welding temperature (0.8-0.9 of melting point). As preheating increased the amount of heat generation by friction and plastic deformation is also reduced with the reduction of plunging force and yield stress with increase in temperature. So, the process efficiency of FSW with preheating is calculated in respect of heat generation from FSW without preheating.

$$\text{Process efficiency of FSW } (\eta) = \frac{\text{Heat generation from FSW}}{\text{Mechanical energy input from FSW}} \times 100 \qquad (5.4)$$

$$\text{Mechanical energy input from FSW} = \text{Angular velocity} \times \text{Torque} \quad (5.5)$$

$$Overall\ efficiency\ of\ P-FSW\ (\eta_{overall}) = \frac{Total\ heat\ generation\ from\ P-FSW}{Total\ energy\ input\ from\ P-FSW} \times 100 \quad (5.6)$$

$$Total\ heat\ generation\ from\ P-FSW = Heat\ generation\ from\ FSW + Heat\ input\ from\ preheating \quad (5.7)$$

$$Total\ energy\ input\ from\ P-FSW = Mechanical\ energy\ input\ from\ FSW + Heat\ input\ from\ preheating \quad (5.8)$$

Process efficiency is calculated for similar and dissimilar material joining where FSW parameters are constant such as tool rotation (815 rpm), welding speed (98mm/min) and tool geometry (shoulder diameter 20 mm and pin diameter 6 mm) but other parameters are varying with preheating such as plunging force, yield strength and coefficient of friction. Plunging force is output parameter which are measured during experiment. But yield strength and coefficient of friction are intended from corresponding temperature estimated during simulation just ahead of FSW tool. After estimating the input parameters for heat generation calculation, the heat generation during FSW is calculated from **Eq. 3.23**. The analytical result for heat generation can be correlated with mechanical energy input from FSW tool. The plunge force is taken from experimental observations and the estimated analytical heat generation is 1493.19 W based on the experimental average plunge force F = 5.51 kN observed during welding phase. Substituting known values for the parameters, tool dimensions of shoulder radius = 10 mm, pin radius = 3 mm, pin height = 5.7 mm, and rotation speed of $\omega = 85.34$ rad s^{-1}, and gives a value of $\mu = 0.3$. The analytical estimate for the heat generation equals the mechanical energy input from FSW tool ($M \times \omega$) is 1792.14 W. Therefore, the process efficiency of FSW without preheating is 83.39 %. In case of preheating, the heat input form preheating source is calculated from **Eq. 3.5.** At preheating condition of 15 A total heat input is equal to 252 J/mm from preheating source with 70 % efficiency of heat input from preheating source. The efficiency of FSW process is 88.03% with overall efficiency of P-FSW is 84.5%. **Table 5.3** shows the variable input parameters at different preheating condition and efficiency of hybrid FSW for similar aluminum joint. As the preheating current is increased the average value of plunging force during welding phase

is also decreased up to 77.3 %. Similarly, yield strength of material is also reduced with increase in preheating current. Therefore, heat input required from FSW tool to plasticize and stir the material is also decreased. The efficiency of FSW is also improved with preheating as shown in **Table 5.3**.

Table 5.3 Input parameters for heat generation calculation and hybrid FSW process efficiency at different preheating condition for aluminum joint.

Preheating Current (A)	Torque (N-m)	Plunging force (KN)	Yield stress (N/mm^2)	Coefficient of friction (μ)	Efficiency (η)	Overall efficiency ($\eta_{overall}$)
0	21	5.51	23	0.3	83.39	83.3
15	17.5	5.01	19.1	0.3	88.03	84.5
25	15.8	4.63	16.8	0.3	88.61	82.8
35	14.5	4.10	15.1	0.3	85.93	79.4
45	13.0	3.72	12.5	0.3	84.40	77.3

Table 5.4. Input parameters for heat generation calculation and hybrid FSW process efficiency at different preheating condition for Cu-Al joint.

Preheating Current (A)	Torque (N-m)	Plunging force (KN)	Yield stress (N/mm^2)	Coefficient of friction (μ)	Efficiency (η)	Overall efficiency ($\eta_{overall}$)
0	38.1	8.10	55	0.33	82.89	82.89
25	30.9	7.25	47	0.33	89.53	85.91
35	28.2	6.98	40	0.33	89.28	84.29
45	25.3	6.41	32	0.33	86.31	80.87
55	20.2	6.08	19	0.33	87.50	79.91

Table 5.4 shows the variable input parameters at different preheating condition and efficiency of hybrid FSW for dissimilar Cu-Al joint. The process efficiency of FSW without

preheating is 82.89 %. During dissimilar joint similar trend is observed for torque, plunging force and yield stress with the application of preheating. The heat input from FSW is reduced with increases in preheating. With increase in preheating efficiency of FSW is improved but overall efficiency of P-FSW is decreased at higher preheating current due to higher heat loss from preheating source.

5.5 Effect of tool off-set for dissimilar materials

Tool offset is one of the most significant parameters during joining of dissimilar Al-Cu materials by friction stir welding process. An investigation is carried out on the effect of tool offset on the weld morphology, material flow pattern, and mechanical properties of the joint. It was found that offsetting tool towards aluminum side along with a plasma-assisted heat source is an effective way to address one of the most important apprehensions in aluminum-copper solid state welding process. The offset influences the amount of intermetallic at the joint interface and in-effect impacts on final strength and material flow behaviour. The relationship between microstructure with reference to intermetallic compounds and the mechanical properties of weld joint is investigated as well. The plasma arc is placed on the copper plate to preheat the copper (up to 420 – 470 K) that is 13 mm away from the weld center with an angle of 60˚ with respect to the FSW tool axis and at plasma current of 55 A. The tool rotational speed is 815 rpm and welding speed is 98 mm/min. Stainless steel of grade H13 is used as FSW tool material which have a 20 mm diameter flat shoulder, 6 mm diameter straight cylinder pin and 5.7 mm pin length. Total eight set of experiments are conducted with variation of tool offset in Al side as 0.0, 0.5, 1.0, 1.25, 1.75, 2.0, 2.25, and 2.75 mm.

The optimum strength of weld joint for dissimilar materials is indirectly influenced by the mixing ratio of two materials since the formation of intermetallic partly depends on this mixing ratio. The quantitative estimation of mixing ration is represented as a function of tool offset (X) where the geometric shape and size of the tool shoulder and pin stir the material volume for a particular transverse speed independent of tool rotational speed. Therefore, the interaction volume of two materials is analytically found out with the effect

of tool offset. So, the area covers under the shoulder with respect to two different materials (Cu-Al) as shown in **Fig. 5.46** is calculated as follows:

$$Area\ of\ a\ circle\ segment\ ODB = \pi R^2 \frac{\theta}{360} \quad (5.9)$$

$$Area\ of\ right\ triangle\ OEB = \frac{1}{2} X * BE \quad (5.10)$$

$$A_\theta = Area\ of\ a\ circle\ segment\ ODB - Area\ of\ right\ triangle\ OEB \quad (5.11)$$

$$Distance\ travel\ at\ velocity\ 'V'\ CD = Time * V \quad (5.12)$$

$$ED = R - X \quad (5.13)$$

$$A_V = ED * CD \quad (5.14)$$

$$A_{total}(ABCD) = 2A_\theta + A_V \quad (5.15)$$

$$Shoulder\ cover\ area\ in\ copper\ side = A_{total}(ABCD) \quad (5.16)$$

$$Total\ area\ cover\ by\ tool\ shoulder = (CD * (2 * R)) + \pi R^2 \quad (5.17)$$

$$Shoulder\ cover\ area\ in\ aluminum\ side = Total\ area\ cover\ by\ tool\ shoulder - Shoulder\ cover\ area\ in\ copper\ side \quad (5.18)$$

where OE and OB is tool offset and tool shoulder radius respectively.

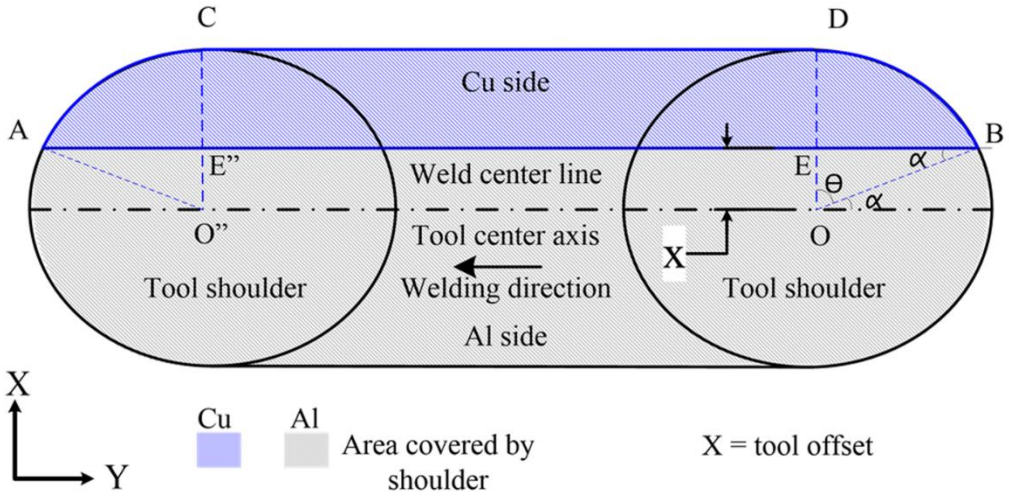

Figure 5.45. Schematic illustration of mixing amount of two dissimilar materials with respect to tool offset under the shoulder.

Figure 5.46(a) depicts the projected area of material mixing zone for both the materials as a function of tool offset. The shear layer thickness in Al side (δ_{Al}^{eff}) and Cu side (δ_{Cu}^{eff}) is considered as 0.25 mm and 0.15 mm, respectively [329]. It is also assumed that shoulder creates a uniform shear layer (δ_{eff}) in both the materials (**Fig 5.46a**). Analytically, the mixing ratio of Cu and Al with respect to tool offset is estimated in the following way. Total area in Cu side is

$$A_{Cu} = (R_{shoulder} - X) * \delta_{eff} + \left((R_{pin} - X) + \delta_{Cu}^{eff}\right) * H_{pin} + (R_{pin} - X) * \delta_{Cu}^{eff} \quad (5.19)$$

Similarly, total area in Al side is

$$A_{Al} = (R_{shoulder} + X) * \delta_{eff} + \left((R_{pin} + X) + \delta_{Al}^{eff}\right) * H_{pin} + (R_{pin} + X) * \delta_{Al}^{eff} \quad (5.20)$$

The mass flow rate is estimated as

$$M_{total} = A_{Cu} * v * \rho_{Cu} + A_{Al} * v * \rho_{Al} \quad (5.21)$$

where v is the transverse velocity of the tool.

Due to uncertainty of shear layer thickness, the mixing ratio is calculated with respect to different ratio of δ_{eff}/H_{pin}. The quantitative estimation of mixing ratio between Al and Cu with respect to tool offset is depicted by **Fig. 5.46(b)**. The mixing ratio does not vary much with respect to different ratio of shear layer and tool pin height. However, tool off-set influences much more on the mixing ratio. The optimum joint strength is obtained at the mixing ratio ~ 15 - 20 % i.e. the wt. % of Cu ~ 13 – 17 % which is corresponds to tool off-set ~ 2 – 2.25 mm. The literature also indicated that 1.5 to 2 mm pin offset is preferred to achieve good quality dissimilar Cu–Al FSW joint [330]. However, the optimum tool pin offset depends on the tool design and thickness of the workpiece to be welded. It is an effective way of solving the formation of large amounts of intermetallic-rich structures that deeply influence the final strength of the welds.

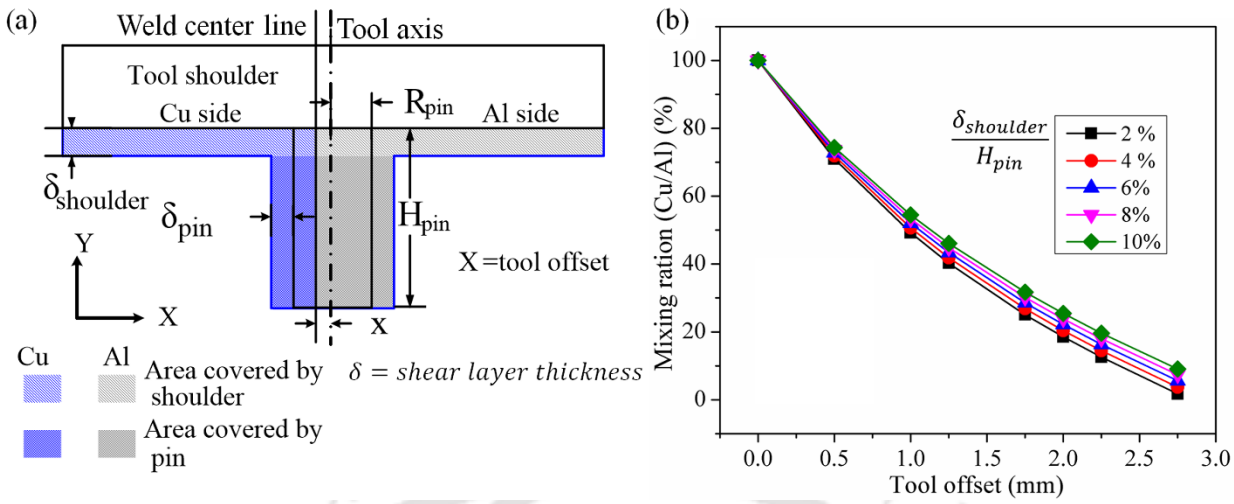

Figure 5.46. (a) Schematic illustration of the amount of copper and aluminum stir by tool. (b) Effect of tool off-set on the mixing ratio (Cu/Al) with respect to variation in shear layer thickness.

Figure 5.47 shows the temperature history of advancing side (**Fig. 5.47a**) and retreating side (**Fig. 5.47b**) at welding condition of 815 rpm, 98 mm/min welding speed, without tool off-set (0 mm) and with preheating current of 55 A. With preheating in copper side, the maximum temperature during welding is observed in the copper side (at 15 mm) which is significantly higher than the aluminium side (at 15 mm) with slight increase in temperature is observed in aluminium side. The peak temperature difference observed between copper side and aluminium side is approximately ~ 65 ˚C. Therefore, adequate preheating in copper side shows improved mixing in stir zone due to reduced plasticized state difference [331]. Additionally, it's also observed that at optimum process temperature there is considerable amount of diffusion of copper particle in the aluminium and improve the joint quality. There is a significant variation in the axial forces with respect to different phase of welding. **Figure 5.47(c)** shows the actual and average welding force during tool travel at without tool off-set. The average welding force is around ~ 7 kN. It's shows that axial force during welding is reached steady state condition with minimum variation due to obtaining required welding temperature and stabilized welding condition.

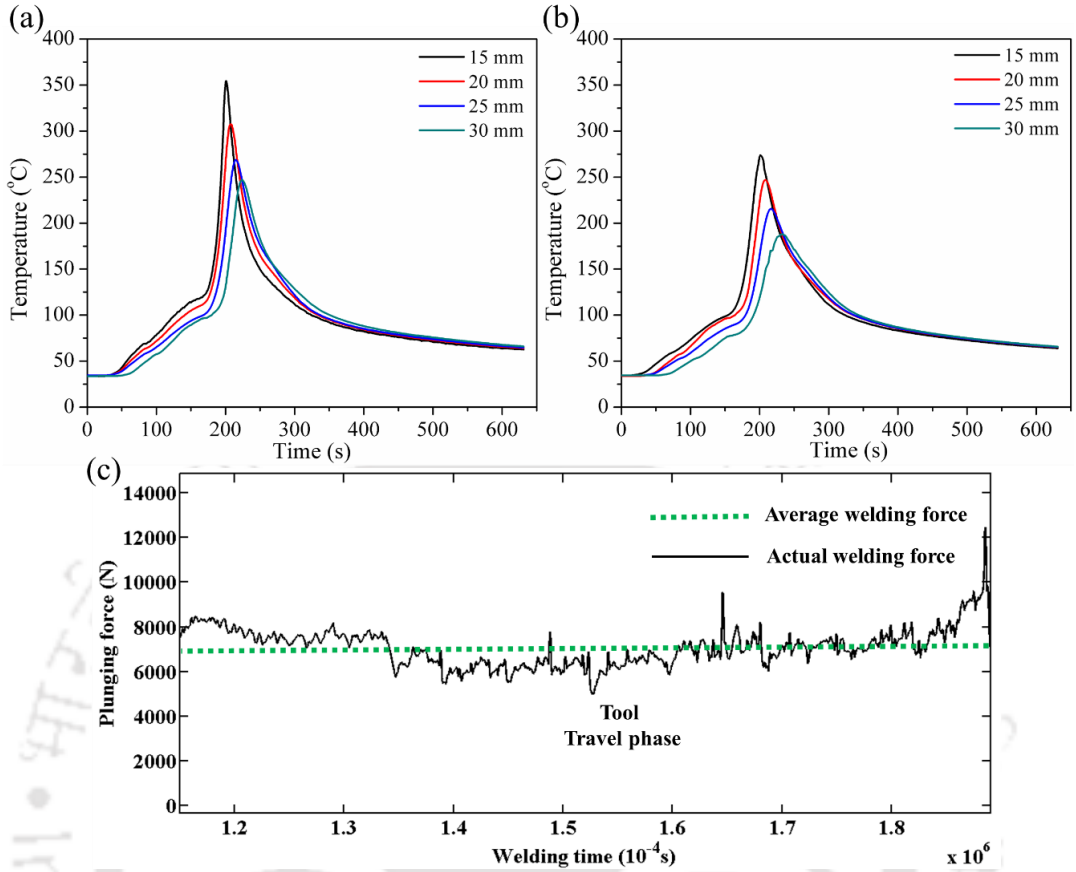

Figure 5.47. (a) Thermal history in advancing side (b) Thermal history in retreating side and (c) Welding force at experimental condition of 815 rpm, 98 mm/min welding speed and without tool off-set (0 mm) with preheating current of 55 A.

Figure 5.48 illustrate the influence of different tool offset on peak temperature at 15 mm on both side (**Fig. 5.48a**) and average welding force (**Fig. 5.48b**) during tool travel phase. It is more beneficial to maintain high temperature difference between copper side and aluminum side (60-70 ^{o}C at 5 mm from shoulder edge) during dissimilar joint. With increase in tool offset there is minor increase in temperature difference while keeping constant offset of preheating source with respect to weld center line in copper side. The tool offset does not produce any significant effect on thermal history and peak temperature. Whereas, **Fig. 5.48(b)** shows little significant effect on the magnitude of average welding force during welding period with respect to variation of tool offset. The average welding force reduces around 0.15-0.25 kN with increase in tool offset. The plunge force decreases with increase in tool pin offset, because of the tool pin is immersed into soft material (Al), while at lower

pin offset the plunge load increased. However, the optimum location of tool offset is significant to control intermetallic compound formation. Overall, the variation in temperature difference and welding force strongly depends on preheating current as compared to tool offset.

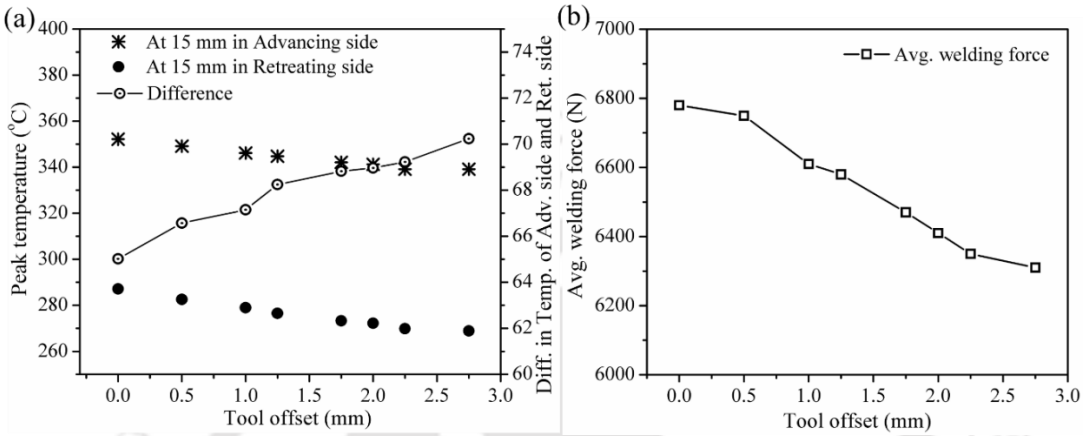

Figure 5.48. (a) Peak temperature and difference in peak temperature at different tool offset and (b) Average welding force at different tool offset.

Figure 5.49(a) depicts the tensile strength at different tool off-set. It is observed that as the tool off-set is increased to aluminum side, joint strength and ductility is improved considerably. At tool off-set of 2 mm with 55 A plasma current shows the maximum tensile strength. Further increase in tool off-set value does not improve the joint strength and the ductility. At zero off-set equal volume mixing probably produces large amount of IMCs because of high chemical affinity between Al and Cu. The presence of these brittle IMCs in overall structure do not produces good amount of joint strength and ductility. The impression of hybrid FSW process lies on the fact that preheating improves interaction between two materials and tool off-set control IMCs formation through controlling of the stirred volume. But tool offset higher than 2 mm (for Φ 6 mm pin) reduces the volume of interaction and bonding propensity which results in low joint strength. The fracture toughness of a specimen can also be determined using a three-point flexural test. This test is very sensitive to defects near the surface of the weld bead, such as root flaws. During the test a 1 mm/min cross-head speed is used and one specimen for each type of weld and base materials are tested. No root flaws or other defects are detected in most of the joints. From the **Fig. 5.49(b)** it is observed that, the ultimate bending strength and the displacement at

joint failure point is optimum at tool off-set of 2 ~ 2.25 mm. So, the sizes of Cu particles are being maintained through tool pin offset parameter. In addition to this, the larger tool pin offset toward an Al material gives more stirring at Al side which leads to form Al matrix and that provides a better path to the smaller Cu particles. These smaller Cu particles help to make good metallurgical bonding with an Al matrix by reducing the amount of IMCs [332].

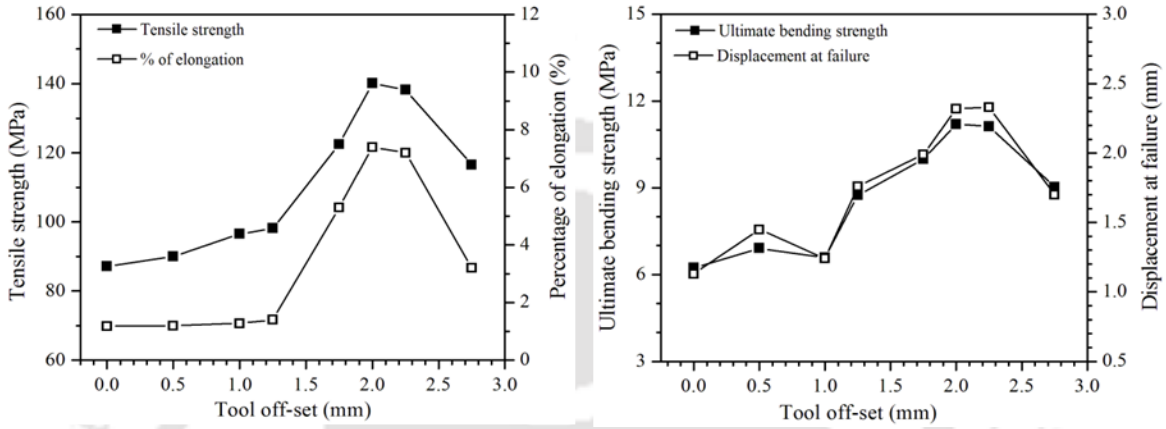

Figure 5.49. Tensile strength and bending strength at various tool offset.

In order to find the reason behind variation in joint efficiency, the tensile fracture surface is analyzed using SEM and EDS methods. **Fig. 5.50** shows the results of SEM analysis of tensile fractured surface at tool offset (a) 0.0 mm, (b) 0.5 mm, (c) 1.25 mm and (d) 2.0 mm. As shown in **Fig. 5.50(a, b)**, fracture patterns of crack propagation exhibited brittle dominating fracture mode. The fracture surface is accompanied with layered flat surfaces at the fracture surface which indicate brittle fracture mode. It is due generating large amounts of IMCs in the weld area which decreases the weld strength of the joint [333]. Also high tool pin insertion (i.e., 0 mm) gives poor joints and produces many defects. The welds without and low tool offset shows the brittle fracture behavior. On the other hand, features of ductile fracture mechanism like small dimples can also be seen from **Fig. 5.50(c, d)** at some regions. The fracture surface is accompanied with layered flat surfaces at the fracture surface and locally some dimple which indicate brittle fracture mode. However, layered flat surfaces have covered more region than the dimples on fractured surface. So, brittle fracture mechanism was dominant on ductile fracture mechanism. The causes of these defects may be attributed to generation of the brittle IMCs. It indicates that IMCs may have

been presented at different fractured locations that subsequently give brittle fracture mechanism. IMC phases such as Cu_9Al_4 and $CuAl_2$ were likely to have been presented at these locations based on atomic percentage values of XRD analysis.

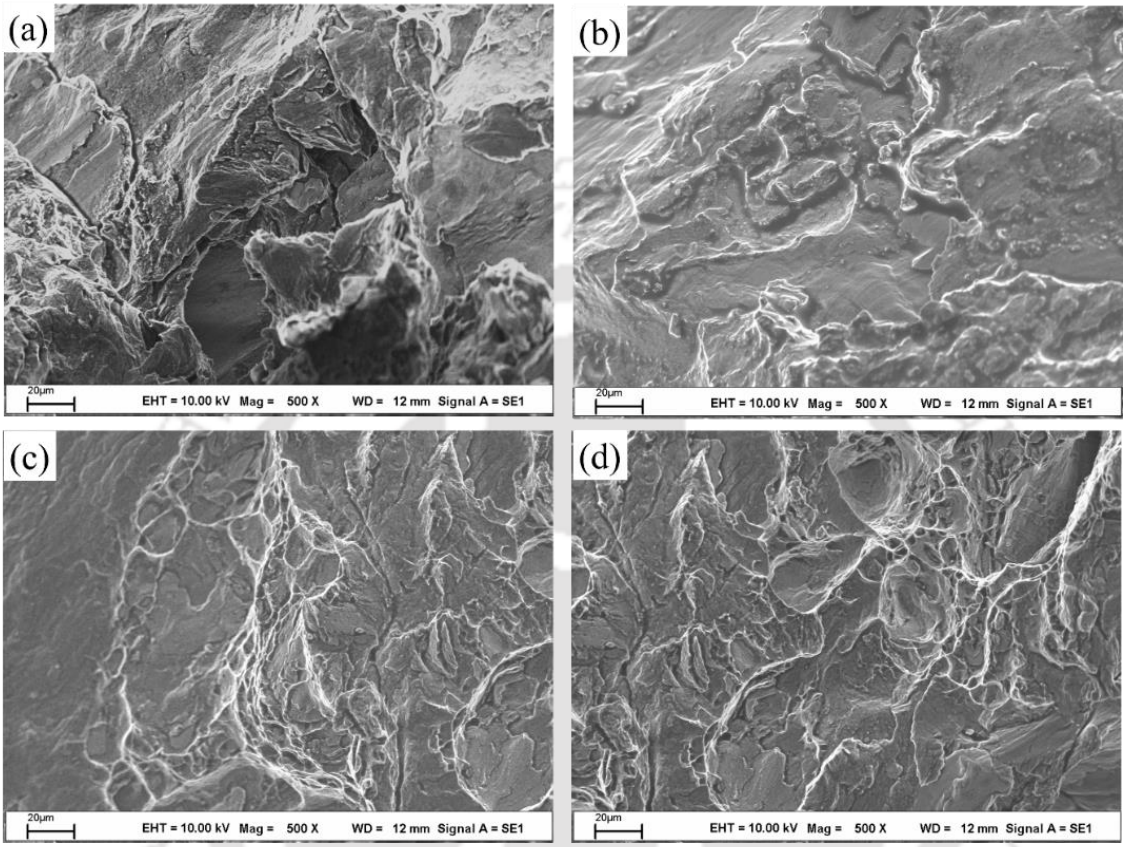

Figure 5.50. Fracture surface morphologies of joints in zone at tool offset (a) 0.0 mm, (b) 0.5 mm, (c) 1.25 mm and (d) 2.0 mm.

Figure 5.51(a) shows the hardness distributions at tool offset 0.0 mm which is measured along the transverse cross section of welded specimen at three different line in the weld zone. From **Fig. 5.51(a)** at without tool offset the value of hardness reaches 63 HV to 176 HV at interface. The increase in percentage of copper at without and low tool offset causes more interaction of copper in stir zone which increases the amount of IMCs as well as types of IMCs. So, hardness of joint area increases as the tool offset in copper side along with influence of preheating. These IMCs are responsible to increase hardness and brittleness in the stir zone and that also causes defects. Therefore, hardness distribution, amount of hardness and size of Cu particles strongly depend on tool pin offset. However, in

dissimilar joint the amount of interaction of two materials at interface is attributed to joint quality. So, hardness distribution in weld zone at interface can visualize material flow and fraternization of two different materials. **Figure 5.51(b)** shows the variation of average hardness at 4 mm on both side of weld center line along the transverse cross section of welded specimen. It's observed that as tool offset towards aluminum side, the amount of copper intricate in weld zone is reduced and the average hardness in weld zone is also decreases. At without and smaller tool pin offset generates large amounts of IMCs in the weld zone due to more inter-diffusion of copper through extreme deformation and intense stirring under the influence of copper preheating. Its attributed to the formation of the intermetallic compounds ($CuAl_2$, CuAl, Cu_9Al_4) due to high temperature associated with strong stirring of Al and Cu. These intermetallic compounds lead to inhomogeneous hardness distribution in weld zone and causes many defects along with decrease in joint strength. On the other hand, when the pin offset is large (~ 2 mm) toward an Al material gives more stirring at Al side which leads to form Al matrix and that provides a better path to the smaller Cu particles. These smaller Cu particles help to make good metallurgical bonding with an Al matrix by reducing the amount of IMCs.

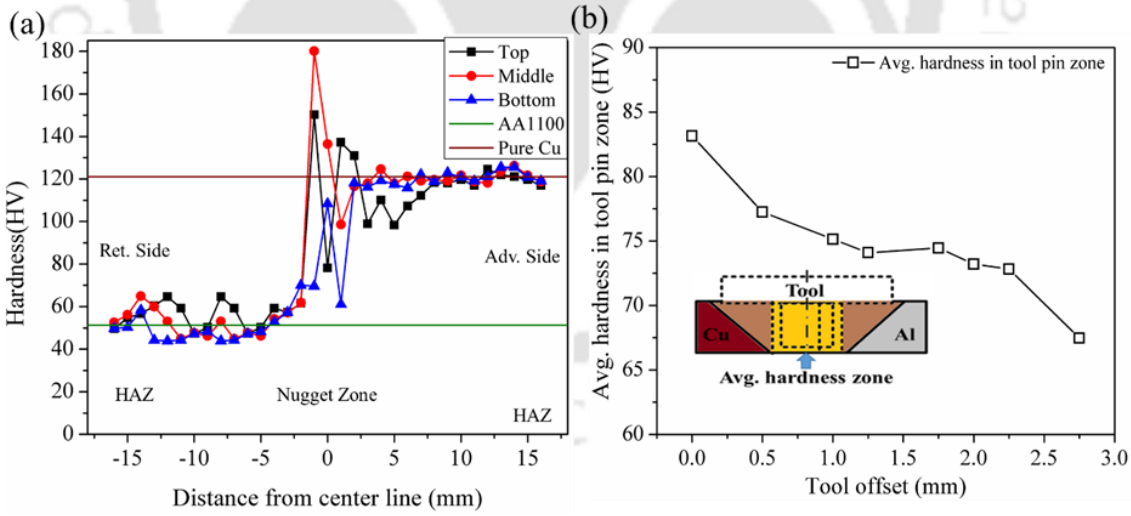

Figure 5.51. (a) Hardness distributions on the transverse cross-section at 0.0 mm tool offset and (b) Variation of average hardness at 4 mm on both side of weld centre line.

Figure 5.52 illustrates the material flow pattern in nugget zone at tool offset of 0.0 mm and 2.0 mm. Without any tool offset bulk amount of copper interact with aluminum due

to improved plastic flow caused by preheating. This interaction develops thick intermetallic layer with composition of copper rich brittle IMC having tendency of crack during cooling. However, at 2 mm tool offset proper interaction between Cu-Al is occurred, which gave rise to the smooth uniform and continuous thin intermetallic layer all along Al/Cu interface. Therefore, the sound joint is achieved from a proper material flow and metallurgical bonding through a narrow intermetallic layer at the interface by the occurrence of lamellar composite structure in the stir zone [332].

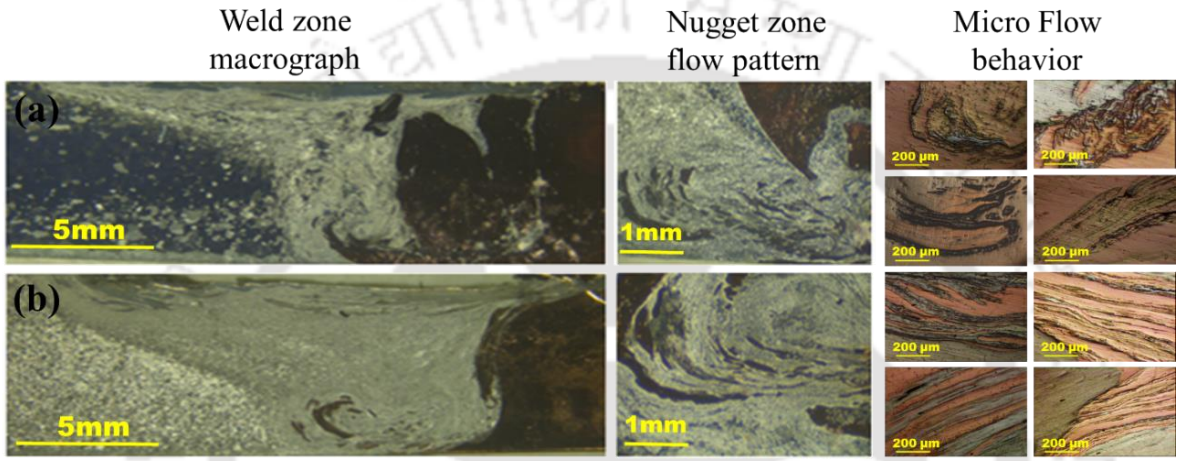

Figure 5.52. Macrograph of weld zone and material flow pattern in nugget zone at tool offset (a) 0.0 mm and (b) 2.0 mm.

The harmful effect of intermetallic is alleviated by producing small quantity of these compounds, discrete and fine IMC and finally the thinness of the continuous intermetallic layers at the interface. **Figure 5.53** shows the quantitative estimation of intermetallic layer at lamellar composite structure of the nugget zone. At low tool off-set relatively thicker layer of intermetallic is observed which is mostly non-uniform and discontinuous and follows wide variability. The thinness of the layer was probably the factor preventing its deleterious effect on the tensile strength of the weld zone. Most of the joints are defect free; but there are some joints having voids and cracks at low tool off-set (**Fig. 5.54a**). **Figure 5.54(f)** depicts the variation of intermetallic layer at different tool off-set value. At 2 mm tool off-set, a thin-continuous intermetallic layer is observed without any micro defect. At higher temperature more quantity of copper islands and particles dispersed inside the nugget zone and extend diffusion deeper into them, therefore making the intermetallic layer thicker than

the intermetallic layer at higher tool offset. Overall, the rate of formation of intermetallic is controlled largely by the rate of diffusion of aluminum atoms into copper lattices by controlling the amount of interaction and heat input. Heating by plasma arc helps in generating continuous intermetallic structure supported by improved plastic flow in nugget zone. However, further increase in tool off-set the intermetallic layer thickness decreases (**Fig. 5.54h**). This is probably not a continuous intermetallic layer and there is insufficient metallurgical bonding between Al/Cu.

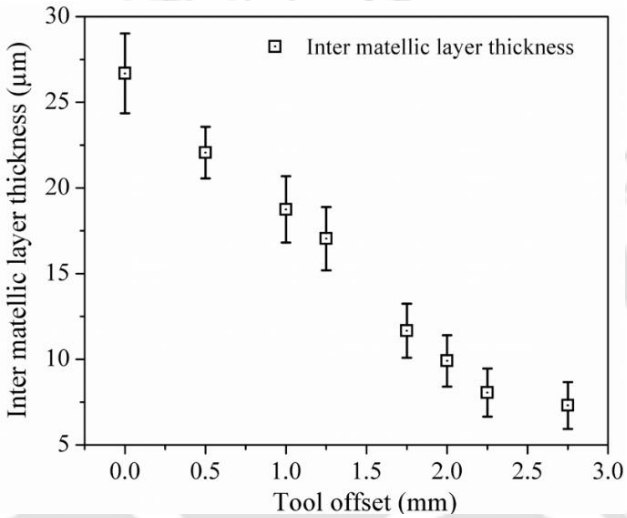

Figure 5.53. Variation of average intermetallic compound layer thickness at different tool offset.

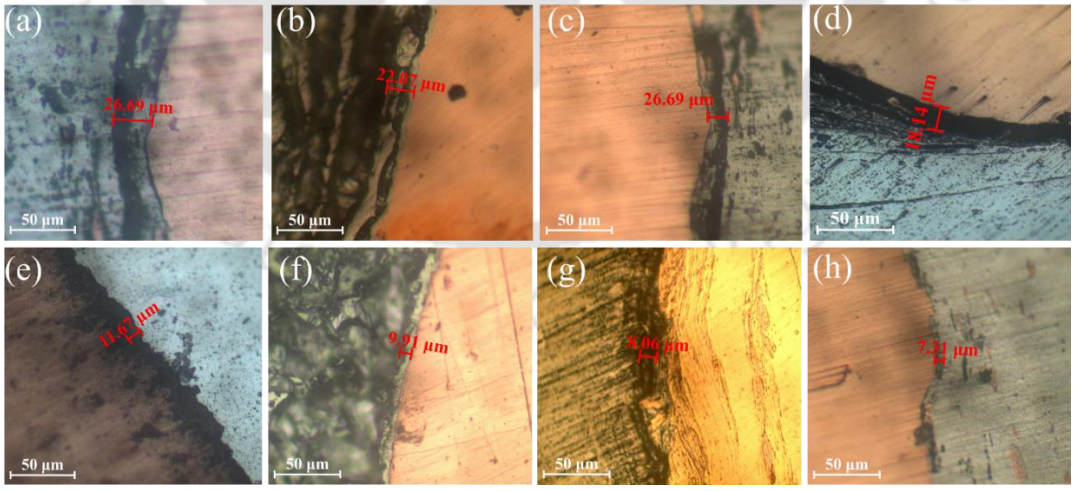

Figure 5.54. Micrograph of intermetallic layer at different tool offset (a) 0.0 mm, (c) 0.5 mm (d)1.0 mm, (e) 1.25 mm, (f) 1.75mm, (g) 2.0 mm, (h) 2.25 mm and (d) 2.75 mm.

Figure 5.55 shows XRD patterns of weld zone to distinguish intermetallic compounds without tool offset (Fig. 4a) and 2 mm tool offset (Fig. 4b) at the weld centre-line. According to the ratio of elements Al and Cu, the nano scaled stoichiometric IMCs Al_4Cu_9 (γ) and Al_2Cu (θ) formed. In some occasion, the phase AlCu (η) formed as well. It is observed that high amounts of $CuAl_2$ and Cu_9Al_4 are generated around the larger Cu particles without any tool offset. However, at 2 mm offset (Fig. 4b), the weld nugget contains $CuAl_2$ intermetallic compound that increases with higher offset and preheating. These intermetallic compounds are found as continuous non-linear layer in the Al side and worked as dispersed particles which provide a reinforcing effect in this zone.

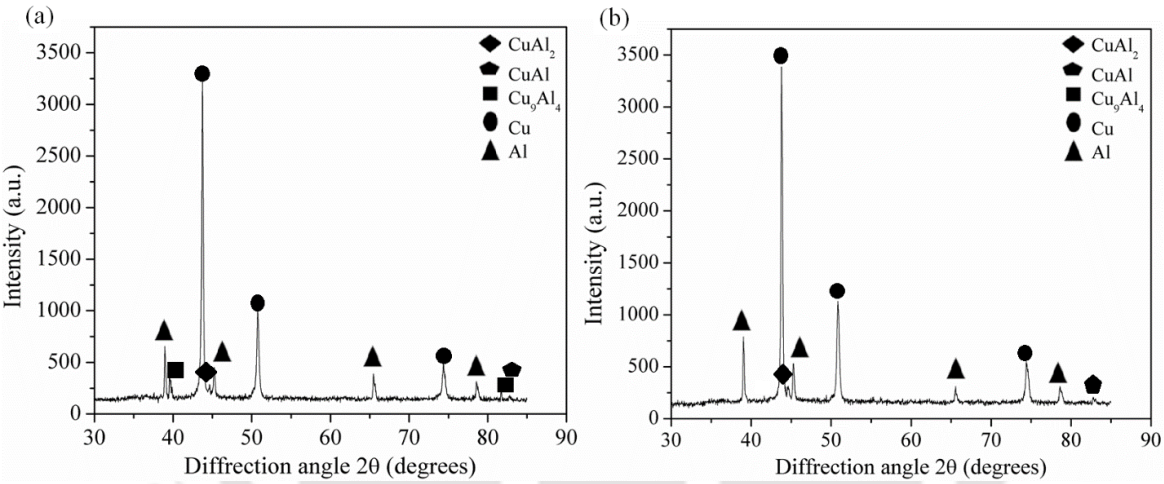

Figure 5.55. XRD patterns of weld zone at (a) without tool offset and (b) 2 mm tool offset at the weld center in nugget zone.

5.6 Cooling rate and microstructure

The microstructure and mechanical properties of the welded joint is significantly affected by welding parameters such as heat input during welding, the composition of the material used, and the rate of heating and cooling of the welded zone [334]. Therefore, this section illustrates the effect of preheating condition and process parameters on cooling rate and microstructure during P-FSW of similar and dissimilar joints. Here the cooling rate is estimated by change in temperature with respect to change in time ($\sim dT/dt$) for a fixed thermocouple location. **Figure 5.56** illustrates the rate of change in temperature with respect to time i.e. the heating and cooling rate corresponding to time-temperature profile for nearest thermocouple location for welding condition of 815 rpm, 98 mm/min welding speed and 2

mm tool-offset. It is obvious that there is wide variation of cooling rate in copper and aluminium side. Preheating builds up heat and it takes little longer time to cool down to ambient temperature. The maximum rate of temperature change is less than 35 K/s in copper side and 15 K/s in aluminium side are observed. This much variability in cooling rate influence more on microstructural changes on aluminium side as compared to copper side. Also the coexistence of deformation and temperature during FSW cause to dynamic restoration phenomena such as dynamic recovery and recrystallization. It is also observed that, at high temperature, as the strain rate decreases the growth of grains progress towards its maximum value [335]. Therefore, the grain coarsening effect in this temperature range is occurred.

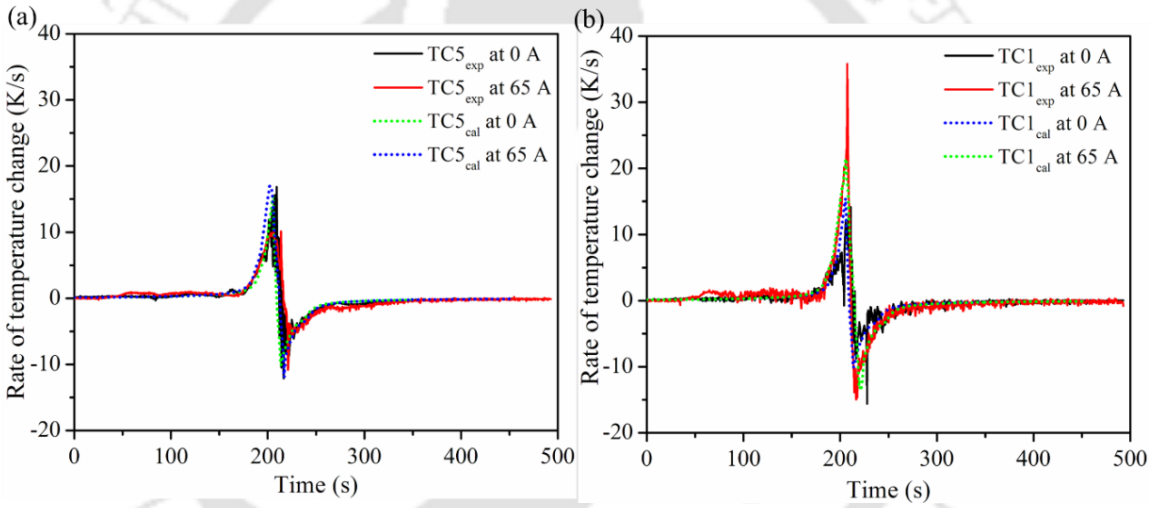

Figure 5.56. Comparison of calculated and experimental rate of temperature change at 815 rpm, 98 mm/min welding speed and 2 mm tool-offset: (a) Aluminium side and, (b) Copper side.

Figure 5.57 shows the microstructure of weld nugget on aluminum side at varying preheating current. Grain size increases with increase in peak temperature. At 65 A plasma current, the average grain size of nugget zone is 28.34 μm whereas it is 23.47 μm without the effect of preheating. Thus it is obvious the grain coarsening effect is predominant with the effect of preheating. In the weld nugget zone, the grains are finer as compared to base material structure. The attainment of high temperature and dynamic stirring force of the tool pin promotes continuous dynamic recrystallization in the nugget zone for highly deformed

aluminium. However, the amount and type of transformations is directly affected by the maximum temperature (mostly related to rotational speed) and cooling rate (mostly related to advancing speed). Other external heating (e.g., plasma) and cooling during FSW also play a critical role in altering these phase transformations and the resulting grain size for specific materials. It is observed that the microstructural changes are found excessive in aluminum as compared to copper. This is possible due to difference in melting temperature between aluminum and copper and produces considerably more changes in microstructure for aluminum. The estimation of the maximum temperature for aluminum side is 80 % of melting temperature whereas only 50 % for copper although these temperature would be a reasonable feature of the FSW process to join between aluminium and copper.

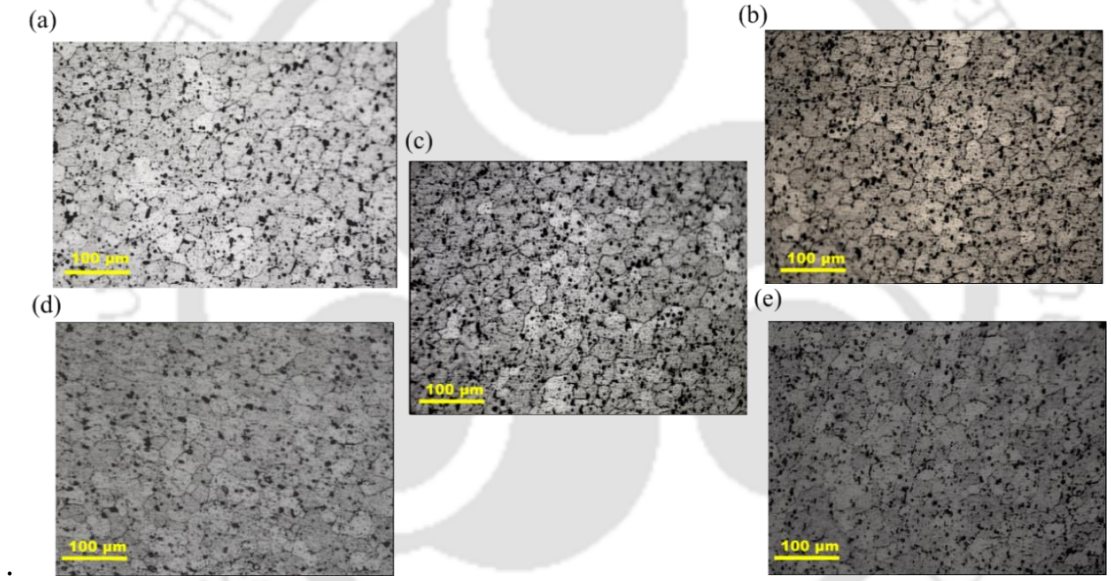

Figure 5.57. Comparison of microstructure of nugget zone in Al side at different preheating current from 0 to 65 A at 815 rpm, 98 mm/min welding speed and 2 mm tool-offset: (a) 0 A, (b) 35 A, (c) 45 A, (d) 55 A and (e) 65 A.

As the preheat current increases, the time to reduce the maximum temperature at the interface slightly increases but consequently, the cooling gradient becomes steep due to the rapid heat adsorption by the adjacent region. This leads to change the microstructure in the nugget zone of aluminium side with respect to change in cooling gradient as shown in **Fig. 5.58**. The average grain size within the nugget zone is about 20-28 µm for the maximum cooling rate of 16.1 - 48.2 K/s. At equivalent peak temperature, the grain size in the nugget

zone of aluminium side increases with preheating current (**Fig. 5.58a**). Offset towards aluminum side does not affect much on grain size and cooling rate (**Fig. 5.58b**). The peak temperature and strain rate in nugget zone are deemed to be more effective factors as compared to cooling rate which dominates to generate final grain size. Additionally, higher degree of deformation results in finer grain stirred zone (**Fig. 5.58c**) where higher peak temperatures result in coarse grains (**Fig. 5.58d**). The recrystallized grains in the nugget zone are due to heat input and mechanical action of the tool pin that is governed by continuous dynamic recrystallization and grain growth process [336]. Generally, the average grain size decreases with decreasing working temperature and increasing stain rate. But the final grain size in nugget zone is not attributed by the natural aging since the cooling rate in FSW is low as compared to the critical cooling rate in quenching after the isothermal heating [289].

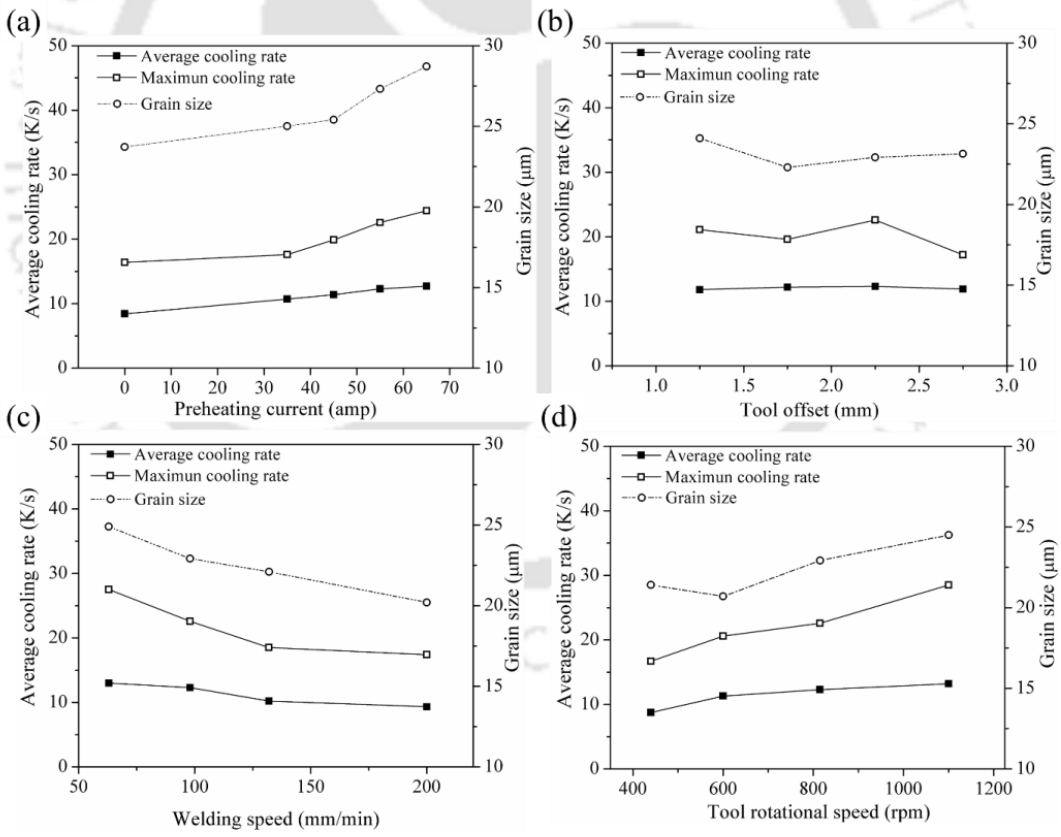

Figure 5.58. Effect of process parameters on variation of grain size in nugget zone of Al side with respect to average and maximum cooling rate at TC5 (a) Preheating current (b) Tool offset (c) Welding speed and (d) Tool rotational speed.

5.7 Summary

The present chapter demonstrates the performance of heat transfer analysis of FSW and P-FSW, in which the numerical model predicts the thermal history. At first, the heat transfer analysis has been performed for conventional FSW process. Effect of heat generation due to plastic deformation by the tool pin is accompanied to estimate heat flux for moving heat source. The heat generation both from the pin side and the bottom surfaces has effective role in this analysis. Temperature distributions are not symmetric around welding line and maximum temperature occurs behind the tool pin. The comparison between experimentally measured and calculated thermocouple point agrees well, even though the advancing side temperature underestimates and the retreating side overestimates the predicted temperature due to symmetric heat generation by sliding and sticking conditions. Percentage error of peak temperature between experimental and calculated results at different locations is less than 5.5%, which is reasonable for the reliability of the developed numerical model. The inclusion of non-symmetric heat source model will definitely enhance the scope of predicting different temperature profiles between advancing and retreating sides. This is the future scope of the work to enhance the reliability of mathematical modelling. The analytical model to predict recrystallized grain size distribution in weld zone under the shoulder shows adequate accuracy. The final grain size in the weld zone depends on temperature and strain rate in FSW process.

P-FSW for joining of AA 1100 has been investigated where plasma arc is used to preheat the material ahead of FSW tool and enhances the material flow to improve the weld quality. An attempt has been made to study the effect of plasma current on the thermal history of friction stir welded joint. A fair agreement between experimental and computed temperature distribution using a 3D non-linear transient heat transfer model is achieved. However, the calculated values of weld nugget for P-FSW require further verification. In P-FSW, 30 K more peak temperature is achieved outside of the stirred zone (minimum distance location of thermocouple) as compared to conventional FSW process. As the preheating current increases the temperature ahead of FSW tool is also improved along with the improvement in plasticized state temperature up to a certain limit. Preheating ahead of tool reduces yield stress up to ~ 12 MPa at 55 A current which improves the plastic flow of

material. Preheating also builds up additional heat during welding which decreases the variability of cooling rate in welded joint.

The thermal analysis of P-FSW of dissimilar AA 1100 and pure copper has been performed. The thermal history of the weld joint has been investigated experimentally and through the development of numerical model. A preheat is beneficial to increase the temperature of the harder workpiece in front of the tool pin during dissimilar material joint, making the material easy to be welded, and possibly reduces tool wear due to difference in flow stress value. The Maximum temperature obtained in copper side at the nearest thermocouple location is ~ 316–378 K higher than the aluminum side that aims to reduce the difference in plasticized state temperature. The heat transfer model used to describe heat inputs during hybrid friction stir welding process is relatively adequate and precise to predict peak temperature of the process. The overall error in peak temperature is 5–12% and the maximum reliability is achieved as 0.84. Preheating in copper side reduces yield stress difference up to ~ 10 MPa which facilitate the stirring of dissimilar materials by FSW tool. Therefore, the satisfactory interaction between two materials is achieved at the joint interface in presence of preheating. It is also observed that, at high temperature, as the strain rate decreases the growth of grains progress towards its maximum value. Therefore, the grain coarsening effect in this temperature range is occurred. Generally, the average grain size decreases with decreasing working temperature and increasing stain rate. But the final grain size in nugget zone is not attributed by the natural aging since the cooling rate in FSW is low as compared to the critical cooling rate in quenching after the isothermal heating.

Process efficiency is calculated for similar and dissimilar material joining where FSW parameters are constant at different preheating condition. During dissimilar joint, the trend is observed for torque, plunging force and yield stress as observed in similar material joint with the application of preheating. With increase in preheating efficiency of FSW is improved but overall efficiency of P-FSW is decreased at higher preheating current due to higher heat loss from preheating source. It’s also found that during P-FSW of dissimilar aluminum-copper joint the quality of defect free weld depends on optimum tool off-set. The ultimate tensile strength of 142 MPa is achieved at 2 mm tool off-set which is about 98% of Al alloy and its elongation to fracture is 7.27%. The lamellar composite structure is

observed in the weld nugget zone at relatively high tool off-set value. The occurrence of lamellar composite structure in the stirred zone improves joint strength and reduces the brittleness. The results suggest that in addition to welding parameters and preheating by plasma arc, tool off-set also has a strong influence on intermetallic phase formation and on joint quality.

Chapter 6

Conclusions and future scope

6.0 Introduction

Solid state welding techniques have been widespread and potential joining process to be introduced in several industries and solving problems that are not possible to resolve through the most common technologies. This welding technique based on friction and plastic deformation mechanisms and shows high potential for joining similar and dissimilar material that has been studied since its discovery on 1991. It can weld aluminum, magnesium and copper alloys and particular materials interest for the energy sector. Despite being robust, FSW has encountered a number of challenges in the welding of similar and dissimilar materials with intermediate and high hardness and higher melting points as mentioned previously.

Therefore, additional heat source is used with friction stir welding (FSW) processes to overcome the shortcomings of the conventional FSW process. The additional heat source used for this purpose are thermal energy from electric resistance heat, induction heat, laser, plasma, arc, etc. and mechanical energy in the form of ultrasonic vibration. This inevitably reduces the downward force on the tool and would increase the tool life and tool performance. In summary, it is clear that the additional heat source assisted FSW processes are employed in the welding of different soft, hard as well as dissimilar materials with entirely different physical properties. This preheating integrated into FSW exhibits remarkably positive effects on the welding process, heat generation, material flow, weld mechanical properties, surface morphology and, to some extent, microstructure.

6.1 Conclusions of the Present Work

In the present work, friction stir welding of similar or dissimilar materials is performed under different process conditions. To reveal details of effect of tool system designing and hybrid technology on weld quality. The quality of a FSW weld is a key issue, and in many cases a weld must fulfill some specific quality requirements. The idea of hybrid FSW is to reduce the stresses of the tool which can be used to improve the productivity or to increase the range of applications. Heat sources integrated with the FSW tool are far more complex and P-FSW process is intended to improve welding efficiency, to reduce the welding defects, to extend the tool service life, and to encompass the feasibility of FSW technology for high-strength alloys. External heating is also beneficial for dissimilar material combinations since the heat can be applied individually to one of the parts being joined together. The effect of preheating on the thermal history and microstructure of a joint has been investigated experimentally and through the development of numerical model. The conclusions that can be drawn from the present research work are listed as follows:

- Effect of heat generation due to plastic deformation (surface) is accompanied in the pin to estimate heat flux for moving heat source. The heat generation both from the pin side and the pin bottom surfaces has effective role in this analysis. Temperature distributions are not symmetric around welding line and maximum temperature occurs behind the tool pin.
- The comparison between experimentally measured and calculated thermocouple record agrees well, even though the advancing side temperature underestimates and the retreating side overestimates the predicted model results due to symmetric heat generation by sliding and sticking conditions. Percentage error of peak temperature in experimental and calculated thermocouple record at different locations is less than 4.5%, which is reasonable for the reliability of the proposed model.
- The result of analytical approach shows that the microstructural features of the weld zone are controlled by strain rate and temperature generated during welding.
- The temperature distribution and strain-rate distribution across the weld zone agrees well with the existing understanding. This indicates that the analytical models are efficient to predict the outputs during FSW with acceptable accuracy.

- Plasma arc heat is used to preheat the workpiece at a localized area ahead of the rotating probe, thus enhance the plasticization of local volume of material ahead of the probe. The preheating source basically enhances metal flow around the tool and reduces the plunging force over present range of process parameters.
- The high temperature ahead of the rotating tool softens the workpiece and enables joining without strong clamping fixtures. Less force is needed to move the welding tool forward, hence, wear is reduced. A further advantage of plasma arc energy for this process is the ability to weld at higher rates without causing excessive wear to the welding tool.
- Preheating builds up additional heat during aluminum alloy which decreases the variability of cooling rate in welded joint. In P-FSW 300 K, higher peak temperature is achieved outside of the stirred zone (minimum distance location of thermo-couple). The average plunging force reduces 22-28% in present range of process parameters due to effect of pre-heating in P-FSW.
- Substantial increases in tensile strengths and micro-hardness are observed in P-FSW of aluminum alloy as compare to FSW. However, the hardness is almost uniformly distributed with less variability in preheated samples. Overall increment of friction stir-welded joint is mainly attributed to strengthening effect induced by the finely dispersed Al_2O_3 particles.
- During dissimilar material joining preheat is beneficial to increase the temperature of the harder workpiece in front of the tool pin during dissimilar material joint, making the material easy to be welded, and possibly reduces tool wear due to difference in flow stress value.
- The maximum temperature obtained in copper side at the nearest thermocouple location is ~ 589 – 651 K higher than the aluminum side that helps to reduce the difference in plasticized state temperature. There is significant difference in peak temperature and average welding force in variation with tool offset is case of dissimilar aluminum-copper welding.
- The heat transfer model used to describe heat inputs during hybrid friction stir welding process is relatively adequate and precise to predict peak temperature of the process. The

overall error in peak temperature is 5 ~ 12 % and the maximum reliability is achieved as 0.84.

- Preheating in copper side reduces yield stress difference up to ~ 10 MPa which facilitate the stirring of dissimilar materials by FSW tool. Therefore, the satisfactory interaction between two materials is achieved at the joint interface in presence of preheating.
- P-FSW is a hybrid technology which can resolve the weldability of other dissimilar materials and have a potential application for industrialization.
- In general, P-FSW of similar and dissimilar materials join, UTS of welded joint increases with increases in heat input. For joining of similar materials, the micro-hardness in HAZ and nugget zone is approximately uniform throughout the weldment even with increase in heat input.

An innovative welding technique, plasma assisted hybrid friction stir welding, is successfully applied to the joining of aluminum alloy and pure copper. Although, the preheating technique in FSW process is quite effective to improve joining efficiency and it needs to investigate from various aspects. The preheating in FSW (P-FSW) can be potentially used for relatively harder materials and joining of dissimilar materials.

6.2 Scope of future work

By any standard the industrial adoption of friction stir welding as the preferred joining technique for a range of aluminum alloys, represents a remarkable progress in technical development of joining process. Furthermore, a range of non-ferrous and ferrous materials has also been shown to be readily welded by HFSW in the laboratory. Based on this work, the following areas are suggested for further research:

- The P-FSW techniques with additional heat source is innovative joining process with remarkably positive effects on the welding process. However, development of these variants, their experimentation, etc. are still in their preliminary stage and systematic investigations on the process optimization, weld joint efficiency, weld performance, etc. is required to explore.
- The feasibility of P-FSW to harder and complex materials is yet to be testified in more details.

- Apart from development of P-FSW, improvement of tool design through the practical implementation of some fundamental concepts with unconventional tool material is also required. These concepts can be further fine-tuned by computer-based stress analysis of the complex tool geometry such as bobbin tool using a flared-triflute probe, and the skew-stir and re-stir techniques, self-reacting tool and external non-rotational shoulder assisted tool.
- Material flow analysis of P-FSW to justified the enhancement in material flow through auxiliary heat source.
- The inclusion of non-symmetric heat source model will definitely enhance the scope of predicting different temperature profiles between advancing and retreating sides. This is the future scope of the work to enhance the reliability of mathematical modelling.
- FSW most commonly used joint configuration is the butt joints, in particular, square butt joint and is most suitable for components which are flat and long (plates and sheets), but can be adapted for pipes and hollow sections welding.
- In order to automate this process and to make it more efficient, it must incorporate a technique for in-process monitoring of the tool condition and the weld formation.
- Development of physics-based model approach for detecting discontinuities during friction stir welding.
- Development of adaptive manufacturing technique based on friction stir process such as friction stir channeling and surfacing techniques. Friction stir channeling (FSC) technique for manufacturing continuous channels that can be applied in heat exchanging applications. Surfacing techniques are of particular interest because they can improve the mechanical properties of a certain material making it more robust to the environmental conditions.
- A new technique of self-refilling friction stir welding (SRFSW) relying on non-consumable joining tool has been developed to repair the keyhole with both metallurgical and mechanical bonding characteristics, and the FSW seam can be achieved without keyhole or other defects.

References

1. R. S. Mishra and Z. Y. Ma: Friction Stir Welding and Processing, Materials Science and Engineering: R, 50, 2005, 1–78.
2. P. L. Threadgill, A. J. Leonard, H. R. Shercliff and P. J. Withers: Friction stir welding of aluminium alloys, International Materials Reviews, 54, 2009, 49–93.
3. M. B. Uday, M. N. Ahmad Fauzi, H. Zuhailawati and A. B. Ismail: Advances in friction welding process: a review, Science and Technology of Welding and Joining, 15, 2010, 534–558.
4. R. Nandan, T. DebRoy and H. K. D. H. Bhadeshia: Recent advances in friction-stir welding—Process, weldment structure and properties. Progress in Materials Science, 53, 2008, 980–1023.
5. T. DebRoy and H. K. D. H. Bhadeshia: Friction stir welding of dissimilar alloys - a perspective, Science and Technology of Welding and Joining, 15, 2010, 266–270.
6. G. Kohn, Y. Greenberg, I. Makover and A. Munitz: Laser-assisted friction stir welding, Welding Journal, 81, 2002, 46–48.
7. X. He, F. Gu and A. Ball: A review of numerical analysis of friction stir welding, Progress in Materials Science, 65, 2014, 1-66.
8. R. Nandan, G. G. Roy and T. Debroy: Numerical simulation of three-dimensional heat transfer and plastic flow during friction stir welding, Metallurgical and materials transactions A, 37 (4), 2006, 1247-1259.
9. G. Cam and S. Mistikoglu: Recent Developments in Friction Stir Welding of Al-alloys, Journal of Materials Engineering and Performance, 23, 2014, 1936–1953.
10. M. Mijajlović and D. Milčic: Analytical Model for Estimating the Amount of Heat Generated During Friction Stir Welding: Application on Plates Made of Aluminium Alloy 2024 T351, Welding Processes, Radovan Kovacevic (Ed.), 2012.
11. W. M. Thomas, K. I. Johnson and C. S. Wiesner: Friction stir welding - recent developments in tool and process technologies, Advanced Engineering Materials, 5(7), 2003, 485-490.
12. R. Rai, A. De, H. K. D. H. Bhadeshia and T. DebRoy: Review: friction stir welding tools, Science and Technology of welding and Joining, 16(4), 2010, 325-342.
13. Y. N. Zhang, X. Cao, S. Larose and P. Wanjara: Review of tools for friction stir welding and processing. Canadian Metallurgical Quarterly, 51(3), 2012, 250-261.
14. H. K. D. H.Bhadeshia and T. DebRoy: Critical assessment: friction stir welding of steels. Science and Technology of Welding and Joining, 14(3), 2009, 193-196.
15. G. Oeystein, K. A. Ove, O. T. Midling and N. Hydro: Modified friction stir welding, International patent application no. WO1999039861 A1, August; 1999.

16. G. K. Padhy, C. S. Wu and S. Gao: Auxiliary energy assisted friction stir welding – status review, Science and Technology of Welding and Joining, 20(8), 2015, 631-649.
17. J. Luo, W. Chen and G. Fu: Hybrid-heat effects on electrical current aided friction stir welding of steel, and Al and Mg alloys, Journal of Materials Processing Technology, 214, 2014, 3002–3012.
18. G. Kohn, Y. Greenberg, I. Makove and A. Munitz: Laser assisted friction stir welding, Welding Journal, 81, 2002, 46–48.
19. Y. F. Sun, Y. Konishi, M. Kamai and H. Fujii: Microstructure and mechanical properties of S45C steel prepared by laser-assisted friction stir welding, Material and Design, 47, 2013, 842–849.
20. A. H. Lotfi and S. Nourouzi: Predictions of the optimized friction stir welding process parameters for joining AA7075-T6 aluminum alloy using preheating system, The International Journal of Advanced Manufacturing Technology, 73, 2014, 1717–1737.
21. P. S. De and R. S. Mishra: Friction stir welding of precipitation strengthened aluminium alloys: scope and challenges, Science and Technology of Welding and Joining, 16, 2011, 343–347.
22. C. J. Dawes and W. M. Thomas: Friction stir process welds aluminum alloys, Welding Journal, 75, 1996, 41–45.
23. W. Tang, X. Guo, J. C. McClure, L. E. Murr, and A. Nunes: Heat Input and Temperature Distribution in Friction Stir Welding, Journal of Materials Processing and Manufacturing Science, 7(2), 1988, 163–172.
24. Z. Zhang, J. T. Chen, Z. W. Zhang, H. W. Zhang: Coupled thermo-mechanical model based comparison of friction stir welding processes of AA2024-T3 in different thicknesses, Journal of Materials Science, 46 2011, 5815–5821.
25. K. J. Colligan and R. S. Mishra: A conceptual model for the process variables related to heat generation in friction stir welding of aluminum, Scripta Materialia, 58(5), 2008, 327–331.
26. J. E. Gould and Z. L. Feng: Heat flow model for friction stir welding of aluminum alloys, Materials Processing and Manufacturing Science, 7, 1998, 185–194.
27. Y. J. Chao and X. Qi: Thermal and thermo-mechanical modeling of friction stir welding of aluminum alloy 6061-T6, Journal of Materials Processing and Manufacturing Science, 7, 1998, 215–233.
28. P. A. Colegrove and H. R. Shercliff: Experimental and numerical analysis of aluminium alloy 7075-T7351 friction stir welds, Science and Technology of Welding and Joining, 8, 2003, 360–368.

29. M. J. Russell and H. R. Shercliff: Analytical modelling of friction stir welding, Proc. 7th Int. Conf. on 'Joints in aluminium' (INALCO '98), Cambridge, UK, April 1998, TWI Ltd, 197–207.
30. Ø. Frigaard, Ø. Grong and O.T. Midling: A process model for friction stir welding of age hardening aluminum alloys, Metallurgical and Materials Transactions A, 32, 2001, 1189–1200.
31. M. Song and R. Kovacevic: Heat transfer modelling for both workpiece and tool in the friction stir welding process: a coupled model, Proceedings of the Institution of Mechanical Engineers, Part B: Journal of Engineering Manufacture, 218, 2004, 17–33.
32. Y. J. Chao, X. Qi and W. Tang: Heat transfer in friction stir welding – experimental and numerical studies, Journal of Manufacturing Science and Engineering, 125, 2003, 138–145.
33. H. Schmidt, J. Hattel and J. Wert: An analytical model for the heat generation in friction stir welding, Modelling and Simulation in Materials Science and Engineering, 12, 2004, 143–157.
34. V.S. Gadakh and K. K. Adepu: Heat generation model for taper cylindrical pin profile in FSW, Journal of Materials Research and Technology, 2 (4), 2013, 370–375.
35. P. Biswas and N. R. Mandal: Effect of tool geometries on thermal history of FSW of AA1100, Welding Journal, 90, 2011, 129–135.
36. M. Z. H. Khandkar and J. A. Khan: Thermal modeling of overlap Friction Stir Welding for Al-alloys, Journal of Materials Processing and Manufacturing Science, 10, 2001, 91-105.
37. M. Z. H. Khandkar, J. A. Khan and A. P. Reynolds: Prediction of temperature distribution and thermal history during friction stir welding: input torque based model, Science and Technology of Welding and Joining, 8, 2003, 165-174.
38. J. A., L. Khan, S. Xu and Y. J. Chao: Prediction of nugget development during resistance spot welding using coupled thermal-electrical mechanical model, Science and Technology of Welding and Joining, 4, 1999, 201-207.
39. S. Xu, X. Deng, A. P. Reynolds, and T. U. Seidel: Finite element simulation of material flow in friction stir welding, Science and Technology of Welding and Joining, 6, 2001, 191-193.
40. H. B. Schmidt and J. H. Hattel: Thermal modelling of friction stir welding, Scripta Materialia, 58(5), 2008, 332–337.
41. M. Mijajlović: Investigation and development of analytical model for estimation of amount of heat generated during FSW. Diss. Ph. D. thesis, Faculty of Mechanical Engineering Nis, University of Nis, Nis, Serbia, 2012.
42. C. Bitondo, U. Prisco, A. Squilace, P. Buonadonna, G. Dionoro: Friction-stir welding of AA 2198 butt joints: mechanical characterization of the process and of the welds through DOE analysis, International Journal of Advanced Manufacturing Technology, 53(5), 2011, 505–516.

43. A. C. F. Silva, D. F. O. Braga, M. A. V. de Figueiredo and P. M. G. P. Moreira: Ultimate tensile strength optimization of different FSW aluminium alloy joints, International Journal of Advanced Manufacturing Technology, 79(5), 2015, 805–814.
44. D. H. Lammlein, B. T. Gibson, D. R. DeLapp, C. Cox, A. M. Strauss, and G. E. Cook: The friction stir welding of small-diameter pipe: an experimental and numerical proof of concept for automation and manufacturing, Proceedings of the Institution of Mechanical Engineers, Part B: Journal of Engineering Manufacture, 226(3), 2011, 383-398.
45. J. P. Martin, C. Stanhope and S. Gascoyne: Novel techniques for corner joints using friction stir welding, Paper presented at TMS 2011 Annual Meeting & Exhibition. San Diego, CA., USA. 2011.
46. D. H. Lammlein, B. T. Gibson, D. R. DeLapp, C. Cox, A. M. Strauss and G. E. Cook: Friction stir welding of small diameter pipe: an experimental and numerical proof of concept for automation and manufacturing. Proceedings of the Institution of Mechanical Engineers, Part B: Journal of Engineering Manufacture, 2011, 1-16.
47. P. K. Baghel: Design and development of fixture for friction stir welding, Innovative Systems Design and Engineering, 12, 2012, 40-47.
48. L. Fratini, F. Micari, G. Buffa and V. F. Ruisi: A new fixture for FSW processes of titanium alloys, CIRP Annals - Manufacturing Technology, 59, 2010, 271-274.
49. P. Edwards and M. Ramulu: Identification of the process parameters for Ti-6Al-4V alloy friction stir welding, Journal of Engineering Materials and Technology, 132, 2010, 1–10.
50. P. L. Threadgill and M. E. Nunn: A Review of Friction Stir Welding: Part 1, Process Overview, Industrial Members Report No: 760/2003, TWI Ltd, Cambridge, UK, 2003.
51. J. Luo: New technological methods and designs of stir head in resistance friction stir welding, Science and Technology of Welding and Joining, 6(4), 1999, 209-212.
52. Ø. Frigaard, Ø. Grong and O.T. Midling: A Process Model for Friction Stir Welding of Age Hardening Aluminum Alloys, Metallurgical and Materials Transactions A, 32A, 2001, 1189-2000.
53. R. Johnson, and N. L. Horrex: Preliminary examination of forces generated during the friction stir welding process, TWI Core Research Report No: 69612000, Cambridge, UK, 2000.
54. R. Johnson: Forces in friction stir welding of aluminium alloys - further studies, TWI Core Research Report No. 716/2000, Cambridge, UK, 2000.
55. A. P. Reynolds, K. Linder, W. Tang and T. U. Siedel: Weld efficiency and defect formation correlation between experiment and simple models, Proceedings of the 6th International Trends in Welding Research Conference, ASM, Pine Mountain, 2003.

56. T. J. Lienelt, W. L. Stellwag, and H. Shao: Determination of load, torque, and tool temperatures during friction stir welding of aluminium alloys: EWI Core Research Report No: SR0019, Ohio, US, 2000.
57. H. Fujii, L. Cui, M. Maeda and K. Nogi: Effect of tool shape on mechanical properties and microstructure of friction stir welded aluminum alloys, Materials Science and Engineering: A, 419, 2006, 25–31.
58. J. Teimournezhad and A. Masoumi: Experimental investigation of onion ring structure formation in friction stir butt welds of copper plates produced by non-threaded tool pin, Science and Technology of Welding and Joining, 15(2), 2010, 166–170.
59. S. M. Chowdhury, D. L. Chen, S. D. Bhole and X. Cao: Tensile properties of a friction stir welded magnesium alloy: Effect of pin tool thread orientation and weld pitch, Materials Science and Engineering: A, 527, 2010, 6064–6075.
60. R. A. Prado, L. E. Murr, K. F. Soto and J. C. McClure: Self-optimization in tool wear for friction-stir welding of Al 6061 z 20% Al_2O_3 MMC, Materials Science and Engineering: A, 349, 2003, 156–165.
61. T. Weinberger, N. Enzinger and H. Cerjak: Microstructural and mechanical characterisation of friction stir welded 15–5PH steel, Science and Technology of Welding and Joining, 14(3), 2009, 210–215.
62. S. Park, Y. Sato, H. Kokawa, K. Okamoto, S. Hirano and M. Inagaki: Boride formation induced by pcBN tool wear in friction-stir-welded stainless steels, Metallurgical and Materials Transactions A, 40(3), 2009, 625–636.
63. K. Reshad Seighalani, M. K. Besharati Givi, A. M. Nasiri and P. Bahemmat: Investigations on the effects of the tool material, geometry, and tilt angle on friction stir welding of pure titanium, Journal of Materials Engineering and Performance, 19(7), 2010, 955–962.
64. R. Ayer, H. W. Jin, R. R. Mueller, S. Ling and S. Ford: Interface structure in a Fe–Ni friction stir welded joint, Scripta Materialia, 53(12), 2005, 1383–1387.
65. M. Mahoney, T. Nelson, C. Sorensen and S. Packer: Friction stir welding of ferrous alloys: current status, Materials Science Forum, 41, 2010, 638–642.
66. Y. Zhang, Y. S. Sato, H. Kokawa, S. H. C. Park and S. Hirano: Stir zone microstructure of commercial purity titanium friction stir welded using pcBN tool, Materials Science and Engineering: A, 488, 2008, 25–30.
67. M. Mijajlovi, D. Milcic, B. Andjelkovic, M. Vukicevic and M. Bjeli: Mathematical model for analytical estimation of generated heat during friction stir welding. Part 1, Journal of Balkan Tribological Association, 17(2), 2011, 179-191.

68. M. Mijajlovi, D. Milcic, B. Andjelkovic, M. Vukicevic and M. Bjeli: Mathematical model for analytical estimation of generated heat during friction stir welding. Part 2, Journal of Balkan Tribological Association, 17(3), 2011, 361-370.
69. M. Song and R. Kovačević: Thermal modeling of friction stir welding in a moving coordinate and its validation, Int. J. Machine Tool Manufacturing, 43(6), 2003, 605–615.
70. H. R. Shercliff and P. A. Colegrove: Modelling of friction stir welding, Mathematical Modelling of Weld, 6, 2002, 927-974.
71. H. Schmidt, J. Hattel: Modelling heat flow around tool probe in friction stir welding, Science and Technology of Welding & Joining, 10(2), 2006, 176-186.
72. Z. Zhang, H. W. Zhang: Effect of contact model on numerical simulation of friction stir welding, Acta Metall Sinica, 44, 2008, 85–90.
73. P. Ferro and F. Bonollo: A semi-analytical thermal model for fiction stir welding, Metallurgical and Materials Transactions A, 41, 2010, 440–449.
74. H. Wang, P. A. Colegrove and J. F. Dos Santos: Numerical investigation of the tool contact condition during friction stir welding of aerospace aluminium alloy, Computational Materials Science, 71, 2013, 101–108.
75. Z. Zhang and J. T. Chen: Computational investigations on reliable finite element-based thermo-mechanical coupled simulations of friction stir welding, International Journal of Advanced Manufacturing Technology, 60, 2012, 959–975.
76. K. Kumar, C. Kalyan, S. V. Kaias and T. S. Srivatsan: An investigation of friction during friction stir welding of metallic materials, Materials and Manufacturing Processes, 24(4), 2009, 438-445.
77. O. Frigaard and O. Grong: Modeling of the heat flow phenomena in friction stir welding of aluminum alloys, Paper presented at: INALCO ’98. Proceedings of the Seventh International Conference on Joints in Aluminum, Cambridge, 15–17. April, 1998.
78. H. Schmidt and J. Hattel: A local model for the thermomechanical conditions in friction stir welding, Modelling and Simulation in Materials Science and Engineering, 13, 2005, 77-93.
79. M. J. Russell and H. R. Shercliff: Analytical modeling of microstructure development in friction stir welding, Proceedings of the first International Symposium on Friction Stir Welding, Thousand Oaks, CA June 1999.
80. P. Ulysse: Three-dimensional modelling of the friction stir-welding process, International Journal of Machine Tools & Manufacture, 42, 2002, 1549-1557.
81. A. Steuwer, M. Peel P. J. Withers, T. L. Dickerson, Q. Shi and H. R. Shercliff: Measurement and prediction of residual stresses in aluminium friction stir welds, Journal of Neutron Research, 11, 2003, 267-272.

82. T. L. Dickerson, Q. Y. Shi and H. R. Shercliff: Heat flow into friction stir welding tools, Proceeding of 4th International Symposium on Friction Stir Welding, Salt Lake City, Utah, USA, May 2003.
83. R. W. Fonda and S. G. Lambrakos: Analysis of friction stir welds using an inverse problem approach, Science and Technology of Welding and Joining, 7(3), 2002, 177-181.
84. J. H. Hattel, H. N. B. Schmidt and C. Tutum: Thermomechanical modelling of friction stir welding, trends in welding research, Proceedings of the 8th International Conference, ASM International, Materials Park, Ohio, USA.
85. H. N. B. Schmidt and J. Hattel: Heat source models in simulation of heat flow in friction stir welding, International Journal of Offshore and Polar Engineering, 14(4), 2004, 1053-5381.
86. Y. J. Chao and X. H. Qi: Thermal and thermo-mechanical modeling of friction stir welding of aluminum alloy 6061-T6, Journal of Materials Processing & Manufacturing Science, 7(2), 1998, 215-233.
87. X. K. Zhu and Y. J. Chao: Numerical simulation of transient temperature and residual stresses in friction stir welding of 304L stainless steel, Journal of Materials Processing Technology, 146, 2004, 263-272.
88. J. E. Gould and Z. L. Feng: Heat flow model for friction stir welding of aluminum alloys, Materials Processing and Manufacturing Science, 7, 1998, 185–194.
89. O. T. Midling and O. Grong: A process model for friction welding of Al-Mg-Si alloys and Al-SiC metal matrix composites-i. haz temperature and strain rate distribution, Acta Metallurgica, 42(5), 1994, 1595–1609.
90. O. Frigaard, O. Grong and O. T. Milding: Modeling of heat flow phenomena in friction stir welding of aluminum alloys: Proceeding of the INALCO'98, 1998, Cambridge, UK.
91. P. A. Colegrove, M. Painter, D. Graham and T. Miller: 3 Dimensional flow and thermal modeling of the friction stir welding process, Proceeding of the 2nd International Symposium on Friction Stir Welding, Gothenburg, Sweden, 2002, p. 26–28.
92. M. Song and R. Kovacevic: A New heat transfer models for friction stir welding, Transactions of North American Manufacturing Research Institution of SME, 120(175), 2002, 565–572.
93. H. B. Schmidt and J. H. Hattel: Thermal modeling of friction stir welding: Scripta Materialia, 58, 2008, 332–337.
94. W. Tang, X. Guo, J. C. McClure, L. E. Murr, A. Nunes: Heat input and temperature distribution in friction stir welding, Journal of Materials Processing and Manufacturing Science, 7, 1998, 163–172.

95. C. C. Tutum, H. Schmidt, J. Hattel and M. Bendsøe: Estimation of the welding speed and heat input in friction stir welding using thermal models and optimization. 7th World Congress on Structural and Multidisciplinary Optimization, Seoul, 2007, 2639–2646.
96. P. A. Colegrove, H. R. Shercliff: 3-Dimensional CFD modelling of flow round a threaded friction stir welding tool profile, Journal of Materials Processing Technology, 169(2), 2003, 320–327.
97. M. J. Russell and H. R. Shercliff: Analytical modelling of microstructure development in friction stir welding, Proceeding of the 1st International Symposium on Friction Stir Welding, 1999, Thousand Oaks, California.
98. M. Maalekian: Comparative analysis of heat generation in friction welding of steel bars, Acta Materialia, 56(12), 2008, 2843-2855.
99. P. Dong, F. Lu, J. K. Hong and Z. Cao: Coupled thermomechanical analysis of friction stir welding process using simplified models, Science and Technology of Welding and Joining, 6, 2001, 281-287.
100. M. Song, R. Kovacevic, Thermal modeling of friction stir welding in a moving coordinate system and its validation, International Journal of Machine Tools and Manufacture, 43 (2003) 605–615.
101. M. Song, R. Kovacevic: Numerical simulation and experimental analysis of heat transfer process in friction stir welding process, Proceeding of Institution of Mechanical Engineers, Part B, Journal of Engineering Manufacture, 216(12), 2002, 73–85.
102. A. Arora, R. Nandan, A. P. Reymolds and T. Debroy: Torque, power requirement and stir zone geometry in friction stir welding through modeling and experiments; Scripta Materialia, 60(1), 2009, 13–16.
103. V. Soundararajan, S. Zekovic and R. Kovacevic: Thermo-mechanical model with adaptive boundary conditions for friction stir welding of Al 6061, International Journal of Machine Tools & Manufacture, 45, 2005, 1577–1587.
104. G. Buffa, H. Hua, R. Shivpuri and L. Fratini: A continuum based fem model for friction stir welding-model development; Materials Science and Engineering, 419(1), 2006, 389–396.
105. Z. Zhang and H. W. Zhang: A fully coupled thermo-mechanical model of friction stir welding; The International Journal of Advanced Manufacturing Technology, 37(3), 2007, 279–293.
106. Y. H. Zhao, S. B. Lin, Z. Q. He and L. Wu: Microhardness prediction in friction stir welding of 2014 aluminium alloy, Science and Technology of Welding & Joining, 11(2), 2010, 178-182.

107. Y. G. Kim, H. Fujii, T. Tsumura, T. Komazaki, K. Nakata: Effect of welding parameters on microstructure in the stir zone of FSW joints of aluminum die casting alloy, Materials Letters, 60(29-30), 2006, 3830–3840.

108. J. H. Hattel, K. L. Nielsen and C. C. Tutum: The effect of post-welding conditions in friction stir welds: From weld simulation to ductile failure, European Journal of Mechanics A/Solids, 33, 2012, 67-74.

109. K. Kumar and S. V. Kailas: The role of friction stir welding tool on material flow and weld formation, Materials Science and Engineering: A, 485 (1), 2008, 367-374.

110. Z. W. Chen and S. Cui, On the forming mechanism of banded structures in aluminium alloy friction stir welds, Scripta Materialia, 58, 2008, 417-420.

111. R. M. Leal and A. Loureiro: Effect of overlapping friction stir welding passes in the quality of welds of aluminium alloys, Materials & Design, 29, 2008, 982-991.

112. W. J. Arbegast, Z. Jin, A. Beaudoin, T. A. Bieler and B. Radhakrishnan: Hot Deformation of Aluminum Alloys III, TMS, Warrendale, PA, USA, 2003, p. 313.

113. N. Dialami, M. Chiumenti, M. Cervera, C. Agelet de Saracibar, J. P. Ponthot: Material flow visualization in friction stir welding via particle tracing, International Journal of Material Forming, 8(2), 2015, 167-181.

114. T. U. Seidel and A. P. Reynolds: Visualization of the material flow in AA2195 friction-stir welds using a marker insert technique, Metallurgical and Materials Transactions A, 32, 2001, 2879–2884.

115. J. A. Schneider and A. C. Nunes: Characterization of plastic flow and resulting micro-textures in a friction stir weld, Metallurgical and Materials Transactions A, 35, 2004, 777–783.

116. Y. Morisada, H. Fujii, Y. Kawahito, K. Nakata and M. Tanaka: Three-dimensional visualization of material flow during friction stir welding by two pairs of X-ray transmission systems, Scripta Materialia, 65, 2011, 1085–1088.

117. K. Colligan: Material flow behavior during friction stir welding of aluminium, Welding Journal, 78(7), 1999, 229–237.

118. M. Guerra, C. Schmidt, J. C. McClure, L. E. Murr and A. C. Nunes: Flow patterns during friction stir welding, Materials Characterization, 49, 2003, 95–101.

119. J. A. Schneider and A. C. Nunes: Friction Stir Welding and Processing II, 43-51; 2003, WmTendale, PA, TMS.

120. Y. H. Zhao, S. B. Lin, F. X. Qu and L. Wu: Influence of pin geometry on material flow in friction stir welding process, Science and Technology of Welding and Joining, 22, 2006, 45–50.

121. J. A. Schneider, A. C. Nunes: Characterization of plastic flow and resulting microtextures in a friction stir weld, Metallurgical and Materials Transactions B, 35, 2004, 777–783.

122. S. Muthukumaran, S. K. Mukherjee: Multi-layered metal flow and formation of onion rings in friction stir welds, International Journal of Advanced Manufacturing Technology, 38, 2008, 68–73.

123. K. N. Krishnan: On the formation of onion rings in friction stir welds, Materials Science and Engineering: A, 327, 2002, 246–251.

124. L. Ke, L. Xing and J. E. Indacochea: Material flow patterns and cavity model in friction stir welding of aluminum alloys, Metallurgical and Materials Transactions B, 35, 2004, 153–160.

125. W. J. Arbegast: A flow-partitioned deformation zone model for defect formation during friction stir welding, Scripta Materialia, 58, 2008, 372–376.

126. H. Zhang, Z. Zhang and J. Chen: The finite element simulation of the friction stir welding process, Materials Science and Engineering: A, 403, 2005, 340–348.

127. C. Hamilton, S. Dymek and M. Blicharski: A model of material flow during friction stir welding, Materials Characterization, 59, 2008, 1206–1214.

128. P. Ulysse: Three-dimensional modelling of the friction stir-welding process, International Journal of Machine Tools & Manufacture, 42, 2002, 1549-1557.

129. P. A. Colegrove and H. R. Shercloff: 3-D CFD modeling of flow round a threaded friction stir welding tool profile, Journal of Material Processing Technology, 169, 2005, 320-327.

130. H. Badarinarayan, J. H. Kim, C. Kim, K. Okamoto, R. H. Wagoner and K. C. Dongun Kim: Numerical simulation of friction stir butt welding process for AA5083-H18 sheets, European Journal of Mechanics A/Solids, 29, 2010, 204-215.

131. R. Nandan, G. G. Roy, T. J. Lienert and T. Debroy: Numerical modelling of 3D plastic flow and heat transfer during friction stir welding of stainless steel, Science and Technology of Welding and Joining, 11, 2006, 526-537.

132. M. Grujicic, G. Arakere, B. Pandurangan, J. M. Ochterbeck, C. F. Yen, B. A. Cheeseman, A. P. Reynolds and M. A. Sutton: Computational analysis of material flow during friction stir welding of AA5059 aluminum alloys, Journal of Materials Engineering and Performance, 21(9), 2012, 1824–1840.

133. H. Pashazadeh, A. Masoumi and J. Teimournezhad: Numerical modelling for the hardness evaluation of friction stir welded copper metals, Materials & Design, 49, 2013, 913–921.

134. Z. Zhang, H. W. Zhang: Numerical studies on controlling of process parameters in friction stir welding, Journal of Materials Processing Technology, 209, 2009, 241–270.

135. E. Feulvarch, J. C. Roux, J. M. Bergheau: A simple and robust moving mesh technique for the finite element simulation of Friction Stir Welding, Journal of Computational and Applied Mathematics, 246, 2013, 269–277.

136. F. Al-Badour, N. Merah, A. Shuaib and A. Bazoune: Coupled Eulerian Lagrangian finite element modeling of friction stir welding processes, Journal of Materials Processing Technology, 213(8), 2013, 1433–1439.

137. G. Bendzsak, T. North and C. Smith: An experimentally validated 3D model for friction stir welding, Proceedings of the 2nd international symposium on friction stir welding, Gothenburg, Sweden, 2000.

138. S. Pal, and M. Phaniraj: Determination of heat partition between tool and workpiece during FSW of SS304 using 3D CFD modeling, Journal of Materials Processing Technology, 222, 2015, 280–286.

139. X. C. Liu and C. S. Wu: Material flow in ultrasonic vibration enhanced friction stir welding, Journal of Materials Processing Technology, 225, 2015, 32–44.

140. D. J. Spinella, E. T. Streicher and R. Kastelic: Resistance heated stir welding, US patent no. 5 829 664, published 3 November 1998.

141. W. A. Ferrando: Electrically assisted friction stir welding, The United States of America as represented by the Secretary of the Navy, Washington, DC, USA, US patent no. 8 164 021 B1, published 21 April 2012.

142. X. Long and S. K. Khanna: Modelling of electrically enhanced friction stir welding process using finite element method, Science and Technology of Welding and Joining, 10, 2005, 482–487.

143. J. Luo, F. Li and W. Chen: Experimental researches on resistance heat aided friction stir welding of Mg alloy, Quarterly Journal of the Japan Welding Society, 31, 2013, 65–68.

144. T. G. Santos, R. M. Miranda and P. Vilaca: Friction stir welding assisted by electrical joule effect to overcome lack of penetration in aluminium alloys, Key Engineering Materials, 611, 2014, 763–772.

145. T. G. Santos, R. M. Miranda and P. Vilaca: Friction stir welding assisted by electrical Joule effect, Journal of Materials Processing Technology, 214, 2014, 2127–2133.

146. H. Potluri, J. J. Jones and L. Mears: Comparison of electrically assisted and conventional friction stir welding processes by feed force and torque'. Proc. ASME 2013 Int. Manufacturing Science and Engineering Conf., Madison, WI, USA, June 2013, ASME, paper MSEC2013-1192.

147. X. Liu, S. Lan and J. Ni: Electrically assisted friction stir welding for joining Al 6061 to TRIP780 steel, Journal of Materials Processing Technology, 219, 2015, 112–123.

148. G. J. Grant, M. Khaleel, J. J. Eberhardt, B. Arbegast, G. Stone, S. Howard and C. Allen: Friction stir joining and processing of advanced materials including MMCs, High Strength Weight Reduction Materials, 2005 Progress Report, 112–121.

149. P. C. Sinclair, W. R. Longhurst, C. D. Cox and D. H. Lammlein: Heated friction stir welding: an experimental and theoretical investigation into how preheating influences process forces, Materials and Manufacturing Processes, 25, 2010, 1283–1291.

150. I. Alvarez, M. Garcia, G. Pena, J. Sotelo and D. Verdera: Evaluation of an induction-assisted friction stir welding technique for super duplex stainless steels, Surface and Interface Analysis, 46, 2014, 892–896.

151. F. Palm: Laser supported friction stir welding method, US patent no. 6 793 118, September; 2004.

152. K. H. Song, T. Tsumura and K. Nakata: Development of microstructure and mechanical properties in laser-FSW hybrid welded Inconel 600, Materials Transactions, 50, 2009, 1832–1837.

153. S. L. Campanelli, G. Casalino, C. Casavola and V. Moramarco: Analysis and comparison of friction stir welding and laser-assisted friction stir welding of aluminum alloy, Materials, 6, 2013, 5923–5941.

154. W. S. Chang, S. R. Rajesh, C. K. Chun and H. J. Kim: Microstructure and mechanical properties of hybrid laser-friction stir welding between AA6061-T6 Al Alloy and AZ31 Mg Alloy, Journal of Materials Science & Technology, 27, 2011, 199–204.

155. M. Merklein and A. Giera: Laser assisted friction stir welding of drawable steel-aluminium tailored hybrids, International Journal of Material Forming, 1, 2008, 1299–1302.

156. H. S. Bang, and H. S. Bang: A Study on the weldability and mechanical characteristics of dissimilar materials butt joints by laser assisted friction stir welding, Journal of the Korean Welding and Joining Society, 28, 2010, 678–683.

157. S. Kou and G Cao: Arc-enhanced friction stir welding, US patent no. 7 078 647, July, 2006.

158. H. S. Bang, H. S. Bang, G. H. Jeon, I. H. Oh and C. S. Ro: Gas tungsten arc welding assisted hybrid friction stir welding of dissimilar materials Al6061-T6 aluminum alloy and STS304 stainless steel, Materials & Design, 37, 2012, 48–55.

159. H. S. Bang, H. S. Bang, H. J. Song and S. M. Joo: Joint properties of dissimilar Al6061-T6 aluminum alloy/Ti- %Al-4%V titanium alloy by gas tungsten arc welding assisted hybrid friction stir welding, Materials & Design, 51, 2013, 544–551.

160. S. M. Joo: Joining of dissimilar AZ31B magnesium alloy and SS400 mild steel by hybrid gas tungsten arc friction stir welding, Metals and Materials International, 19, 2013, 1251–1257.

161. A. Siddiq and T. E. Sayed: Ultrasonic-assisted manufacturing processes: variational model and numerical simulation, Ultrasonics, 52, 2012, 521–529.

162. R. L. Lai, D. Q. He, L. Liu, S. Y. Ye and K. Yang: A study of the temperature field during ultrasonic-assisted friction-stir welding, International Journal of Advanced Manufacturing Technology, 73, 2014, 321–327.

163. L. Shi, C. S. Wu and X. C. Liu: Modeling the effects of ultrasonic vibration on friction stir welding, Journal of Materials Processing Technology, 222, 2015, 91–102.

164. B. Strauss, G. Wagner and D. Eifler: Realization of Al/Mg-hybridjoints by ultrasound supported friction stir welding, Materials Science Forum, 783, 2014, 1814–1819.

165. X. C. Liu, C. S. Wu and G. K. Padhy: Improved weld macrosection, microstructure and mechanical properties of 2024Al-T4 butt joints in ultrasonic vibration enhanced friction stir welding, Science and Technology of Welding & Joining, 20, 2015, 345–352.

166. X. C. Liu, C. S. Wu and G. K. Padhy: Characterization of plastic deformation and material flow in ultrasonic vibration enhanced friction stir welding, Scripta Materialia, 102, 2015, 95–98.

167. X. C. Liu and C. S. Wu: The mechanical properties of 2024-T4 aluminium alloy joints in ultrasonic vibration enhanced friction stir welding, China welding, 22, 2013, 8–13.

168. D. H. Choi, C. Y. Lee, B. W. Ahn, J. H. Choi, Y. M. Yeon, K. Song, S. G. Hong, W. B. Lee, K. B. Kang and S. B. Jung: Hybrid friction stir welding of high-carbon steel, Journal of Materials Science & Technology, 27, 2011, 127–130.

169. R. J. Ding and P. A. Oelgoetz: Auto-adjustable probe tool for friction stir welding, US Patent no. 5893507, 1999.

170. M. Skinner and R. L. Edwards: Improvements to the FSW process using the self-reacting technology, Materials Science Forum, 426, 2003, 2849–2854.

171. A. P. Reynolds and W. D. Lockwood: Digital image correlation for determination of weld and base metal constitutive behavior', Proc. 1st Int. Conf. on 'Friction stir welding', Thousand Oaks, CA, USA, June 1999, TWI.

172. T. W. Nelson, B. Hunsaker and D. P. Field: Local texture characterization of friction stir welds in 1100 aluminum, Proc. 1st Int. Conf. on 'Friction stir welding', Thousand Oaks, CA, USA, June 1999, TWI.

173. W. M. Thomas, E. D. Nicholas, J. C. Needham, P. Temple-Smith, S. W. K. W. Kallee and C. J. Dawes: Friction stir welding, UK Patent Application 2306366, 1996.

174. T. Nishihara and Y. Nagasaka: Development of micro-FSW', Proc. 5th Int. Conf. on 'Friction stir welding', Metz, France, September 2004, TWI.

175. W. M. Thomas, E. D. Nicholas and S. D. Smith: Friction stir welding-tool developments, Proc. Aluminum Automotive and Joining Sessions, 213–224; 2001, Warrendale, PA, TMS.

176. K. J. Colligan, J. Xu and J. R. Pickens: Welding tool and process parameter effects in friction stir welding of aluminum alloys, Friction stir welding and processing II', 181–190; 2003, Warrendale, PA, TMS.

177. C. J. Dawes, W. M. Thomas: Development of improved tool designs for friction stir welding of aluminium. Proceedings of the 1st International Friction Stir Welding Symposium, Oaks, CA, USA, (1999).

178. K. Elangovan and V. Balasubramanian & M. Valliappan: Influences of tool pin profile and axial force on the formation of friction stir processing zone in AA6061 aluminium alloy, International Journal of Advanced Manufacturing Technology, 38, 2008, 285–295.

179. S. M. Chowdhurya, D. L. Chena, S. D. Bholea, X. Caob: Effect of pin tool thread orientation on fatigue strength of friction stir welded AZ31B-H24 Mg butt joints, Procedia Engineering, 2, 2010, 825–833.

180. Y. Zhao, S. Lin, L. Wu and F. Qu: The influence of pin geometry on bonding and mechanical properties in friction stir weld 2014 Al alloy, Material Letters, 59, 2005, 2948–2952.

181. X. Cao and M. Jahazi: Effect of welding speed on the quality of friction stir welded butt joints of a magnesium alloy, Material and Design, 30, 2009, 2033–2042.

182. R. Zettler, S. Lomolino, J. F. dos Santos, T. Donath, F. Beckmann, T. Lipman and D. Lohwasser: A study of material flow in FSW of AA2024-T351 and AA 6056-T4 alloys, Proc. 5th Int. Conf. on 'Friction stir welding', Metz, France, September 2004, TWI.

183. R. S. Mishra and M. W. Mahoney: Friction stirs welding and processing, Production Processes and Systems, 6(1), 2007, 6 - 19.

184. H. J. Liu, J. C. Feng, H. Fujiii and K. Nogi: Wear characteristics of a WC – Co tool in friction stir welding of AC4A + 30 vol% SiCp Composite, International Journal of Machine Tools & Manufacture 45, 2005, 1635 -1639.

185. B. Thompson, and S. S. Babu: Tool degradation characterization in the friction stir welding of hard metals, Welding Journal, 89, 2010, 256-261.

186. R. A. Prado, L. E. Murr, K. F. Soto and J. C. McClure: Self-optimization in tool wear for friction-stir welding of Al 6061 +20% Al2O3 MMC, Materials Science and Engineering: A, 349, 2003, 156-165.

187. R. A. Prado, L. E. Murr, D. J. Shindo, J. C. McClure: Friction-stir welding: a study of tool wear variation in aluminum alloy 6061+20% Al2O3; K.V. Jata, M.W. Mahoney, R.S. Mishra, S.L.

Semiatin, D.P. Field (Eds.), Friction Stir Welding and Processing, TMS (The Minerals, Metals, and Materials Society), Warrendale, PA; (2001), pp. 105–116.

188. L. H. Wu, D. Wang, B. L. Xiao and Z. Y. Ma: Tool wear and its effect on microstructure and properties of friction stir processed Ti–6Al–4V, Materials Chemistry and Physics, 146(3), 2014, 512–522.
189. S. Park, Y. Sato, H. Kokawa, K. Okamoto, S. Hirano and M. Inagaki: Boride formation induced by pcBN tool wear in. friction-stir-welded stainless steels, Metallurgical and Materials Transactions A, 40 2009, 625–636.
190. A. Steuwer, S. J. Barnes, J. Altenkirch, R. Johnson and P. J. Withers: Friction stir welding of HSLA-65 steel: Part-II. The influence of weld speed and tool material on the residual stress distribution and tool wear, Metallurgical and Materials Transactions A, 43, 2012, 2356–2365.
191. A. L. Pilchak, W. Tang, H. Sahiner, A. P. Reynolds and J. C. Williams: Microstructural evolution during friction stir welding of mill-annealed Ti-6Al-4V, Metallurgical and Materials Transactions A, 42, 2011, 745–762.
192. P. Agrarwal, P. Nageswaran, N. Arivazhagan and K. D. Ramkumar: Development of friction stir welded butt joints of AA6063 aluminum alloy and pure copper, In Proceeding of International Conference on Advanced Research in Mechanical Engineering (ICARME-2012), Trivendum, India, 2012. 46–50.
193. J. Wildn and J. P. Bergmann Manufacturing of titanium/aluminum and titanium/steel joints by means of diffusion welding, Welding and Cutting, 3(5), 2004, 285−290.
194. J. W. Ren, Y. J. Li, and T. Feng: Microstructure characteristics in the interface zone of Ti/Al diffusion bonding, Materials Letters, 56(5), 2002, 647−652.
195. J. F. Guo, H. C. Chen, C. N. Sun, G. Bi, Z. Sun and J. Wei: Friction stir welding of dissimilar materials between AA6061 and AA7075 Al alloys effects of process parameters: Materials and Design, 56, 2014, 185–192.
196. N. S. Sundaram and N. Murugan: Tensile behavior of dissimilar friction stir welded joints of aluminium alloys, Materials and Design, 31, 2010, 4184–4193.
197. R. Palanivel, P. Koshy Mathews, N. Murugan and I. Dinaharan: Effect of tool rotational speed and pin profile on microstructure and tensile strength of dissimilar friction stir welded AA5083-H111 and AA6351-T6 aluminum alloys, Materials and Design, 40, 2012, 7–16.
198. M. Aonuma and K. Nakata: Dissimilar Metal Joining of 2024 and 7075 Aluminium Alloys to Titanium Alloys by Friction Stir Welding, Materials Transactions, 52(5), 2011, 948-952.

199. M. Dehghani, S. A. A. Akbari Mousavi and A. Amadeh: Effects of welding parameters and tool geometry on properties of 3003-H18 aluminum alloy to mild steel friction stir weld, Transactions of Nonferrous Metals Society of China, 23, 2013, 1957−1965.

200. T. Watanabe, H. Takayama and A. Yanagisawa: Joining of aluminum alloy to steel by friction stir welding, Journal of Materials Processing Technology, 178(3), 2006, 342–349.

201. T. Tanaka, T. Morishige and T. Hirata: Comprehensive analysis of joint strength for dissimilar friction stir welds of mild steel to aluminum alloys, Scripta Materialia, 61(7), 2009, 756−759.

202. Y. G. Kim, H. Fujii, T. Tsumur, T. Komazaki and K. Nakata: Three defect types in friction stir welding of aluminum die casting alloy, Materials Science and Engineering A, 415(2), 2006, 250−254.

203. E.T. Akinlabi, A. Els-Botes and P. J. McGrath: Effect of travel speed on joint properties of dissimilar metal friction stir welds. In Proceedings of 2nd International Conference on Advances in Engineering and Technology (AET), Uganda, 2011.

204. Y. Fotouhi, S. Rasaee,; A. Askari and H. Bisadi: Effect of transverse speed of the tool on microstructure and mechanical properties in dissimilar butt friction stir welding of Al5083–copper sheets, Engineering Solid Mechanics, 2(3), 2014, 239–246.

205. A. A. Zadeh, T. Saeid and B. Sazgari: Microstructural and mechanical properties of friction stir welded aluminum/copper lap joints, Journal of Alloys and Compounds, 460, 2008, 535–538.

206. C. M. Chen and R. Kovacevic: Joining of Al 6061 alloy to AISI 1018 steel by combined effects of fusion and solid state welding, International Journal of Machine Tools and Manufacture, 44(11), 2004, 1205−1214.

207. P. Xue, B. L. Xiao, D. R. Ni and Z. Y. Ma: Enhanced mechanical properties of friction stir welded dissimilar Al–Cu joint by intermetallic compounds, Materials Science and Engineering A, 527(22), 2010, 5723–5727.

208. P. Xue, D. R. Ni, D. Wang, B. L. Xiao and Z. Y. Ma: Effect of friction stir welding parameters on the microstructure and mechanical properties of the dissimilar Al–Cu joints, Materials Science and Engineering A, 528, 2011, 4683–4689.

209. Z. Song, K. Nakata, A. Wu, J. Liao and L. Zhou: Influence of probe offset distance on interfacial microstructure and mechanical properties of friction stir butt welded joint of Ti6Al4V and A6061 dissimilar alloys, Material and Design, 57, 2014, 269–278.

210. A. Elrefaey, M. Gouda, M. Takahashi and K. Lkeuchi: Characterization of aluminum/steel lap joint by friction stir welding, Journal of Materials Engineering and Performance, 14, 2005, 10–17.

211. T. Saeid, A. Abdollah-zadeh and B. Sazgari: Weldability and mechanical properties of dissimilar aluminum–copper lap joints made by friction stir welding, Journal of Alloys and Compounds, 490, 2010, 652–655.

212. K. Kimapong and T. Watanabe: Effect of welding process parameters on mechanical property of FSW lap joint between aluminum and steel, Materials Transactions, 46, 2005, 2211–2217.

213. M. A. Mofid, A. Abdollah-zadeh and C. Hakan Gür: Investigating the formation of intermetallic compounds during friction stir welding of magnesium alloy to aluminum alloy in air and under liquid nitrogen, The International Journal of Advanced Manufacturing Technology, 71(5), 1493-1499.

214. U.F.H. Suhuddin, V. Fischer and J.F. dos Santos: The thermal cycle during the dissimilar friction spot welding of aluminum and magnesium alloy, Scripta Materialia, 68, 2013, 87–90.

215. S. Kobayashi and T. Yakou: Control of intermetallic compound layers at interface between steel and aluminum by diffusion-treatment, Materials Science and Engineering: A, 338(2), 2002, 44–53.

216. R. Cao, G. Yu, J.H. Chen and P.C. Wang: Cold metal transfer joining aluminum alloys-to galvanized mild steel, Journal of Materials Processing Technology, 213(10), 2013, 1753–1763.

217. R. Borrisutthekul, T. Yachi, Y. Miyashita and Y. Mutoh: Suppression of intermetallic reaction layer formation by controlling heat flow in dissimilar joining of steel and aluminum alloy, Materials Science and Engineering: A, 467(2), 2007, 108–113.

218. G. Madhusudhan Reddy, A. Sambasiva Rao and T. Mohandas: Role of electroplated interlayer in continuous drive friction welding of AA6061 to AISI 304 dissimilar metals, Science and Technology of Welding and Joining, 13(7), 2008, 619–628.

219. X. Sun, E.V. Stephens, M.A. Khaleel, H. Shao and M. Kimchi: Resistance spot welding of aluminum alloy to steel with transition material-from process to performance-part I: experimental study, Welding Journal, 83(7), 2004, 188–195.

220. G. K. Hyung, M. K. Sang, Y. L. Jae, R. C. Mi, H. C. Si, H. K. Ki, S. R. Jae, K. Sangshik, Z. H. Seung, Y. K. Won and H. L. Sung, Microstructural evaluation of interfacial intermetallic compounds in Cu wire bonding with Al and Au pads, Acta Materialia, 64, 2014, 356–366.

221. M. Akbari, P. Bahemmat, M. Haghpanahi and M. K. Besharati Givi: Enhancing metallurgical and mechanical properties of friction stir lap welding of Al–Cu using intermediate layer, Science and Technology of Welding and Joining, 18(6), 2013, 518–524.

222. A. Elrefaey, M. Takahashi and K. Lkeuchi: Preliminary investigation of friction stir welding aluminum/copper lap joints, Welding in the World, 49(4), 2005, 93–101.

223. I. Galvao, J. C. Oliveira, A. Loureiro and D. M. Rodrigues: Formation and distribution of brittle structures in friction stir welding of aluminium and copper: influence of process parameters. Science and Technology of Welding and Joining, 16(8), 2011, 681–689.

224. M. H. Shojaeefard, A. Khalkhali, M. Akbari and M. Tahani: Application of Taguchi optimization technique in determining aluminum to brass friction stir welding parameters, Materials and Design, 52, 2013, 587–592.

225. H. Okamura and K. Aota: Joining of dissimilar materials with friction stir welding, Welding International, 18(11), 2004, 852–860.

226. C. Genevois, M. Girard, B. Huneau, X. Sauvage, G. Racineux: Interfacial reaction during friction stir welding of Al and Cu, Metallurgical and Materials Transactions A, 42(8), 2011, 2290–2295.

227. I. Galvao, J. C. Oliveira, A. Loureiro, D. M. Rodrigues: Formation and distribution of brittle structures in friction stir welding of aluminum and copper: influence of process parameters, Science and technology of welding and joining, 16(8), 2011, 681–689.

228. M. N. Avettand-Fenoel, R. Tailard, G. Ji and D. Goran: Multiscale study of interfacial intermetallic compounds in a dissimilar Al 6082-T6/Cu friction stir weld. Metallurgical and Materials Transactions A, 43, 2012, 4655–4666.

229. J. Adamowski and M Szkodo: Friction-stirwelds (FSW) of Aluminum alloy AW6082- T6, Journal of Achievements in materials and Manufacturing Engineering, 20(2), 2007, 49-54.

230. L. E. Murr, G. Liu, and J. C. Mcclure: Dynamic recrystallization in friction-stir welding of aluminium alloy 1100, Journal of Materials Science Letters, 16, 1997, 1801–1803.

231. Y. S. Sato, Y. Kurihara, S. H. C. Park, H. Kokawa and N. Tsuji: Friction stir welding of ultrafine grained Al alloy 1100 produced by accumulative roll-bonding, Scripta Materialia, 50(1), 2004, 57–60.

232. D. Yadav and R. Bauri: Effect of friction stir processing on microstructure and mechanical properties of aluminium, Materials Science and Engineering: A, 539, 2012, 85 - 92.

233. A. Scialpi, L. A. C. De Filippis and P. Cavaliere: Influence of shoulder geometry on microstructure and mechanical properties of friction stir welded 6082 aluminium alloy, Materials & Design, 28(4), 2007, 1124–1129

234. D. M. Rodrigues, A. Loureiro, C. Leitao, R. M. Leal, B. M. Chaparro, and P. Vilaca: Influence of friction stir welding parameters on the micro-structural and mechanical properties of AA 6016-T4 thin welds, Material and Design, 30, 2009, 1913-1921.

235. L. Y. Wei, and T. W. Nelson: Correlation of microstructures and process variables in FSW HSLA-65 steel, Welding Journal, 5, 2011, 95-101.

236. K. Ramanjaneyulu, G. Madhusudhan Reddy, A. Venugopal Rao and R. Markandeya: Structure-property correlation of aa2014 friction stir welds: Role of tool pin profile, Journal of Materials Engineering and Performance, 22, 2013, 2224-2240.

237. K. Elangovan and V. Balasubramanian: Influences of tool pin profile and welding speed on the formation of friction stir processing zone in AA2219 aluminium alloy, journal of materials processing technology 200, 2008, 163–175.

238. C. Yeni, S. sayer, O. Ertugrul and M. Pakdil: Effect of Post Weld-aging on the Mechanical and Micro Structural Properties of Friction-stir Welded Aluminum alloy 7075, Achieves of Material Science and Engineering, 34(2), 2008, 105-109.

239. I. Z. Radisavljevic, A. B. Zivkovic, V. K. Grabulov and N. A. Radovic: Influence of pin geometry on mechanical and structural properties of butt friction stir welded 2024-T351 aluminum alloy, Hemijska industrija, 69(3), 2015, 323–330.

240. A. Ikuta, Y. H. Yin, T. H. North: Influence of tool thread on mechanical properties of dissimilar Al alloy friction stir spot welds, Science and Technology of Welding and Joining, 17(8), 2012, 622–629.

241. R. W. Fonda and J. F. Bingert: Precipitation and grain refinement in a 2195 Al friction stir weld, Metallurgical and Materials Transactions A, 37(12), 2006, 3593-3604.

242. Y. Sun and H. Fujii: The effect of SiC particles on the microstructure and mechanical properties of friction stir welded pure copper joints, Materials Science and Engineering A, 528, 2011, 5470−5475.

243. K. H. Song, T. Tsumura and K. Nakata: Development of microstructure and mechanical properties in laser-FSW hybrid welded Inconel 600, Materials Transactions, 50, 2009, 1832–1837.

244. S. L. Campanelli, G. Casalino, C. Casavola and V. Moramarco: Analysis and comparison of friction stir welding and laser assisted friction stir welding of aluminum alloy, Materials, 6, 2013, 5923–5941.

245. B. Strass, G. Wagner, C. Conrad, B. Wolter, S. Benfer and W. Fuerbeth: Realization of Al/Mg-hybrid-joints by ultrasound supported friction stir welding - mechanical properties, microstructure and corrosion behavior, Advanced Materials Research, 966, 2014, 521–535.

246. R. B. G. Biallas, C. D. Donne, G. Staniek and W. A. Kaysser: Mechanical properties and corrosion behavior of friction stir welds, Proceedings of the 1st International Symposium on Friction Stir Welding, Thousand Oaks, CA, 1999.

247. P. L. Threadgill: Friction Stir Welding—State of the Art, TWI Report 678/1999.

248. G. R. Cui, Z. Y. Ma, and S. X. Li: Periodical plastic flow pattern in friction stir processed Al–Mg alloy, Scripta Materialia, 58, 2008, 1082–1085.

249. T. J. Yoon, J. G. Yun, C. Y. Kang: Formation mechanism of typical onion ring structures and void defects in friction stir lap welded dissimilar aluminum alloys, Materials & Design, 90, 15, 2016, 568-578.

250. A. Gerlich, P. Su, M. Yamamoto and T. H. North: Material flow and intermixing during dissimilar friction stir welding, Science and Technology of Welding & Joining, 13(3), 2008, 254-264.

251. S. A. Khodir and T. Shibayanagi: Dissimilar friction stir welded joints between 2024-t3 aluminum alloy and az31 magnesium alloy, Materials Transactions, 48(9), 2007, 2501-2505.

252. A. J. Leonard: Proc. 2nd Int. Symp. on 'Friction stir welding', Gothenburg, Sweden, June 2000, TWI.

253. Y. Yong, Zhang Da-Tong, Qiu Cheng, Zhang Wen, "Dissimilar friction stir welding between 5052 aluminum alloy and AZ31 magnesium alloy", Trans. Nonferrous Met. Soc. China 20 (2010), pp. 619-623.

254. R. W. Fonda, K. E. Knipling, and J. F. Bingert: Microstructural evolution ahead of the tool in Al friction stir welds, Scripta Materialia, 58, 2007, 343-348.

255. A. A. Zadpoor, J. Sinke and R. Benedictus: Global and local mechanical properties and microstructure of friction stir welds with dissimilar materials and/or thicknesses, Metallurgical and Materials Transactions A, 41(13), 2010, 3365-3378.

256. W. H. Jiang, and R. Kovacevic: Feasibility study of friction stir welding of 6061-T6 aluminium alloy with AISI 1018 steel, Proceedings of the Institution of Mechanical Engineers, Part B: Journal of Engineering Manufacture, 218, 2004, 1323-1331.

257. X. W. Li, D. T. Zhang, C. Qiu and W. Zhang: Microstructure and mechanical properties of dissimilar pure copper/1350 aluminum alloy butt joints by friction stir welding. Transactions of Nonferrous Metals Society of China, 22(6), 2012, 1298–1306.

258. L. E. Murr, Y. Li, R. D. Flores, E. A. Trillo and J. C. Mcclure: Intercalation vortices and related microstructural features in the friction-stir welding of dissimilar metals, Materials Research Innovations, 2, 1998, 150-163.

259. D. M. Neto and P. Neto: Numerical modeling of friction stir welding process: a literature review, The International Journal of Advanced Manufacturing Technology, 65(1), 2013, 115-126.

260. A. Simar, Y. Bréchet, B. D. Meester, A. Denquin, C. Gallais and T. Pardoen: Integrated modeling of friction stir welding of 6xxx series al alloys: process, microstructure and properties, Progress in Materials Science, 57, 2012, 95–183.

261. R. Nandana, G. G. Roya, T. J. Lienertb and T. Debroya: Three-dimensional heat and material flow during friction stir welding of mild steel, Acta Materialia, 55, 2007, 883–895.

262. R. W. Fonda and S. G. Lambrakos: Analysis of friction stir welding using an inverse-problem approach, Science and Technology of Welding and Joining, 7, 2002, 177–181.

263. J. W. Qian, J. L. Li, T. J. Xiong, F. S. Zhang, W. Y. Li and X. Lin: Periodic variation of torque and its relations to interfacial sticking and slipping during friction stir welding, Science and Technology of Welding and Joining, 17, 2012, 338–341.

264. H. B. Schmidt and J. H. Hattel: Thermal modeling of friction stir welding: Scripta Materialia, 58, 2008, 332–337.

265. N. Rebelo and S. Kobayashi: A coupled analysis of visco-plastic deformation and heat transfer, Part I, International Journal of Mechanical Sciences, 22, 1983, 699 – 705.

266. R. S. Saluja, R. G. Narayanan and S. Das: Cellular automata finite element (CAFE) model to predict the forming of friction stir welded blanks, Computational Materials Science, 58, 2012, 87–100.

267. B. M. Darras and M. K. Khraisheh: Analytical modelling of strain rate distribution during friction stir processing, Journal of Materials Engineering and Performance, 17, 2008, 168–177.

268. Z. Zhang and J. T. Chen: Computational investigations on reliable finite element-based thermo mechanical coupled simulations of friction stir welding, The International Journal of Advanced Manufacturing Technology, 60, 2012, 959–975.

269. W. Woo, L. Balogh, T. Ungár, H. Choo and Z. Feng: Grain structure and dislocation density measurements in a friction-stir welded aluminum alloy using X-ray peak profile analysis, Materials Science and Engineering: A, 498, 2008, 308–313.

270. R. Uejia, H. Fujiib, L. Cuib, A. Nishiokac, K. Kunishigea and K. Nogi: Friction stir welding of ultrafine grained plain low-carbon steel formed by the martensite process, Materials Science and Engineering: A, 423, 2006, 324–330.

271. K. Li, D. K. Aidun and P. Marzocca: Time-varying FGM Thermal Modeling of FSW Joint of Dissimilar Metals. Trends in Welding Research Proceedings of the 8th International Conference, Pine Mountain, Georgia, 2008.

272. J. Woo and S. A. Meguid: Nonlinear analysis of functionally graded plates and shallow shells, International Journal of Solids and Structures, 38, 2001, 7409–7421.

273. G. N. Praveen and J. N. Reddy: Nonlinear transient thermoelastic analysis of functionally graded ceramic metal plates, International Journal of Solids and Structures, 35, 1998, 4457–4476.

274. H. Liu, H. Fujii, M. Maeda and K. Nogi: Tensile properties and fracture locations of friction-stir-welded joints of 2017-T351 aluminum alloy, Journal of Materials Processing Technology, 142, 2003, 692–696.

275. S. Rajakumar and V. Balasubramanian: Establishing relationships between mechanical properties of aluminium alloys and optimized friction stir welding process parameters, Materials and Design, 40, 2012, 17–35.

276. J. R. Davis: Tensile Testing, 2nd Edition, ASM International, Brittleness, 2004, 283 pages.

277. C. Weisman: Welding Handbook, American Welding Society, 1976 116 pages.

278. Proceedings of the ASME Materials Division, American Society of Mechanical Engineers, 2004.

279. P. Biswas, D. A. Kumar and N. R. Mandal: Friction stir welding of aluminum alloy with varying tool geometry and process parameters. Proceedings of the Institution of Mechanical Engineers, Part B: Journal of Engineering Manufacture, 226(4), 2012. 641–648.

280. B. Das, S. Pal and S. Bag: Defect detection if friction stir welding process using signal information and fractal theory, Procedia Engineering, 144, 2016, 172 – 178.

281. M. Ilangovan, S. Rajendra Boopathy and V. Balasubramanian: Effect of tool pin profile on microstructure and tensile properties of friction stir welded dissimilar AA 6061–AA 5086 aluminium alloy joints, Defence Technology, 11(2), 2015, 174–184.

282. G. Rambabu, D. Balaji Naik, C.H. Venkata Rao, K. Srinivasa Rao and G. Madhusudan Reddy: Optimization of friction stir welding parameters for improved corrosion resistance of AA2219 aluminum alloy joints, Defence Technology, 11(4), 2015, 330–337.

283. S. Yutaka Sato, C. Seung Hwan Park and K. Hiroyuki: Microstructural factors governing hardness in friction-stir welds of solid-solution-hardened Al alloys, Metallurgical and Materials Transactions A, 32 (12), 2001, 3033–3042.

284. K. Elangovan, V. Balasubramanian and V. Valliappan: Effect of tool pin profile and tool rotational speed on mechanical properties of friction stir welded AA6061 aluminium alloy, Materials and Manufacturing Processes, 23, 2008, 251–260.

285. G. R. Cui, Z. Y. Ma and S. X. Li: The origin of non-uniform microstructure and its effects on the mechanical properties of a friction stir processed Al–Mg alloy, Acta Materialia, 57, 2009, 5718–5729.

286. C. I. Chang, C.J. Lee and J. C. Huang: Relationship between grain size and Zener–Holloman parameter during friction stir processing in AZ31 Mg alloys, Scripta Materialia, 51(6), 2004, 509–514.

287. A. P. Reynolds, W. Tang, T. G. Herold, and H. Prask: Structure, properties, and residual stress of 304L stainless steel friction stir welds, Scripta Materialia, 48(9), 2003, 1289-1294.

288. S. A. Khodir, T. Shibayanagi and M. Naka: Microstructure and Mechanical Properties of Friction Stir Welded AA2024-T3 Aluminum Alloy, Materials Transactions, 47(1), 2006, 185-193.

289. E. T. Akinlabi, S. A. Akinlabi: Effect of Heat Input on the Properties of Dissimilar Friction Stir Welds of Aluminium and Copper, American Journal of Materials Science, 2(5), 2012, 147-152.

290. M. Bauccio: ASM Metals Reference Book, 3rd Edition, ASM International, 1993, 614 pages.

291. V. A. Mayer and J. L. Barrett: ASTM Standards for Welding, American Society for Testing & Materials, 2015, 201 pages.

292. G. E. Dieter: ASM Handbook: Materials Selection and Design, Taylor & Francis, 20, 1997, 901 pages.

293. H. Kuhn and D. Medlin: Mechanical Testing and Evaluation, ASM International, 2000, 998 pages.

294. A. Bachmaier, M. Hafok and R. Pippan: Rate Independent and Rate Dependent Structural Evolution during Severe Plastic Deformation, Materials Transactions, 51(1), 2010, 8–13.

295. M. Warmuzek and A. Gazda: An Analysis of Cooling Rate Influence on the Sequence of Intermetallic Phases Precipitation in Some Commercial Aluminium Alloys, Journal of Analytical Atomic Spectrometry, 14, 1999, 535–537.

296. J. Martin, Micromechanisms in Particle Hardened Alloys, Cambridge University Press, Cambridge, 1980.

297. J. Q. Su, T. W. Nelson and C.J. Sterling: Grain Refinement of Aluminum Alloys by Friction Stir Processing, Materials Science and Engineering: A, 405, 2006, 277–286.

298. J. Guo, S. Amira, P. Gougeon and X.G. Chen: Effect of the Surface Preparation Techniques on the EBSD Analysis of a Friction Stir Welded AA1100-B4C Metal Matrix Composite, Materials Characterization, 62, 2011, 865–877.

299. R. W. Fonda, K. E. Knipling and J. F. Bingert: Microstructural Evolution Ahead of the Tool in Aluminum Friction Stir Welds, Scripta Materialia, 58, 2007, 343–348.

300. 205. A. A. Zadeh, T. Saeid and B. Sazgar: Microstructural and mechanical properties of friction stir welded aluminum/copper lap joints, Journal of Alloys and Compounds, 460, 2008, 535–538.

301. D. Zuo, S. Hu, J. Shen and Z. Xue: Intermediate layer characterization and fracture behavior of laser-welded copper/aluminum metal joints, Materials & Design, 58, 2014, 357–362.
302. L. E. Murr, R. D. Flores, O. V. Flores, J. C. McClure, G. Liu and D. Brown: Friction stir welding: microstructural characterization, Materials Research Innovations, 1, 1998, 211–223.
303. W. S. Chang, S. R. Rajesh, C. K. Chun and H. J. Kimy: Microstructure and mechanical properties of hybrid laser-friction stir welding between AA6061-T6 Al alloy and AZ31 Mg alloy, Journal of Materials Science & Technology, 27, 2011, 199–204.
304. H. S. Bang, H. S. Bang, G. H. Jeon, I. H. Oh and C. S. Ro: Gas tungsten arc welding assisted hybrid friction stir welding of dissimilar materials Al6061–T6 aluminum alloy and STS304 stainless steel, Materials & Design, 37, 2012, 48–55.
305. W. S. Chang, S. R. Rajesh, C. K. Chun and H. J. Kimy: Microstructure and mechanical properties of hybrid laser-friction stir welding between AA6061-T6 Al alloy and AZ31 Mg alloy, Journal of Materials Science & Technology, 27, 2011, 199–204.
306. H. J. Liu, J. J. Shen, L. Zhou, Y. Q. Zhao, C. Liu and L. Y. Kuang: Microstructural characterisation and mechanical properties of friction stir welded joints of aluminium alloy to copper, Science and Technology of Welding and Joining, 16(1), 2011, 92–99.
307. T. B. Massalski: The Al−Cu (Aluminum-Copper) system. Bulletin of Alloy Phase Diagrams, 1, 1980, 27–33.
308. P. Liu, Q. Shi, W. Wang, X. Wang and Z. Zhang: Effects of Tool Pin Design on Formation of Defects in Dissimilar Friction Stir Welding, Mater Lett 62, 2008, 4106–4108.
309. S. Rajakumar, C. Muralidharan and V. Balasubramanian: Influence of friction stir welding process and tool parameters on strength properties of AA7075-T6 aluminium alloy joints, Material & Design, 32, 2011, 535–549.
310. M. Shamsujjoha, B. K. Jasthi, M. West and C. Widener: Friction Stir Lap Welding of Aluminum to Steel Using Refractory Metal Pin Tools, Journal of Engineering Materials and Technology, 137, 2015, 20–28.
311. Z. Chen, S. Yazdanian and G. Littlefair: The role of joint interface on tensile-shear fracture strength of friction stir lap diffusion al-to-steel welds, TWI 9th International Symposium on Friction Stir Welding, Huntsville, AL, 2012.
312. J. Ouyang, E. Yarrapareddy and R. Kovacevic: Microstructural evolution in the friction stir welded 6061 aluminum alloy (T6-temper condition) to copper, Journal of Engineering Materials and Technology, 172, 2006,110–122.

313. W. Li, Z. Zhang, J. Li and Y. J. Chao: Numerical Analysis of Joint Temperature Evolution During Friction Stir Welding Based on Sticking Contact, Journal of Materials Engineering and Performance, 21(9), 2011, 1849-1856.

314. S. Xu, X. Deng, A. P. Reynolds and T. U. Seidel: Finite Element Simulation of Material Flow in Friction Stir Welding, Science and Technology of Welding and Joining, 2001, 6(3), 191–193.

315. H. K. Mohanty, M. M. Mahapatra, P. Kumar, P. Biswas and N. R. Mandal: Study on the effect of tool profiles on temperature distribution and material flow characteristics in friction stir welding. Proceedings of the Institution of Mechanical Engineers, Part B: Journal of Engineering Manufacture, 226(9), 2012, 1527–1535.

316. X. K. Zhu and Y. J. Chao: Numerical Simulation of Transient Temperature and residual Stresses in Friction Stir Welding of 304L Stainless Steel. Journal of Materials Processing Technology, 146, 2004, 263-272.

317. F. Gemme, Y. Verreman, L. Dubourg and M. Jahazi: Numerical analysis of the dwell phase in friction stir welding and comparison with experimental data, Materials Science and Engineering A, 527, 2010, 4152–4160.

318. T. J. Miller, S. J. Zinkle and B. A. Chin: Strength and Fatigue of Dispersion-Strengthened Copper. Journal of Nuclear Materials, 179 - 181, 1991, 263 – 266.

319. J. W. Qian, J. L. Li, T. J. Xiong, F. S. Zhang, W. Y. Li and X. Lin: Periodic variation of torque and its relations to interfacial sticking and slipping during friction stir welding, Science and Technology of Welding and Joining, 17, 2012, 338 –341.

320. J. A. Schneider, R. Beshears and A. C. Nunes, Interfacial sticking and slipping in the friction stir welding process, Materials Science and Engineering A, 435, 2006, 297–304.

321. S. Bag and A. De, Error analysis of forward and reverse heat conduction and convection calculations considering uncertainties in welding, Science and Technology of Welding and Joining, 14, 2009, 662 –668.

322. L. E. Murr, R. D. Flores, O. V. Flores, J. C. McClure, G. Liu and D. Brown: Friction-stir welding: microstructural characterization, Material Research Innovations, 1(4), 1998, 211–223.

323. Typical Mechanical Properties of Wrought Aluminum Alloys at Various Temperatures, Properties of Aluminum Alloys: Tensile, Creep and Fatigue Data at High and Low Temperatures, ASM International, Materials Park, Ohio, USA.

324. H. Bang and H. S. Bijoy: Temperature behavior in dissimilar butt joint during TIG assisted friction stir welding, Journal of Korean Weld Joining Society, 29, 2011, 561 –569.

325. J. Yang and B. Cao: Investigation of resistance heat assisted ultrasonic welding of 6061 aluminum alloys to pure copper, Material and Design, 74, 2015, 19 –24.

326. I. Galvao, J. C. Oliveira, A. Loureiro and D. M. Rodrigues: Formation and distribution of brittle structures in friction stir welding of aluminium and copper: influence of process parameters. Science and Technology of Welding and Joining, 16(8), 2011, 681–689.

327. G. Buffa, L. Fratini and R. Shivpuri: CDRX modelling in friction stir welding of AA7075-T6 aluminum alloy: analytical approaches, Journal of Materials Processing Technology, 191, 2007, 356–359.

328. Y. Sato, M. Urata and H. Kokawa: Parameters controlling microstructure and hardness during friction-stir welding of precipitation-hardenable aluminum alloy 6063. Metallurgical & Materials Transactions A, 33(3), 2002, 625–635.

329. Mehta, K. P.; Badheka, V. J. A Review on Dissimilar Friction Stir Welding of Copper to Aluminum: Process, Properties and Variants. Materials and Manufacturing Processes 31, 2016, 233–254.

330. H. S. Bang, H. S. Bang, G. H. Jeon, I. H. Oh, and C. S. Ro: Gas tungsten arc welding assisted hybrid friction stir welding of dissimilar materials Al6061–T6 aluminum alloy and STS304 stainless steel, Materials & Design, 37, 2012, 48–55.

331. A. Esmaeili, M. K. BesharatiGivi, H. R. Zareie Rajani: A metallurgical and mechanical study on dissimilar Friction Stir welding of aluminum 1050 to brass (CuZn30). Materials Science and Engineering: A, 528, 2011, 7093– 7102.

332. H. R. Zareie Rajani, A. Esmaeilli, M. Mohammadi, M. Sharbati and M. K. B. Givi: The role of metal-matrix composite development during friction stir welding of aluminum to brass in weld characteristics. Journal of Materials Engineering and Performance, 21, 2012, 2429–2437.

333. H. Fujii, L. Cui, N. Tsuji, M. Maeda, K. Nakata and K. Nogi: Friction stir welding of carbon steels, Materials Science and Engineering: A, 429, 2006, 50 –57.

334. H. Bisadi, A. Tavakoli, M. T. Sangsaraki and K. T. Sangsaraki: The in fluences of rotational and welding speeds on microstructures and mechanical properties of friction stir welded Al5083 and commercially pure copper sheets lap joints, Materials & Design, 43, 2013, 80 –88.

335. T. Q. Su, T. W. Nelson, R. Mishra and M. Mahoney: Microstructural investigation of friction stir welded 7050-T651 aluminium, Acta Materialia, 51, 2003, 713 –729.

Bibliography

1. Md. Ibrahim Khan: Welding Science and Technology: New Age International, 2003, 267 pages.
2. R. Mohler: Practical Welding Technology: Industrial Press Inc., 2007, 221 pages.
3. L. F. Jeffus: Welding, Principles and Applications: CengageBrain.com, 100 pages.
4. R. W. Messler: Principles of Welding: john wiley and sons, 2002, 578 pages.
5. R. S. Mishra, M. W. Mahoney, Y. Sato, Y. Hovanski, R. Verma: Friction Stir Welding and Processing VI, John Wiley & Sons, 2011, 916 pages.
6. J. A. Goldak and M. Akhalaghi: Computational Welding Mechanics, Springer, 2005, 321 pages.
7. L. E. Lindgren: Computational Welding Mechanics: Thermomechanical and Microstructural simulations, Woodhead Publishing Limited, 2007, 231 pages.
8. N. T. Nguyen: Thermal analysis of welds, WIT Press, 2004, 334 pages.
9. M.-K. Besharati-Givi and P. Asadi: Advances in Friction-Stir Welding and Processing, Elsevier, 2014, 796 pages.
10. D. Lohwasser and Z. Chen: Friction Stir Welding: From Basics to Applications, Elsevier, 2009, 436 pages.
11. N. Kumar, R. S. Mishra and W. Yuan: Friction Stir Welding of Dissimilar Alloys and Materials, Butterworth-Heinemann, 2015, 134 pages.

List of publications

A. Journal Papers

1. D. Yaduwanshi, S. Bag and S. Pal: Effect of heat input on joint properties in plasma assisted hybrid friction stir welding of dissimilar aluminium-copper (**Under review**).

2. D. Yaduwanshi, S. Bag and S. Pal: On the effect of tool offset in hybrid friction stir welding of dissimilar aluminium-copper, ***Materials and Manufacturing Processes***, in press, 2017.

3. D. Yaduwanshi, S Pal and S. Bag: Numerical modeling and experimental investigation on plasma-assisted hybrid friction stir welding of dissimilar materials, ***Materials and Design***, 92, 166–183, 2016.

4. D. Yaduwanshi, S. Bag and S. Pal: Heat transfer analyses in friction stir welding of aluminum alloy, ***Proceedings of IMechE, Part B: Journal of Engineering Manufacture***, 29(10), 1722-1733, 2015.

5. D. Yaduwanshi, S. Bag and S. Pal: Effect of preheating in hybrid friction stir welding of aluminum alloy, ***Journal of Materials Engineering and Performance***, 23(10), 3794 - 3803, 2014.

B. Book Chapters

6. D. Yaduwanshi, S. Bag and S. Pal: Hybrid Friction Stir Welding of Similar and Dissimilar Materials, Edited by R. Ganesh Narayanan & Uday S. Dixit in ***Advances in Material Forming and Joining***, Springer Publishing, 2014.

7. S. Bag, **D. Yaduwanshi** and S. Pal: Heat transfer and material flow in friction stir welding process, Edited by Besharati-Givi & Asadi in ***Advances in Friction- Stir Welding and Processing***, Woodhead Publishing, Chapter 2, 2014.

C. Conference papers

8. D. Yaduwanshi, S. Pal and S. Bag: Effect of Preheating on Mechanical Properties of Hybrid Friction Stir Welded Dissimilar Joint, ***5th International and 26th All India Manufacturing Technology, Design and Research Conference AIMTDR 2014***, 12th-14th December, 2014, Guwahati.

9. D. Yaduwanshi, S. Pal and S. Bag: Dissimilar hybrid friction stir welding of pure copper and AA1100, ***Advancements in Welding, Cutting & Surfacing Technologies for Improved Economy, Reliability & Sustainable Environment, IIW International Congress 2014***, 9th - 11th April, 2014, New Delhi.

10. D. Yaduwanshi, S. Bag and S. Pal: Thermal analysis on plasma assisted friction stir welding of aluminum alloy, ***Recent Development in Welding and Joining Technologies, 7th Asia Pacific IIW International Congress***, 8th - 10th July, 2013, Singapore.

11. D. Yaduwanshi, S. Pal and S. Bag: Theoretical and Experimental Development of Plasma Assisted Friction Stir Welding, ***National Conference on Manufacturing: Vision for Future***, October 12-13, 2013, IIT Guwahati.

Acknowledgement

First of all I would give my admiration and thanks to the God for his showers of blessings throughout my life and during period of research work to complete the research successfully.

This thesis is the result of five years of work at IIT Guwahati whereby I have been accompanied and supported by many people. I would like to express my deep appreciation and sincere gratitude to both guides, Dr. Sukhomay Pal and Dr. Swarup Bag. They gave me many prospects to complete my research as well as lots of mental support. Their exuberance and integral view on research has made a deep impression on me. I owe them lots of gratitude for their guidance.

I would like to express my sincere gratitude to my doctoral committee chairman, Prof. P. S. Robi for his critically evaluating my research activities time to time. I would also like to thank my doctoral committee members Dr. S. N. Joshi and Dr. T. K. Mondal for their insightful comments and encouragement, but also for the hard question which incented me to widen my research from various perspectives. I am also grateful to head of the mechanical engineering department Prof. A. K. Das for providing excellent facilities and environment to conduct research work.

Secondly, I would also like to thanks Mr. Rituraj Saikia, Mr. Pranjaul Pal, Mr. Sanjib Sarma, Mr. Jiten Basumatary, Mr. Nip Borah and Mr. Saiffuddin Ahmed, for their support in carrying out the research work. I am very much thankful to the junior technical officer Mr. Chandan Banikya, and workshop technicians Mr. Dilip Chetri, Mr. Dhaneswar Khaklary, Mr. Minesh C. Medhi, Mr., Mrinal Sarma, Mr. Dipak Kr. Deka, Mr. Manoj Kr. Baishya, Mr. Nidul Saikia, and Mr. Upen Gohain for providing their expertise knowledge that greatly assisted the experimental work and their willingness to help me in fabricating the experimental setup precisely and accurately.

I am extremely grateful to my mother for her love, prayers, caring and sacrifices for educating and preparing me for my future. I am very much thankful to my wife and my son for their love, understanding, prayers and continuing support to complete this research work. Also I express my thanks to my sisters, brother and brother in law for their support and valuable prayers. My Special thanks goes to my friends Mr. Raj Kumar Surin, Mr. Puneet Raguwanshi and Mr. Pavan Maheta for their mental support and keen interest shown to complete this thesis successfully.

Feb. 2017

Deepak Kumar Yaduwanshi
IIT Guwahati